APPROVAL SHEET

Title of Dissertation: Theoretical Modeling and Multiwavelength Observations of Powerful Quasar Jets

Name of Candidate: Peter Breiding
Doctor of Philosophy, 2018

Dissertation and Abstract Approved: [signature]
Eileen Meyer
Assistant Professor
Physics

Date Approved: 6 Sept 2018

NOTE: *The Approval Sheet with the original signature must accompany the thesis or dissertation. No terminal punctuation is to be used.

Abstract

Title of Dissertation: Theoretical Modeling and Multiwavelength Observations of Powerful Quasar Jets
Dissertation Directed by: Dr. Eileen Meyer

The Chandra X-ray Observatory has discovered kpc-scale X-ray jets in many powerful quasars over the past 2 decades (Harris & Krawczynski, 2006). In many cases, these X-rays cannot be explained by the extension of the radio-optical spectrum produced by synchrotron-emitting electrons in the jet, since the observed X-ray flux is too high and/or the X-ray spectral index is too hard. A widely accepted model for the X-ray emission, first proposed by Celotti et al. (2001) and Tavecchio et al. (2000), posits that the X-rays are produced when relativistic electrons in the jet up-scatter ambient cosmic microwave background (CMB) photons via inverse-Compton scattering from microwave to X-ray energies (the IC/CMB model). However, modeling the X-ray emission in these jets with the IC/CMB model requires high levels of IC/CMB gamma-ray emission (Georganopoulos et al., 2006), which we have looked for using the Fermi/LAT gamma-ray space telescope. Another viable model for the large scale jet X-ray emission, favored by the results of Meyer et al. (2015) and Meyer & Georganopoulos (2014), is a second population of synchrotron-emitting electrons with up to multi-TeV energies. In contrast with the second synchrotron interpretation, the IC/CMB model requires jets with high kinetic powers (exceeding the Eddington luminosity in some cases), which remain highly relativistic ($\Gamma \sim 10$) up to kpc scales. In this thesis, I will present recently obtained deep gamma-ray upper-limits from the Fermi/LAT which rule out the IC/CMB model in a large sample of sources previously modeled with IC/CMB, and discuss the properties of the growing sample of non-IC/CMB anomalous X-ray jets and the implications for jet energetics and environmental impact. Additionally, I will present a model for the GeV emission observed in powerful gamma-ray flaring blazars, thought to originate several pc away from the central engine.

UNIVERSITY OF MARYLAND, BALTIMORE COUNTY

DOCTORAL THESIS

Multi-wavelength Observations and Theoretical Modeling of Powerful Quasar Jets

---

Author:
Peter BREIDING

Supervisor:
Dr. Eileen T. MEYER

A thesis submitted in fulfillment of the requirements
for the degree of Doctor of Philosophy

in the

Physics Department
University of Maryland, Baltimore County

September 28, 2018

Contents

Chapter 1

Introduction

1.1 A brief history of Active Galactic Nuclei

The history of Active Galactic Nuclei (AGN) dates back to the early 20th century and the discovery of galaxies beyond our own Milky Way, when astronomers were speculating on the nature of the "spiral nebula". These fuzzy, spiral-shaped celestial objects were thought to be either nearby gas clouds, or distant, unresolved collections of stars. These two views were famously debated in 1920 by Harlow Shapley and Heber Curtis, in what is known as "The Great Debate" at the Smithsonian Museum of Natural History. Answering this question was the primary motivation for Arthur Fath's spectroscopic observations of spiral nebulae in 1909 (Fath 1909) at the Lick Observatory in California. Fath found that most of these objects had a continuous spectrum with stellar absorption lines, consistent with the interpretation that these nebula were a collection of stars. However, he also discovered that one of the nebulae, NGC 1068, had bright emission lines with line widths up to $\sim$3000 km/s in addition to stellar absorption lines, akin to those seen in nearby gaseous nebulae like the Orion Nebula. This discovery was mysterious as it seemed to support both interpretations of these spiral nebulae.

The debate on the origin of these spiral nebulae was soon settled by Edwin Hubble in the early 1920s. He utilitzed Cepheid variables to confirm that the nebulae were indeed other galaxies (Hubble 1929). It was not until the work of Carl Seyfert that a systematic study of galaxies with bright emission lines began. Seyfert observed six galaxies whose nuclei showed a star-like spectrum, but with high-excitation emission lines superimposed. Some of the lines were broad, with line-widths reaching up to 8500 km/s, while others were narrow (Seyfert 1943). High-excitation nuclear emission lines are now known to be a prominent feature in AGN. However, AGN did not become a major focus in astronomy until the advent of radio astronomy.

The origin of radio astronomy can be traced back to the work of Karl Jansky, an engineer working at Bell Telephone Laboratories, who was investigating the sources of static affecting early radio communications. In the early 1930s, Jansky used an antenna mounted on a rotating platform in order to map the radio waves coming from different directions. As a result, Jansky discovered a diffuse signal that seemed to be associated with the plane of the Milky Way, in addition to static he associated with the activity of thunderstorms (Shields 1999).

By the late 1940s, improvements in radio astronomy led to the discovery of several discrete radio sources, some of which had exceedingly high brightness temperatures (in excess of 10^6 K), making a thermal origin for the radio emission very unlikely (e.g., Morris, Palmer, and Thompson 1957; Bolton and Stanley 1948). A few optical counterparts were identified, showing at least some of these radio sources to be associated with known galaxies (e.g., Bolton, Stanley, and Slee 1949; Baade and Minkowski 1954). Around 1960, the 3C and 3CR radio catalogs were completed, surveying the radio sky at 158 MHz and 178 MHz with a flux limit around 9 Jy. These surveys resulted in the identification of many more radio sources, but the low angular resolution and positional uncertainties prevented many of these from being identified with optical counterparts.

In 1963, the two radio sources 3C 48 and 3C 273 were identified with star-like sources which had a complex optical spectrum, showing a continuum with strong, broad emission lines which were not easily identifiable with known atomic transitions. However, Schmidt 1963 showed that the emission lines in 3C 273 were consistent with the Hydrogen Balmer and Mg II lines with the source at a redshift of z=0.16. Presuming the redshift was due to the expansion of the universe, this placed 3C 273 well outside our galaxy and implied a luminosity orders of magnitude above typical spiral galaxies, but coming from an unresolved point source. An early idea was that these discrete radio sources could be a peculiar kind of "radio star" within our galaxy due to their small angular sizes and rapid variability, leading to their naming as "quasi stellar radio sources" or quasars for short.

Soon, many more quasars with high redshifts were identified (e.g., Greenstein and Schmidt 1964a; Greenstein and Schmidt 1964b). The consensus that developed among astronomers was that these redshifts were cosmological in origin, placing quasars as extragalactic objects. However, the question as to what quasars *were* was puzzling due to the large luminosities implied by their cosmological redshifts, as well as their rapid variability and small angular sizes. Many explanations were put forth, including chain reactions of supernovae in dense star clusters at the cores of galaxies, pulsar storms, and super-massive stars (Shields 1999). However, the eventual description that emerged and survived scrutiny to this day was the accretion of matter onto a super-massive black hole (Salpeter 1964; Zel'dovich 1964) in the form of an accretion disk. This idea was initially ignored, but gained favor after Lynden-Bell (1969) argued that accretion of matter onto a black hole was capable of producing the high quasar luminosities for the right combination of black hole mass and accretion rate (typically on the order of 10^6-10^{10}M$_\odot$ and a few M$_\odot$/yr). In addition, he argued that the thermal continuum resulting from such an accretion disk could result in photo-ionization and broad-line emission, suggesting that this might be the process behind both Seyfert galaxies and quasars. The widespread acceptance that accretion of matter onto a black hole could be the mechanism powering quasars started to grow with the discovery of stellar mass black holes in our own galaxy. Astronomers now believe that this black hole accretion model is the physical mechanism behind all forms of AGN.

1.2 Current picture of AGN

In Figure 1.1, I show a cartoon of the currently accepted model for AGN. At the heart is the super massive black hole (SMBH), which it the central engine behind all AGN activity. Gravitational potential energy serves as the main energy source for the AGN luminosity. Gas and dust in the accretion disk is pulled towards the black hole as it loses angular momentum through viscous or turbulent processes, heating up as the gravitational energy is converted into thermal energy. The disk glows in the optical/UV part of the spectrum (which is referred to as the "big blue bump" in AGN spectra).

This accretion disk provides a photo-ionizing continuum which illuminates the surrounding clouds of gas, which subsequently produce strong optical/UV emission lines. The clouds of gas within $\sim$0.1 pc from the black hole are rapidly orbiting the black hole in Keplerian orbits, forming what is known as the Broad Line Region (BLR), where the name reflects the observed line widths. Due to Doppler broadening, the BLR clouds can produce emission lines with widths on the order of 10^3-10^4km/s (Gaskell 2009). Much further out (hundreds to thousands of pc) are lower density and slower moving clouds, which consequently have emission lines of a narrower width. This region is known as the Narrow Line Region (NLR). The gas densities for the broad and narrow line regions are inferred from the ratio of line strengths we observe for each. In the case of narrow lines, we observe both permitted and forbidden emission lines, while we only observe permitted broad lines (Osterbrock and Mathews 1986). This distinction between permitted and forbidden lines is quantum mechanical. Forbidden lines have very low transition probabilities compared to permitted lines, and therefore the time it takes for the transition to occur is substantially longer. For a high density gas, collisional de-excitation keeps the forbidden transitions from occurring, while in a low density gas the timescale between collisions can be substantially longer, and the atoms will be able to emit forbidden lines. This is the reason the NLR gas clouds are believed to be much lower density than BLR clouds.

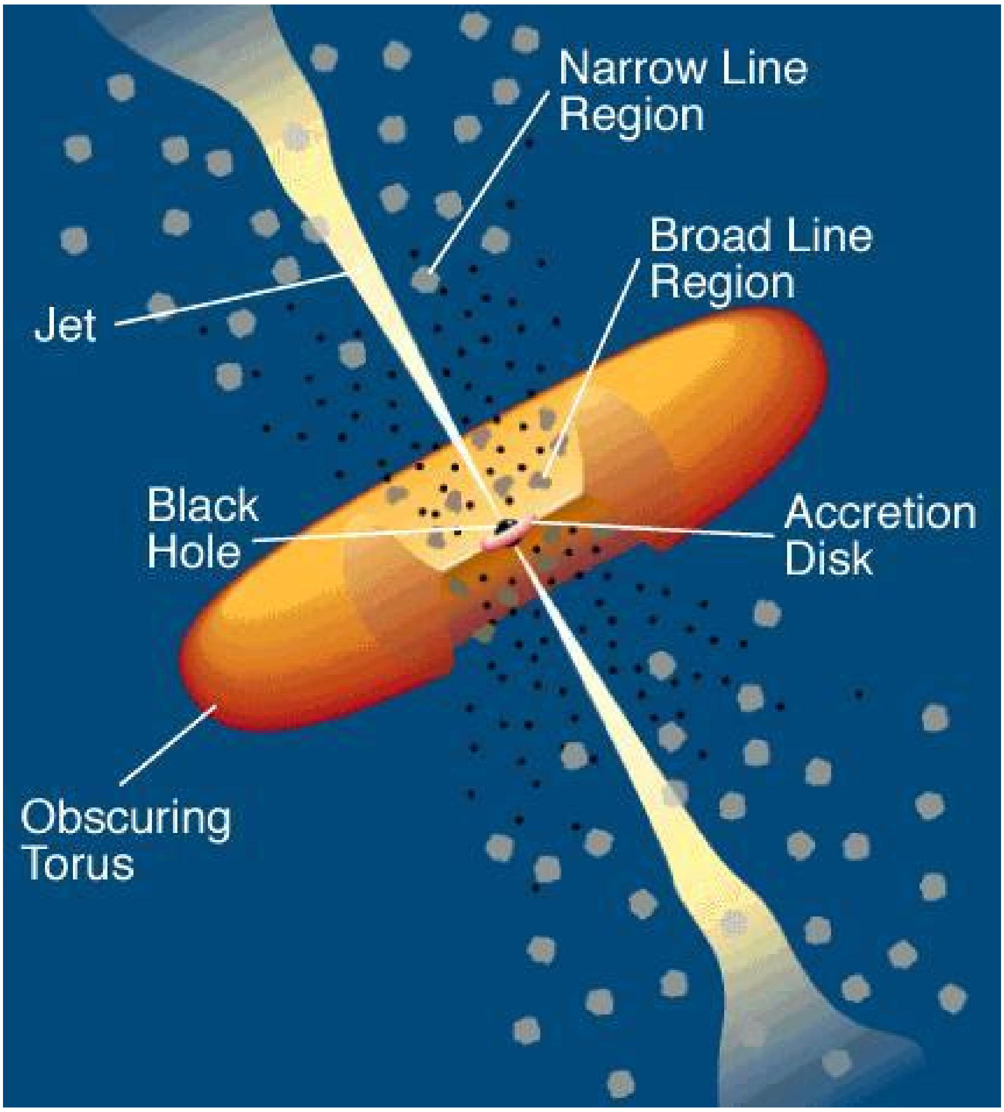

FIGURE 1.1: Cartoon model of AGN, not drawn to scale (adapted from Urry and Padovani 1995).

Early in AGN studies, a puzzling observation was the presence of broad lines in some, but not all, AGN (Khachikian and Weedman 1974). Those with broad lines are referred to as type I AGN, while those without are referred to as type II. In what is now referred to as the unified model of AGN, it was proposed that the lack of broad lines in type II AGN could be understood as a viewing angle selection effect. Antonucci and Miller (1985) introduced the idea of an obscuring toroidal structure of dust in the plane of the accretion disk known as the molecular torus, which when viewed edge on would hide the broad lines from the direct view of the observer. This is reflected in the above cartoon picture for AGN (Figure 1.1), where the BLR is a small region contained within about 0.1 pc of the central SMBH. In this picture, when the AGN is seen edge on with respect to the accretion disk and molecular torus, the molecular torus blocks the BLR from view. This leads to the source lacking visible broad lines and being classified as a type II AGN. When the AGN is seen face on, the broad lines are now visible, and the source is seen as a type I. This view was greatly supported by the observation of broad emission lines in the type 2 AGN NGC 1068 when viewed in polarized light (Antonucci and Miller 1985). The interpretation was that electrons in the polar regions scattered the obscured broad emission lines into the observer line of sight so they were visible in polarized light, but not otherwise. This idea of the viewing angle determining the type of AGN we observe has proved crucial to our understanding of AGN, including those with jets.

In about 10% of AGN there are giant collimated jets of radio-emitting plasma emanating from the SMBH as shown in Figure 1.1. These jets can extend to many times larger than the host galaxy and are the subject of this thesis. In the next section, I will briefly go through the different classes of AGN, which are based on both intrinsic and observational (i.e., viewing angle) differences.

1.3 AGN taxonomy

The term AGN has come to represent a broad class of astrophysical sources, ranging in apparent luminosity[1] from 10^{41}-10^{48} erg s^{-1}, with black hole masses ranging from $10^6 - 10^{10} M_{\odot}$. Historically, AGN have been separated into two classes, radio-loud and radio-quiet. Radio-loud AGN constitute $\sim$ 10% of AGN, and are defined as having radio (5 GHz) to optical (B-band) flux ratios in excess of 10 (Kellermann et al. 1989). To first order, the radio-loud sources correspond to those AGN with observed radio-emitting jets, while the radio-quiet sources are non-jetted. However, some argue radio-quiet sources may simply have much smaller and less powerful jets (Ulvestad,

[1]The convention in determining the luminosity of the source is to assume isotropic emission. Assuming a luminosity distance of D and observed flux from the source of F, the luminosity would be given as $L = F \times 4\pi D^2$. This of course does not give the actual luminosity for sources which have anisotropic emission, as is thought to be the case for jets in AGN.

Antonucci, and Barvainis 2005). I will first go over the main classes of radio-quiet AGN, before focusing on the radio-loud sources.

1.3.1 Radio-quiet AGN

Seyfert galaxies (named after Carl Seyfert who pioneered their study in the 1940s) were the first detected AGNs, and are the most common class of AGN in the local universe (Osterbrock 1991). They are lower luminosity AGN, with the generally accepted cutoff of absolute B-band optical magnitude M_B>23 separating them from the quasar class (Schmidt and Green 1983). They often appear in optical imaging as spiral galaxies with a very bright core (or nucleus), in contrast with quasars where the host galaxy is not visible because of the bright core (Adams 1977). The cores of Seyfert galaxies have an optical spectrum very similar to that of quasars, showing a strong blue continuum with high excitation emission lines. Seyfert galaxies are further divided into type I and II sources based upon their nuclear emission lines (Khachikian and Weedman 1974). Seyfert I galaxies show both narrow and broad emission lines, while Seyfert II galaxies show only narrow emission lines. This is now understood to be primarily due to the relative angle of the observer's line-of-sight to the AGN, though recent work has shown there may be some intrinsic differences (e.g., LaMassa et al. 2015). Type I sources, where both broad and narrow lines are observed, are those in which our line-of-sight is unobstructed by the molecular torus and the broad emission lines are free to propagate to us.

The other radio-quiet AGN is the radio-quiet quasar or Quasi Stellar Object (QSO). It is now commonplace that the term quasar is synonymous with QSO, and when unqualified, refers exclusively to radio-quiet sources. In the radio-loud AGN community, quasars can be used for powerful, broad-lined radio-loud sources. Similar to Seyfert galaxies, radio-quiet quasars show high excitation emission lines, where those with broad emission lines are referred to as type I, and those with only narrow emission lines are referred to as type II (with the same angle-dependent interpretation for these types). However, unlike Seyfert galaxies, the host galaxies of radio-quiet quasars are typically elliptical galaxies and are too faint compared to the extremely bright nucleus to be seen in images (McLure et al. 1999).

1.3.2 Radio-loud AGN

Radio-loud AGN are the sub-class of AGN hosting bi-polar relativistic jets of plasma, almost universally found in massive elliptical galaxies (Matthews, Morgan, and Schmidt 1964). The first set of AGN to be identified with optical counterparts were radio galaxies (e.g., Bolton, Stanley, and Slee 1949; Baade and Minkowski 1954). The term 'radio galaxies' refers to AGN with misaligned radio jets, such that considerable structure can be seen in their jets, and optical imaging clearly reveals the host galaxy in nearby sources. Fanaroff and Riley (1974) divided radio galaxies into two classes based upon their observed morphology, FR I and FR II, where it was shown that the FR II sources are more radio luminous than the FR I sources. FR I type sources have plume-like jets which are brighter towards the base of the jet. FR II type sources have highly collimated jets, which are "edge-brightened" and terminate in bright hot-spots which are thought to be where the jet is slamming into the inter-galactic medium (Bridle et al. 1994). Often, FR II sources also show giant lobes of radio emission surrounding their hot-spots, which are thought to be slowed (non-relativistic) plasma flowing back towards the galaxy after escaping the hot-spots. In Figure 1.2, I show typical examples of FR I and FR II radio galaxies.

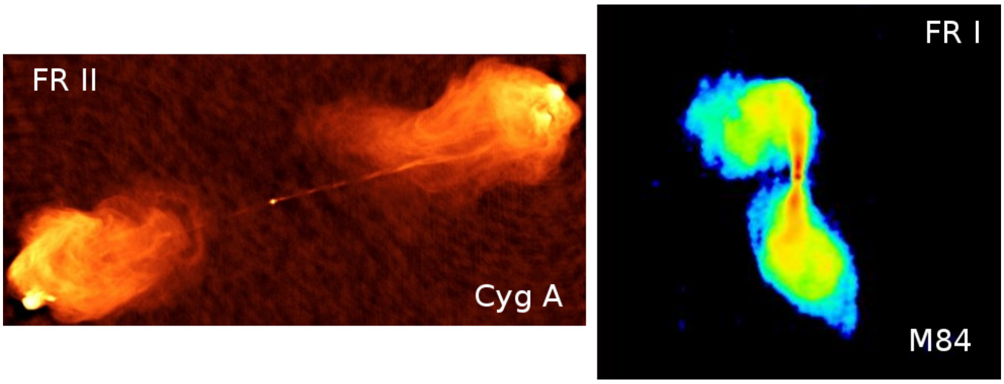

FIGURE 1.2: Shown at left is the radio galaxy Cygnus A, a typical FR II source with a long, highly collimated and barely visible jet ending in bright hot-spots and giant lobes of radio emission (image from http://images.nrao.edu). Shown at right is a typical FR I source, M84, with a plume-like jet brighter towards the base than the end of the jets (image from http://www.jb.man.ac.uk/atlas).

The other major class of radio-loud AGN are the blazars. Unlike the radio galaxies, blazars have their jets pointed at small angles with respect to our line-of-sight. Classically, blazars are divided into flat spectrum radio quasars (FSRQs) which have optical spectra containing broad emission lines, and BL Lacs which typically have featureless optical spectra. Due to an effect known as relativistic beaming (discussed further in section 1.5.3), blazars appear orders of magnitude brighter than radio galaxies as the radiation produced by their jets is enhanced along the axis of motion.

Blazars are observed to be "core dominated", meaning the bulk of their observed radio emission is associated with the unresolved radio core, where the plasma is highly relativistic (Lister et al. 2009). This is in contrast with radio galaxies, which are observed to be "lobe dominated", where the bulk of the radio emission is associated with the extended and isotropic emission of the radio lobes (Meyer et al. 2012). Under the unified model of Urry and Padovani (1995), the orientation of the jet to the line-of-sight completely accounts for the higher core-dominance of blazars in comparison to radio galaxies. Since blazars are very nearly aligned to the line-of-sight, the enhanced emission from the relativistically beamed radio core swamps the emission from the lobes. When the jets are pointed away from our line-of-sight, as in misaligned radio galaxies, the radiation from the core is beamed away from us, and it is the isotropic emission from the lobes which begins to dominate.

Sources which are believed to be intermediate in alignment between radio galaxies and blazars are steep spectrum radio quasars (SSRQs). The SSRQs show a steeper radio spectrum due to an increased contribution from their lobes, which tend to have steep radio spectra compared to the radio core, which typically has a much flatter radio spectrum.

The model of AGN described in section 1.2 allowed astronomers to unify this zoo of AGN with all of their distinct properties under a common physical picture, namely the accretion of matter onto a SMBH. In the next section, I will focus on the evidence for these black holes, and their role as the drivers of AGN activity.

1.4 The Central Engine: The Super Massive Black Hole

Early observations showed quasars to be both very luminous due to their cosmological redshifts and highly variable. Bright quasars can reach bolometric luminosities of $\sim 10^{47}$erg s^{-1} (Trakhtenbrot et al. 2011) and variability timescales on the order of days (Peterson 2001). The variability timescale gives an upper limit on the size of the emitting region, because the luminosity can only change substantially on timescales greater than the light-crossing time of the emitting region in order for the region to be causally connected and obey special relativity. When viewed in X-rays, it is common to see large amplitude variability on the timescale of days (McHardy 1989), which corresponds to emitting regions smaller than light days in diameter, comparable to the size of the solar system. The only model which has survived to this date capable of producing such extreme luminosities in such small regions is the accretion of matter onto a super massive black hole (Lynden-Bell 1969; Salpeter 1964; and Zel'dovich 1964).

1.4.1 Accretion onto SMBHs and the Eddington limit

Accretion of matter onto compact objects, like black holes, is the most efficient means of energy production known. For a black hole of mass M, accreting at a rate of $\dot{M}$, the accretion luminosity can be written as

$$L_{acc} = \eta \dot{M} c^2, \tag{1.1}$$

where η represents the efficiency of conversion of the rest mass energy of the accreting material into radiation. While η is only around 0.007 for nuclear fusion, it is greater than 0.06 for accreting black holes (Laor and Netzer 1989), and depends on the degree of rotation of the black hole and other details of the accretion process which are not well-understood.

Based on the above equation, it would seem arbitrarily high accretion luminosities would be obtained by suitably high accretion rates. However, this is not the case. As accretion luminosity increases, the radiation pressure becomes strong enough to overcome the force of gravity and halt accretion, mostly through the Thomson scattering on free electrons. For the case of a spherically symmetric and steady accretion flow of fully ionized hydrogen onto a mass M, an idealized limiting luminoisty can be derived, known as the Eddington luminosity:

$$L_{Edd} = 1.3 \times 10^{38} (M/M_{\odot}) erg\ s^{-1}. \tag{1.2}$$

When accretion occurs only over a fraction f of a compact object, but otherwise depends only on radial distance, the Eddington luminoisity is modified by a factor f (Frank, King, and Raine 2002). Similarly, if there is a substantial number of elements besides hydrogen which have retained some bound electrons, the effective cross section is increased due to the absorption of photons in spectral lines. Thus, both of these act to decrease the Eddington luminosity, and it should not be taken as an absolute limit. An important thing to note is that the Eddington luminosity depends on the mass of the accreting object. Higher mass objects have a stronger gravitational potential, and can therefore have higher accretion luminosities before reaching their Eddington limits. Restricting the accretion luminosity to be less than the Eddington limit, therefore, implies extremely high masses of the accreting black hole. For bright quasars with luminosities of 10^{47}erg s^{-1}, Eddington-limited accretion implies a central black hole mass greater than $\sim 10^9 M_\odot$. Therefore, the masses implied for these accreting black holes in AGN are truly very massive, and this is why the moniker super massive black hole is used to describe them.

1.4.2 Evidence for SMBHs

From early on in the study of quasars, we have known them to be more numerous at higher redshift relative to their co-moving volume (Schmidt 1968), with the now believed peak of quasar activity believed to be at $z \sim 2-3$ (Schmidt, Schneider, and Gunn 1995). If SMBHs are required in all AGN, this means there should be wealth of dormant or non-active SMBHs in the local universe, residing in the centers of non-active galaxies.

One of the primary methods used to look for these SMBHs in local galaxies is their effect on the dynamics of nuclear stars within the black hole's gravitational influence. However, since the sphere of influence for these SMBHs is relatively small (sub-pc), this method has only been very useful for nearby galaxies with telescopes of very high angular resolution. In the 1980s, several groups reported the first few black hole detections based upon optical absorption-line spectroscopy of unresolved nuclear stellar populations. The Hubble Space Telescope (HST) solidified these early detections and added many more due to its improved angular resolution, and is now responsible for a majority of SMBH kinematic detections (see Kormendy and Ho 2013 for a review). However, the SMBH in the center of our own Milky Way galaxy still remains the strongest observational case for a SMBH. Since the galactic center is so close (~8 kpc), we can resolve the individual stars which orbit its center, referred to as Sgr A*. Based upon the proper motions of the nuclear stars, we have been able to deduce a central mass of $\sim 4.3 \times 10^6$ $M_\odot$, within a region < 122 AU (Genzel, Eisenhauer, and Gillessen 2010). In principle, this density might be achieved by a dense cluster of stars, but the cluster would be dynamically unstable over the timescale of millions of years (Maoz 1998). The new Event Horizon Telescope is an international collaboration, consisting of an array of radio telescopes around the planet, with the aim of directly observing the immediate environment of Sgr A*, with angular resolution comparable to its event horizon (the surface beyond which nothing escapes). This would not only teach us a lot about the physics of black holes, but would be the most direct evidence for the existence of a SMBH.

In the context of AGN, additional techniques are available to probe the physical scales of the central SMBH. In a technique known as reverberation mapping, variations in the continuum flux from the central accretion disk can be correlated with broad line emission from the BLR, which helps to constrain the size of the BLR (Blandford and Payne 1982). When combined with an estimation of the broad-line widths which are assumed to be velocity broadened due to the central SMBH, the black hole mass can be measured using the virial theorem (assuming the broad line clouds are moving on roughly Keplerian orbits). There are currently several dozen AGN with black hole masses determined by this method, and the masses range from millions to billions $M_{\odot}$ (Bentz et al. 2009). Combining the requirement of such large masses with the observations of rapid variability for the central AGN (on the order of days or less in some cases) amounts to strong evidence in general for the SMBH paradigm.

1.4.3 Launching the Jet

Jets are believed to be powered either from the gravitational energy of accreting matter onto the SMBH or by the rotational energy of the black hole itself. Blandford and Payne (1982) argue that centrifugal forces could allow the ejection of matter from the accretion disk along magnetic field lines frozen into and emanating from the disk, at the cost of angular momentum of the accretion disk. Alternatively, Blandford and Znajek (1977) argue that a black hole rotating in the magnetic field supported by the accretion disk can give rise to a Poynting flux (referring to energy stored in electromagnetic fields) at the cost of black hole spin energy. Some argue that both accretion and black hole rotational power could be important in jet formation (e.g., Begelman, Blandford, and Rees 1984). One observation in support of the disk-powered model is the linear correlation seen between jet power and accretion power for AGN (e.g., Willott et al. 1999). Meanwhile, recent numerical simulations have shown that only the spin power of the black hole is capable of producing jets with more power than contained in their accretion disks (Tchekhovskoy, Narayan, and McKinney 2011), which has been strongly indicated for several AGN (Rawlings and Saunders 1991; McNamara, Rohanizadegan, and Nulsen 2011).

While we are still uncertain of the mechanism giving rise to these jets, another open question which we are still trying to answer is that of their composition. Observations of polarized radio and optical emission in AGN jets is strong evidence for synchrotron emission of electrons gyrating in a magnetic field. However, these electrons have Lorentz factors $\gtrsim 2000$, and radiative losses from inverse-Compton scattering the cosmic microwave background preclude them from surviving the observed length of most jets (Harris and Krawczynski 2007). Therefore, they are not responsible for the bulk of the mechanical energy transported from the SMBH to the hot spots and lobes in radio-loud AGN. I will refer to material responsible for the energy transport in jets as the jet medium, which is not necessarily the medium giving rising to the non-thermal emission we observe. The main contenders for the jet medium are protons, lower energy electrons and positrons, and Poynting flux. Neutral particles, such as neutrons, have been suggested for the underlying medium (Atoyan and Dermer 2004), but this model has difficulties both with forming the jet and observations of jet bending for many AGN. The reality may be a mix between the above possibilities, or the jet medium transitioning from one state to another. Sikora et al. (2005) suggest the jet is initially Poynting-flux dominated, but quickly transitions to being particle-dominated with protons as the main energy carrier. It will take more theoretical and observational work to help answer the question of what these jets are made of.

1.5 Radiative Processes in AGN Jets

The first AGN jet resolved by a telescope dates back to the 1918 discovery of the 20″ optical jet associated with M87 in the Virgo Cluster (Curtis 1918). It was not until the latter half of the twentieth century and the methods of radio interferometry before radio telescopes had sufficient angular resolution to clearly identify these jets (e.g., Northover 1973; Turland 1975; van Breugel and Miley 1977). We now know these jets can extend from tens of pc in the most compact sources (O'Dea 1998) to a few Mpc in the case of giant radio galaxies (Dabhade et al. 2017). Telescopes with resolutions on the arcsecond scale were needed in order to unambiguously image these jets.

We now know that roughly 10% of AGN host jets, and these jets can emit across the entire electromagnetic spectrum, from radio up to gamma-rays via non-thermal emission processes. In the following sections, I will present an overview of jet observations pertinent to this thesis and how they have informed our understanding of them. However, first we need to discuss some basics of radiative processes and relativistic beaming which are essential to understanding the nature of jets in AGN (largely following the treatment in Rybicki and Lightman 1979).

1.5.1 Synchrotron Emission

Over a broad range of radio wavelengths, AGN jets have a power-law spectral shape of the form $F_\nu \propto \nu^{-\alpha}$, where F_ν is the flux density, ν the frequency, and α the spectral index. We will use this definition of the spectral index for the remainder of the thesis. In addition, these jets often show a high degree of linear polarization, up to 30% or more in some cases (e.g., Angel and Stockman

1980; Scarpa and Falomo 1997). For these reasons, it is believed the radio emission in AGN is due to synchrotron radiation of relativistic electrons. Charged particles moving relativistically in a magnetic field are accelerated by the Lorentz force and gyrate around the magnetic field in a helical trajectory. As a consequence of this acceleration, the charged particles emit what is called synchrotron radiation. If the particle is an electron and has an energy $E = \gamma m_e c^2$ (where γ is the Lorentz factor and m_e is the electron mass), then the critical frequency at which most of the radiation due to synchrotron emission occurs can be written as:

$$\nu_c = \frac{3\gamma^2 eB}{4\pi m_e c} \tag{1.3}$$

Here, B is the strength of the magnetic field, e is the electron charge, and c is the speed of light. To first order, the spectrum emitted from a single electron can be considered monochromatic at ν_c, though it really has an exponential decrease past ν_c and a form $\propto \nu^{1/3}$ at frequencies much less than ν_c. To produce radiation at $\nu \sim 10\ GHz$ in a magnetic field of $B \sim 10^{-4}\ G$ requires electrons with $\gamma \sim 10^5$, which is highly relativistic (values of are 10-10^7 are typical for jets). Highly efficient particle acceleration must be at work to accelerate electrons to such high energies in these jets.

When one considers an ensemble of electrons, with a power-law electron energy distribution of the form $n(\gamma) \propto \gamma^{-s}$ (where $n(\gamma)$ is the number density of electrons and s some index), the spectrum of synchrotron radiation emitted also has a power-law, with the form $F_\nu \propto \nu^{-\alpha}$ (where $\alpha = \frac{s-1}{2}$). In addition, synchrotron radiation from a population of electrons can reach polarizations of up to 75% if the electrons are in a homogeneous magnetic field, but can be significantly reduced if the emitting region contains a (more realistic) inhomogeneous magnetic field.

The power emitted by a single electron through synchrotron radiation can be written as:

$$P_{synch} = 4/3\sigma_T c\gamma^2\beta^2 U_B \tag{1.4}$$

Here, β is the speed of the electron in units of c, σ_T is the Thomson cross section, and U_B is the energy density of the magnetic field. Using this power, the cooling time of such an electron can be expresses as $t_{cool} = \frac{E}{P_{synch}} = 2.4 \times 10^5(\gamma/10^4)^{-1}(B/10^{-4}G)^{-2}yr$. For low frequency radio emission, this timescale can be much longer than the age of the radio source. However, for higher frequencies, such as optical or X-ray emission, this timescale can be very short. As I will come back to later in the thesis, such high frequency synchrotron radiation many kpc from the central black hole implies local in situ particle acceleration.

Finally, since the frequency of synchrotron radiation depends on both the electron Lorentz factor and magnetic field, these two quantities cannot be measured independently. The common practice is to assume an equipartition between the magnetic field and electron energy which is the minimum energy state for the system (Burbidge 1959). Such an assumption can allow one to calculate the electron energy with an assumed equipartition magnetic field value. However, this assumption may not hold in all cases.

1.5.2 Inverse-Compton Scattering

In addition to emission processes, scattering of photons by electrons can also be an important process for our understanding the observed spectrum of jets. In the case of a relativistic electron encountering a low energy photon, the electron is able to scatter the photon to a higher energy in a process known as inverse-Compton scattering. For photons with energies $h\nu \ll m_e c^2/\gamma$, the Thomson cross section can be assumed in the rest frame of the electron, and the approximate energy of the photon after scattering is given by $E_f \sim \gamma^2 E_i$ (where E_i is the initial photon energy). The resulting power in scattered radiation for a single electron in a photon field of energy density U_{ph} can be written as

$$P_{IC} = 4/3\sigma_T c\gamma^2\beta^2 U_{ph}. \tag{1.5}$$

When combined with the above power for synchrotron radiation, the ratio of synchrotron to inverse-Compton radiation for an electron can be written as $P_{synch}/P_{IC} = U_B/U_{ph}$. Therefore, it is the relative strength of the photon field to magnetic field that dictates which process is more significant in terms of energy output.

1.5.3 Relativistic Beaming

For a source of radiation which moves relativistically (i.e., velocities approaching the speed of light), as is thought to be the case in AGN jets, an effect known as relativistic beaming or Doppler boosting becomes important. Relativistic beaming enhances the power emitted along the direction of motion of the source while decreasing the power emitted into large off-axis angles. The effect is due to a combination of the relativistic aberration of angles, the Doppler blue-shift of the radiation frequency, and the shortening of arrival times for photons. When a source of radiation is relativistically beamed, the observed flux is modulated by the relativistic Doppler factor, given by:

$$\delta = \frac{1}{\Gamma(1 - \beta cos\theta)} \tag{1.6}$$

Here, β is the speed of the source in units of the speed of light, θ is the angle between the direction of motion and the line-of-sight, and Γ is the Lorentz factor of the source given by $\Gamma = 1/\sqrt{1-\beta^2}$. For sources where Γ is on the order of a few or greater, relativistic beaming can have a huge impact on the observed luminosity of a source compared to its intrinsic luminosity. In the case of isotropic emission in the rest frame of the emitting plasma, as is thought to be the case for synchrotron emission, the following equation (Dermer 1995) gives the expected relativistic beaming enhancement to the observed luminosity:

$$L_{obs} = L_0 \delta^{n+\alpha}. \tag{1.7}$$

Here, L_{obs} is the observed luminosity and L_0 is the intrinsic luminosity of the source in the rest frame of the flow. The index n takes the value of 2 in the case of a continuous flow and 3 for discrete moving blobs, while α is the spectral index of the observed radiation (Lind and Blandford 1985). In the case of inverse-Compton scattering on external photon fields to the jet (also known as external Compton (EC) scattering), the expected beaming pattern is different since the emission is no longer expected to be isotropic in the rest frame of the plasma, and in fact the degree of beaming is enhanced. For the case of EC scattering on an isotropic external photon field such as the cosmic microwave background, the beaming equation is now given by the following relation (Georganopoulos, Kirk, and Mastichiadis 2001; Dermer 1995):

$$L_{obs} = L_0 \delta^{n+1+2\alpha}. \tag{1.8}$$

Relativstic beaming accounts for why many jetted AGN appear to be one sided (Urry and Padovani 1995). It is believed there are really two jets, but the jet coming towards us is enhanced by relativistic beaming while the jet moving away from us has the radiation beamed out of our line-of-sight and is said to be "de-beamed". However, the AGN in which relativistic beaming effects are most significant are the blazars, which are the brightest class of AGN we observe. Enhancements to the observed luminosity from relativistic beaming become significant for high Doppler factors, which is the case for small angles to the line-of-sight and large bulk flow Lorentz factors, Γ. Therefore, in order for relativistic beaming to account for the large apparent luminosities of blazars, we should expect them to be closely aligned to the line-of-sight, and have large Γ values. In the next section I will go over some direct evidence for these properties of blazar jets.

1.6 Superluminal Motion

In the early 1970s, the peculiar discovery was made that some AGN jets showed emission components which moved with velocities greater than the speed of light, apparently contradicting special relativity (e.g., Whitney et al. 1971; Cohen et al. 1971). This phenomenon is now understood to be a geometric effect which results from the jet being oriented at a small angle with respect to our line-of-sight. In Figure 1.3, I show the geometry behind this effect. A source of photons has a velocity v=βc, and moves at an angle θ with respect to our line-of-sight at Earth (where c is the speed of light). The source emits photons for the time it takes to travel from position A to position B, Δ t_e. Since the photons emitted at position A have already traveled a distance cΔt_e towards the observer, the photons emitted at B only lag behind those emitted at A by a distance of vΔ $t_e\cos\theta$. Therefore, an observer at Earth will see the source emitting photons for the time period of $\Delta\ t_{app} = \Delta t_e(1 - \beta\ \cos\theta)$. When combined with the apparent displacement of the source during this time interval, vΔ $t_e\sin\theta$, the source has an apparent velocity given by:

$$\beta_{app} = \frac{\beta sin\theta}{1 - \beta cos\theta} \tag{1.9}$$

It is easy to see as $\beta \to 1$ and $\theta \to 0$, β_{app} can exceed one, and the motion is *apparently* superluminal. However, the source of radiation is still moving at sub-relativistic speeds; it only appears to be superluminal due to the light travel time arguments given above. β_{app} is maximized for $\beta = \cos\theta$, giving $\beta_{app} = \beta\Gamma \approx \Gamma$. Here, Γ is the Lorentz factor of the source. This means that a measurement of β_{app} actually represents a lower limit on Γ. Similarly, the requirement that the source be moving at velocities less than the speed of light leads to an upper limit on θ given by $\theta < \cos^{-1}\left(\frac{\beta_{app}^2-1}{\beta_{app}^2+1}\right)$.

In Figure 1.4, I show the example of the M87 jet where the authors measured apparent velocities on kpc scales up to 6 times the speed of light using HST observations (Biretta, Sparks, and Macchetto 1999). In this case, the authors found an angle of the jet to the line-of-sight less than 19° and a lower limit on Γ of 6. Very long baseline interferometry (VLBI) observations have shown

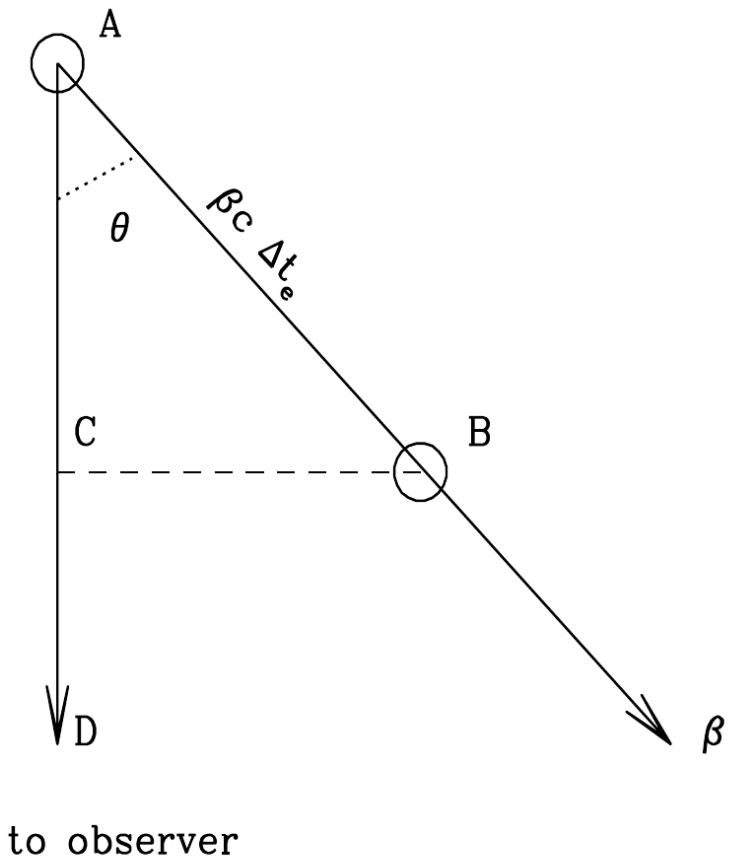

FIGURE 1.3: Figure adapted from Ghisellini (2000) showing the geometry behind apparent superluminal motion.

that superluminal velocities are common occurence in blazar jets, providing direct evidence that they are closely aligned to the line-of-sight. VLBI is a radio interferometric technique which uses very long baselines among multiple radio telescopes to reach extremely high angular resolutions. In the case of the Very Long Baseline Array (VLBA), these baselines can reach up to 8,000 km (across continents) yielding angular resolutions on the sub-milliarsecond scale, which probes the inner pc-scale region of blazar jets (Jorstad et al. 2017). In a VLBA study monitoring the apparent motions of pc-scale radio features at the base of 135 radio-loud AGN, 123 of which were blazars, Lister et al. (2009) found a peak in the distribution of maximum apparent speed around 10c, with some cases extending up to 50c. This is strong evidence for the interpretation that blazars are closely aligned to the line-of-sight. In the next section, I will give a brief overview of blazars, with a focus on their observed spectra.

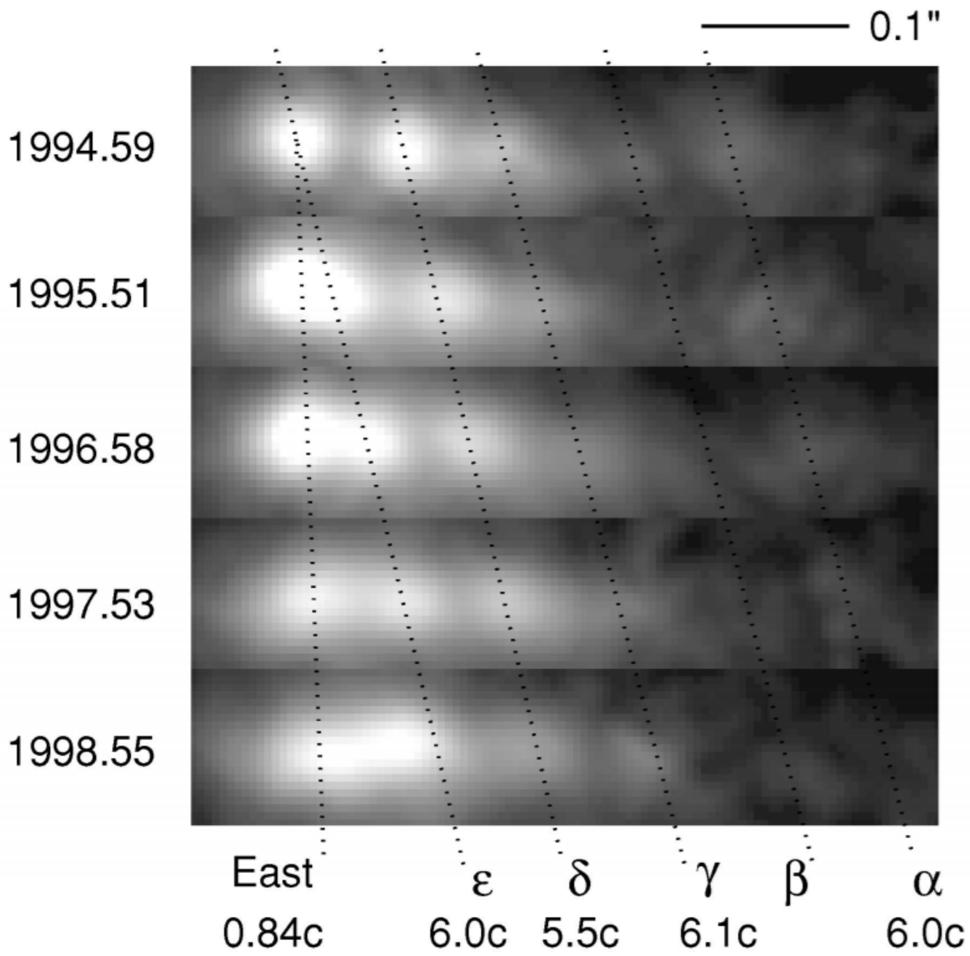

FIGURE 1.4: Figure adapted from Biretta, Sparks, and Macchetto (1999) showing superluminal motion in the jet of M87 using multiple HST observations.

1.7 Blazars

Blazars are a class of radio-loud AGN which emit radiation across the entire electromagnetic spectrum (from radio up to high energy gamma-rays), with associated variability seen at all wavelengths (Urry 1996; Raiteri et al. 2012). The observed variability can be very rapid, extending down to hours (Kataoka et al. 2001; Sobolewska et al. 2014) and even minutes at gamma-ray energies (e.g., Aharonian et al. 2007). In particular, powerful flares of gamma-ray emission are a very common occurence in blazars (Abdo et al. 2010). The rapid variability combined with their large luminosities are strong indicators that blazar emission originates in relativistic jets pointed at small angles to the line-of-sight (Blandford and Rees 1978; Schlickeiser 1996). As a result, blazar spectra are dominated by the emission from the unresolved core associated with the inner pc-scale portion of the jet, rather than extended emission associated with the kpc to Mpc scale jet or lobes (Urry and Padovani 1995).

Blazar spectra are dominated by two broad non-thermal components (Fossati et al. 1998). The lower-energy component extending from the radio to UV or X-ray energies in some cases (Costamante et al. 2001) is believed to be synchrotron radiation from a population of relativistic electrons, usually assumed to have a power-law distribution in number density with respect to energy. The major piece of evidence in favor of the synchrotron origin for this component is the high degrees of polarization observed, often as high as 50% (e.g., Angel and Stockman 1980; Scarpa and Falomo 1997). However, the origin of the higher-energy component which covers X-ray and gamma-ray energies is still a matter of debate.

In Figure 1.5, I show the average SEDs for a sample of 126 blazars where these two humps are clearly visible, taken from the paper Fossati et al. (1998). The authors found that when they binned the average SEDs by the radio power, transitioning from higher power to lower-power jets resulted in an overall decreasing luminosity, an increasing peak frequency for both spectral components, and a transition from mostly FSRQs to BL Lacs. This anti-correlation between the synchrotron peak luminosity and synchrotron peak frequency is referred to as the blazar sequence. One interpretation of this sequence is that higher power jets may have more efficient radiative cooling, leading to lower peak frequencies (Ghisellini et al. 1998). In subsequent work, Meyer et al. (2011) expanded the blazar sequence into an envelope with the inclusion of radio galaxies. Meyer et al. (2011) showed that two populations, roughly corresponding to FSRQs and BL Lacs, formed the two upper edges of the envelope, with more misaligned radio galaxies filling in the envelope.

There are two broad classes of models which are invoked to explain the origin of the high-energy component, *leptonic* and *hadronic* (for a review of the applications of these models to blazars, see Boettcher 2010). Hadronic models assume there are a substantial number of ultra-relativistic protons in the jet which contribute to the high-energy radiation, while leptonic models assume only relativistic electrons are responsible. In hadronic models, the high-energy radiation is explained as either direct proton synchrotron radiation (Aharonian 2000), or the result of photo-hadronic interactions (e.g., Atoyan and Dermer 2001). In the case of photo-hadronic interactions, protons interacting with ambient photons can decay to electron-positron pairs in the Bethe-Heitler process, which themselves can contribute to the high-energy component through synchrotron radiation (Mannheim and Biermann 1992). Alternatively, proton-photon interactions can lead to pion production which can either directly decay to gamma-rays in the case of neutral pions (Sahu, Oliveros, and Sanabria 2013), or eventually decay to electron-positron pairs in the case of charged

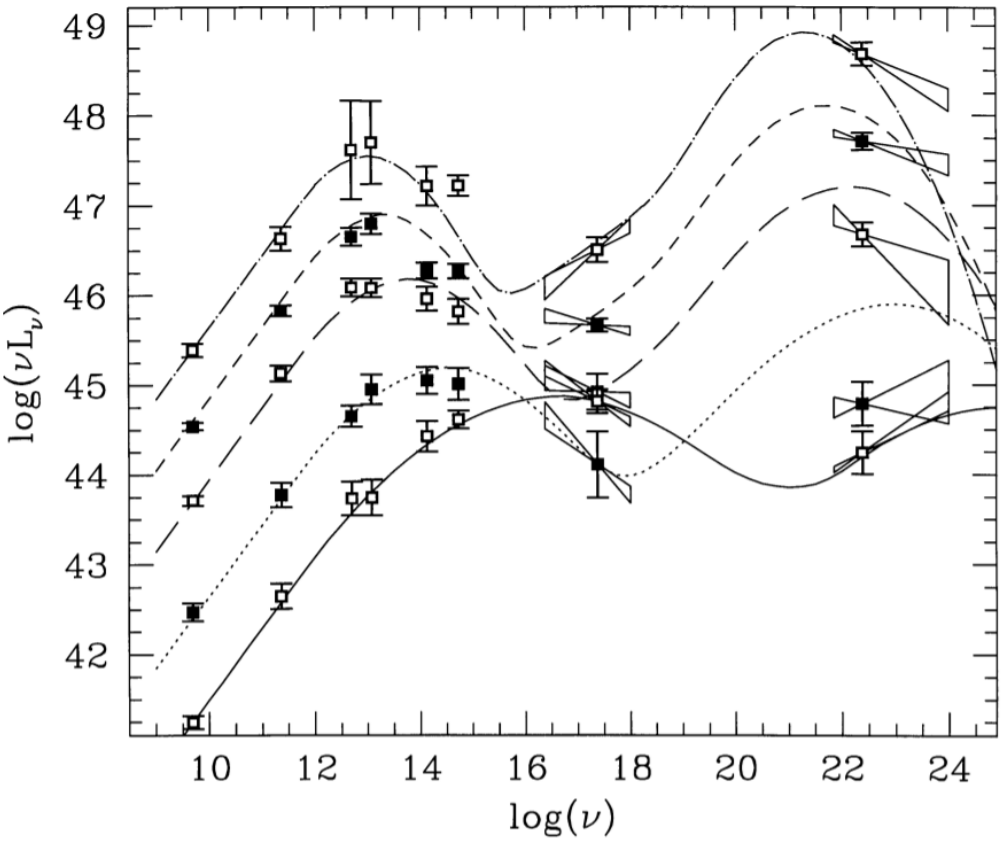

FIGURE 1.5: Average SEDs for a sample of 126 blazars, binned according to the mechanical jet power, adapted from Fossati et al. (1998). The trend seen is that as the jet power decreases, the overall luminosity decreases as the peak frequencies of both spectral components increases. This trend is referred to as the "blazar sequence".

pions (after first decaying to muons). In the latter scenario, it is again the synchrotron radiation of the electron-positron pairs which adds to the observed high-energy component (Petropoulou and Mastichiadis 2012). While hadronic models are not ruled out, they seem to be disfavored by the requirement of large jet kinetic powers (sometimes exceeding the Eddington luminosity) and inability to reproduce the hard X-ray spectra of some blazars (Böttcher et al. 2013; Sikora et al. 2009).

In leptonic models, the radiative output of the jet is dominated by electrons (and possibly positrons), where it is assumed protons are not accelerated to high enough energies to substantially contribute to the spectrum (Böttcher et al. 2013). The process invoked to explain the high-energy emission is the inverse-Compton (IC) scattering of low-energy "seed" photons to X-ray and gamma-ray energies by electrons in the jet. There are generally two sources of seed photons considered: the synchrotron photons produced by the scattering electrons themselves (e.g., Maraschi, Ghisellini, and Celotti 1992) and photons external to the jet, referred to as synchrotron-self Compton (SSC) and external Compton (EC) models, respectively. While SSC has been successful in modeling the high-energy component in low-power blazars (Boettcher 2010; Potter and Cotter 2013), it has been found inadequate in high-power blazars (Meyer et al. 2012; Sikora et al. 2009). In EC models, the most common sources of seed photons are the optical/UV emission lines in the sub-pc sized broad-line region (BLR, Sikora, Begelman, and Rees 1994) and thermal infrared photons from the inner pc-scale regions of the molecular torus (MT, Błażejowski et al. 2000; Sikora et al. 2009). These seed photons are in turn produced when the semi-isotropically emitting accretion disk illuminates the BLR and MT with optical/UV photons. In the case of the BLR, the optical/UV photons of the accretion disk are reprocessed into optical/UV emission lines by the recombination of atoms in BLR clouds. In the case of the MT, the optical/UV photons of the accretion disk heat up the inner MT which then radiates infrared photons through thermal black body emission.

All leptonic models for the high-energy emission in blazars rely on emission regions located within a pc or less from the black hole, in order for the photon fields from the BLR and inner MT to be dense enough for EC scattering (Nalewajko, Begelman, and Sikora 2014). However, there is evidence for gamma-ray flares occurring pc beyond this region (e.g., Marscher et al. 2012).

1.7.1 Evidence for gamma-ray flares outside the BLR and inner MT

Multiwavelength monitoring, including very long baseline interferometry (VLBI) imaging, reveals that at least a fraction of gamma-ray flares occur at the location of the VLBI core, several pc from the black hole (Marscher et al. 2012). The core is often the brightest feature of the blazar jet and the feature located closest to the black hole. It may be the site of a standing shock few to several pc downstream of the central engine (e.g., D'Arcangelo et al. 2007). Alternatively, it can be the location where the jet at the frequency of observation becomes optically thick due to synchrotron self-absorption (e.g., Lobanov 1998), again few to several pc downstream of the central engine. In this case, optically thick means that the radiation is completely absorbed by the intervening jet plasma before it can reach the observer. One can discriminate between these two possibilities, as in the first case the location of the core does not change with the frequency of VLBI observation, while in the second it shifts closer to the central engine as the frequency of observation increases (e.g., Hada et al. 2011).

The inference that some gamma-ray flares originate near the location of the VLBI core results from the strong correlations seen in light curves from radio through gamma-ray wavelengths during these flares, and the fact that often a superluminal component is seen ejected from the VLBI core near the peak time of the GeV flare. In PKS 1510-089, one of the most well documented cases

(Marscher et al. 2010), a radio and optical flare takes place at the same time as a GeV flare, and a new component emerges from the VLBI core. Observations of the blazar OJ 287 even place the origin of the gamma-ray emitting region beyond the core, >14 pc from the central engine (Agudo et al. 2011). The authors observed two gamma-ray flares coincident with two mm-wavelength flares using the *Fermi*/LAT and very long baseline array (VLBA) observatories respectively, with associated peaks in mm-wavelength polarization of a bright stationary feature >14 pc from the core. The authors argue these correlations are best explained by co-spatial emission at radio and gamma-ray wavelengths, originating in this radio-bright stationary feature >14 pc from the core.

In chapter 2, I present a model of gamma-ray flares of powerful blazars thought to originate several pc beyond the BLR and hot inner MT. Chapter 3 forms the main focus of this thesis, which is concerned with understanding the resolved X-ray emission of radio-loud AGN on the kpc scale (i.e., X-ray emission associated with the large-scale radio jet, not just the blazar core). In the next section, I will give an overview of the X-ray emission observed in the jets of radio-loud AGN.

1.8 X-ray Emission from AGN Jets

Early X-ray missions in the 1960s and early 1970s were successful in detecting X-rays from AGN (e.g., Friedman and Byram 1967; Gursky et al. 1971). However, these telescopes did not have the angular resolution to detect the jet separate from the central AGN point source. The first telescopes capable of resolving the X-ray jets in AGN were the *Einstein* and *ROSAT* X-ray observatories, launched in 1978 and 1990 respectively, which had angular resolutions of $\sim$5″ on axis (see Singh 2013 for a brief overview of the history of X-ray observations of AGN). These two observatories successfully detected X-ray jets associated with the very nearby radio galaxies M87 and Cen A, and the low-redshift (z=0.16) quasar 3C 273 (Feigelson et al. 1981; Willingale 1981; Schreier, Gorenstein, and Feigelson 1982; Röser et al. 2000). For the nearby radio galaxies, resolving the jets was much easier since arcsecond scale resolution corresponds to tens of pc projected size at the source. However, for much more distant quasars, arcsecond scale resolving power corresponds to kpc (Schwartz 2010). Ultimately, improved angular resolution was necessary to resolve the X-ray emission associated with the more distant AGN jets, where the projected jet lengths range from the tens to hundreds (in the more extreme cases) of kpc from the central AGN (Harris and Krawczynski 2006).

This was achieved with the launch of the *Chandra* X-ray Observatory in 1999, which has an angular resolution of ∼0.5″ and improved sensitivity over the previous X-ray telescopes. *Chandra's* first astrophysical target was the source PKS 0637-752, a powerful quasar with a radio jet of FR II morphology. The target was chosen in order to perform the initial focusing of the optics, as it was expected to be a moderate strength point source. However, unexpectedly a bright X-ray jet was found coincident with the inner portion of the radio jet (radio and X-ray image shown in Figure 1.6).

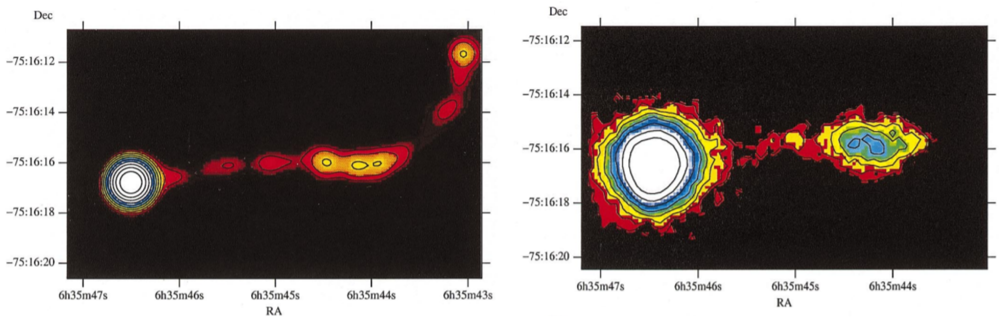

FIGURE 1.6: Left: Radio image of PKS 0637-752 at 8.6 GHz using *ATCA*. Right: X-ray image of PKS 0637-752 using *Chandra*. Image adapted from Chartas et al. (2000).

Since the launch of *Chandra*, over 150 AGN X-ray jets have been discovered (a large number of these can be found at the website http://hea-www.harvard.edu/XJET/). The radio-to-X-ray spectrum of the weak FR I jets is typically well described by a single synchrotron component. For leptonic jet models, this usually means that the underlying physical model is taken to be a power-law distribution of electrons emitting synchrotron radiation by gyrating in the jet's magnetic field, resulting in a power law spectrum, as is the case for the famous FR I jet, M87 (see Figure 1.7).

However, many X-ray-detected FR II jets have shown a spectrum which is either too high in flux or hard to be an extension of the radio-to-optical synchrotron spectrum. For the rest of this thesis, I refer to any jet with evidence of multiple spectra as a Multiple Spectral Component or "MSC" jet. This anomalously high and/or hard X-ray spectrum was first seen in PKS 0637-752 in *Chandra's* first pointed observation. In Figure 1.8, I show the spectral energy distribution (SED) for the jet[2]. As shown by the jet SED, the X-ray emission for the bright knot WK7.8 is far above the radio and optical fluxes, precluding a single spectral component from radio to X-rays.

In the discovery papers of the PKS 0637-752 X-ray jet (Chartas et al. 2000; Schwartz et al.

[2]Note that the SED is usually plotted in log-log plots as νF_ν vs ν, where ν is the frequency and $F\nu$ is the flux density. The reason for this is because in log-space, νF_ν is the correct measure for how the energy is distributed in a spectrum. Thus, equal values of νF_ν correspond to equal levels of energy output in a logarithmic plot.

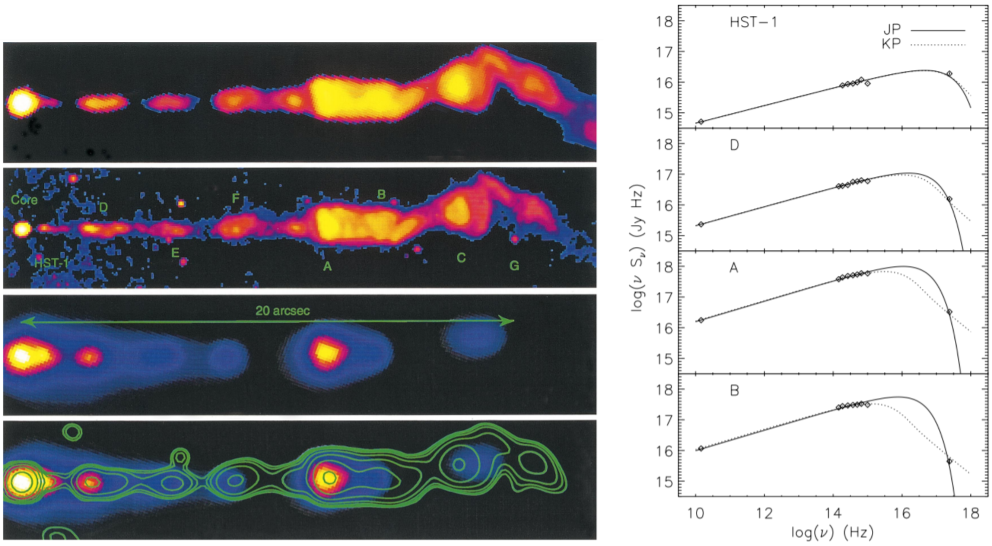

FIGURE 1.7: Left: Images of the M87 jet in the radio, optical, and X-ray wavelengths from top to bottom, where the bottom image is the X-ray image with overlaid optical contours. Right: Radio to X-ray spectrum for the knots in the M87 jet, where a single synchrotron component is used to model each knot. Figure adapted from Marshall et al. (2002).

2000), the authors considered several possible emission mechanisms for the X-rays which were ultimately ruled out. Synchrotron Self-Compton was found to undepredict the observed X-ray flux by several orders of magnitude when the authors assumed an equipartition magnetic field. The magnetic field would have to be orders of magnitude below the equipartition value in order for SSC to work, implying a total energy in particles and field 1,000 times greater than the minimum energy which posed problems for models of particle acceleration and jet confinement. Thermal bremsstrahlung was also considered, but it predicted very high electron densities at odds with the lack of observed rotation measures for such a high-density plasma.

It was proposed independently by Tavecchio et al. (2000) and Celotti, Ghisellini, and Chiaberge (2001) that these X-rays could be coming from the inverse-Compton (IC) scattering of the Cosmic Microwave Background (CMB) by those electrons producing the radio-to-optical synchrotron emission (known commonly as the IC/CMB model). However, the IC/CMB model required the jet to be highly relativistic on the kpc-scale (with bulk flow Lorentz factor $\Gamma \sim 10$), and be pointed at a small angle with respect to our line-of-sight (on the order of a few degrees). Over the intervening years, IC/CMB became the preferred model for explaining the kpc-scale X-ray emission for jets in which the X-ray spectrum was too high and/or hard to be the high-energy tail of the radio-to-optical synchrotron spectrum (e.g., Sambruna et al. 2004; Kharb et al. 2012; Jorstad and Marscher 2006; Marshall et al. 2011; Stanley et al. 2015; Miller et al. 2006; Tavecchio et al. 2007; Perlman et al. 2011; Sambruna et al. 2002). However, there are several aspects of the IC/CMB

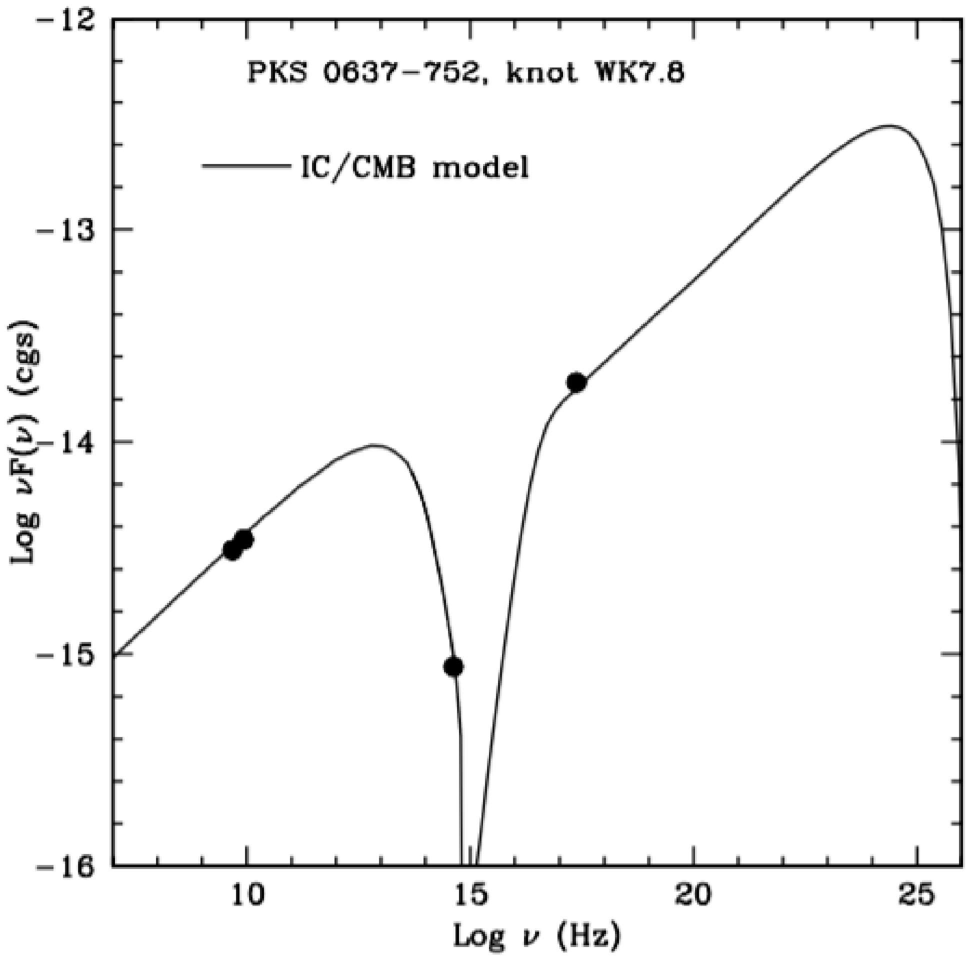

FIGURE 1.8: SED for PKS 0637-752 showing the X-ray flux to be too high to be an extension of the radio to optical synchrotron spectrum. The X-ray emission is fit with the IC/CMB model. Figure adapted from Tavecchio et al. (2000).

model which are at odds with multi-wavelength observations.

1.9 Problems with the IC/CMB model

One problematic aspect of the IC/CMB model is that it is energetically costly, with kinetic jet powers at or exceeding the Eddington luminosity (Dermer and Atoyan 2004). This is primarily because it requires extending the electron energy distribution to very low energies to provide electrons of the right energy to produce the observed X-ray emission from upscattered infrared CMB photons. This low-energy extension (i.e., a low $\gamma_{\rm min}$ value) of the electron energy distribution greatly increases the total energy content of the jet by requiring a much larger total number of electrons. While such an extension is possible, there is no direct evidence for these low energy electrons since their synchrotron radiation would be at frequencies much less than our GHz-frequency radio observations.

The radiative losses of the electrons responsible for the X-ray emission are very weak in the IC/CMB model, with radiative lifetimes in excess of 10^6 years (Harris and Krawczynski 2006). In the simplest case, we would thus expect continuous X-ray emission along the entire jet length rather than the observed X-ray knots as noted by Atoyan and Dermer (2004) and Stawarz et al. (2004). This problem can be avoided if the X-ray emitting plasma is confined to moving blobs rather than a continuous jet flow (Tavecchio, Ghisellini, and Celotti 2003). This solution would require these X-ray emitting blobs to be propagating with a high Γ which may be observable with proper motion studies for nearby sources. However, in the case of 3C 273, Meyer et al. (2016) found that the knots are stationary with a limit of apparent speed $\beta_{app} < 1c$, corresponding to a limit of $\Gamma < 2.9$, which is incompatible with the IC/CMB interpretation for the X-rays.

Along similar lines, comparing the radio and X-ray emission profiles in MSC jets poses further problems for the IC/CMB model. The electrons producing IC/CMB X-rays should have much lower Lorentz factors than the electrons producing the observed GHz synchrotron radiation (i.e., a γ of $\sim$100 rather than several thousand). Since the cooling time for synchrotron and IC/CMB radiation is proportional to γ^{-1}, we should expect much longer cooling times of the electrons responsible for the IC/CMB X-rays, and correspondingly the X-ray emission to persist downstream of the radio emission (Worrall 2009). However, this is the opposite of what is observed in all cases, where the X-ray flux drops off faster than the radio flux (e.g., Schwartz et al. 2000; Marshall et al. 2001; Jorstad and Marscher 2004; Siemiginowska et al. 2002; Sambruna et al. 2004).

A feature of some of these MSC jets is offsets in peak brightness between radio, optical, and X-ray wavelengths when observed with similar angular resolutions (see the case of 3C 111 in Clautice et al. 2016 for a clear example of this). There is no reasonable explanation for these offsets in the IC/CMB model since they are inconsistent with the idea that the X-ray, radio, and optical emission is produced by the same population of relativistic electrons, where we would expect co-spatial emission regions. Similarly, since the same electron population is responsible for the radio and X-ray emission, we would expect the radio and X-ray spectral indices to match. However, in a study of the anomalous X-ray emission in the jet of 3C 273, Jester et al. (2006) found X-ray spectral indices softer (higher) than the corresponding radio spectral indices. Again, this would not be expected under the IC/CMB model, where if anything, the X-ray spectral index should be harder (less) than the radio. This conclusion can be arrived at after considering the fact that electrons producing the observed IC/CMB X-rays are expected to be of much lower energy than the electrons producing the observed GHz radio emission. Therefore, we would expect stronger radiative losses from the GHz-emitting electrons, softening this part of the electron distribution compared to the electrons producing IC/CMB X-rays.

Another expectation from the IC/CMB model is an increase of the X-ray emission relative to the radio, as sources are located at higher redshifts. The reason for this is because the CMB energy density increases with redshift as $(1+z)^4$. Combining this with the fact that the IC/CMB X-ray emissivity should be proportional to the CMB energy density (see section 1.5.2), we should expect the ratio of X-ray to radio emission to follow this trend with redshift, assuming the synchrotron radio emission is not redshift dependent. However, no such trend has been observed in large sample studies of these X-ray jets (e.g., Kataoka and Stawarz 2005a; Marshall et al. 2018). One way in which the IC/CMB model is able to remain viable is if other jet properties like the magnetic field or Lorentz factor also depend on redshift. Since these properties can affect the relative strength of the X-ray to radio emission in the IC/CMB model, they would be able to wash out the correlation. However, there is currently no evidence for a redshift dependence of either the magnetic field or Lorentz factor.

In addition to the above difficulties, there have been several observations of MSC jets which directly challenge the IC/CMB model. HST polarization measurements of the rising UV-component in the jet of PKS 1136-135, clearly part of the second spectral component, show fractional polarization measures in excess of 30% for several knots (Cara et al. 2013). Since IC/CMB emission is expected to have very low polarization (see McNamara, Kuncic, and Wu 2009; Uchiyama 2008a), it is extremely unlikely that the second component is produced by the IC/CMB mechanism in this source. Another recent study by Hardcastle et al. (2016) of the nearby FR II radio galaxy Pictor A shows IC/CMB to be incompatible with the observed jet to counter-jet flux ratio (as is also the case for 3C 353, shown in Kataoka et al. 2008). They found a ratio orders of magnitude less than what would be expected if IC/CMB were the source of the X-rays (in which case $\Gamma \geq 5$ and a jet angle less than a few degrees is required). Additionally, Marshall et al. (2010) found significant variability in the flux from a X-ray knot in Pictor A on the timescale of only a few years. Such rapid variability cannot be explained in the IC/CMB model, where the electrons have cooling times in excess of 10^6 years (Harris and Krawczynski 2006).

Despite these observations, the IC/CMB model is still widely used to model MSC jets (e.g., Lucchini, Tavecchio, and Ghisellini 2017; Zhang et al. 2018; Harris et al. 2017). However, there are alternate models which can account for the X-ray emission. A second higher-energy distribution of electrons producing synchrotron X-rays (Jester et al. 2006; Hardcastle 2006) and hadronic models (Petropoulou, Vasilopoulos, and Giannios 2017; Kusunose and Takahara 2017) are both consistent with the observations. In Figure 1.9 I show a schematic of what the two electron energy distributions might look like in the second synchrotron model. If the second synchrotron model is operating in MSC jets, it would have implications for particle acceleration models, since these high-energy electrons would need to be accelerated in-situ many kpc from the central engine due to the high radiative losses of such electrons. Meanwhile, hadronic models would imply a strong proton component in these jets which requires high jet powers (e.g., Aharonian 2002; Petropoulou, Vasilopoulos, and Giannios 2017; Kusunose and Takahara 2017). Determining whether IC/CMB or a different model is responsible for the X-ray emission in these jets is important since these models imply radically different properties of these jets, which may inform our understanding of how they are powered/launched and interact with their environment. If IC/CMB is correct, it would imply these jets can remain highly relativistic on kpc scales, are much longer than in the second synchrotron model owing to the small angles to the line-of-sight, and are more powerful than in the second synchrotron model. On the other hand, the second synchrotron model implies these jets are capable of accelerating electrons up to very high energies (in the TeV energy range) many kpc from the central black hole. For those jets with quasi-continuous X-ray emission, the second synchrotron interpretation even requires a distributed acceleration mechanism (rather than acceleration at a few bright knots), since the lifetime of the electrons emitting synchrotron X-rays would be extremely low, in some cases on the order of years (Harris and Krawczynski 2006). Stawarz and Ostrowski (2002) have argued that this can be achieved by turbulent boundary layer acceleration in a spine-sheath structure of the jet, where a slower moving sheath surrounds a faster-moving spine.

While the IC/CMB model is incompatible with the observations of some X-ray jets, it is not clear that this is the case for all sources. For any jets which remain highly relativistic on the kpc scale and are oriented at low angles to the line-of-sight, the IC/CMB mechanism would be capable of producing significant X-ray and even gamma-ray emission (Meyer et al. 2015). In the work presented here, I test the IC/CMB model using observations from the *Fermi* gamma-ray space telescope where we look for the expected IC/CMB gamma-rays. I will briefly go over the theory behind this test in the next section.

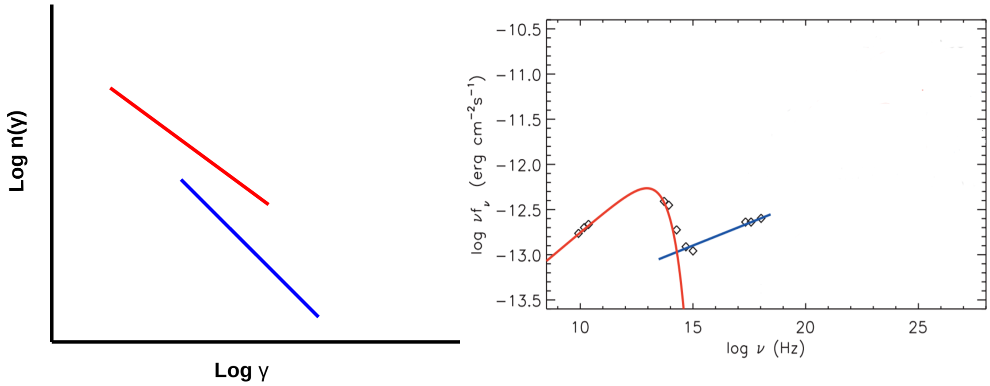

FIGURE 1.9: . At left is a schematic of what the two electron energy distributions (EEDs) might look like in the second synchrotron model, where the axes represent the number density of electrons of Lorentz factor γ as a function of γ. At right is a model SED showing the corresponding synchrotron spectrum for each EED as red and blue curves. The color of the curve corresponds to the color of the EED producing it. The SED is adapted from Georganopoulos et al. (2006).

1.10 Using Fermi to test the IC/CMB model

One consequence of modeling the high X-ray fluxes seen in AGN jets with IC/CMB is an unavoidable high level of gamma-ray flux which should be detectable with the *Fermi* Large Area Telescope (LAT) (Georganopoulos et al. 2006). This is due to the fact that the IC/CMB spectrum is essentially an exact copy of the radio-to-optical synchrotron spectrum, shifted in frequency and luminosity by an amount proportional to (B/δ) and $(B/\delta)^2$ respectively (where B is the magnetic field strength and δ is the Doppler factor for the emitting plasma). The full expressions for the shifts (first derived in Georganopoulos et al. 2006) are given below, but it is important to note that the only free parameter in these shifts is (B/δ).

$$\frac{\nu_c}{\nu_s} = \frac{2\pi m_e c(1+z)\nu_0}{e(B/\delta)} \tag{1.10}$$

$$\frac{L_c}{L_s} = \frac{32\pi U_0(1+z)^4}{3(B/\delta)^2} \tag{1.11}$$

Here, ν_c and ν_s are the observed IC/CMB and synchrotron frequencies with corresponding luminosities, L_c and L_s. The redshift is given by z, ν_0 is the CMB peak frequency at z=0, m_e is the electron mass, c is the speed of light, and U_0 is the CMB energy density at z=0. Since the only free parameter is (B/δ), it must be fixed to match the observed X-ray flux. However, fixing (B/δ) so that the IC/CMB spectrum matches the observed X-ray flux leads to a fixed high level of gamma-ray flux.

In Figure 1.10, I show a SED for a synchrotron and IC/CMB model fit. While the second synchrotron model has no constraints on the level of gamma-ray emission, the IC/CMB model has a fixed level of gamma-ray emission set by the requirement of reproducing the observed X-ray flux. In this thesis work, I present our use of the *Fermi*/LAT to look for the IC/CMB gamma-rays for many of these MSC jets, where the predicted level of gamma-ray emission is very high in many cases. When these gamma-rays are not detected with *Fermi*, upper limits to the gamma-ray flux which lie below the IC/CMB predictions allow us to stringently rule out the IC/CMB model. Next, I will go over the multi-wavelength data that we used to apply this test to jets modeled with IC/CMB X-rays.

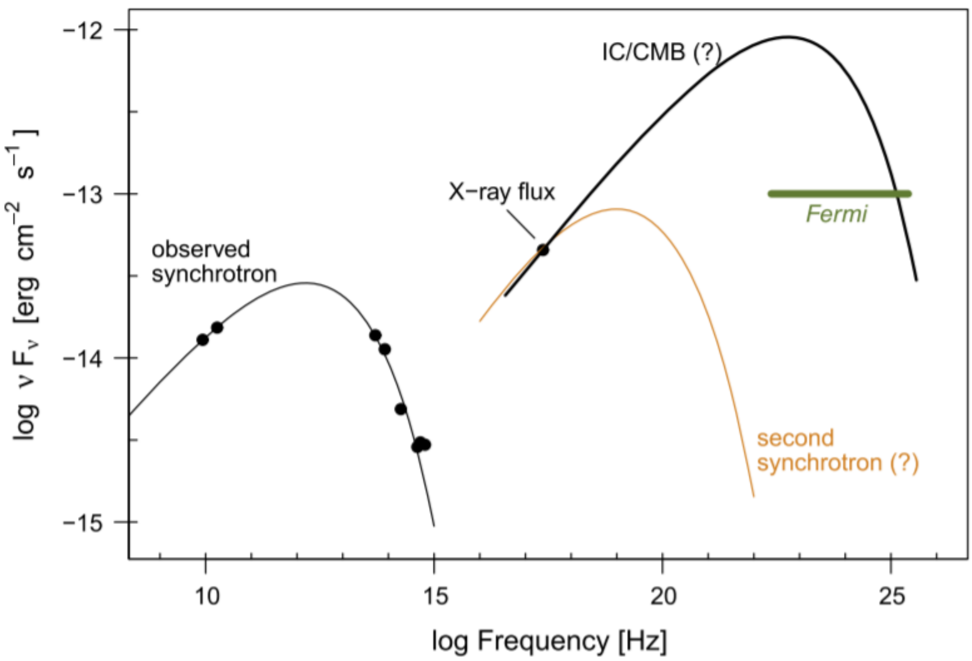

FIGURE 1.10: Model SED of an MSC jet with synchrotron and IC/CMB models applied. The IC/CMB curve is a copy of the observed synchrotron curve shifted in frequency and luminosity to match the observed X-ray flux from the jet. This leads to an unavoidably high prediction of gamma-rays that *Fermi* is well-suited to look for. Note that a second synchrotron model is able to avoid this prediction of high gamma-ray fluxes. Figure adapted from Meyer et al. (2015).

1.11 Multi-wavelength Data used in this Thesis

This thesis makes use of multi-wavelength data, from radio up to gamma-ray observations of extragalactic jets in AGN. I will give a brief overview of the primary observatories used for the work in this thesis.

1.11.1 The Fermi Large Area Telescope

The *Fermi* Large Area Telescope (LAT) is a gamma-ray space telescope developed at the SLAC national accelerator laboratory and NASA Goddard Space Flight Center (see Atwood et al. 2009 for a comprehensive overview of the instrument). The LAT is one of two main observatories on the *Fermi* gamma-ray space telescope, the other being the gamma-ray burst monitor (GBM) designed to detect gamma-ray bursts. *Fermi* was launched in August of 2008, and is still in operation as of 2019. It is an all-sky survey telescope, obtaining data from the entire sky roughly once every three hours (with occasional pointed observations), and data is made public very quickly. The LAT operates from about 20 meV to 300 GeV, with a field of view covering 20% of the sky. It has an angular resolution that ranges from $\sim 3°$ at 100 meV to $\sim 0.04°$ at 100 GeV. In Figure 1.11 I show the angular resolution of the LAT as a function of observing energy. It is important to note that since the angular resolution does not extend to the arcsecond scale, Fermi cannot resolve extragalactic jets separate from the central AGN. However, the predicted IC/CMB gamma-ray flux may still be detected when the core emission is quiescent. In the case where *Fermi* does not detect any gamma-rays, upper limits to the gamma-ray flux can be used to rule out the IC/CMB model.

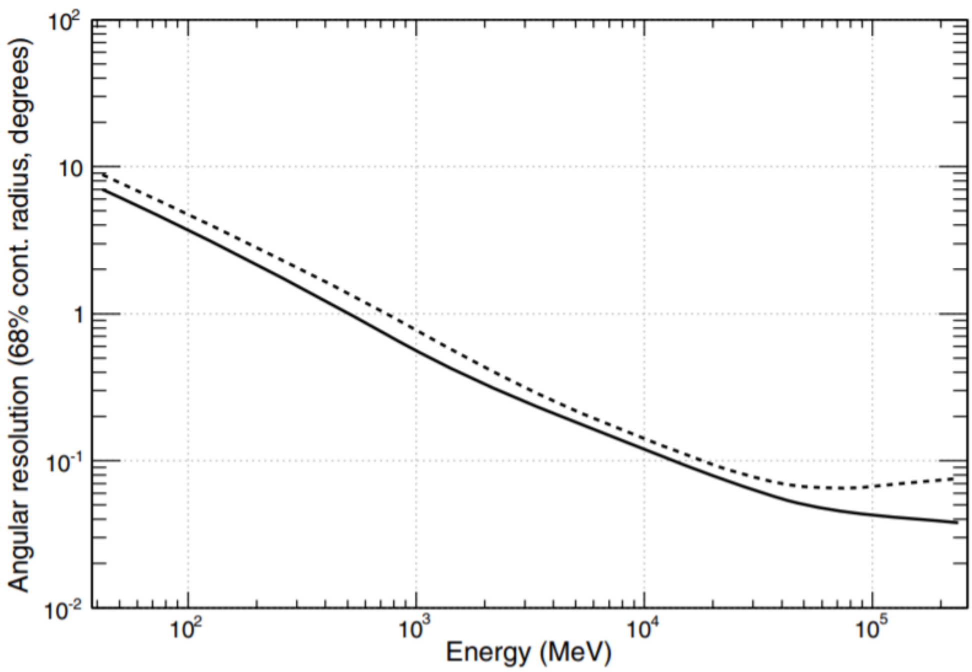

FIGURE 1.11: 68% containment radius vs. energy at normal incidence (solid curve) and at 60° off-axis (dashed curve) for conversions in the thin section of the tracker. Figure adapted from Atwood et al. (2009).

The principle of gamma-ray detection with the LAT is the conversion of incoming gamma-rays to electron-positron pairs by a high atomic number and thin metal foil. The pair is then tracked through position-sensitive layers of silicon strip detectors using technology similar to particle accelerators. There are 16 layers of metal foil interleaved with silicon strip detectors. After passing through these layers, the pair enters a calorimeter to record the total energy of these particles. The tracking data along with the data from the calorimeter are then used to reconstruct the incoming gamma-ray path, energy, and time of arrival.

1.11.2 Interferometric Radio and Sub-mm Observatories

In order to study extragalactic jets, high-resolution and sensitive imaging is necessary owing to the fact these jets are faint and typically on the order of tens of arcseconds projected on the plane of the sky. This was achieved for radio observatories with the advent of interferometric techniques, which allowed the correlation of signals from an array of radio dishes to reconstruct brightness maps of sources using Fourier transformation. With this method, one obtains the same resolution as a single dish with the diameter corresponding to the largest separation of dishes in the array.

One of the primary radio observatories used for this thesis work is the *Very Large Array* (VLA) located in the San Augustin Plains in New Mexico. Built in the 1970s, the VLA consists of twenty seven 25 m radio dishes mounted upon a Y-shaped track that allows the positions of the telescopes to be adjusted into what are called configurations. The configurations range from A-D, with corresponding baselines of 22.6 to 0.6 miles. The larger baselines allow for higher angular resolutions at the cost of surface brightness sensitivity. The VLA operates from 74 MHz to 45 GHz, with angular resolutions that can reach as high 0.04 arcseconds at the highest frequency and largest configuration.

Interferometric techniques are also utilized in observing at mm and sub-mm wavelengths. The primary facility at use in this thesis was the *Atacama Large Millimeter/Sub-millimeter Array* (ALMA) located in northern Chile. ALMA has twelve 7 m dishes, and fifty four 12 m dishes capable of reaching baselines as large as 16 km. It operates at larger frequencies than the VLA, from 31 GHz to 950 GHz, with angular resolutions ranging from 12.5 to 0.02 arcseconds (Warmels et al. 2018). Observing these jets at these high frequencies has proved critical to sampling the synchrotron spectrum at much higher energies. Better characterization of the spectrum at these energies gives us a better characterization of the IC/CMB spectrum at gamma-ray energies.

1.11.3 Hubble Space Telescope

The *Hubble Space Telescope* (HST) is a space-based 2.4 m reflecting telescope launched to low earth orbit in 1990, and is a cooperative program between the European Space Agency (ESA) and the National Aeronautics and Space Administration (NASA). Due to its 2.4 m aperture and lack of atmospheric blurring from being in orbit, the HST can reach resolutions down to 0.043 arcseconds at 500 nm and operates at wavelengths of 90 nm to 3 μm. The HST has three cameras and two spectrographs currently on board, but the two instruments most important to the study of extragalactic jets currently in use in recent years are the Advanced Camera for Surveys (ACS) and Wide Field Camera 3 (WFC3). The Wide Field Channel (WFC) detector, which is the only one currently working on the ACS, consists of two charge couple devices (CCDS) with a total of 16 megapixels, with an effective field of view of $\sim 202'' x 202''$, and wavelength coverage of 350 nm-1100 nm. The WFC3 camera has a Near Infrared and UV channel operating from 850 nm-1700 nm and 200 nm-1000 nm respectively, with corresponding fields of view of $\sim 123'' x 137''$ and $\sim 160'' x 160''$. Historically, the Space Telescope Imaging Spectrograph (STIS) and the Wide Field and Planetary Camera 2 (WFPC2) also observed many jets and were used to provide optical fluxes.

HST imaging of extragalactic jets is essential in determining those cases where a single synchrotron spectrum from radio to X-rays is not viable, as for instance when the optical flux is well below the power-law extrapolation from radio to X-rays. In most cases where detected, the optical emission is interpreted as the high-energy tail of the radio synchrotron emission, typically in the exponential-cutoff part of the spectrum.

1.11.4 Chandra

The *Chandra X-ray Observatory* (CXO) is an X-ray space telescope launched in 1999. It operates from roughly 0.1 keV-10 keV energies with a field of view of 1° diameter. Incoming X-rays are focused by 4 nested cylindrical mirrors so the X-rays just graze the mirrors, in order to avoid being absorbed. The X-rays are then focused onto the science instruments about 30 m away. The primary detector used for this thesis was the Advanced CCD Imaging Spectrometer (ACIS). ACIS consists of ten 1024x1024 pixel CCD chips and allows imaging down to 0.5” (Garmire et al. 2003).

Chandra is the only X-ray telescope which is able to resolve extragalactic jets at <1”. Its discovery of very bright X-ray jets whose X-ray emission is still a mystery is the motivation for much of the work in this thesis.

1.12 Overview of this Thesis

In this thesis, I present theoretical and observational studies of extragalactic jets in AGN aimed at understanding the underlying radiative processess at work and physical properties of these jets. In chapter 2, I introduce a theoretical model for the gamma-ray emission observed in powerful blazars, largely drawn from Breiding, Georganopoulos, and Meyer (2018). Chapter 3, which comprises the bulk of this thesis work, concerns the multi-wavelength observations of large scale jets in AGN and is drawn from Breiding et al. (2017) and a forthcoming publication Breiding et al. (2019). In chapter 4, I will offer a summary of the results, as well as some thoughts on future directions and larger context.

Chapter 2

Blazar Sheath Illumination of the Outer Molecular Torus: A Resolution of the Seed Photon Problem for the Far-GeV Blazar Flares

2.1 Introduction

As detailed in 1.7, blazars are radio-loud AGN with their relativistic jets pointed at small angles to the line-of-sight (Blandford and Rees 1978). A prominent feature observed in blazars is powerful flares of gamma-ray emission (e.g. Abdo et al. 2010). In the context of leptonic models, the gamma-ray emission of powerful blazars is considered to be due to inverse Compton (IC) scattering of low-energy seed photons from the sub-pc sized broad-line region (BLR; Sikora, Begelman, and Rees 1994) and/or the pc-scale molecular torus (MT, Błażejowski et al. 2000). These seed photons are in turn produced when the semi-isotropically emitting accretion disk illuminates the BLR and MT. In the case of the BLR, ionizing radiation from the accretion disk is absorbed by atoms in BLR clouds, and reprocessed into recombination lines. In the case of the MT, the accretion disk radiation heats up the MT dust, which then re-radiates thermal black body emission, mainly in the infrared.

A related seed photon production mechanism that motivated this work is the illumination of BLR clouds by the beamed optical-UV radiation of the blazar itself (Ghisellini and Madau 1996). The mechanism here is the same as when the accretion disk photons are reprocessed by the BLR clouds. However, since the blazar emission is beamed within a small angle ($\sim 1/\Gamma \lesssim 5^{\circ}$, where

$\Gamma \gtrsim 10$ is the bulk Lorentz factor of the flow), this model requires the existence of BLR clouds within this very small polar beaming angle. In Figure 2.1, I show schematics for the gamma-ray emission of blazars under external Compton (EC) scenarios where the seed photons originate outside of the jet.

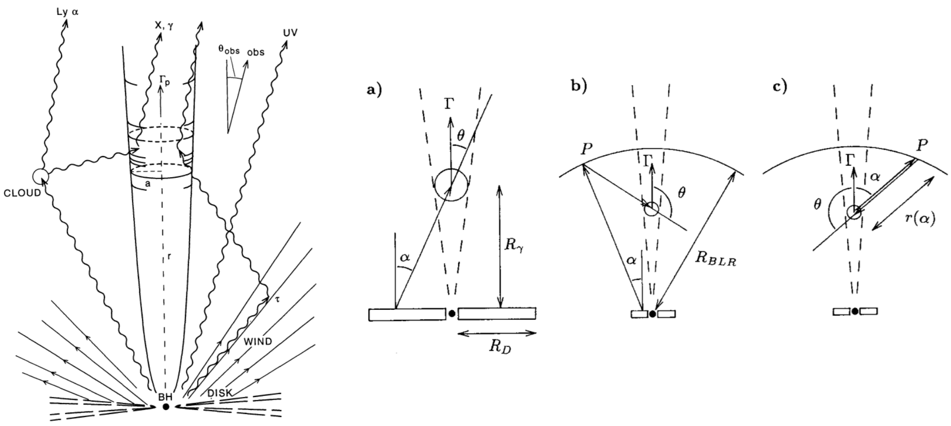

FIGURE 2.1: At left is a schematic where optical/UV radiation of the accretion disk is reprocessed by BLR clouds into emission lines, which serve as the seed photons for the IC scattering to gamma-rays by a moving blob in the jet (image adapted from Sikora, Begelman, and Rees 1994). At right is a schematic where the authors considered three sources of seed photons for IC scattering. In the first picture, a, the seed photons are the direct optical/UV accretion disk photons. In b, the optical/UV photons from the accretion disk illuminate BLR clouds which then produce the seed photons for IC scattering. In c, the optical/UV radiation of the blazar emitting region itself is reprocessed by BLR clouds to the seed photons for IC scattering to gamma-ray energies. The right three images are adapted from Ghisellini and Madau (1996).

The above mechanisms posit that the GeV-emitting region is within a pc or less from the central engine. At distances much greater than this, there is no substantial source of seed photons for the IC process from the BLR or the MT, as both photon fields illuminate the blazar emitting region from behind and are therefore substantially de-beamed in the comoving frame of the emitting plasma (Dermer, Schlickeiser, and Mastichiadis 1992; Nalewajko, Begelman, and Sikora 2014). However, there is evidence that the high-energy emission in blazars originates several to tens of pc from the black hole, where there is no obvious source of seed photons for the IC process to operate (see section 1.7.1).

2.1.1 Alternate sources of seed photons

An alternative source of seed photons arises if we consider that the jet is characterized by a fast spine in which the plasma flows with a Lorentz factor of the order of $\Gamma_{sp} \sim 10 - 20$, surrounded by a slow sheath through which the plasma flows with a Lorentz factor of the order of $\Gamma_{sh} \sim$

few (Ghisellini, Tavecchio, and Chiaberge 2005). It is important to stress that the Lorentz factor Γ represent the bulk Lorentz factor for the plasma in the jet, not the Lorentz factor of individual electrons in the rest frame of the flow, usually denoted as γ. This model is also referred to as a "two zone" model, as the sheath and spine have different physical properties. Single zone models refer to cases where the same physical parameters can describe the emission region. In Figure 2.2, I show a schematic of this spine-sheath structure for the jet.

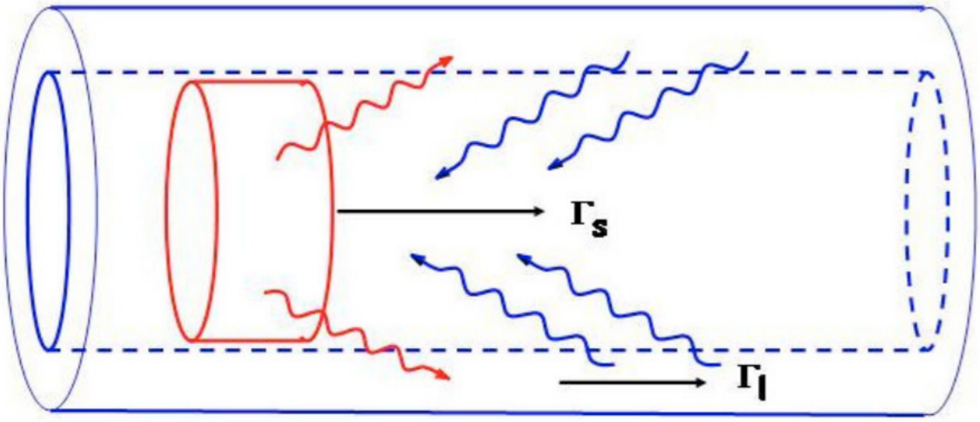

FIGURE 2.2: Schematic showing the spine-sheath structure for the jet, adapted from Ghisellini, Tavecchio, and Chiaberge (2005). Here, Γ_{sp} represents the Lorentz factor of the spine plasma, while Γ_l represents the Lorentz factor of the sheath plasma. In the context of the model from MacDonald et al. (2015), the spine plasma IC scatters the synchrotron radiation of the sheath plasma to GeV energies, shown as the blue squiggly arrows from the sheath turned to the red squiggly arrows leaving the spine.

In this case, the energy density of the sheath photons will be seen to be Doppler boosted in the spine comoving frame by $\sim \Gamma_{sp}^2/(4\Gamma_{sh}^2)$ (Nalewajko, Begelman, and Sikora 2014). MacDonald et al. 2015 applied the spine-sheath model to the blazar PKS 1510-089 and showed that with a judicious choice of model parameters, it can reproduce the observed variability. However, Nalewajko, Begelman, and Sikora 2014 argued that the spine-sheath boosting is inadequate for producing the required seed photon energy density in the frame of the spine, without requiring a sheath spectral energy distribution (SED) that overproduces the observed blazar SED.

2.1.2 The molecular torus as the source of seed photons

Our current view of the MT suggests another source of seed photons. Originally, the AGN unification scheme (e.g. Antonucci 1993) suggested that the dichotomy between type I and type II AGN spectra can be explained as an orientation effect due to an opaque equatorial MT. Type I AGN are those with broad emission line spectra, and type II AGN are those without. Therefore, an opaque equatorial MT when viewed at high inclination angles (edge on) would block the sub-pc sized BLR surrounding the black hole and obscure the broad emission lines. Similarly, when viewed at low inclination angles, the BLR would become visible, and the AGN would be classified as a type I.

The picture that developed among researchers was of a smooth donut-shaped torus of obscuring material surrounding the black hole and BLR (Krolik and Begelman 1986). Furthermore, the obvious candidate for the obscuring material was dust, as it both provided the necessary obscuration but also emits strongly in the infrared, helping to explain the observed infrared bump seen in AGN spectra (Neugebauer et al. 1979). Additional evidence for dust as the obscuring material of the MT was a spectral turnover between the big blue bump (optical/UV thermal emission from the accretion disk) and the infrared at 1μm (Hoenig 2013). Assuming the infrared is emission from a black body in thermal equilibrium, this wavelength roughly corresponds with the temperature at which dust sublimates. Therefore, the spectrum dips at wavelengths less than 1μm, since the dust is sublimated at the high temperatures necessary to produce this part of the spectrum.

More recent observational and theoretical work (e.g. Nenkova et al. 2008; Elitzur 2012; Netzer 2015) support the idea that the MT is clumpy (Krolik and Begelman 1988), and that the distribution of the dusty clumps is a gradually declining function of decreasing polar angle, allowing for some fraction of dusty clumps to lie at relatively small polar angles (e.g., García-González et al. 2017; Khim and Yi 2017). The inner radius R_d of the MT is set by dust sublimation due to the radiation of the accretion disk, and has been measured by near-IR interferometry (e.g., Kishimoto et al. 2011) and near IR reverberation mapping (e.g., Koshida et al. 2014) of nearby Seyferts to have a size that for bright AGN (accretion disk luminosity $L_{optical-UV} \sim 10^{46}$ erg s^{-1}) would be $R_d \sim 1$ pc (Nenkova et al. 2008). At distances less than the dust sublimation radius, the MT clouds are heated to temperatures higher than the dust sublimation temperature, and the clouds are sublimated. At greater distances, the clouds are progressively cooler due to the decreasing photon flux received from the accretion disk.

The BLR is contained within the dust sublimation radius R_d. The outer radius of the MT is found both with modeling the MT SED (Fuller et al. 2016) and through Atacama Large Millimeter/submillimeter aray (*ALMA*) observations (García-Burillo et al. 2016; Gallimore et al. 2016) to be of the order of a few to several pc, several times larger than R_d, with most of the MT power emitted in the IR from the clouds at $\sim R_d$ (Nenkova et al. 2008). With this configuration, it is plausible that the blazar radio core, identified with the blazar GeV flaring site (e.g. Marscher et al. 2010) is located beyond R_d but within the outer bounds of the MT.

Here we show that in the context of a spine-sheath configuration, a moderately relativistic sheath located within the MT beyond R_d can illuminate a substantial solid angle of the clumpy dusty material that lies beyond it, out to the outer bounds of the MT. In §2.2, we show that the radiation of these illuminated clumps, seen in the frame of the fast spine, can dominate over the sheath radiation in the spine co-moving frame and act as the required external photon field for IC scattering. In §2.3, we present a general model SED using a motivated set of model parameters, and in §2.4, we present our conclusions and discuss some of the implications of our model.

2.2 The photon energy density in the jet spine

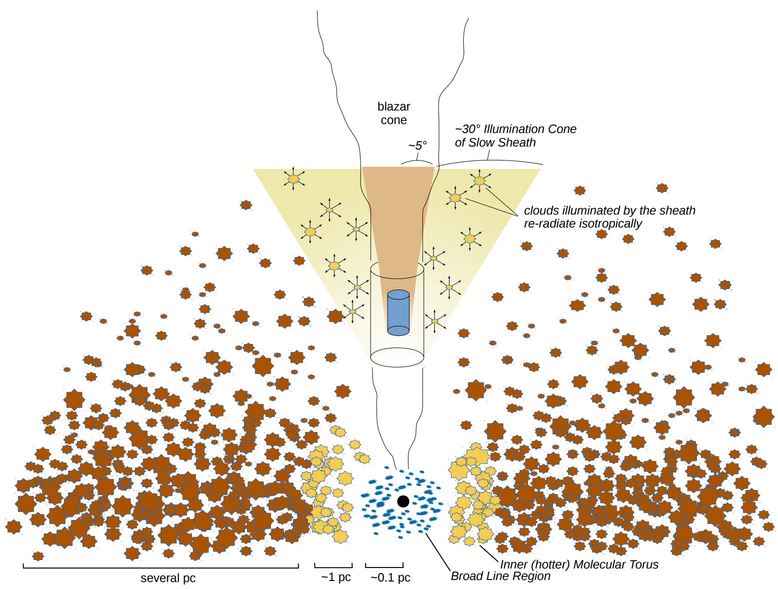

FIGURE 2.3: A schematic representation of the spine-sheath blazar embedded in the MT (not to scale). The MT is clumpy and the clouds have a number density that declines with decreasing polar angle. The blazar site is far beyond its traditional location within the BLR and/or the inner, hotter part of the MT; it is at a distance of a few pc but still within the MT. The wide beaming angle of its sheath synchrotron emission illuminates and heats the MT clouds within the Sheath's synchrotron emission opening angle, and these in turn radiate isotropically. This radiation can provide the dominant seed photon field for IC scattering in the spine comoving frame. Note that the spine beaming angle is very small ($\lesssim 5°$), and it is not expected to be intercepted by any MT clouds.

Our picture (figure 2.3) for the far GeV blazar emission posits a standing jet feature, possibly a recollimation shock, a few to several pc from the black hole. Plasma flows through the standing feature, which has a spine bulk Lorentz factor $\Gamma_{sp} \sim 10-20$ and a slower outer sheath with bulk Lorentz factor $\Gamma_{sh} \sim 2-4$. To keep the study analytically tractable, we approximately assume $1 \ll \Gamma_{sh} \ll \Gamma_{sp}$. Dusty molecular clouds within the wide (up to $\theta_{sh} \sim 1/\Gamma_{sh} \lesssim 30°$) beaming angle of the synchrotron-emitting sheath reprocess a fraction of this radiation, which is then relativistically amplified in the fast spine rest frame. The observed GeV emission is attributed to IC scattering of these photons by the relativistic electrons in the fast spine, provided this photon energy density dominates over that of the sheath photon field directly entering the spine.

We assume that the sheath produces an isotropic synchrotron luminosity L'_{sh} in its comoving frame, peaking in the sub-mm to IR, as the synchrotron SEDs of powerful blazar usually do (e.g. Meyer et al. 2011). In the galaxy frame, the solid-angle integrated luminosity (the luminosity that a hypothetical detector covering all 4π of the sky of the source would measure) is $L_{sh} = \Gamma_{sh} L'_{sh}$, valid assuming that the sheath is a stationary feature. Most of this radiation is beamed into a solid angle $\Omega_{sh} = \pi/\Gamma_{sh}^2$ (opening half-angle $\sim 1/\Gamma_{sh}$), and for simplicity we assume that within this angle the intensity of the radiation does not vary. An observer within this solid angle that assumes that the source is isotropic in her/his frame will infer a luminosity

$$L_{sh,obs} = L_{sh} 4\pi/\Omega_{sh} = 4\Gamma_{sh}^2 L_{sh} = 4\Gamma_{sh}^3 L'_{sh}. \tag{2.1}$$

The sheath synchrotron radiation illuminates MT dust clouds, which for simplicity we assume are isotropically and homogenously distributed within the solid angle Ω_{sh}, starting from the sheath radius R_{sh} and extending to some distance R_{out}, with a sheath covering factor C (where C is the fraction of obscured solid angle within the sheath beaming cone). We treat the dust clouds as ideal spherical black bodies which act as perfect absorbers to the sheath emission. The dust clouds then absorb and are heated by the sheath radiation. Sublimation of the dust occurs for those clouds that are at distances from the sheath less than their sublimation radius

$$R_{sub} = \left(\frac{L_{sh,obs}}{16\pi\sigma T_{sub}^4} \right)^{1/2}, \tag{2.2}$$

where T_{sub} is the dust sublimation temperature, and $\sigma = 5.67 \times 10^{-5}$ erg cm^{-2} deg^{-4} s^{-1} is the

Stefan-Boltzmann constant. The minimum $L_{sh,obs}$ that can cause sublimation is found by the requirement $R_{sub} = R_{sh}$ and is

$$L_\star = 16\pi\sigma T_{sub}^4 R_{sh}^2 = 2.85 \times 10^{45}\, T_{sub,3}^4 R_{sh,18}^2 \,\mathrm{erg\,s^{-1}}, \tag{2.3}$$

where $T_{sub,3}$ is the dust sublimation temperature in units of 1000 K, and $R_{sh,18}$ is the sheath radius in units of 10^{18} cm. For $L_{sh,obs} < L_\star$, the sheath radiation heats but does not sublimate the dust, while for $L_{sh,obs} > L_\star$ the dust is sublimated up to a distance R_{sub} given by equation (2.2). As we require that the observed blazar SED is dominated by the spine and not by the sheath, and as the typical synchrotron SED for powerful blazars has an observed power of $\sim 10^{46}\,\mathrm{erg\,s^{-1}}$ (e.g. Meyer et al. 2011), we assume here that $L_{sh,obs} < L_\star$ (i.e. $\eta \equiv L_{sh,obs}/L_* < 1$) and no sublimation takes place.

2.2.1 Photon energy density in the spine due to sheath radiation reprocessed by the clouds

We proceed now to derive the intensity of the radiation received back from the dust clouds within Ω_{sh}, and from this the corresponding photon energy density in the co-moving frame of the fast spine. For this we assume that all of the sheath power absorbed by the clouds found at $R_{sh} < R < R_{out}$ and within Ω_{sh} is isotropically re-radiated as thermal black body radiation for the dust clouds .

At a distance r from the center of the spine-sheath system, the sheath power absorbed by a shell of differential width dr is

$$dP_{abs} = \frac{L_{sh}C}{R_{out} - R_{sh}} dr = \frac{L_{sh,obs}\Omega_{sh}C}{4\pi(R_{out} - R_{sh})} dr. \tag{2.4}$$

This power is then re-radiated by each shell with an emissivity given by:

$$\epsilon = \frac{dP_{abs}}{dV} = \frac{dP_{abs}}{\Omega_{sh} r^2 dr} = \frac{L_{sh,obs}C}{(R_{out} - R_{sh})4\pi r^2}. \tag{2.5}$$

Assuming isotropic emission for each shell, the emission coefficient, J, can be written as $J = \epsilon/4\pi$. The intensity contribution from each infinitesimal shell is then given by $dI(r) = J dr$, and the total intensity of the radiation field received back from the dust clouds is

$$I = \int_{R_{sh}}^{R_{out}} J dr = \frac{L_{sh,obs}C}{16\pi^2 R_{out} R_{sh}} = \frac{L_{sh,obs}C}{16\pi^2 a R_{sh}^2}, \tag{2.6}$$

where $a \equiv R_{out}/R_{sh} > 1$.

The energy density of this radiation field in the host galaxy frame at the location of the spine is $U = (1/c)\int_{\Omega_{sh}} I d\Omega = (1/c) I \Omega_{sh}$ (c is the speed of light), as in our approximate treatment the intensity does not have an angular dependence within Ω_{sh}. Using $\Omega_{sh} = \pi/\Gamma_{sh}^2$ we then obtain:

$$U = \frac{\pi I}{c\Gamma_{sh}^2} = \frac{L_{sh,obs}C}{16\pi a R_{sh}^2 c\Gamma_{sh}^2}. \tag{2.7}$$

Recalling that $\eta = L_{sh,obs}/L_*$ and using equation (2.3) allows us to put this equation in the following form:

$$U = \frac{4\sigma T_{sub}^4}{c} \frac{\eta C}{4a\Gamma_{sh}^2}. \tag{2.8}$$

Note that the first fraction in the above equation is a blackbody energy density and the second fraction is a dimensionless dilution factor. The energy density in the rest frame of the spine flow plasma can be shown to be $U'' = 4U\Gamma_{sp}^2$ (following a calculation similar to Dermer and Schlickeiser 1994), where double primed variables refer to the co-moving frame of the spine flow:

$$U'' = \frac{L_{sh,obs}C}{4\pi a R_{sh}^2 c} \frac{\Gamma_{sp}^2}{\Gamma_{sh}^2} = \frac{4\sigma T_{sub}^4}{c} \frac{\eta C}{a} \frac{\Gamma_{sp}^2}{\Gamma_{sh}^2} \tag{2.9}$$

2.2.2 Photon energy density in the spine coming directly from the sheath

Assuming isotropic emission in the rest frame of the sheath, the energy density of the sheath's synchrotron radiation in its comoving frame is given by:

$$U'_{sh} = \frac{L'_{sh}}{4\pi R_{sh}^2 c} = \frac{L_{sh,obs}}{16\pi R_{sh}^2 c\Gamma_{sh}^3}, \tag{2.10}$$

where we have used eq. (2.1). The energy density of this photon field in the spine frame is $U''_{sh} = (4/3)U'_{sh}\Gamma_{rel}^2$ (Dermer and Schlickeiser 1994), where Γ_{rel} is the relative Lorentz factor between the spine and the sheath, given by $\Gamma_{rel} = \Gamma_{sh}\Gamma_{sp}(1 - \beta_{sh}\beta_{sp}) \approx \Gamma_{sp}/(2\Gamma_{sh})$. Using these we can write:

$$U''_{sh} = \frac{L_{sh,obs}\Gamma_{sp}^2}{48\pi R_{sh}^2 c\Gamma_{sh}^5} = \frac{4\sigma T_{sub}^4}{c}\eta \frac{\Gamma_{sp}^2}{12\Gamma_{sh}^5}, \tag{2.11}$$

where we have used equation (2.3).

2.2.3 Comparison of the energy densities in the spine

The ratio of the energy density in the spine rest frame due to the photon field received in the spine from the illuminated MT clouds to the photon field directly illuminating the spine by the sheath is

$$\frac{U''}{U''_{sh}} = \frac{12C\Gamma^3_{sh}}{a}. \tag{2.12}$$

In the case of a low but non-negligible covering factor, as is plausible in this setting (see §2.4), we can set $12C = 1$. Also, the sheath is constrained to be substantially slower than the $\Gamma_{sp} \sim 10 - 20$ spine, and still be relativistic, as otherwise we would detect the sheath in counter-jets with VLBI observations. A plausible value for the sheath Lorentz factor is $\Gamma_{sh} = 3$. For these values of C and Γ_{sh}, the condition for the cloud-reprocessed radiation energy density in the spine to be comparable to or dominate over that coming directly from the sheath becomes $a = R_{out}/R_{sh} \lesssim 27$. For example, adopting and setting $R_{sh} = 0.2$ pc (MacDonald et al. 2015), we see that the cloud processed photon energy density dominates if the sheath-spine system is embedded in the MT by less than $\sim 10\, R_{sh} \sim 2$ pc. In the framework where some GeV flares come from distances of a few pc and the clumpy MT extends for a few pc, this condition is plausible.

2.2.4 Viability of SSC for powerful blazars

We now address the viability of SSC for explaining the GeV emission of powerful blazars (e.g. Maraschi, Ghisellini, and Celotti 1992). To evaluate this, we approximate the emission region with a sphere of radius R, permeated by a magnetic field B, and moving relativistically with Doppler factor δ relative to the observer. Electrons of Lorentz factor γ, injected in the source at the rate of Q electrons per second, produce the observed flux at the peak of the synchrotron and SSC components. With five model parameters and five observables, namely the peak frequency of the synchrotron component ν_s, the peak frequency of the SSC component ν_{SSC}, the peak luminosity of the synchrotron component L_s, the Compton dominance k (the ratio of the GeV to synchrotron luminosity), and the variability timescale t_{var} of the gamma-ray emission, the system of equations is closed and the Doppler factor of the emission region is given by the following expression that contains only observables:

$$\delta = 100 \left[\frac{2}{c^3 B_{cr}^2} \frac{L_{s,46}\, \nu_{ssc,22}^2}{\nu_{s,13}^4\, t_{var,1d}^2\, k_2} \right]^{1/4} \tag{2.13}$$

where $B_{cr} = 4.4 \times 10^{13}$ G is the critical magnetic field, $\nu_{s,13} = \nu_s/10^{13}$Hz, $\nu_{SSC,22} = \nu_{SSC}/10^{22}$Hz, $L_{s,46} = L_s/10^{46}$erg s^{-1}, $k_2 = k/100$ and $t_{var,1d}$ is the variability timescale of the gamma ray emission region in units of one day, all typical values for powerful blazars (e.g. Abdo et al. 2010; Bonnoli et al. 2011). For the powerful blazars, on which we focus here, the Doppler factor given by equation (2.13) is significantly higher than the typical values found from superluminal proper-motions studies (**lister09**; e.g. Jorstad et al. 2001). In addition, such high δ values require either a jet with an opening angle of $\sim 1/\delta$ that is extremely well aligned to the observer and therefore with unrealistic de-projected lengths, or a jet with opening angle much greater than $1/\delta$ that would have to be extremely powerful. For these reasons, we disfavor a SSC interpretation of the GeV emission of powerful blazars. Similar conclusions about the inadequacy of the SSC process for explaining the Gev emission of powerful blazars have been reached before (e.g., Abdo et al. 2010).

The SSC process can still be important for powerful blazars, as the synchrotron photon energy density in the spine comoving frame $U_s = L_{s,46}/(4\pi c^3 t_{var}^2 \delta^6)$ can be a non-negligible fraction of the photon energy U'' in the spine due to the sheath radiation reprocessed by the clouds. For reasonable jet parameters, the peak of the SSC SED is in the hard X-ray regime. For example, using equation (2.13) with $\delta = 10$ and requiring that the SSC component has comparable power to the synchrotron one ($k = 1$), we find that the peak of the SSC component is at $\nu_{SSC} = 10^{19}$ Hz, an energy of ~ 40 KeV. This is in agreement with modeling of the SEDs of powerful blazars (e.g., Böttcher et al. 2013).

2.3 An example SED

We now apply the above scenario to evaluate if the resulting SED from the spine compares well to that of high-power blazars. The SED of powerful blazars is characterised by two spectral components, the first peaking at sub-mm to IR and the second below/around ~ 100 MeV, with the high energy component dominating in apparent luminosity by $\sim 10 - 100$. In the context of leptonic models, there is significant contribution or even dominance of SSC at the X-ray band (e.g., Sikora,

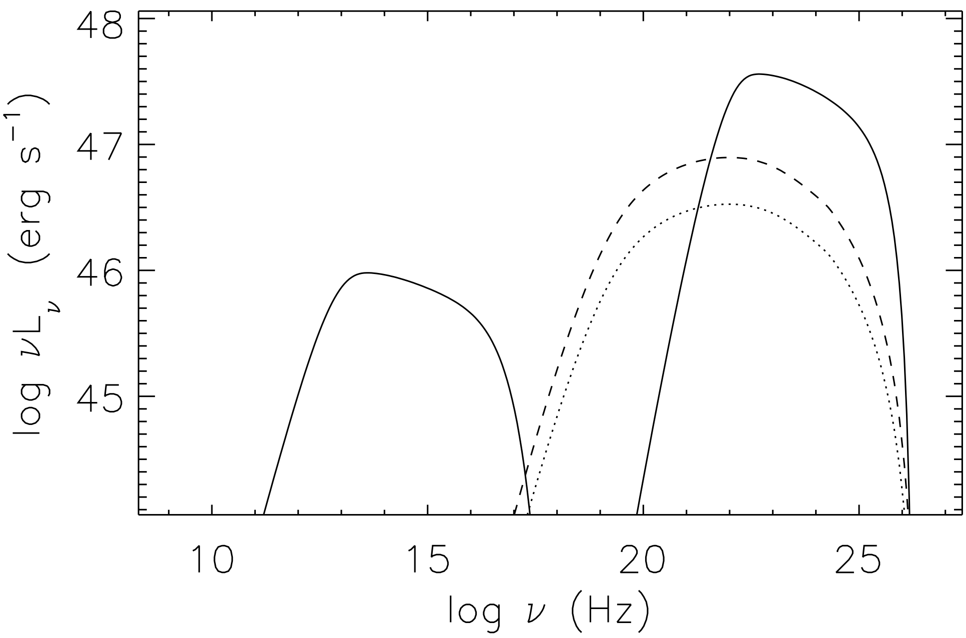

FIGURE 2.4: The SED resulting from the parameter values motivated in §2.3. The low frequency solid line is the spine synchrotron SED, while the high frequency solid line is the spine IC emission from seed photons coming from the MT that is heated by the sheath emission. The broken line is due to SSC within the spine. We also anticipate spine IC emission with the seed photons being sheath synchrotron photons directly entering the spine. As discussed, for this component we anticipate a level of ~ 10 below the IC component resulting from seed photons coming from the MT, but its exact spectral shape depends on the unobservable synchrotron emission of the sheath. For demonstration purposes, we plot this component as a dotted line, assuming an SED similar to the spine's SSC component but with a peak luminosity ~ 10 times lower than the spine IC emission resulting from the MT seed photons.

Begelman, and Rees 1994). However, EC models are usually invoked to explain the gamma-ray emission.

To simulate our proposed scenario, we adopt a covering factor $C = 0.1$, a sheath plasma Lorentz factor $\Gamma_{sh} = 3$ and a ratio $a = R_{out}/R_{sh} = 3$. With this set of parameters, using equation (2.12) we find that the energy density in the spine's rest frame due to the MT is a factor of 10 higher than the energy density of the radiation coming directly from the sheath. We then use the above parameters in equation (2.9) to find $U'' = 1.2 \times 10^{-2}$ erg cm^{-3} by setting $T_{sub} = 1200$ K, $\eta = L_{sh,obs}/L_* = 1/2$, and $\Gamma_{sp} = 20$ (note that at distances of several pc the energy density of the accretion disk and BLR are at least $\sim \Gamma_{sp}^4$ lower as their photons are entering the spine from behind). To obtain a Compton dominance of ~ 30, we require $B = (U''/(30 \times 8\pi))^{1/2} = 0.1$ G.

The spectrum of MT radiation will be a superposition of black bodies, with the hottest coming from the innermost radius R_{sh} and the coolest coming from the outermost radius of the MT R_{out}, with $T(r) = (L_{sh,obs}/16\pi\sigma r^2)^{1/4}$. Using this and equation (2.3) we obtain $T(R_{sh}) = \eta^{1/4} T_{sub}$ and

$T(R_{out}) = a^{-1/2}\eta^{1/4}T_{sub}$. This means that for small values of a, as in this example where $a = 3$, the temperature ratio $T(R_{sh})/T(R_{out}) = a^{1/2}$ is not a large number. Therefore, we can approximate the SED of the sheath radiation with a single black body function at $T_{eff} = [T(R_{sh})T(R_{out})]^{1/2}$ and energy density in the spine rest frame given by equation (2.9), which can now be written as

$$U'' = \frac{4\sigma T_{eff}^4}{c}\frac{C\,\Gamma_{sp}^2}{\Gamma_{sh}^2}, \tag{2.14}$$

an expression that absorbs η and a in the definition of T_{eff}.

To reproduce typical variability timescales of a few hours to a day, we set the spine radius $R_{sp} = 2 \times 10^{16}$ cm. The electron energy distribution (EED) injected in the spine is a power law of index $p = 2.5$ confined between electron Lorentz factors γ_{min} and γ_{max}. Because the system is in the fast cooling regime, the peaks of the synchrotron and IC emission are produced by electrons of Lorentz factor $\sim \gamma_{min}$. Requiring a synchrotron peak at $\nu_s \approx 10^{13}$ Hz, sets $\gamma_{min} = 10^3$. The requirement that the synchrotron mechanism cuts off before the X-rays is satisfied with $\gamma_{max} = 10^5$. The comoving injected power is set by requiring a blazar GeV luminosity of $L_{GeV} \approx 5 \times 10^{47}$ erg s^{-1}, as seen in bright GeV blazars (e.g. Abdo et al. 2010). Using an equation similar to equation (2.1), we find $L_{inj} = L_{GeV}/(4\Gamma_{sp}^3) = 2 \times 10^{43}$ erg s^{-1}. Using the parameter values we just motivated, we plot in figure (2.4) the SED produced by the spine. Our single-zone code applies an implicit numerical scheme for solving the electron kinetic equation similar to that of Graff et al. (2008), first introduced by Chang and Cooper (1970). Our code follows the radiative losses in the injected EED and uses the full Klein-Nishina cross section for IC scattering energy losses and emission calculations.

2.4 Discussion

Recent mutiwavelength campaigns (e.g., Marscher et al. 2010) strongly suggest that a fraction of the *Fermi* observed blazar flares take place a few to several pc from the central engine. This conclusion was motivated by the correlation of radio through gamma-ray light curves with ejections of superluminal components from the blazar vlbi core. At these distances, there is no significant external photon field for producing the GeV emission of observed blazar gamma-ray flares via IC scattering from jet relativistic electrons; the BLR is confined within the IR-bright inner part of the MT, which in turn does not exceed a distance of $\sim$ 1 pc from the central engine (e.g,. Koshida et al. 2014; Nenkova et al. 2008) for the powerful sources under consideration. A plausible solution is a spine-sheath geometry for the emitting region, where the sheath synchrotron photons are the seed photons for IC scattering to gamma-ray energies by relativistic electrons in the jet spine (MacDonald et al. 2015, but see Nalewajko, Begelman, and Sikora 2014 that argue that this mechanism would become relevant only for observed sheath luminosity that would rival that of the spine).

Here we suggest another seed photon mechanism. We start by adopting a picture of the MT that extends for a few pc beyond the IR-emitting inner radius and has a dust cloud angular distribution that extends with a diminishing density to small polar angles (e.g., Nenkova et al. 2008).

We then show that for a spine-sheath jet configuration located within the MT there is a reasonable part of parameter space in which the seed photon energy density in the spine is dominated by sheath photons that have been reprocessed by the dust clouds within the wide opening angle of the sheath synchrotron radiation. This differs from the model of Ghisellini and Madau (1996) in which the blazar illuminates BLR clouds which act to reprocess the radiation into emission line seed photons, as it avoids the problem of requiring reprocessing clouds to be within the very small opening angle of the spine radiation.

We now explore plausible values of the AGN covering factor at low polar angles. Recent high resolution mid-IR observations and modeling of nearby quasars (Martínez-Paredes et al. 2017) with the clumpy molecular torus model (Nenkova et al. 2008), show that non-negligible covering factors are plausible at small polar angles. For a cloud distribution $N = N_0\,Exp[-(\theta - 90^o)^2/\sigma^2]$, where N_0 is the number of clouds encountered by a line of sight in the equatorial direction, σ is the $1/e$ angular opening of the clumpy torus and θ is the angle of the line of sight to the polar direction, the covering factor of the clouds at θ is $C = 1 - e^{-N}$. Adopting $N_0 = 5$, $\sigma = 30^\circ$, $\theta = 30^\circ$, within a wide permitted range (see table 11 of Martínez-Paredes et al. 2017), we obtain a covering factor of 0.1. This shows that a clumpy molecular torus can provide a non-negligible covering factor at low polar angles.

Recent observations have also strengthened the case for dust in the polar regions of AGN, making our model more plausible. Infrared interferometry has shown that dust in the form of an equatorial disk dominates in the near-IR, but mid-IR flux can be dominant in the polar regions of AGN (e.g., López-Gonzaga et al. 2016; Tristram et al. 2014). The interpretation is that the inner, hotter part of the MT dominates at shorter wavelengths, but there is a significant amount of cooler dust in the polar regions in an elongated structure giving rise to the mid-IR emission. This may

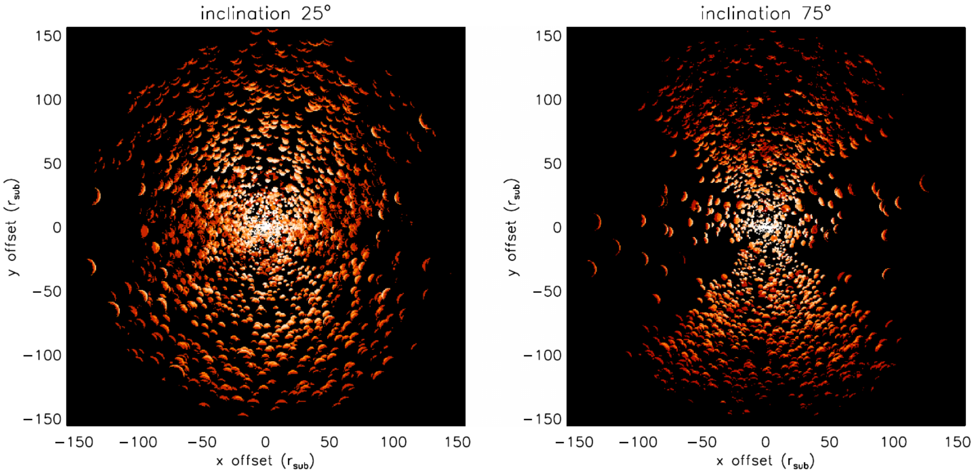

FIGURE 2.5: Figure adapted from Hönig and Kishimoto 2017, showing radiative transfer images of the dust cloud distribution in the CAT3D-WIND model. They show the 12μm emission from dust clouds for a face on view of the AGN at left, and edge on view at right. In the edge on view, a polar dusty wind of lower cloud density can be seen lifted from the central accretion disk.

be the result of a dusty wind launched from radiation pressure of the accretion disk acting on dust grains, causing them to lift towards the polar regions of the AGN (e.g., Roth et al. 2012). In Figure 2.5, I show images from the CAT3D-WIND radiative transfer model of the MT, which uses the dusty polar wind to correctly map the infrared emission seen in AGN (Hönig and Kishimoto 2017). In this scenario, it is speculated that the hot inner MT serves as the optically thick obscurer to the BLR for edge on views, while the dusty polar wind does not provide high enough column densities to obscure the AGN when viewed face on (Hönig et al. 2012). This allows for the model to preserve type I/II AGN unification, but motivates dust in the polar regions of AGN with a physical model.

Variability in our model can result from a range of disturbances in the system. We consider here two types of variations in the injected EED. In the first case, the injected EED amplitude increase takes place only in the sheath. Then, for both the spine-sheath-only model and the spine-sheath embedded in the MT model, the synchrotron emission of the spine is not expected to vary significantly, as neither the spine magnetic field, nor the spine EED varies. This would result in GeV orphan flares as in blazar PKS 1222+216 (Ackermann et al. 2014), as the seed photon energy density would increase in the spine frame for both models. A difference between the two models that could be used to discriminate between them is that while in the spine-sheath embedded in the MT model only the GeV part of the high energy component should vary, in the spine-sheath only model the hard X-ray to MeV flux would also vary with similar amplitude. This is because the

MT-embedded spine-sheath model (spine-sheath only model) seed photons have a narrow (broad) spectral distribution, and this is reflected in the energy width of their IC spectra. Consider now the case where in the MT-embedded spine-sheath model the maximum energy of the EED increases in both the spine and the sheath. In this case, the luminosity of both the spine and the sheath increases and it is possible that dust is sublimated within the sheath radiation opening angle (that would be the case when $L_{sh,obs} > L_{\star}$). If the maximum EED energy increases sufficiently, the sheath will produce synchrotron UV ionizing photons which will illuminate the clouds from which the dust has been sublimated, which in turn will produce line emission (we think of such clouds as parts of the polar part of the MT, possibly parts of an outflow, e.g., Netzer 2015). This line emission would temporally correlate with the optical-UV variations of the spine and sheath synchrotron emission. Such correlations between the optical-UV continuum and emission line variability have been tentatively detected by Isler et al. (2013) and León-Tavares et al. (2013) in the blazar 3C 454.3, and very recently reported with high statistical significance by Jorstad et al. (2017) in the blazar CTA 102.

Chapter 3

Testing IC/CMB with the *Fermi*/LAT

3.1 Introduction

As introduced section 1.8, the first astrophysical target observed by the *Chandra* X-ray Observatory was PKS 0637-752, a moderately distant (z = 0.651) radio-loud AGN. Unexpectedly, *Chandra* discovered high levels of X-ray emission associated with the previously known kpc-scale radio jet (Schwartz et al. 2000; Chartas et al. 2000). The *Chandra* observations revealed bright X-ray knots roughly co-spatial with the radio knots, but with an X-ray flux density far too high and an X-ray spectrum far too hard to be consistent with a single radio-optical-X-ray synchrotron spectrum. In the years that followed, this phenomenon of bright X-ray jets in which the X-ray emission could not be explained by an extrapolation of the radio-optical synchrotron spectrum was found to operate in dozens of other sources, nearly always in more powerful jets with a FR II morphology. As explained in section 1.8, we refer to these jets with evidence of multiple spectra as Multiple Spectral Component or "MSC" jets (this includes those cases in which the anomaly is seen in the UV instead of or in addition to the X-rays). Typically the observed X-ray emission in less powerful FR I jets is more consistent with a single radio to X-ray synchrotron spectrum (e.g. Wilson and Yang 2002), although this is not always the case (e.g. M84, Meyer et al. 2018)

As explained in section 1.9, the IC/CMB model is the most prevalent explanation for the X-ray emission observed in MSC jets in the literature. However, there are many aspects of the IC/CMB model which are at odds with observations, including: a high degree of UV polarization in the high-energy spectral component in the PKS 1136-135 jet (Cara et al. 2013), rapid X-ray variability in Pictor A (Marshall et al. 2010), a low jet-to-counterjet flux ratio in 3C 353 (Kataoka et al. 2008), and substantial offsets between radio and X-ray knots (e.g., Clautice et al. 2016 – see Chapter 4 for a more detailed summary of other lines of evidence against the IC/CMB model). There are several alternative models which might explain the X-ray emission observed in MSC jets. In particular, a second higher-energy population of synchrotron-emitting electrons (Atoyan and Dermer 2004; Harris, Mossman, and Walker 2004; Kataoka and Stawarz 2005b; Hardcastle 2006; Jester et al. 2006; Uchiyama et al. 2006) and various hadronic emission models (Aharonian 2002; Petropoulou, Vasilopoulos, and Giannios 2017; Kusunose and Takahara 2017). Until recently it has been difficult to reject the IC/CMB model in favor of any alternative, since in most cases any model can be tuned to reproduce the somewhat sparsely sampled SED. However, the question of which emission process is at work in these X-ray jets is important since these models imply vastly different physical properties.

If the second synchrotron model is correct, it will be important to understand why there are multiple electron energy distributions and how this is connected to the particle acceleration taking place in these jets. An immediate consequence of a higher-energy electron distribution is subsequent TeV gamma-rays produced when these electrons inverse-Compton scatter the CMB (Georganopoulos et al. 2006; Meyer et al. 2015). These TeV gamma-rays may be detectable for low redshift sources with the upcoming Cherenkov Telescope Array (CTA). Alternatively, if the source of the X-rays is due to hadronic emission processes, then this has important implications for the particle make-up and energy content of these jets.

3.1.1 Using the *Fermi*/LAT to test the IC/CMB model

As described in section 1.10, the IC/CMB model predicts a high level of gamma-ray emission from the jet which should be detectable with the *Fermi*/LAT. However, due to the poor spatial resolution of *Fermi* (see Figure 1.11), the jet cannot be resolved separately from the highly variable and luminous core. One solution is to search for the steady gamma-ray IC/CMB emission component at times when the variable core is in a low state. This technique was applied in 3C 273 (Meyer and Georganopoulos 2014) and PKS 0637-752 (Meyer et al. 2015; Meyer et al. 2017), where in both cases the upper limits to the gamma-ray flux during times when the core was quiescent were well below the required level from IC/CMB. This method is useful for the analysis of bright and variable gamma-ray sources. However, a substantial number of MSC jets are associated with sources not detected in the *Fermi*/LAT 3FGL 4-year point source catalog. This strongly suggests that the gamma-ray emission expected under the IC/CMB model may be absent without any complication of gamma-ray emission from the core. For these sources, non-detections using data for the entire

Fermi mission to date can yield upper limits to the gamma-ray flux which violate the IC/CMB model.

In this work, we present the *Fermi* gamma-ray and multiwavelength analysis of all of the known MSC jets (taken from the *XJET* database) not within the 3FGL catalog (amounting to 27 sources), as well as four sources from the 3FGL catalog: PKS 1150+497, PKS 0920-397, 0838+133, and PKS 1127-145. An analysis of the remaining 3FGL catalog sources will be presented in a future work, as the *Fermi* analysis of these sources is both more lengthy and computationally intensive.

3.2 Data Analysis

3.2.1 Sample Properties

In Tables 3.1 and 3.2, I summarize the source properties of 31 sources presented in Breiding et al. (2017) and an upcoming publication in preparation: Breiding et al. (2019). Additionally, two sources presented here were previously published in Meyer et al. (2017), Meyer et al. (2015), and Meyer and Georganopoulos (2014). In columns 2−4, I report the source redshift and corresponding angular size scale in kpc per arcsecond and the black hole mass as M_{BH}, taken from the literature where available as noted in the table. Using data from NED and archival VLA and ALMA observations, Mary Keenan (a co-author) decomposed the radio spectrum of these sources into the extended (isotropic) "lobe" component and beamed "core" component as in Meyer et al. (2011). These spectra are shown in Figure 3.1 for six sources where we have now ruled out IC/CMB (the SEDs for the remaining sources can be found in the Appendix). In column 5 I give the kinetic jet power L_{kin}, where I have scaled from the 300 MHz radio luminosity of the radio lobes using the scaling of Cavagnolo et al. (2010). In column 6 I give the radio core dominance R_{CE}, where this is the logarithmic ratio of the core to extended (i.e., lobe) spectrum at 1.4 GHz, and in column 7 I give the radio crossing frequency ν_c, where this is the frequency that the core spectrum crosses with the lobe spectrum. Also following the methods described in Meyer et al. (2011), Mary Keenan made a simple phenomenological fit to the synchrotron spectrum in order to determine an approximate peak luminosity and frequency (L_p and ν_p respectively), which are given in columns 8 and 9 with the corresponding SED model fits shown in Figure 3.2 for six sources (the remaining sources can be found in the Appendix).

For the complete SEDs, we plot the lobe spectrum as cyan squares, *Fermi*/LAT data in black, the rest of the data with blue circles (data filtered out from the fitting is shown as gray circles), and the model fits as solid red lines. Equipartition magnetic field strength, B_{eq}, is given for the (typically) brightest X-ray knot (in some cases the whole jet) in column 10. In column 11, I give the X-ray dominance, R_x, of the same jet feature. R_x is defined as the logarithmic ratio of the 1 keV X-ray flux density to the 8.6 GHz radio flux density (in νF_ν). Finally, in column 12 I show the main result of this work: whether the IC/CMB model is ruled out for the source on the basis of the *Fermi* observations presented here. For some sources we did not have enough data to reliably produce SED model fits for either the radio spectrum or the synchrotron peak, and therefore we left the relevant columns blank (those SEDs are also omitted from the Appendix). It should be noted that most of these sources have quite high kinetic jet powers (see Figure 4 from Meyer et al. 2011, typical values of L_{kin} range from $10^{43.5} - 10^{45.5}$ erg s^{-1}) and black hole masses (see Figure 1 from Chiaberge and Marconi 2011, typical values of M_{BH} range from $10^7 - 10^9$ $M_\odot$) compared to other radio-loud AGN generally.

TABLE 3.1: Source Properties

(1) Source Name	(2) z	(3) kpc/″	(4) $\log \frac{M_{BH}}{M_\odot}$	(5) $\log L_{kin}$ $(erg\ s^{-1})$	(6) R_{CE}	(7) $\log \nu_c$ (Hz)	(8) $\log \nu_p L_p$ $(erg\ s^{-1})$	(9) $\log \nu_p$ (Hz)	(10) B_{eq} $(10^{-4}\ G)$	(11) R_x	(12) IC/CMB Ruled Out?
0838+133	0.680	7.15	8.67[b]	45.8	-0.15	9.31	45.7	13.3	2.59	0.45	Y
1317+520	1.06	8.23	9.01[b]	...	...	...	...	...	1.38	0.67	Y
1418-064	3.69	7.33	...	46.0	-0.25	9.42	...	...	0.898	2.1	Y
1508+572	4.31	6.88	...	...	...	...	47.3	13.6	0.677	2.2	N
2216-038	0.901	7.90	9.08[b]	45.6	-0.21	9.32	46.6	13.5	1.07	0	N
3C 120	0.0340	0.682	7.36[d]	43.8	0.46	8.6	44.5	13.7	0.353	1.7	Y
3C 17	0.220	3.58	...	45.4	-1.1	10.5	44.4	12.6	1.03	-0.33	N
3C 227	0.0858	1.62	...	44.9	-2.9	12.2	44.3	13.9	0.485	0.99	N
3C 273	0.160	2.65	8.91[c]	45.5	0.37	8.82	45.9	14.4	1.00	1.1	Y
3C 321	0.0962	1.79	...	44.8	-3.8	11.3	...	...	0.189	0.72	N
3C 353	0.0300	0.604	...	42.7	-2.6	12.0	43.3	14.4	0.352	0.50	Y
3C 465	0.030	0.611	...	44.3	-1.6	11.2	42.0	13.0	0.818	0.58	Y
4C 13.41	0.241	3.84	9.1[e]	45.0	-2.1	11.0	45.6	14.1	0.146	0.75	Y
4C 20.24	1.11	8.31	...	46.1	-0.88	10.2	46.6	13.8	0.100	0.29	Y
4C 35.03	0.0370	0.739	...	44.0	-1.5	11.0	...	...	0.485	0.88	Y
4C 62.29	3.89	7.18	...	...	...	...	46.5	12.9	4.92	1.4	Y
4C 65.15	1.63	8.62	9.39[f]	46.1	-3.6	11.1	...	...	2.42	0.32	N
4C 69.21	0.751	7.43	6.85[b]	45.5	-0.29	9.44	46.1	12.7	2.19	0.25	Y
4C 73.18	0.360	5.08	8.35[b]	44.9	0.97	8.41	45.8	13.7	0.330	1.71	Y
B2 0738+313	0.631	6.92	9.57[b]	45.0	0.78	8.53	46.0	13.8	7.27	0.86	Y
PKS 0413-21	0.807	7.63	8.18[b]	45.9	-0.78	9.94	45.3	12.2	1.40	-0.37	Y
PKS 0637-752	0.650	6.75	9.41[a]	45.9	0.19	9.01	46.3	13.4	1.15	0.63	Y
PKS 0920-397	0.591	6.71	...	...	...	...	45.8	13.1	0.837	0.46	N
PKS 1030-357	1.46	8.59	...	...	...	...	...	...	0.924	0.81	Y
PKS 1045-188	0.595	6.74	6.83[e]	45.5	-0.86	9.88	46.0	13.5	0.433	0.25	N
PKS 1046-409	0.620	6.87	...	45.6	0.40	8.83	...	...	0.455	0.46	Y
PKS 1127-145	1.19	8.41	...	45.6	1.3	7.93	46.6	13.7	0.469	0.47	N
PKS 1136-135	0.560	6.26	8.45[b]	45.9	-0.72	10.7	45.4	14.1	0.470	1.3	Y

Black hole masses were obtained from the following literature sources: [a]Chen et al. (2015), [b]Liu, Jiang, and Gu (2006), [c]Kim et al. (2015), [d]Kaspi et al. (2000), [e]Woo and Urry (2002), and [f]Kozłowski (2017).

TABLE 3.2: Source Properties – Continued

(1) Source Name	(2) z	(3) kpc/″	(4) $\log \frac{M_{BH}}{M_\odot}$	(5) $\log L_{kin}$ $(erg\ s^{-1})$	(6) R_{CE}	(7) $\log \nu_c$ (Hz)	(8) $\log \nu_p L_p$ $(erg\ s^{-1})$	(9) $\log \nu_p$ (Hz)	(10) B_{eq} $(10^{-4}\ G)$	(11) R_x	(12) IC/CMB Ruled Out?
PKS 1150+497	0.334	4.83	8.45[b]	45.2	-1.1	10.0	45.3	13.0	0.840	1.3	Y
PKS 1229-021	1.05	7.91	8.70[b]	46.0	0.14	9.00	46.1	14.1	3.20	0.59	Y
PKS 1354+195	0.720	7.03	9.44[a]	45.8	-0.50	9.50	46.0	13.6	2.07	0.10	Y
PKS 2209+080	0.480	5.80	...	45.5	-1.5	10.4	45.6	13.4	1.00	-0.55	Y
QSO 0957+561	1.42	8.58	9.40[f]	...	...	...	...	...	1.11	-0.87	N

Black hole masses were obtained from the following literature sources: [a]Chen et al. (2015), [b]Liu, Jiang, and Gu (2006), and [f]Kozłowski (2017).

In this work, we aim to test whether the high level of steady gamma-ray emission predicted under the IC/CMB model is seen. It is therefore essential that the precise level of the expected gamma-ray emission is known. As discussed in section 1.10 and Meyer et al. (2017), the X-ray to gamma-ray IC component has the same spectral shape as the radio-optical synchrotron spectrum, and the requirement to match the observed X-rays thus fixes the rest of the X-ray spectrum, which usually peaks in the gamma-rays. It is thus critical that we compile the best possible multi-wavelength SEDs for the knots, from radio to X-rays. I describe here the archival and new data used to compile these SEDs.

3.2.2 VLA

As shown in Tables 3.3-3.4, we used both new and the archival VLA imaging of sufficient quality in bands L, C, X, and Ku (A, B, or C configuration) in order to obtain a high-resolution image with the knots distinctly resolved. All sources were analyzed using `CASA`, version `4.7.0` or greater. In all cases, either 3C 286 or 3C 48 was used as the flux density calibrator, and the source itself was used for phase calibration. We applied several rounds of self-calibration before generating the final image with `clean`. In Table 3.3 we list the source, the band and configuration, the central frequency of the observation, the project code, date of observation, the RMS of the final self-calibrated image in μJy, and the size of the restoring beam in arcseconds. These observations were supplied by the co-authors Jennifer Hewitt, Dr. Eileen Meyer, Mary Keenan, Omar French, and Kassidy Kollman.

TABLE 3.3: VLA Archival Data

Source	Band (Config.)	Frequency (GHz)	Project	Date	RMS (μJy)	Beam ($''$)
0838+133	Ku (A)	14.94	AN104	2002 Feb 23	4778	0.15×0.13
1317+520	C (A)	4.86	AM0723	2003 Aug 28	55	0.43×0.37
	Ku (A)	15.0	AJ0300	2003 July 26	416	0.15×0.14
2216-038	L (A)	1.40	AL634	2004 Nov 21	682	1.66×1.33
3C 17	C(A)	4.860	AS179	1985 Mar 08	862	0.48×0.39
3C 120	L(A)	1.477	AW92	1983 Oct 08	12481	1.6×1.48
	C (A)	4.86	AW189	1987 July 05	16280	0.47×0.42
	X (B)	8.46	AC507	1998 July 04	26785	0.91×0.74
	Ku(B)	15.0	AH672	2000 Jan 04	14909	0.50×0.57
3C 321	C (C)	4.85	AV127	1986 Dec 02	415	5.8×4.8
3C 353	C (A)	4.84	AB0389	1986 May 21	109	0.45×0.42
3C 465	X (A)	8.47	AH717	2001 Jan 15	32	0.23×0.21
4C 20.24	L (A)	1.43	AM672	2000 Dec 24	7327	1.98×1.46
4C 35.03	C (A)	4.86	AM221	1987 Aug 15	109	0.39×0.36
	L (A)	1.43	AL604	2004 Oct 24	368	2.62×1.17
4C 62.29	Ku (A)	15.0	15A-357	2015 Jun 22	8	0.15×0.11
4C 65.15	Ku (A)	15.0	15A-357	2015 Jun 22	4	0.11×0.20
4C 69.21	Ku (A)	15.0	15A-357	2015 Jun 22	9	0.16×0.11
4C 73.18	L(A)	1.490	AE27	1983 Nov 01	318	1.60×1.15
B2 0738+313	L (A)	1.490	AG160	1984 Nov 14	41	1.52×1.29
PKS 0413-21	C (A)	4.86	AM672	2000 Nov 05	27	0.63×0.40
PKS 1045-188	L(A)	1.490	AG361	1992 Nov 18	2575	2.25×1.29
PKS 1136-135	C (A)	4.860	AH938	2007 Jun 23	154	0.51×0.43
	X (B)	8.460	AC689	2008 Nov 03	111	1.01×0.74
	Ku (AB)	22.00	AC461	2002 May 27	123	0.25×0.15
PKS 1127-145	L(A)	1.477	AO62	1986 Mar 31	27451	2.67×1.27
PKS 1150+497	C (A)	4.860	AH938	2007 Jun 24	216	0.44×0.33
PKS 1229-021	L (A)	1.505	AK95	1983 Oct 29	510	1.85×1.26
	C (A)	4.848	AK95	1983 Oct 29	305	0.61×0.40
	X (A)	8.350	AK353	1994 Mar 20	58	0.28×0.27
	U (B)	14.94	AK180	1987 Dec 12	72	0.59×0.42

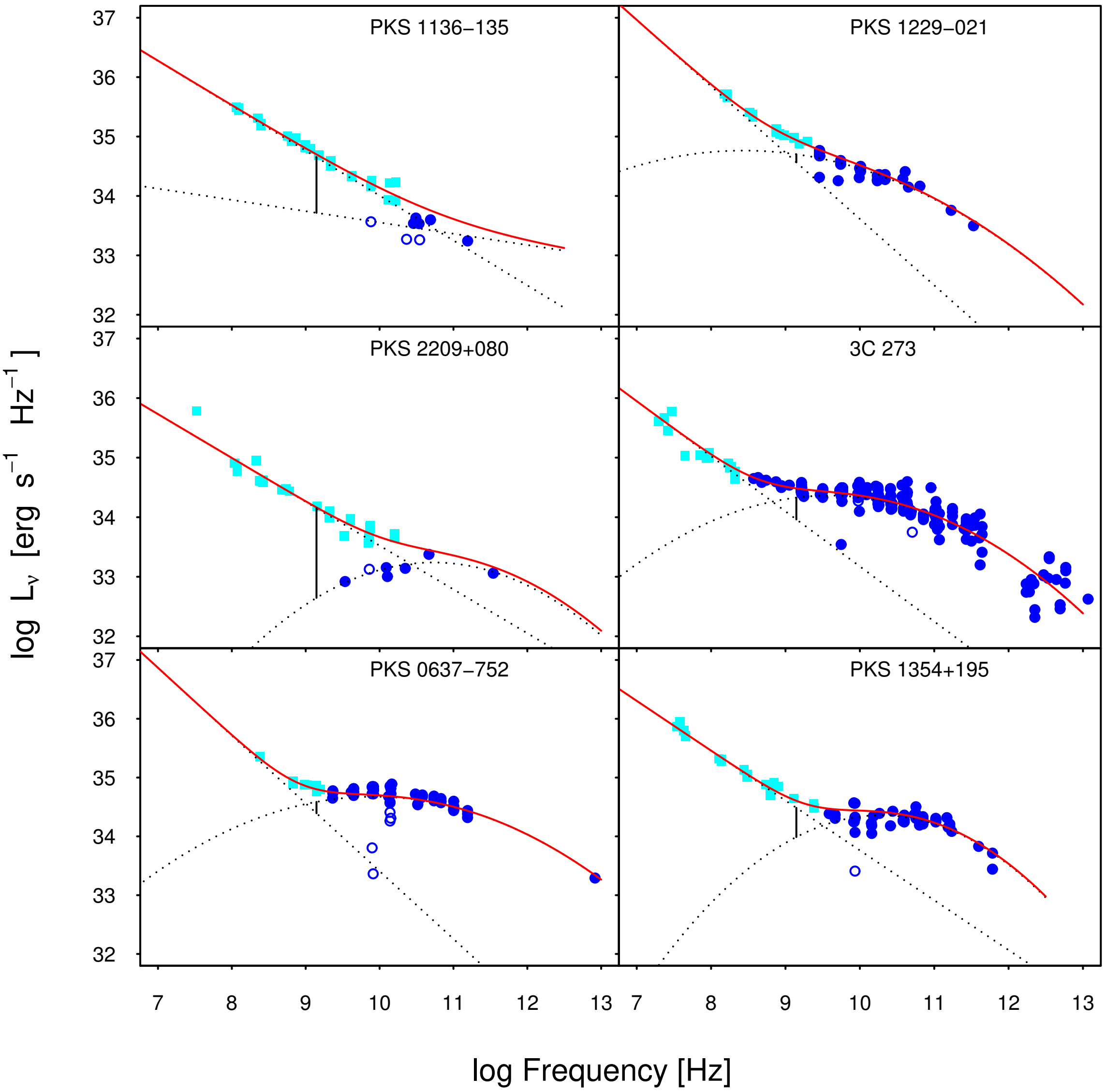

FIGURE 3.1: Low frequency radio SEDs for six sources where we have now ruled out IC/CMB as the X-ray emission mechanism. Data was obtained through the NED database, cyan squares represent extended lobe emission, blue circles represent core emission, and open circles represent data filtered out from the fitting. A power-law model was used to fit the lobe emission and a log parabola was used to fit the core emission, dashed black lines showing each of the individual fits. The solid red line shows the total model fit adding both of these components for the radio spectrum. The solid black line connects the core and extended emission at 1.4 GHz, the ratio of which was used to determine the radio core dominance. This figure was originally published in Breiding et al. (2017).

3.2.3 VLBI

The target PKS 1354+195 was observed four times (in 1997, 1999, 2002, and 2003) as part of the Monitoring Of Jets in Active galactic nuclei with VLBA Experiments (MOJAVE) monitoring

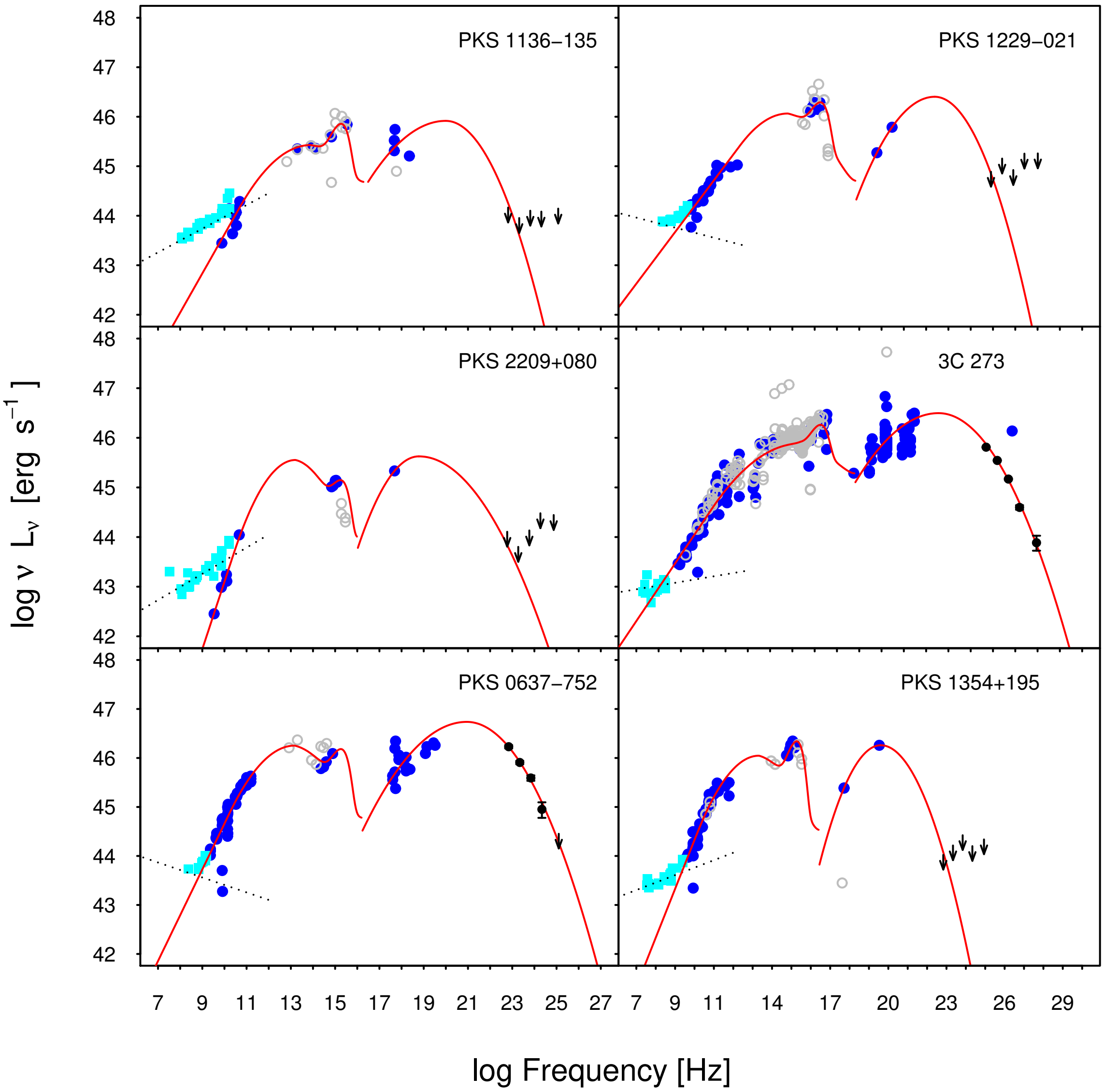

FIGURE 3.2: The SED for each source was fit with the parametric model from Meyer et al. (2011) shown in red to estimate parameters for the synchrotron peak frequencies and luminosities. All data was obtained through NED, with the cyan squares representing the lobe spectrum with the line of best fit as the dotted black line. Blue circles represent the rest of data and gray open circles represent the data that was filtered out and not used in the fitting. The *Fermi*/LAT data points are shown in black, with values taken from the 3FGL catalog for PKS 0637-752 and 3C 273 and the rest being upper limits taken from the analysis done for this paper. This figure was originally published in Breiding et al. (2017).

project (Lister et al. 2009; Lister et al. 2016), although no previous proper motion measurements were reported. We downloaded the fully-reduced `fits` images from the MOJAVE website, and used the publicly available Wavelet Image Segmentation and Evaluation (WISE) code (Mertens and Lobanov 2015; Mertens and Lobanov 2016) to analyze the images for proper motions.

TABLE 3.4: VLA Archival Data – Continued

Source	Band (Config.)	Frequency (GHz)	Project	Date	RMS (μJy)	Beam ($''$)
PKS 1354+195	L (A)	1.425	AB920	1999 Jul 19	900	1.49×1.36
	C (B)	4.860	AB331B	1985 Apr 20	258	1.21×1.12
	X (B)	8.415	BL3	1993 Mar 08	135	1.21×0.77
PKS 2209+080	C (A)	4.86	AM723	2003 Aug 30	107	0.39×0.36
	U (B)	14.93	AM723	2002 Aug 20	90	0.44×0.41
QSO 0957+561	C (A)	4.860	AB263	1983 Nov 01	692	1.04×0.54

The WISE code comprises three main components. First, detection of structural information is performed using the segmented wavelet decomposition method. This algorithm provides a structural representation of astronomical images with good sensitivity for identifying compact and marginally resolved features and delivers a set of two-dimensional significant structural patterns (SSP), which are identified at each scale of the wavelet decomposition. Tracking of these SSP detected in multiple-epoch images is performed with a multi-scale cross-correlation algorithm. It combines structural information on different scales of the wavelet decomposition and provides a robust and reliable cross-identification of related SSP.

The images of PKS 1354+195 were taken with the Very Long Baseline Array (VLBA) at 2 cm (15 GHz) on 18 August 1997, 19 July 1999, 12 August 2002, and 06 January 2003. The images were centered on the core position and required no additional adjustment before analysis with WISE. The final reported proper motion values were obtained using a scale factor of 6, though results were similar across a range of reasonable scale factors for the size of the knots in the jet. We only report those features detected in at least 3 of four epochs. The proper motions analysis was contributed by co-author Dr. Eileen Meyer.

3.2.4 ATCA

Archival imaging from ATCA was used for some targets, shown in Table 3.5. Data were downloaded from the ATCA archive and imported into a UV file using `miriad`. The resulting UV file was imported into `CASA` using the task `'importmiriad'` and all data analysis was conducted in `CASA`. PKS 1934-638 served as the amplitude calibrator and all sources were self-calibrated. In general the analysis proceeded very similarly to that for VLA data. ATCA data analysis was supplied by Dr. Eileen Meyer.

TABLE 3.5: ATCA Archival Data

Source	Frequency (GHz)	Project	Date	RMS (μJy)	Beam ($''$)
PKS 0920-397	19	C890	2004 May 11	25	0.74×0.48
PKS 1030-357	20	C890	2004 May 12	82	0.88×0.47

3.2.5 ALMA

In Table 3.6, we list the new ALMA data used in our analysis (PI: Dr. Eileen Meyer), where we give the observing band, the cycle of the observations, the project code, the effective frequency of the flux measurement, the RMS of the final image and the size of the restoring beam. All programs included observations at band 3 and 6, however only about 40% of the C-rated cycle 3 programs were completed, as well as only about 30% of the C-rated cycle 5 programs. Forthcoming observations are likely to improve on those presented in this work.

TABLE 3.6: ALMA Observations

Source	Band	Cycle	Project	Freq. (GHz)	RMS (μJy)	Beam ($''$)
3C 465	3	5	2017.01572.S	97.5	18	0.18×0.14
4C 20.24	6	5	2017.01572.S	233	435	6.45×4.93
PKS 1229-021	3	4	2016.1.01481.S	97.5	171	0.76×0.53
	6	4		233	93	0.57×0.46
PKS 1354+195	3	4	2016.1.01481.S	97.5	224	0.76×0.53
	6	4		233	96	0.83×0.56
PKS 2209+080	3	3,4	2015.1.00932.S	97.5	246	0.52×0.35
	6	4	2016.1.01481.S	233	161	0.61×0.46

In Table 3.7, we list the archival ALMA data used in our analysis, where we give the band, the central frequency of the observation, the project code, date of observation, the RMS of the final self-calibrated image in μJy, and the size of the restoring beam in arcseconds. PKS 1136-135 was observed in band 3 by ALMA as a calibrator for a project unrelated to jets (program 2016.1.01250.S, PI: C. Peroux), and this data was kindly made available to us by the PI.

TABLE 3.7: ALMA Archival Data

Source	Band	Freq. (GHz)	Project	Date	RMS (μJy)	Beam ($''$)
PKS 0413-210	6	263	2012.1.00999.S	2015 Jan 04	38	1.19×0.66
PKS 0920-397	6	238	2012.1.00610.S	2014 Apr 10	68	0.65×0.55
PKS 1136-135	3	94.8	2016.1.01250.S	2016 Dec 04	28	1.26×1.14

For all sources, the data was first reduced using the provided `scriptForPI.py` script, which produces a calibrated measurement set appropriate for imaging with `clean`. The source scans were split off and several rounds of phase-only (non-cumulative) self-calibration were applied before a final (cumulative) round of amplitude and phase self-calibration. `clean` was used in `mfs` mode, with `nterms=2` and briggs weighting with `robust=0.5`. The final RMS measurements correspond to the primary-beam-corrected image, though we use the uncorrected images in the figures. In the case of PKS 2209+080, we combined together and imaged the somewhat lower-resolution cycle 4 data with the cycle 3 data, after core subtraction. The ALMA data analysis was contributed to this project by co-authors Dr. Eileen Meyer and Jennifer Hewitt.

3.2.6 HST

PKS 2209+080 was observed as part of our HST program GO-13676 (PI: Dr. Eileen Meyer). This source was observed for one orbit with the Wide Field Camera 3 (WFC3) in the near-infrared (IR) channel with filter F160W (λ=1.6μm), and for two orbits with the Advanced Camera for Surveys Wide Field Camera (ACS/WFC) with filter F606W (λ=6000Å). In both cases a dithering pattern was used to better sample the PSF, and the raw images were stacked using a routine similar to AstroDrizzle, but better optimized for Astrometry. In particular, several dozen point sources in the optical image were used as a reference frame on which all images were aligned (final error on the registration is less than 1 mas) – this allowed us to precisely align the optical and IR images, which allows for better identification of common features in both. The final pixel scale in both images is 25 mas. The HST analysis was contributed by Dr. Eileen Meyer.

We did not attempt a galaxy subtraction, as it has a very irregular profile and models produced by `iraf` tasks `ellipse` and `bmodel` left large residual errors. We measured flux densities using contours around each knot, estimating the background by moving the same contour to 6-8 positions at the same radius from the galaxy center. The mean background value was subtracted from the initial flux density measurement, and errors are taken to be $\sqrt{2}$ times the standard deviation of the background flux densities. The flux densities were measured using the `viewer` utility of the `CASA` package.

3.2.7 Fermi

Fermi/LAT event and spacecraft data were extracted using either a 7° or 10° region of interest (ROI), an energy cut of 100 MeV-100 GeV, a zenith angle cut of 90°, and the recommended event class and type for point source analysis for all sources. The time cuts included all available *Fermi* data at the time of analysis, greater than 8 years in all cases. Following the standard methodology for *Fermi*/LAT binned likelihood analysis, a binned counts map was made with 30 logarithmically spaced energy bins and 0.2 degree spatial bins in all cases. An initial spatial and spectral model file for each source was constructed with sources up to 10° outside the ROI using the publicly available `make3FGLxml.py` script. This populates the model file with point and extended sources from the *Fermi*/LAT 3FGL catalog and an extended source catalog respectively. Additionally, the current galactic diffuse emission model, `gll_iem_v06.fits`, and recommended isotropic diffuse emission model for point source analysis, `iso_P8R2_SOURCE_V6_v06.txt`, were used for the analyses. The livetime cubes were computed using 0.025 steps in $cos(\theta)$ (where θ is the inclination with respect to the LAT's z-axis) and 1° spatial binning. Then all-sky exposure maps were computed using the same energy binning as the counts maps. After obtaining converged fits following the maximum likelihood optimizations with the initial model, Test Statistic (TS) residuals maps with 1° spatial binning were created in order to find new point sources not accounted for in the 3FGL catalog following the procedure outlined in Meyer et al. (2015). The TS is defined as twice the logarithmic ratio of the maximum likelihood calculated with an additional point source at the specified location to the maximum likelihood without an additional source and can be taken as roughly the significance squared. As an example, we show in Figure 3.3 the TS residual maps created before and after adding the new sources not accounted for in the 3FGL catalog for four sources. The new source positions are shown with green circles and the sources we obtained upper limits for this paper are shown with white circles.

In locations where TS residual values were greater than ten, we added point sources with power-law spectra to the model files and optimized their positions and spectral parameters. Next, we obtaining converged maximum likelihood fits for the updated model files. For the targets which were not members of the 3FGL 4-year point source catalog for the *Fermi*/LAT, our target of

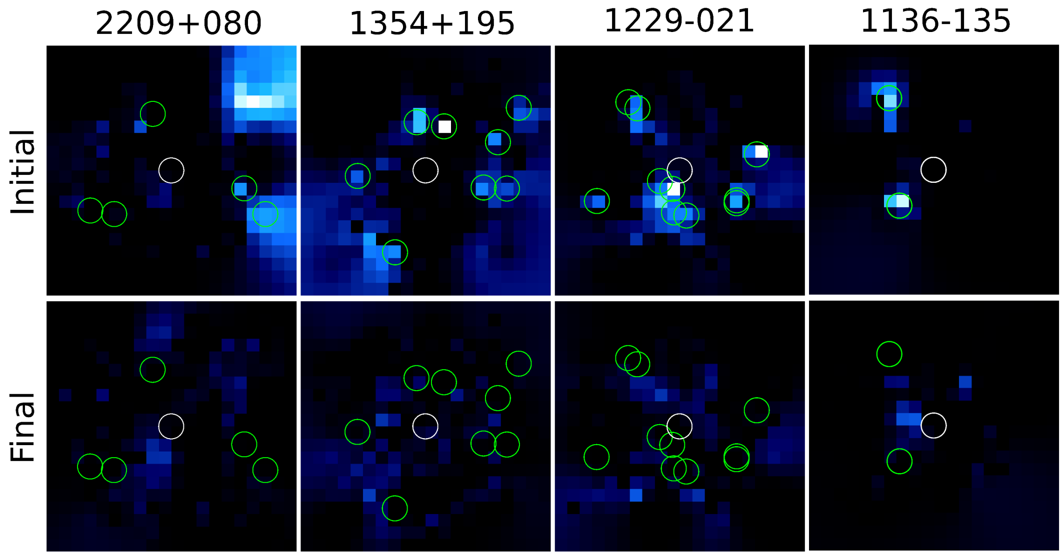

FIGURE 3.3: Initial and final Test Statistic (TS) residual maps for the region around each target, with final localized positions of all new non-3FGL sources shown as green circles, and the source position shown as a white circle. Pixels are one square degree. The intensity scale ranges from a TS of 0 to 25 in all maps and from black to white respectively. This figure was originally published in Breiding et al. (2017).

interest was added to the model file with a fixed photon index if it was not detected (no substantial residual TS near the target location). We used photon indices derived from the implied gamma-ray index of the IC/CMB model for the four targets presented in Breiding et al. (2017). For the rest of the targets, we used a photon index of 2, as this represents a flat gamma-ray spectrum in $\nu F \nu$. After this, the upper limits in the five *Fermi* energy bands of 100 MeV-300 MeV, 300 MeV-1 GeV, 1 GeV-3 GeV, 3 GeV-10 GeV, and 10 GeV-100 GeV were computed by running the analysis tools separately on each data set with the appropriate energy range data cuts. Contributions to the *Fermi* analysis work were made by Adursh Iyer.

For sources which were members of the 3FGL catalog, we used the converged maximum likelihood model files to generate light curves. The light curves were generated by cutting the data into three week time bins and running the analysis tools on each time bin separately. Then maximum likelihood optimizations were run on each time bin to obtain best fit parameters for the target's spectral normalization, with the index of the spectrum fixed (all of the targets were assumed to have a power-law spectral form). After this, the TS was computed for each time bin. We then progressively combined data from each time bin, from lowest to highest TS, one bin at a time. After this, we ran the analysis tools separately again for each contiguous time bin addition, and obtained maximum likelihood fits, before computing upper limits (or flux densities if the TS of the source was greater than 10) in the five *Fermi* energy bands given above. This analysis was done for the sources: 0838+133, PKS 0920-397, PKS 1127-145, and PKS 1150+497.

The assumption behind the combined bin analysis is that during states in which the variable core is quiescent, the TS of the source is lower, while during flaring states it is higher. The IC/CMB gamma-rays are supposed to be constant in time, and so analyzing the data during periods in which the core is quiescent gives us the best chance of observing the IC/CMB gamma-rays from the jet. Alternatively, if the IC/CMB gamma-rays are not detected, then this method gives us the most stringent upper limits.

3.3 Results

For the 31 sources presented in this thesis, we did not find evidence for IC/CMB gamma-rays with the *Fermi*/LAT. For the 27 that were not a member of the 3FGL catalog, we also did not find any evidence for any gamma-ray detection. In Tables A.1-A.5 (shown in the Appendix), we give the 95% flux density upper limits obtained with *Fermi*, along with the predicted flux densities from the IC/CMB model, status on whether the IC/CMB model is ruled out for this source, and the upper limit on the Doppler factor for the jet feature analyzed due to the *Fermi* upper limits (assuming an equipartition magnetic field). In this work, we consider the IC/CMB model to be ruled out for a source if the 95% *Fermi* upper limits were below the level required by the IC/CMB model (for most sources it is clearly ruled out at a much higher level than than 95%). In 21 out of the 31 sources analyzed, we found the IC/CMB model to be ruled out. For the sources in which the upper limits lie *above* the IC/CMB model prediction, it is possible that continued *Fermi* observations will eventually yield limits low enough to rule out IC/CMB. Alternatively, it is possible we may eventually detect IC/CMB gamma-rays from the jet for these sources, as a steady low-level flux.

I will now discuss the observations of six select sources: 4C+62.29, PKS 1136-135, PKS 1150+497, PKS 1229-021, PKS 1354+195, and PKS 2209+080 (four of which were previously published in Breiding et al. 2017). We show in Figure 3.4 the broadband SEDs for (typically) the most X-ray prominent features in these sources, and multi-wavelength images for each source in Figures 3.5-3.10. The SEDs along with radio images of the jet for the remaining sources analyzed in this thesis are given in the Appendix. In the case of PKS 1354+195, we also show the total X-ray flux density of the jet after knot A, and in PKS 1229-021, we show the combined flux density of knots B, C, and D which could not be separately resolved in all imaging. Combining fluxes along the jet is still consistent with the given *Fermi* upper limits, since these upper limits apply to the source as a whole (including contributions from the jet, core, and whatever else may be producing gamma-rays). While adding all the X-ray flux along the entire jet will generally lead to a higher predicted gamma-ray flux level (making it more likely to rule out IC/CMB in a given source), it is more straightforward (and conservative) to rule out IC/CMB for individual knots, given that they may not have the same characteristic Γ or magnetic field. If the IC/CMB model is ruled out in the brighter knots, an alternative X-ray emission mechanism is required, regardless of whether the other knots could still be consistent with IC/CMB. Furthermore, it would be quite coincidental for X-rays of about the same flux level to be produced by two very different processes in the same jet. For this reason, we chose to analyze individual jet features rather than combined ones when possible for all of the sources analyzed.

In Figure 3.4, observed flux densities are plotted (in νF_ν) as blue and green points with thin solid black lines showing the synchrotron model fits to the radio-optical data. In all cases the radio-optical spectrum is modeled as a power law with scaled exponential cutoff as described in the Appendix. The thicker black lines are the IC/CMB model fits to the X-ray flux densities. As described in section 1.10, the IC/CMB model curves are copies of the synchrotron curves shifted in frequency and luminosity by an amount proportional to δ/B and $(\delta/B)^2$ respectively, where δ/B is the only free parameter in the shift set by the requirement to reproduce the observed X-ray flux density (see also Georganopoulos et al. 2006)[1]. The 95% *Fermi* upper limits are shown as red arrows. As can be seen, the *Fermi* upper limits are well below the IC/CMB model curves in each SED and we can reject the IC/CMB model as the X-ray emission mechanism for each source. We plot in gray closed circles where the observed synchrotron data points would lie in the shifted IC/CMB spectrum. This was done to emphasize the point that the *Fermi* upper limits directly violate the IC/CMB predicted flux densities from observed portions of the synchrotron spectrum. In the following sections, we discuss each of the six sources in turn.

[1] B is the magnetic field strength of the emitting region and δ is the Doppler factor given by $\delta = \Gamma/(1 - \beta cos\theta)$. Here Γ is the bulk Lorentz factor, β is the bulk speed flow scaled by c, and θ is the jet angle to the line-of-sight.

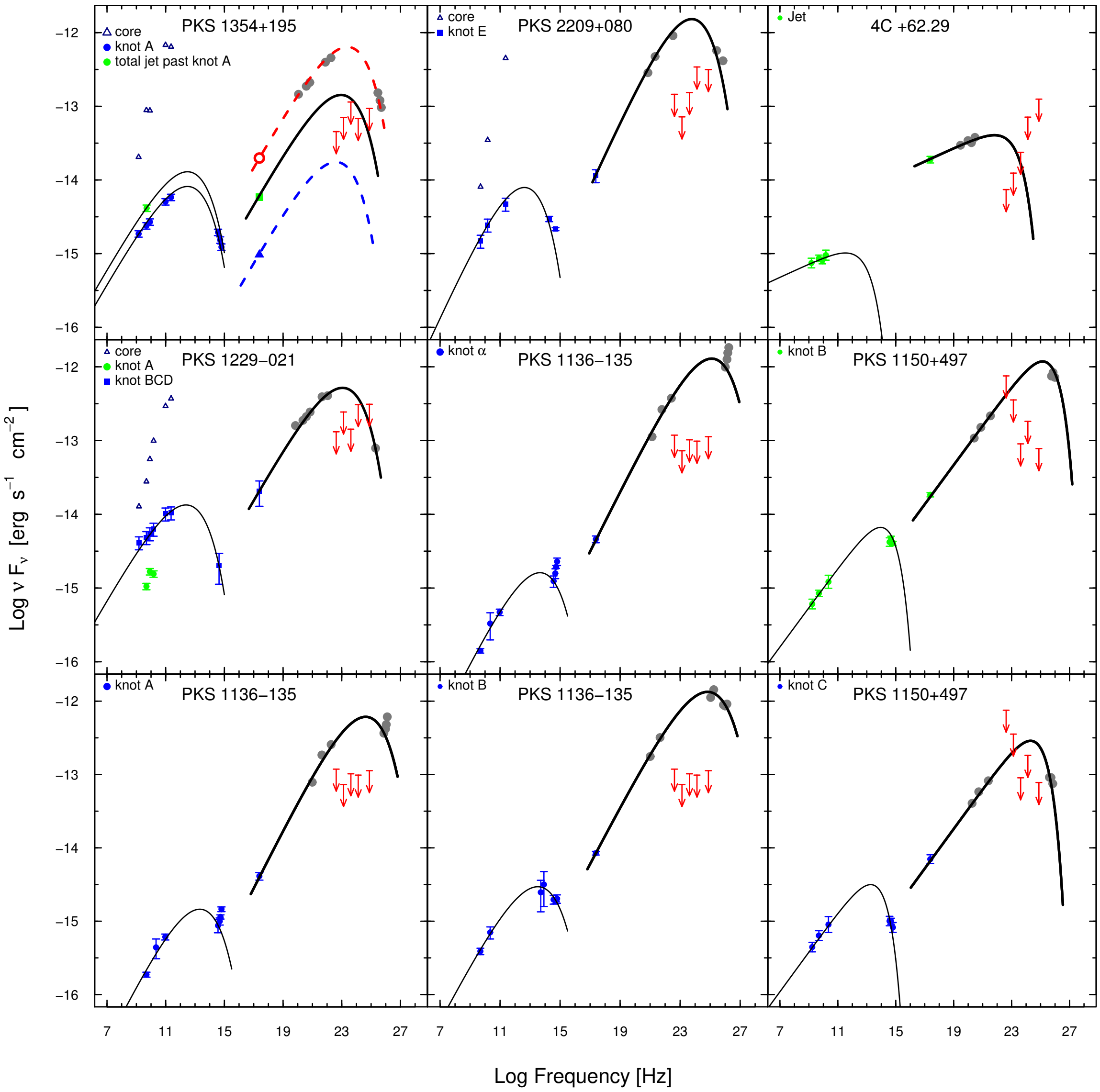

FIGURE 3.4: SEDs for the anomalous jet features of 4C+62.29, PKS 1136-135, PKS 1150+497, PKS 1229-021, PKS 1354+195, and PKS 2209+080. Thin black curves show phenomenological synchrotron model fits and the thick black curves show the corresponding IC/CMB model curves normalized to match the X-ray flux densities. The gray points represent where the radio through optical data points would lie on the IC/CMB model curves after shifting in frequency and luminosity by the appropriate amount. The 95% *Fermi* upper limits are shown in red. For PKS 1229-021, blue data points correspond to the combined data for knots B,C, and D. The green data points for PKS 1354+195 correspond to the combined data for all knots past knot A with the X-ray point being a lower limit and shown as a square (all data for PKS 1354+195 except the *Fermi* limits and the radio/ALMA data of knot A are taken from Sambruna et al. (2004)). The red open circle and red dashed line for PKS 1354+195 shows the original 8.2 nJy X-ray flux density for knot A reported by Sambruna et al. (2002) with the corresponding IC/CMB model fit. The blue triangle for PKS 1354+195 shows the 0.39 nJy upper limit for the X-ray flux density of knot A obtained in private communication with D. Schwartz, with the corresponding IC/CMB model curve shown as a blue dashed line. The thick black line in the PKS 1354+195 SED is the IC/CMB model curve for the total jet past knot A. The radio and X-ray data for 4C+62.29 are taken from Cheung, Stawarz, and Siemiginowska (2006); the X-ray and optical data for PKS 1229-021 are taken from Tavecchio et al. (2007); the X-ray data for PKS 2209+080 are taken from Jorstad and Marscher (2006); the X-ray, infrared, and optical data for PKS 1136-135 are taken from Cara et al. (2013), and the radio, optical, and X-ray data for PKS 1150+497 are taken from Sambruna et al. (2006).

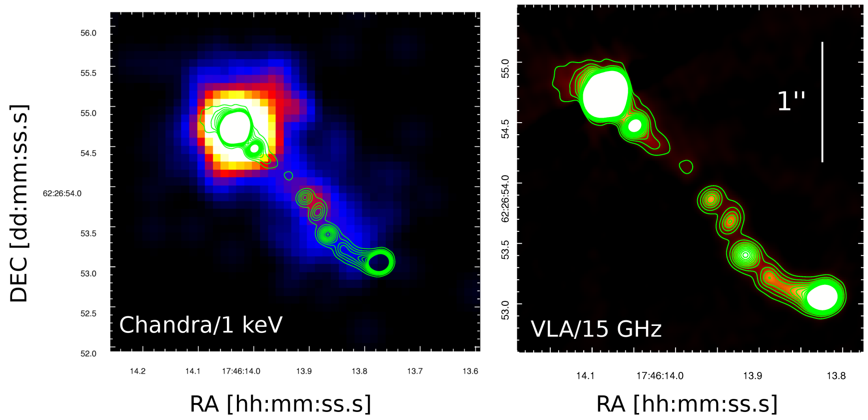

FIGURE 3.5: Right: VLA 15 GHz image of 4C+62.29 with VLA 15 GHz contours. The contours are spaced from 0.1-1 mJy, with 10 levels. Left: *Chandra* 1 keV image with the same VLA 15 GHz contours. The *Chandra* image is smoothed with a Gaussian with a radius of 3 pixels.

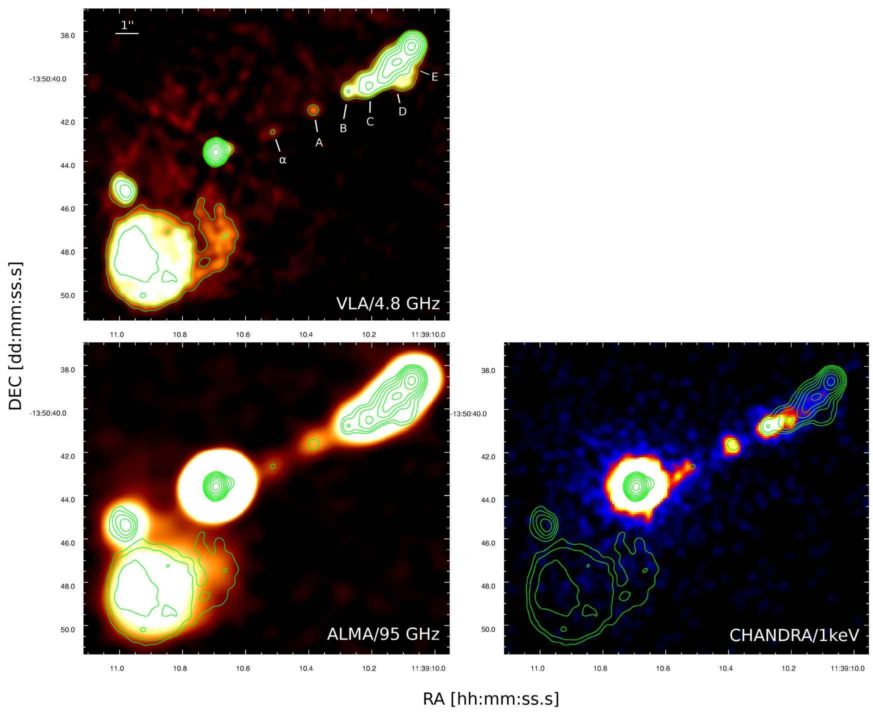

FIGURE 3.6: Multi-wavelength images of PKS 1136-135 where 4.8 GHz VLA contours were used for all images. Contours are spaced by a factor of 2, with a base level of 1.5 mJy. The top left panel is a 4.8 GHz VLA image, the bottom left panel is ALMA band 3, and the bottom right panel is a 1 keV *Chandra* image. The *Chandra* image is smoothed with a Gaussian with a radius of 3 pixels. This figure was originally published in Breiding et al. (2017).

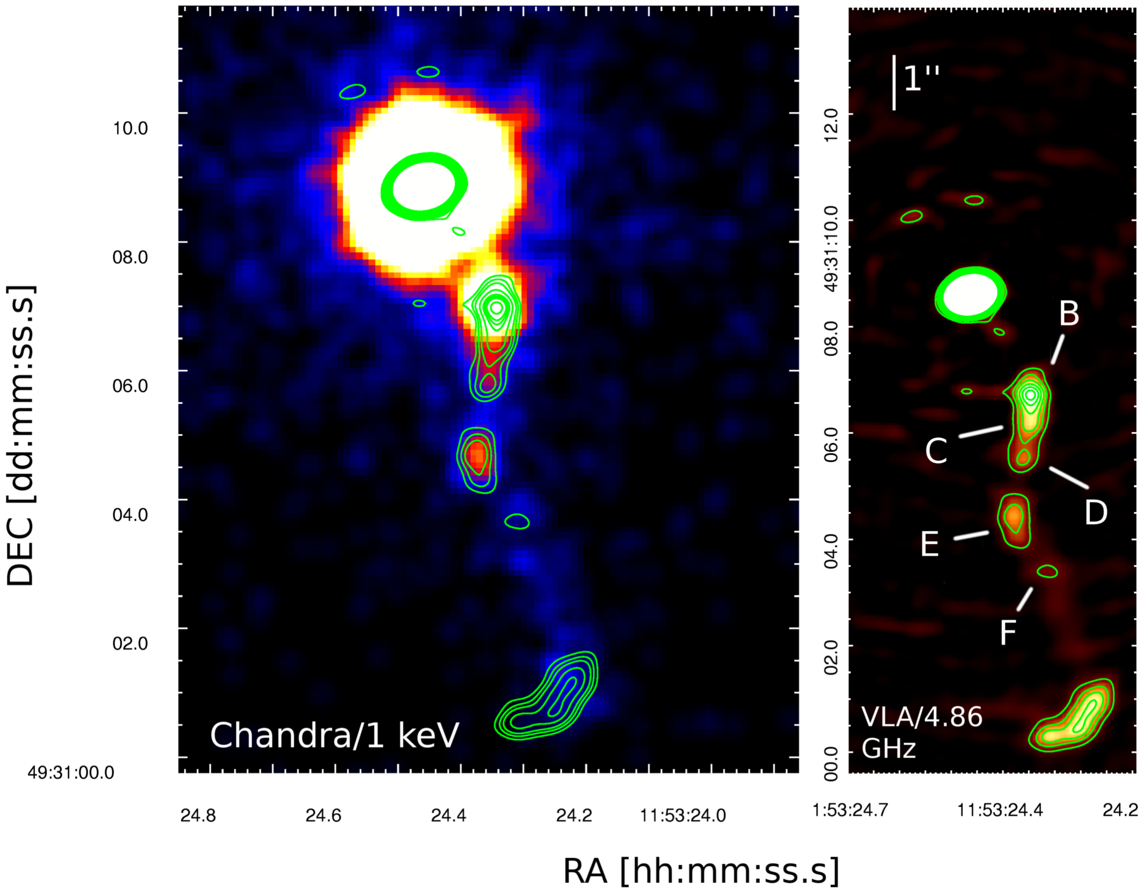

FIGURE 3.7: Right: VLA 4.86 GHz image of PKS 1150+497 with VLA 4.86 GHz contours. The contours are spaced from 2-20 mJy, with 10 levels. Left: *Chandra* 1 keV image with the same VLA 4.86 GHz contours. The *Chandra* image is smoothed with a Gaussian with a radius of 3 pixels.

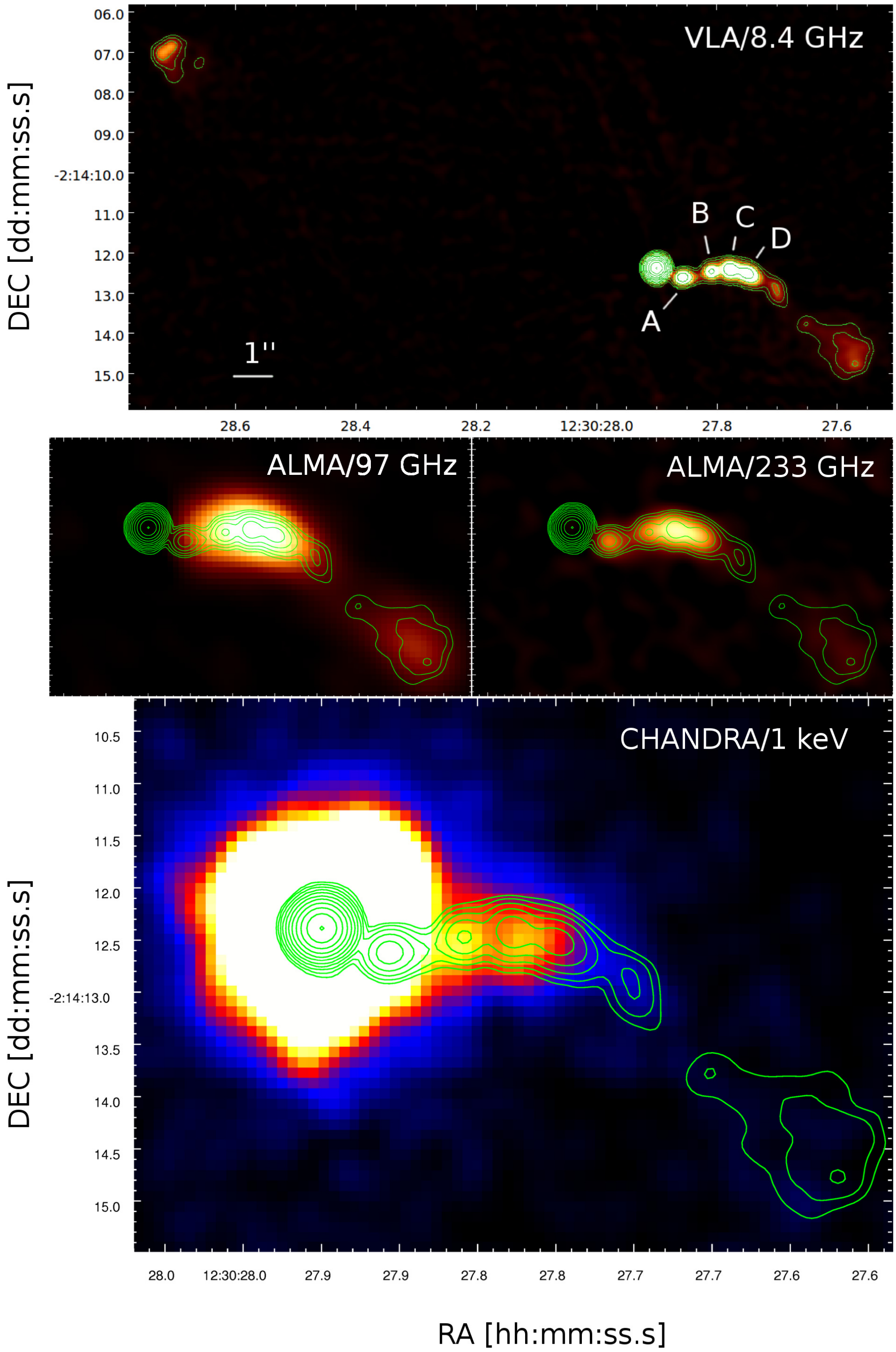

FIGURE 3.8: Multi-wavelength images for PKS 1229-021 where 8.4 GHz VLA contours were used for all images. The contours are spaced by factors of 2, with a base level of 0.63 mJy. The upper panel is an 8.4 GHz VLA image, the middle panels are ALMA band 3 and 6 images, and the lower panel is a *Chandra* 1 keV image. The *Chandra* image is smoothed with a Gaussian with a radius of 3 pixels. The ALMA images are focused on the jet and hot spot, and are core-subtracted. This figure was originally published in Breiding et al. (2017).

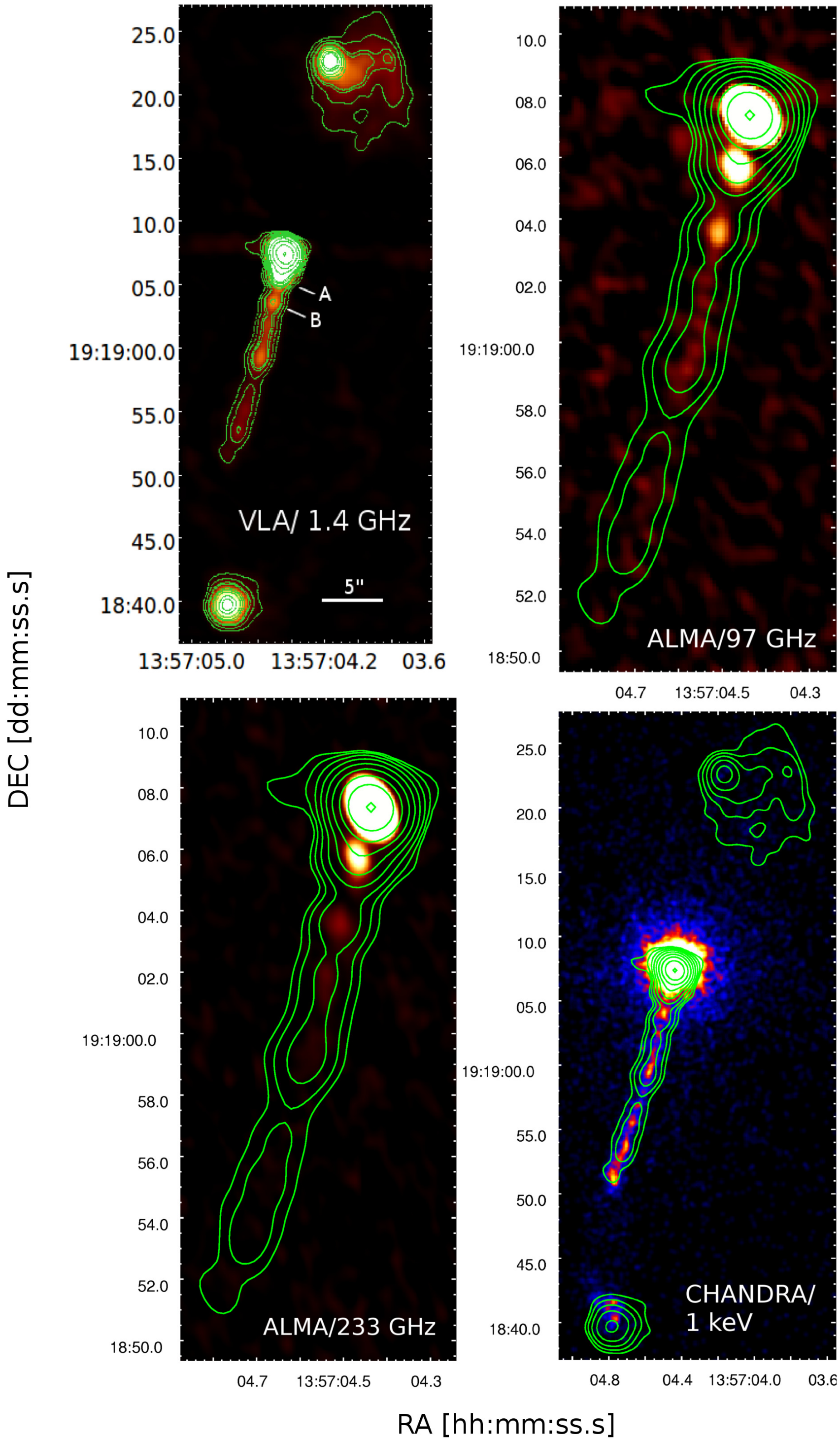

FIGURE 3.9: Multi-wavelength images of PKS 1354+195 where 1.4 GHz VLA contours were used for all images. The contours are spaced by factors of 2, with a base level of 5.2 mJy. The upper left panel is a 1.4 GHz VLA image, the upper right panel is ALMA band 3, the lower left panel is ALMA band 6, and the lower right panel is a 1 keV *Chandra* image. ALMA images are focused on the jet to show the knot structure. The *Chandra* image is smoothed with a Gaussian with a radius of 3 pixels. This figure was originally published in Breiding et al. (2017).

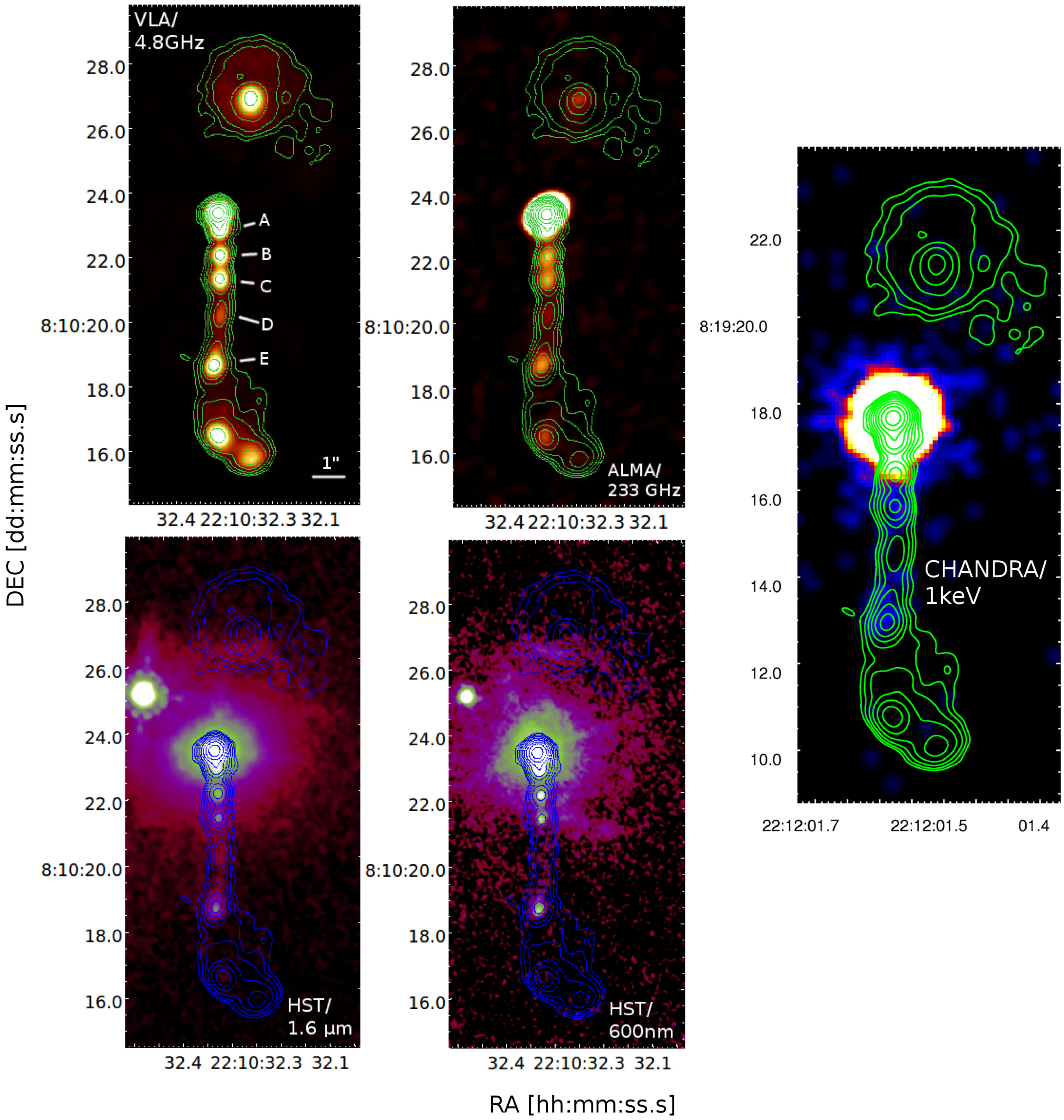

FIGURE 3.10: Multi-wavelength images of PKS 2209+080 with 4.8 GHz VLA contours for all images. The contours are spaced by factors of 2, with a base level of 56 mJy. The upper left panel is a 4.8 GHz VLA image, the upper middle panel is an ALMA band 6 image, the right panel is a 1 keV *Chandra* image, and the lower left images are HST 1.6μm and 600 nm. The 600nm image is smoothed with a Gaussian with a radius of 3 pixels. This figure was originally published in Breiding et al. (2017).

3.3.1 4C+62.29

4C +62.29 is a *very* high redshift (z=3.89) FR II source, previously observed and modeled as an IC/CMB X-ray jet by Cheung, Stawarz, and Siemiginowska (2006), where we used their radio-X-ray flux densities in our SED in Figure 3.4. Shown in Figure 3.5 are radio and X-ray images for the source. This source clearly has a very knotty radio jet ending in a bright hot spot, although these knots are not separately resolved by *Chandra*. There appears to be a slight bend in the jet ∼1.5″ from the core. The high redshift of 4C +62.29 makes an IC/CMB origin for the X-ray emission most favorable, since the energy density of the CMB increases with redshift as $(1+z)^4$. Therefore, many authors model high redshift X-ray jets as IC/CMB sources (e.g., McKeough et al. 2016, Cheung et al. 2012). However, our gamma-ray upper limits shown in Figure 3.4 are well below the IC/CMB curve, and we can confidently rule it out as the X-ray emission mechanism in this case. Observations in sub-mm wavelengths would help to further characterize the high-energy portion of the synchrotron spectrum. Characterizing this portion of the spectrum is important since it dictates what the IC/CMB spectrum looks like at the higher *Fermi* bands. However, this source lies above the $\sim 47^{\circ}$ declination limit for observing with ALMA. Therefore, this target would make a good case for observing with the Submillmeter Array (SMA) located in Maunakea, Hawaii.

3.3.2 PKS 1136-135

PKS 1136-135 is a powerful FR II source previously observed by Sambruna et al. (2006) with *Chandra* and HST, where they modeled the X-ray emission with the IC/CMB model. Our multi-wavelength images are shown in Figure 3.6, where we see a straight and knotty radio jet, with knots brighter towards the hot spot in the radio. Knots B, C, D, and E are not separately resolved by ALMA so we do not include ALMA flux densities for the jet SED. We show in Figure 3.4 the SED of knots α, A, and B, where our gamma-ray upper limits are well below the extrapolated IC/CMB emission in all three cases. Our limits were not deep enough to rule out IC/CMB for the last 3 knots which had low IC/CMB predicted gamma-ray flux densities. In knots α and A there is an upturn in the SED at 815 nm which lies above a single power-law fit for the synchrotron spectrum. Fitting these UV-upturns with an IC/CMB model is problematic since this would require very high levels of X-ray emission not observed by *Chandra*. Therefore, these UV-upturns imply a second higher energy electron distribution also responsible for the X-ray emission, similar to that seen in 3C 273. Cara et al. (2013) showed with HST polarimetry that all of the jet knots had fractional polarization measures in excess of 30% (except knots α and B where they found 2σ upper limits of 15% and 14% respectively). For the cases where the UV emission is clearly part of the second spectral component, these high degrees of polarization provide strong evidence against the IC/CMB model. However, our gamma-ray upper limits provide another independent line of evidence ruling out the IC/CMB model in knot A, while our upper limits show that the IC/CMB model is ruled out for knots α and B which did not have high degrees of polarization. Fitting the UV data with an IC/CMB model for knots α and A would also predict much higher X-ray flux densities than observed, though the UV spectrum is also much harder than would be consistent with an IC/CMB model fit.

3.3.3 PKS 1150+497

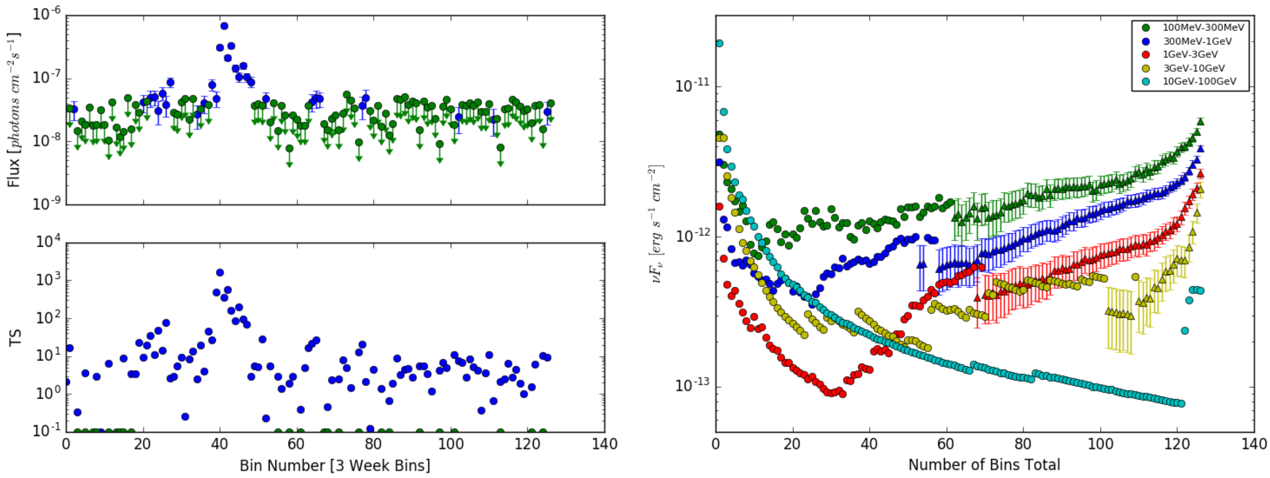

FIGURE 3.11: Left: Light curve (upper panel) for PKS 1150+497 with corresponding TS values for each bin shown in the lower panel. The time bins correspond to three weeks in good time interval (gti), and the flux from the source is the integrated photon flux from 100 meV-100 GeV. The green arrows in the light curve represent upper limits for bins in which the source TS was less than ten. Blue data points are fluxes measured when the TS was greater than ten, with 1σ error bars. In the TS plot, green points are those in which the TS was less than zero, while the blue points represent positive TS values for the source. Right: Combined bin upper limits for PKS 1150+497 shown as closed circles, where upper limits are measured when the source TS was less than 10. Flux densities are shown as triangles with 1σ error bars when the source TS was greater than ten. The upper limits and fluxes are given in the five *Fermi* energy bands: 100 meV-300 meV (green points), 300 meV-1 GeV (blue points), 1-3 GeV (red points), 3-10 GeV (yellow points), and 10-100GeV (cyan points).

PKS 1150+497 is a very powerful FR II source, previously observed and modeled as an IC/CMB X-ray jet by Sambruna et al. (2006), where we used their radio-X-ray flux densities in our SED in Figure 3.4. In Figure 3.7 we show X-ray and radio images of the jet. From the radio and X-ray imaging, the jet appears to bend twice past the bright knots B and E. In the SED, we plot the flux densities for knots B and C, which are the X-ray-brightest knots reported by Sambruna et al. (2006). From the SED, the IC/CMB model is definitively ruled out for these knots. Additionally, the HST flux densities plotted help solidify this result, since they help fix the IC/CMB spectrum in the highest-energy *Fermi* bands as shown by the closed gray circles.

PKS 1150+497 was one of the 3FGL catalog sources we analyzed, and is one in which we used the combined bin analysis to search for IC/CMB gamma-rays from the jet. In Figure 3.11, we show the *Fermi* light curve of the source for the mission elapse time (MET) range of 239557417-513167006 (corresponding to nearly 9 years from the launch of *Fermi*), the corresponding TS of PKS 1150+497 during the light curve time bins, and the corresponding results of the combined bin analysis. As can be seen in the combined bin analysis plot, the upper limits (closed circles) decrease as more time on source is added to the analysis. Additionally, in the two highest-energy *Fermi* bands, discontinuous jumps are seen which reflect individual photon detections. This is consistent with the expectations from the isotropic gamma-ray background which is much higher at lower gamma-ray energies.

We did not find any evidence for IC/CMB gamma-rays from the combined bin analysis, but we were still able to use the deepest upper limits to help rule out the IC/CMB model (shown in the SED in Figure 3.7). From Figure 3.11, PKS 1150+497 appears to have undergone a significant flare roughly 3 years into the launch of *Fermi*. It is possible that future observations with *Fermi* will allow for detection of IC/CMB gamma-rays from the jet, allowing that the core is sufficiently quiescent. This would be reflected in the combined bin analysis as a steady flux component of increasing significance as more time bins are added to the analysis. This component should have a *hard* gamma-ray spectrum, in contrast to the core which is expected to have a *soft* gamma-ray spectrum. Finally, this plateu should precede an increasing flux due to periods of activity from the core. As of yet, we have not seen this behavior in our *Fermi* analyses. However, there is no apriori reason this will not been seen in the analysis of other bright *Fermi* sources.

3.3.4 PKS 1229-021

PKS 1229-021 was previously observed and modeled as an IC/CMB X-ray jet by Tavecchio et al. (2007), where we use their reported HST and *Chandra* densities in our SED (Figure 3.4). The radio images shown in Figure 3.8 show four well-defined 'cannonball'-like knots downstream of the core. Interestingly, similar periodic knot structures are seen in many of the jets discussed in this work. As shown in Figure 3.8, knots B, C, and D are not separately resolved by ALMA and *Chandra*; thus we combined the data for these knots, which are labeled as knot BCD. Past this combined feature, we see the jet is considerably bent, implying a change of jet direction. Our ALMA images (which are core-subtracted) are focused on the jet in order to emphasize the knot structure; we found the western hot spot was only detected by ALMA in band 3 and not in band 6. The HST data presented in Tavecchio et al. (2007) shows that only the combined knot BCD was detected in the HST imaging while knot A is not detected.

3.3.5 PKS 1354+195

Images for PKS 1354+195 are shown in Figure 3.9, where the radio observations show a straight jet with detailed hot spot structure for the northern hot spot. The VLA and ALMA observations again show a well-defined cannonball-like knot structure for knots A and B. This jet was previously observed and modeled as an IC/CMB X-ray jet by Sambruna et al. (2002) and Sambruna et al. (2004), where we use their reported HST and *Chandra* flux densities from the 2004 publication. Initially we focused on knot A, which was reported as brightest in the X-rays. This knot is approximately 2″ from the core and initially reported in Sambruna et al. (2002) to have a flux density of 8.2 nJy (corresponding to about 135 counts) and later revised to 16.1 nJy in Sambruna et al. (2004). However, we later learned (D. Schwartz, private communication) that more recent, deeper *Chandra* observations of PKS 1354+195 suggest that knot A is in fact not detectable separate from the bright quasar core, with an upper limit of $<$0.39 nJy, after taking into account careful modeling of the PSF from the core. We plot the 8.2 nJy *Chandra* flux density in Figure 3.4 as a red open circle. While this flux density implies that the IC/CMB model is ruled out at a very high level of significance (see red dashed line), the much lower revised flux density limit (blue triangle and dashed line) does not. In light of this revision, we also examined the newer *Chandra* observations and can confirm that we do not find a significant excess of counts at the position of knot A in any of the later observations, suggesting that the apparent excess in the early observation (Chandra

Observation ID #2104) was a statistical fluctuation. The jet of PKS 1354+195 is quite straight up to just before the hotspot, suggesting no major bends in or out of our line-of-sight. If knot A has the same radio to X-ray ratio as knot B, we would expect an X-ray flux density of about 2.4 nJy, however the very bright core makes it difficult to conclude much from knot A. Turning to the remaining knots in the jet, and assuming *some* level of X-ray flux density from knot A, we produce the *lower limit* X-ray flux density shown as a green square in the SED figure with a value of 2.4 nJy. Note this is the approximately the same X-ray flux density calculated for knot A assuming the same radio to X-ray ratio as knot B. Using this and the spectral shape determined by knots A and B together from radio-optical, we see that the IC/CMB model is still ruled out.

VLBI proper motions

The results of the WISE analysis for PKS 1354+195 reveal three moving features in the jet. We show the pc-scale jet in the 2002 epoch and the results of the WISE feature tracking in Figure 3.12. Ordered by distance from the core, the moving features show angular motions of 0.17±0.01, 0.21±0.01, and 0.26±0.20 mas/year. At the scale of 7.32 parsecs per mas, this corresponds to a apparent proper motions of 2.33±0.14c, 2.88±0.14c and 3.5±2.7c. The last of these components is only detected in the last three images and has a rather large error bar, but the other two components are secure detections in all four epochs. We re-analyzed the data using a variety of possible scales for the components, and found results very consistent with the above.

3.3.6 PKS 2209+080

PKS 2209+080 was previously observed and modeled as an IC/CMB X-ray jet by Jorstad and Marscher (2006), where we used their X-ray flux density in our SED. As shown in Figure 3.10, PKS 2209+080 has a very knotty and straight jet with the southern hot spot showing two resolved components. Our ALMA and HST observations resolve all of the identified radio knots. As can be seen in both HST images, the host galaxy has an irregular tail structure suggestive of a possible recent merger. Only the southern hot spot is detected in the infrared as shown in the lower-middle panel of Figure 3.10. The only knot reported to show X-ray emission by Jorstad and Marscher (2006) was knot E. In Figure 3.13 we show the SEDs of knots A through D which are upstream of knot E with data shown as squares and synchrotron model fits as solid lines. In knots A through C there is an upturn in the SED at 600 nm which lies above a single power-law fit for the synchrotron

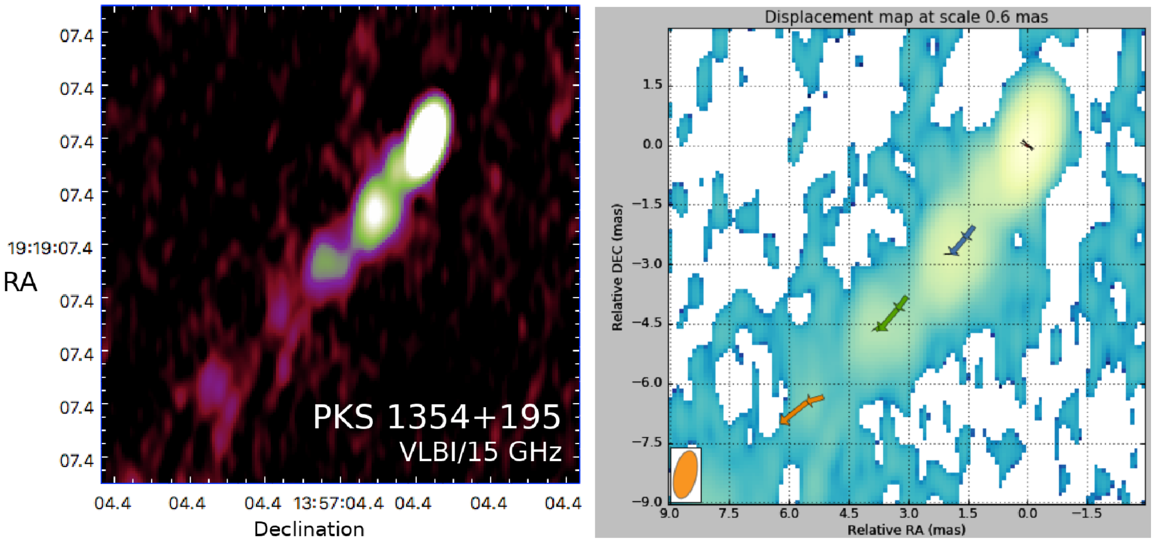

FIGURE 3.12: Left: the parsec-scale jet of PKS 1354+195 in 2002 taken with VLBA at 15 GHz (Lister et al. 2009). Right: the results of the WISE proper motion analysis of the four available VLBA epochs, with arrows showing the motions from epoch-to-epoch for three components in the jet (the core is stationary and consistent with no motion as expected). This figure was originally published in Breiding et al. (2017).

spectrum. Similar to the cases of PKS 1136-135 and 3C 273, fitting these UV-upturns with an IC/CMB model would require X-ray flux densities much higher than observed by *Chandra*.

3.4 Discussion

3.4.1 IC/CMB now ruled out for 23 sources

The IC/CMB model for the bright and/or hard large scale jet X-ray emission associated with powerful quasars has now been ruled out for 23 sources on the basis of over-predicting the observed gamma-ray flux. For 21 sources presented here for the first time, we found upper limits to the gamma-ray flux well below the levels predicted by the IC/CMB model using observations from the *Fermi*/LAT. For the sources not presented in this work, 3C 273 and PKS 0637-752, previous *Fermi*/LAT observations showed similar IC/CMB violating upper limits (Meyer and Georganopoulos 2014; Meyer et al. 2015; Meyer et al. 2017). However, over-predicting the observed gamma-ray flux is not the only line of evidence against the IC/CMB model for these sources.

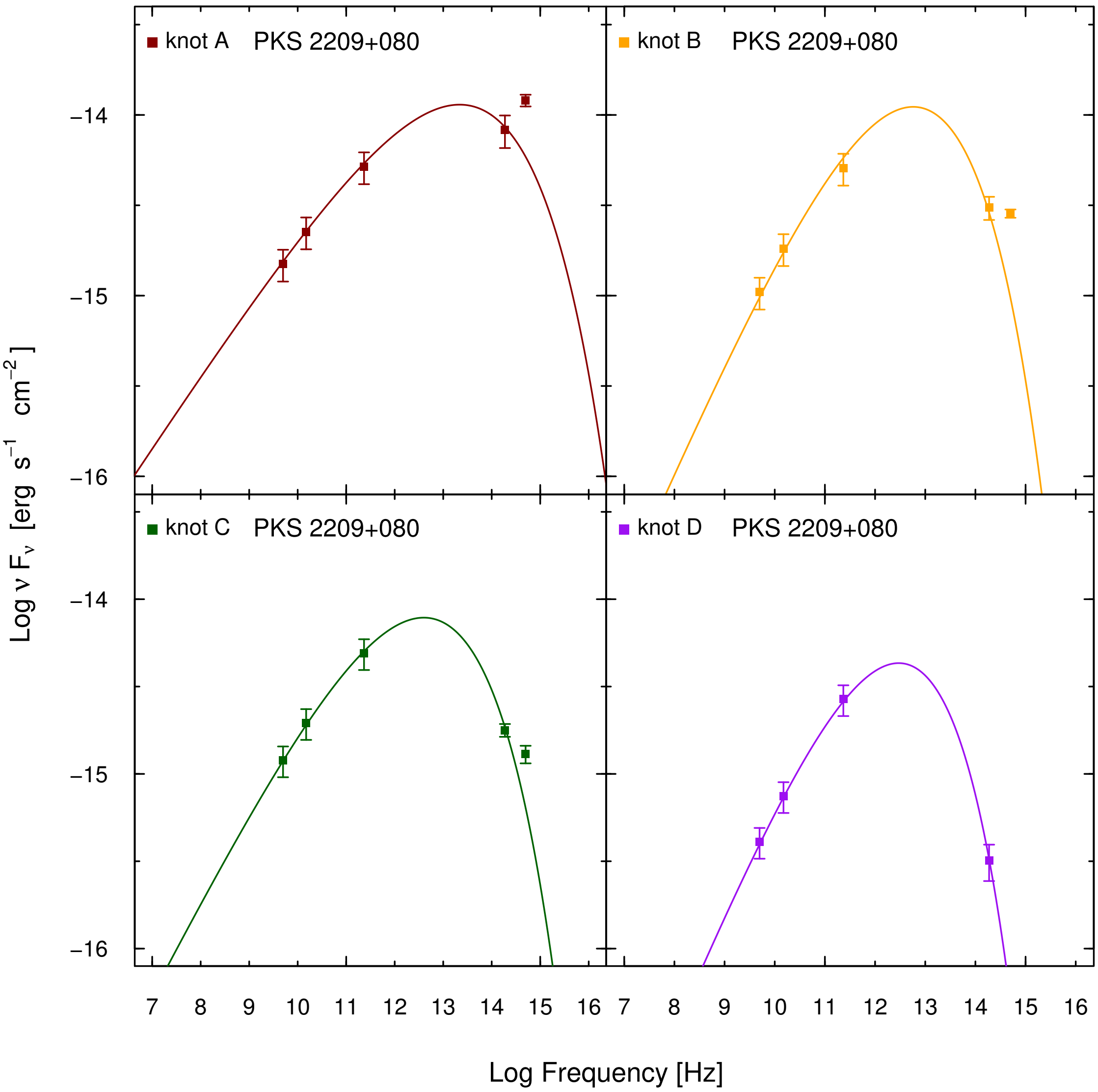

FIGURE 3.13: SEDs of knots A through D for PKS 2209+080. Single power-law fits with scaled exponential cutoffs are used to fit the radio data and first optical data point for each knot. This figure was originally published in Breiding et al. (2017).

3.4.2 UV upturns

In the case of PKS 1136-135, a high degree of UV polarization with fractional polarization measures in excess of 30% for several knots was detected in the rising second component of the jet SEDs (Cara et al. 2013). This implies a synchrotron origin for the second spectral component of these knots (see Jester et al. 2006; Atoyan and Dermer 2004; Harris, Mossman, and Walker 2004; Hardcastle 2006; Uchiyama et al. 2006; Kataoka and Stawarz 2005c) as the IC/CMB emission is expected to have very low polarization (see McNamara, Kuncic, and Wu 2009; Uchiyama 2008a) while synchrotron radiation can be highly polarized. These UV-upturns in the knot SEDs are clearly seen in the case of knots A-C for PKS 2209+080 shown in Figure 3.13 and knots α and A for PKS 1136-135 shown in Figure 3.4. The optical spectrum for these knots is consistently harder than can be fit with a single power law from radio to optical since the exponential cutoff occurs well before the optical. In these cases, fitting the UV-component of the SED with an IC/CMB model would predict much higher X-ray flux densities than are observed. Furthermore, knots α and A in PKS 1136-135 have a UV spectrum which is much harder than an IC/CMB model fit. These inconsistencies are additional lines of evidence against the IC/CMB model and imply another electron distribution higher in energy to produce the UV-upturns and the X-ray emission. Future UV observations with HST could help confirm these upturns in other MSC jets.

3.4.3 Misalignment

Also in tension with the IC/CMB model is the apparent misalignment of the sources. The IC/CMB model is able to reproduce the observed bright X-ray flux densities by requiring very small jet angles to the line of sight so the X-ray emission is highly relativistically beamed (Tavecchio et al. 2000; Celotti, Ghisellini, and Chiaberge 2001). It has been previously shown by Meyer et al. (2011) that blazars have a higher radio core dominance, R_{CE}, and lower crossing frequency, ν_{cross}, than radio galaxies. Figure 3.14, adapted from Meyer et al. (2011), shows the locations of 23 sources from this analysis (those in which we could measure the core dominance and crossing frequency) in the R_{CE}-ν_{cross} plane in addition to other previously classified blazars and radio galaxies. As can be seen in Figure 3.14, our sources do not have the low crossing frequencies and high radio core dominances expected for highly aligned blazars. Additionally, for the sources which we have not ruled out IC/CMB with *Fermi* limits, no trend can be seen which would suggest they are more highly aligned than for those in which it is ruled out.

3.4.4 X-ray versus Radio beaming patterns

As detailed in section 1.5.3, one property of the IC/CMB model is that it predicts a different relativistic beaming pattern than synchrotron emission, where the relativistic beaming pattern describes how the intensity of the radiation is modulated by the angle from the jet axis. The expected beaming pattern for IC/CMB radiation is $L = L'\delta^{p+1+2\alpha_r}$, with p=2 for a continuous flow and p=3 for discrete moving blobs (Dermer 1995; Georganopoulos, Kirk, and Mastichiadis 2001). L is the

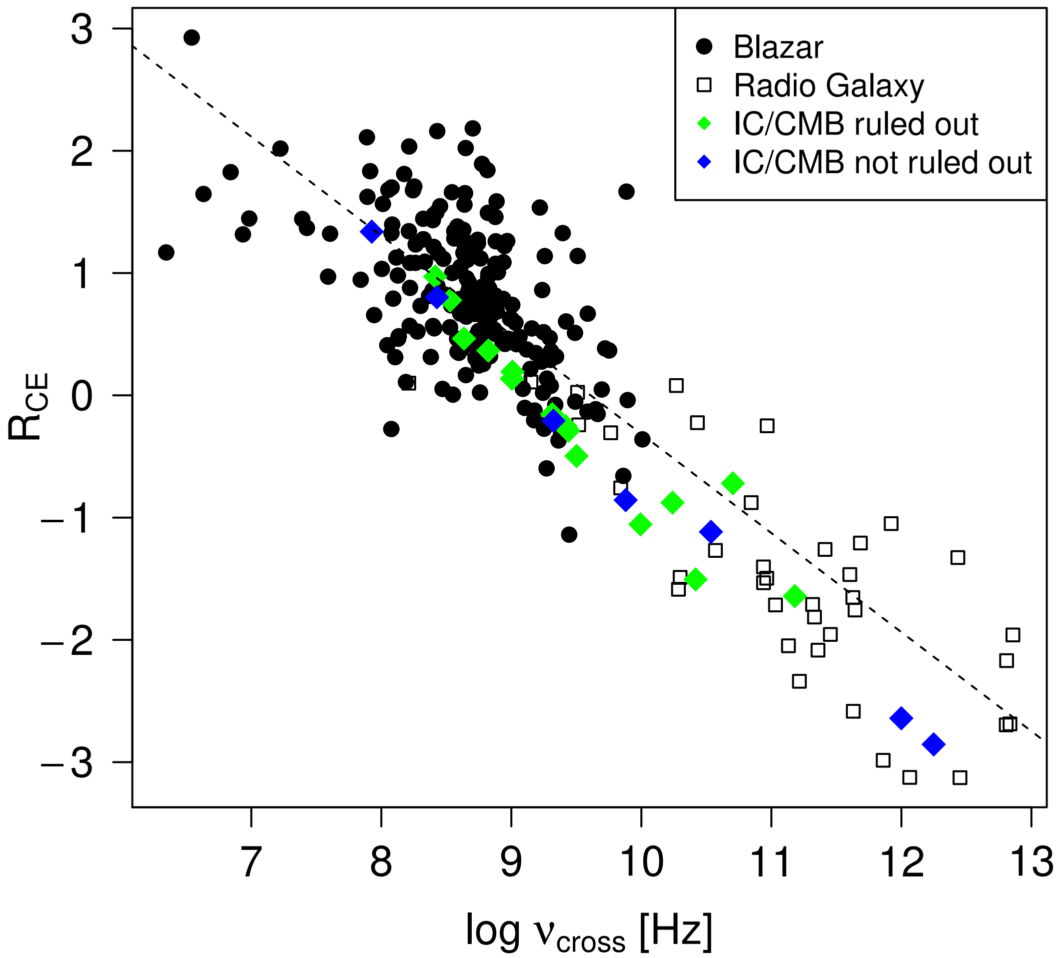

FIGURE 3.14: Plot adapted from Meyer et al. (2011). The radio core dominance, R_{CE}, plotted against ν_{cross}, the frequency at which the jet becomes dominant. Radio galaxies are shown as empty squares and blazars as filled circles. The broken line shown is the linear correlation between the plotted variables (r=0.87). Plotted in diamonds are the 23 sources in which we could obtain values of R_{CE} and ν_{cross}.

luminosity in the galaxy frame assuming isotropy, L' is the solid-angle integrated luminosity in the jet frame, α_r is the radio spectral index, and δ is the Doppler factor. In the case of synchrotron emission, the expected beaming pattern is given by $L = L'\delta^{p+\alpha_r}$ (Dermer 1995). Increasing the angle of the jet to the line-of-sight decreases the value of δ. Therefore, the observed IC/CMB flux should fall off faster than the synchrotron flux as jet misalignment increases due to the stronger dependence on δ of IC/CMB radiation.

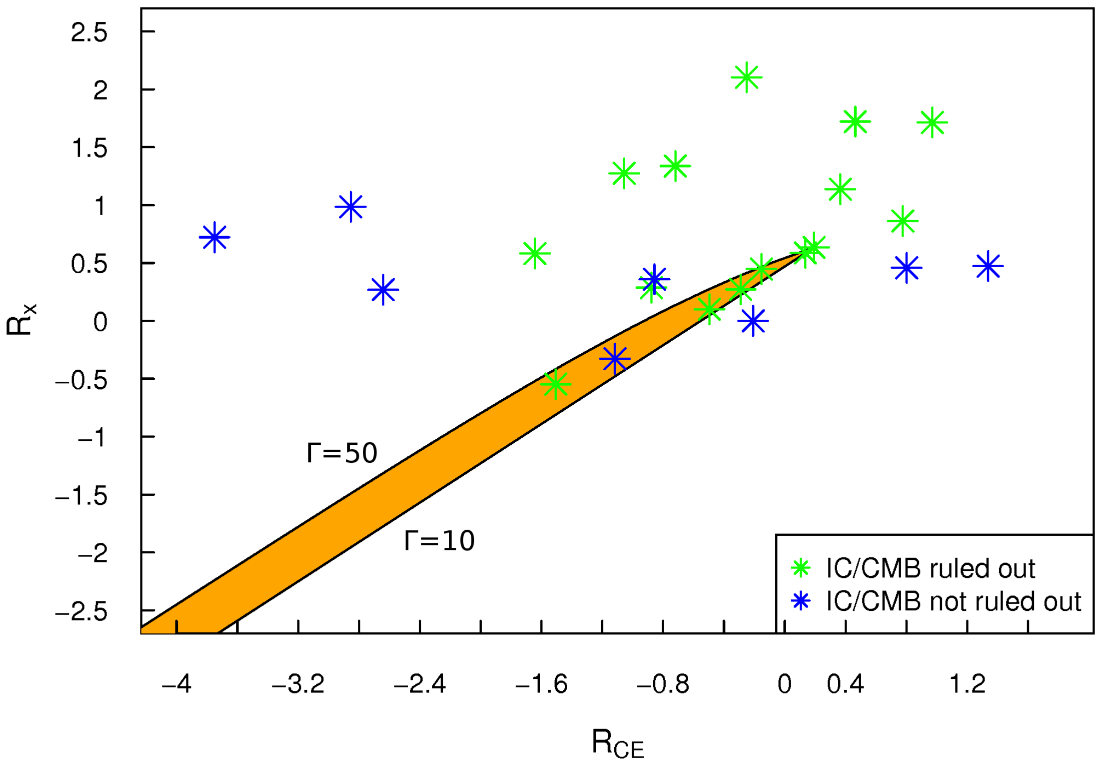

FIGURE 3.15: The X-ray dominance, R_x, plotted against the core dominance, R_{CE}, for the 23 sources in which we could obtain values for R_{CE}. Error bars are not shown as they are on the order of the size of the data points. We plot R_x for the brightest X-ray knot in each source. Smaller values of R_{CE} correspond to more misaligned sources. The black lines show the expected result of misaligning the jet of PKS 0637-752 assuming an initial value of $\delta = 10$ for the knot with an initial misalignment of 5.73°. The upper and lower black lines show the cases where the Lorentz factor of the core is 50 and 10 respectively, with the orange shaded region showing the possible range between those values.

As described in section 3.2.1, the X-ray dominance is defined as the logarithmic ratio of the 1 keV X-ray flux density to the 8.6 GHz radio flux density (in νF_ν). In Figure 3.15 we show the X-ray dominance plotted against the core dominance, R_{CE}, for the (typically) X-ray-brightest features of the 23 sources in which we have measured values of R_{CE}, where R_{CE} is a measure of the relative misalignment of the jet angle to the line-of-sight as can be seen in Figure 3.14. Using the above relativistic beaming equations for IC/CMB and synchrotron emission, it can be shown that $R_x \propto \delta_{knot}^{1+\alpha_{knot}}$ and $R_{CE} \propto \delta_{core}^{p+\alpha_{core}}$. Using these equations, we plot the projected misalignment of PKS 0637-752 in Figure 3.15 as solid black curves assuming $\alpha_{core} = 0$, $\alpha_{knot} = 0.7$, and p=2 for the core which reflects the most likely case in which the core is a standing shock and not a discrete moving feature. The misalignment curves are plotted for a core Γ of 10 and 50 with the shaded orange region representing the range of misalignment curves for a core Γ between 10 and 50. As can be seen in Figure 3.15, the other sources do not fall within this misalignment zone of PKS 0637-752 as would be expected for the stronger beaming of the IC/CMB emission. The lack of correlation between R_x and R_{CE} suggests the radio-optical synchrotron emission and X-ray emission for these knots have the same relativistic beaming profile and not a different one as would be expected if the X-rays were produced by the IC/CMB mechanism. Additionally, the sources in which IC/CMB has not been ruled out show a relatively constant trend along the plot, suggesting that IC/CMB is not the X-ray emission mechanism in these cases as well. The large range in X-ray dominance also suggests that there is some intrinsic variability of the X-ray component within the sample.

3.4.5 Evidence for Jet Deceleration

The IC/CMB model requires large bulk-flow Lorentz factors on kpc scales (i.e. highly relativistic, $\Gamma \sim 10$) in addition to being oriented at small angles to the line-of-sight. As detailed in section 1.6, VLBI observations of apparent superluminal motion for features at the base of the jet provide direct evidence that many jets are highly relativistic on the pc scale. Measurement of the maximum apparent speed for these features, β_{app} (where β is the speed of the feature in units of c), gives the most stringent lower limit on Γ and upper limit on the angle of the jet to the line-of-sight (see section 1.6) on the pc scale. The *Fermi* upper limits presented in this work allow us to place upper limits on δ/B for the kpc-scale jet such that the IC/CMB model curves fall below these limits. If we further assume that the magnetic field is at its equipartition value, then these observations give limits on the Doppler factor, δ.

TABLE 3.8: Jet Deceleration Parameters

Source Name	β_{app} (c)	θ_{max} (°)	Γ_{min}	Γ_{max}
0838+133	13.3[d]	8.59	13.4	3.66
2216-038	6.91[f]	16.5	6.98	...
3C 120	9.08[b]	12.6	9.14	...
3C 273	15.5[f]	7.38	15.5	...
4C 20.24	10.5[e]	10.9	10.5	1.04
4C 62.29	15.2[a]	7.55	15.2	$2.26^{+1.31}_{-0.56}$
4C 69.21	24.9[a]	4.60	24.9	$2.75^{+1.27}_{-0.730}$
4C 73.18	22.4[g]	5.12	22.4	$2.55^{+1.23}_{-0.67}$
B2 0738+313	11.1[d]	10.3	11.1	...
PKS 0637-752	15.3[h]	7.48	15.3	3.14
PKS 0920-397	30.8[g]	3.72	30.8	$4.87^{+2.52}_{-1.67}$
PKS 1045-188	10.9[c]	10.5	10.9	...
PKS 1127-145	24.0[b]	4.78	24.0	$3.59^{+1.86}_{-1.10}$
PKS 1150+497	18.2[f]	6.30	18.2	3.87
PKS 1354+195	3.50	18.6	6.18	...

β_{app} is taken from the following sources: [a]Piner et al. (2012), [b]Jorstad et al. (2017), [c]Lister et al. (2013), [d]Lister et al. (2009), [e]Kellermann et al. (2004), [f]Lister et al. (2016), [g]Piner et al. (2007), and [h]Edwards et al. (2006).

In Table 3.8, we show the maximum β_{app} values obtained with VLBI for the sources in which we could find measurements in the literature, as noted in the table. Additionally, we show the result for PKS 1354+195 obtained from this work. In this table we also give the maximum angle of the jet to the line-of-sight, θ_{max}, and minimum bulk-flow Lorentz factor, Γ_{min} (where θ_{max} and Γ_{min} apply to the pc-scale portion of the base of the jet, as described in section 1.6). Finally, in the last column we give the upper limit to the bulk-flow Lorentz factor, Γ_{max}, for the kpc-scale jet feature analyzed in our jet SEDs, and noted in tables A.1-A.5. Γ_{max} is determined by our upper limits on the Doppler factor, assuming an equipartition magnetic field. We additionally give error bars on Γ_{max}, representing the results for factors of two out of equipartition. Furthermore, we assume the jet angle to the line-of-sight for the kpc-scale jet is less than θ_{max}. This assumption is reasonable allowing that the jet does not significantly bend in the plane of observation. For some sources, the constraints from the Doppler factor and β_{app} were not strong enough to constrain Γ_{max}. Additionally, in some cases being out of equipartition by a factor of two did not allow for constraints on Γ_{max}, and these are given without errors.

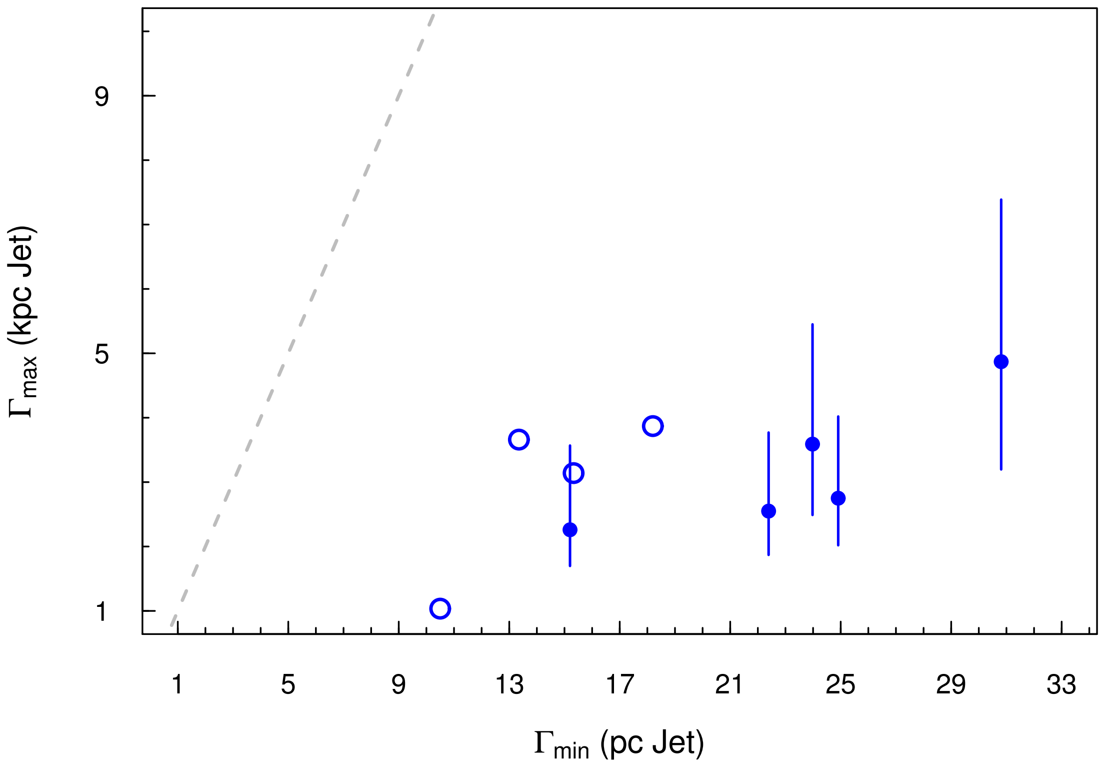

FIGURE 3.16: Plot of the maximum bulk flow Lorentz factor for the kpc-scale jet against the minimum bulk flow Lorentz factor for the pc-scale jet for the sources shown in Table 3.8. The filled in points have error bars showing the result assuming the magnetic field can be out of equipartition by a factor of two. The open circles show the results for the cases where being out of equipartition does not provide constraints on Γ_{max}. The gray dashed line shows the case where $\Gamma_{min} = \Gamma_{max}$.

In Figure 3.16, we plot the maximum Lorentz factor for the kpc-scale jet against the minimum Lorentz factor for the pc-scale jet for the sources in Table 3.8. The straight dashed line shows the case where the Lorentz factors of the pc-scale and kpc-scale jets are equal. The sources plotted all fall well below this line, indicating that the jets are at most mildly relativistic on the kpc scale, or else grossly out of equipartition. It seems very likely that strong deceleration occurs by the kpc scale, given these results. However, these are only a subset of the jets analyzed in this work, and therefore these results may not be generalizable to all MSC jets.

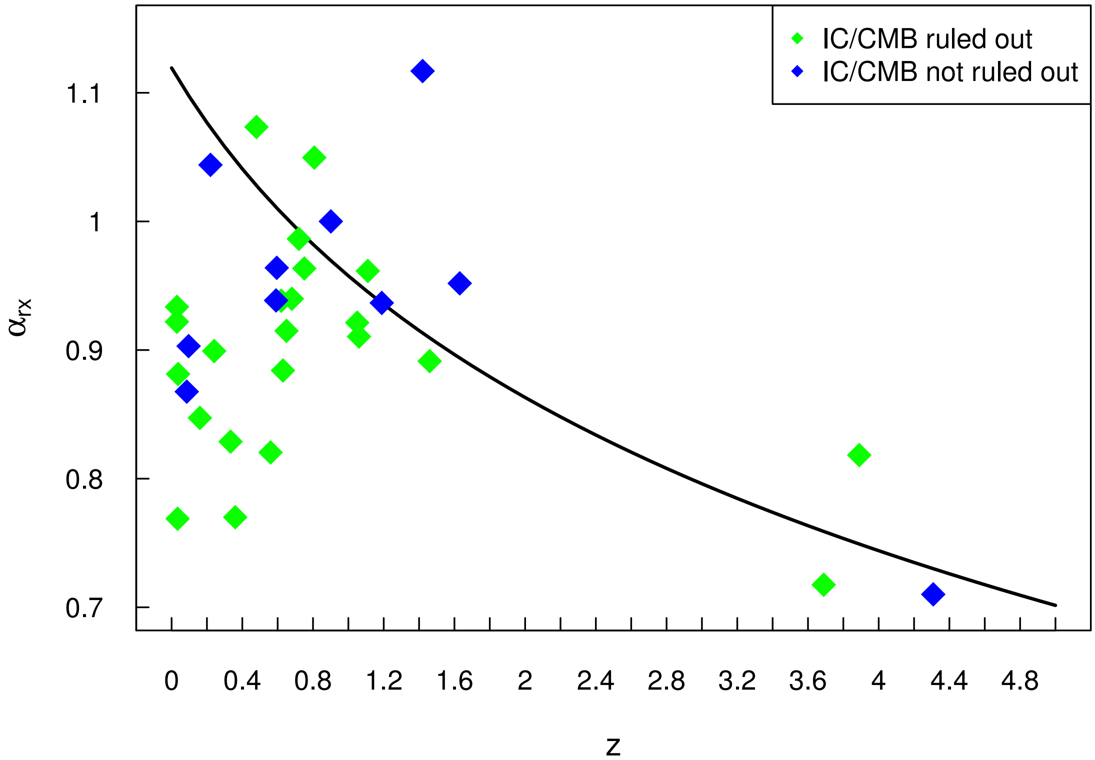

FIGURE 3.17: Plot of the radio to X-ray spectral index, α_{rx}, against redshift for sources in which IC/CMB is not ruled out and for those in which it is from this work. The black curve shows the expected trend under the IC/CMB model.

3.4.6 Trends with Redshift

As previous studies have suggested (e.g., Marshall et al. 2018), if the X-ray emission of these jets is from the IC/CMB mechanism, then we should expect the typical X-ray emission of kpc-scale jets to increase towards a higher redshift, owing to the fact that the CMB energy density increases with redshift as $(1+z)^4$. At the same time, the radio synchrotron emission should not have any inherent redshift dependence. Therefore, the ratio of the X-ray to radio luminosity should vary as $(1+z)^4$ for a large sample of sources in the IC/CMB model, assuming there is not any trend with redshift of the magnetic field or beaming parameters (see Schwartz 2002, Marshall et al. 2018).

In Figure 3.17, we plot the radio to X-ray spectral index, α_{rx}, of our sample of jets (where α_{rx} is calculated between 8.6 GHz and 1 keV). Shown as the black curve is the trend with redshift assuming the IC/CMB model is correct. There is no clear trend along this line for our sample of sources, although there are very few high redshift sources in this figure. Additional intermediate and high-redshift sources would be helpful to determine if this trend is followed to any degree by the sources for which IC/CMB is still viable. Additionally, there may be a lot of scatter introduced into α_{rx} by intrinsic differences from source to source.

We applied a k-correction in computing the α_{rx} values for each source, since we are technically sampling different portions of the intrinsic SED for different redshifts. This could plausibly have a measurable effect on α_{rx} if the radio and X-ray spectrum have different spectral indices, and the source is at a high redshift. However, we found the correction to have a negligible effect on the value of α_{rx}. For example, the source 4C+62.29 is at a redshift of 3.9, with a radio spectral index of 0.93 and a X-ray spectral index of 0.62. For this source, the k-correction increased the value of α_{rx} from 0.82 to 0.84. The majority of our sources are at a low redshift, and the correction has a negligible effect on the value of α_{rx}.

3.4.7 Morphology and Host Properties of the non-IC/CMB sources

Many of these sources show what we term a cannon-ball jet knot structure in the radio with quasi-periodic knot spacing. It has been suggested that this quasi-periodic spacing of the jet knots may be due to re-confinement shocks of the external medium, accretion disk instabilities, or a binary super massive black hole (Godfrey et al. 2012). Another interesting characteristic of the radio morphology is the bright elongated structure at the end of the jet and lack of extended lobe emission for the sources 3C 273 (Bahcall et al. 1995) and PKS 1136-135 (though there is clearly lobe emission connected to the counter jet in PKS 1136-135) which may be identifiable with the "nose cone" jet structure seen in Magneto-hydrodynamics simulations. These nose cone structures are thought to occur when the jets are magnetically confined, and rather than the plasma deflecting back from the interface between the jet and intergalactic medium to form the lobes, it is collected in the end of the jet between the Mach disk and leading bow shock forming the "nose cone". One observational signature associated with the nose cone jets is enhanced radio emission in the nose cone due to an enhanced magnetic field strength and thus synchrotron emissivity, but a decrease in the flux from higher energies due to a lack of particle acceleration in this region from shocks (see Clarke, Norman, and Burns 1986 for a discussion of nose cone jets). This observational characteristic appears to be true in the two cases of 3C 273 and PKS 1136-135 in which we can identify a possible nose cone structure.

The host galaxy of PKS 2209+080 which is visible in our HST observations shows a clear tidal tail structure which is suggestive of the galaxy having undergone a recent merger. The disturbed elliptical host galaxy of 3C 273 has also shown some evidence of being in a recent merger (Martel et al. 2003). These findings are consistent with the work by Chiaberge et al. (2015) suggesting that all radio-loud AGN have undergone major recent mergers.

3.4.8 Alternatives to IC/CMB

One emission mechanism which has not been ruled out for the X-rays in MSC jets is synchrotron radiation from a second higher energy population of electrons. If these X-ray knots are due to a second electron energy distribution, this means that these jets can exhibit highly efficient in situ particle acceleration very far from the central engine (on the order of kpcs). These electrons would need to be highly energetic (at a few to hundreds of TeV energies) and in cases where the IR/optical flux is totally consistent with a single spectrum from radio to optical, have a lower energy cutoff such that they do not overproduce the observed IR/optical emission. One consequence of these multi-TeV energy electrons is that they should inverse-Compton scatter the CMB to TeV gamma-rays which may be detectable with the upcoming CTA for low redshift sources (Meyer et al. 2015; Georganopoulos et al. 2006).

Alternatively, it is possible these X-rays are due to hadronic emission processes whereby the X-rays are produced by direct proton synchrotron radiation or from the synchrotron radiation produced by secondary electrons resulting from photo-hadronic interactions like the Bethe-Heitler process or photopion production (see Petropoulou, Vasilopoulos, and Giannios 2017; Bhattacharyya and Gupta 2016; Kusunose and Takahara 2017). Like synchrotron models, and unlike IC/CMB, hadronic models are highly tunable and can be made to reproduce most observed SEDs since there are a large number of parameters to adjust. However, one distinguishing characteristic of hadronic models would be the expected neutrino emission from charged pion or neutron decay resulting from interactions between high energy protons and photons (Mannheim and Biermann 1989). It has been claimed that the bright gamma-ray flare observed in the blazar PKS B1424-418 is hadronic in nature due to the detection of a PeV-energy neutrino with a high degree of positional and temporal coincidence (Kadler et al. 2016) by the IceCube neutrino detector. Even more recently, IceCube observations revealed a 290 TeV neutrino coincident with a gamma-ray flare from the blazar TXS 0506+056 at the 3σ level, coming from the same location as the blazar (IceCube Collaboration et al. 2018), and analysis of archival IceCube data showed previous correlations between the blazar gamma-ray flux and observed neutrino flux which strengthened the association to the 3.4σ level.

These models for the X-ray emission do not have many of the problematic features of the IC/CMB model. They do not require these jets to remain highly relativistic on large scales or be highly aligned. The observed "knottiness" of these X-ray jets is well-explained by the much stronger radiative losses for these emission mechanisms. Finally, the second synchrotron model naturally explains the high degrees of polarization measured in the UV-upturns for PKS 1136-135 (Cara et al. 2013) and 3C 273 (Jester et al. 2007).

Chapter 4

Conclusions

In this chapter, I will sum up the main findings of this research, how these results fit within the work of others in the AGN research community as well as the broader field of Astronomy, and provide some future directions for research to investigate. This chapter is split into two main sections, which focus separately on the findings from the research descried in Chapters 2 and 3, respectively. First, I will discuss the work from Chapter 2 concerning the gamma-ray emission in blazars, before shifting focus to Chapter 3 regarding the X-ray emission in MSC jets.

4.1 The Location of Gamma-ray Flares in Blazars

Recent observational results have suggested an emission region for GeV gamma-ray flares of powerful blazars many pc beyond the canonical broad line region (BLR) and hot inner molecular torus (MT; e.g., Schinzel et al. 2012; Agudo et al. 2011). However, in the context of leptonic models, there is no substantial source of seed photons for the inverse-Compton scattering to GeV energies in this region of the jet. In this thesis, we have developed a model for these gamma-ray flares in which the blazar illuminates surrounding MT dust clouds with optical/UV synchrotron radiation, which then re-radiate thermal infrared photons serving as the seed photons for inverse-Compton scattering to GeV energies. Additionally, we have shown synchrotron-self Compton to be inadequate in producing these gamma-ray flares on the basis of predicting extremely high Doppler factors (which requires unrealistically long or powerful jets). These results provide a solution to the problem of how these gamma-ray flares can originate in an environment of such low photon density. Additionally, they provide support to the clumpy model of the MT which extends to the polar regions of the AGN over the scale of several to tens of pc. This scenario may by achieved by accretion disk-driven winds of dust, lifted by the radiation pressure of the accretion disk (e.g., Netzer 2015; Roth et al. 2012).

A unique prediction of our model is correlated gamma-ray and broad-line emission when the blazar emits a substantial flux of ionizing UV photons capable of sublimating the dust clouds. This has been tentatively observed for the blazar 3C 454.3 (see Isler et al. 2013 and León-Tavares et al. 2013), and reported at high statistical significance in the blazar CTA 102 (Jorstad et al. 2017). In future work, more correlations between broad-line and gamma-ray flux may help to strengthen the case for our model. This could be accomplished with future optical spectroscopic observations of GeV-flaring blazars.

Another prediction of our model is GeV orphan flares occurring when there is increased optical/UV luminosity from the blazar, leading to an increased seed photon density from the intercepting dust clouds. A Gev orphan flare is one in which the only observed increase in brightness from the blazar is at GeV-gamma-ray energies. This result has been seen in several cases (i.e., PKS 1510-089 by Marscher et al. 2010). However, this result is also consistent with the spine-sheath model advocated by MacDonald et al. (2015), where the synchrotron photons of the sheath serve directly as the seed photons for inverse-Compton scattering by plasma in the jet spine, referred to in this thesis as the spine-sheath-only model. One way to discrimate between the models will be to look for correlated hard X-ray to MeV flares in the case of the spine-sheath only model, which are not predicted by our model due to the narrow spectrum of seed photons received from the MT dust clouds. This could be accomplished with monitoring campaigns by the NuSTAR X-ray observatory of blazars which exhibit orphan GeV flares (like PKS 1510-089).

4.2 X-ray Emission in MSC Jets

In Chapter 1, I have discussed at length the phenomenon of MSC jets, where two or more emission components is seen (one radio-optical, and others in UV and/or X-ray). The physical model which was used to explain the X-ray emission (Tavecchio et al. 2000 and Celotti, Ghisellini, and Chiaberge 2001), and became the widely accepted model for MSC jets (e.g. Lucchini, Tavecchio, and Ghisellini 2017; Sambruna et al. 2004; Kharb et al. 2012; Jorstad and Marscher 2006), was the IC/CMB model. The IC/CMB model was very attractive since it utilized the population of electrons producing the radio-to-optical synchrotron spectrum in order to explain the X-ray emission. However, this model requires these jets to remain highly relativistic on the kpc scale and be oriented at small angles to the line-of-sight (Harris and Krawczynski 2006). Additionally, it requires substantial GeV gamma-ray emission in most cases (see Georganopoulos et al. 2006; Meyer et al.

2017; Meyer et al. 2015). In the following sections, I will reiterate the main results from Chapter 3 before discussing them in a broader context. Finally, I will discuss some of the implications behind ruling out the IC/CMB model in MSC jets, and provide some future research directions to investigate the source of the X-ray emission in MSC jets.

4.2.1 IC/CMB Now Ruled Out in 23 MSC Jets

In this work, we have used the *Fermi*/LAT gamma-ray space telescope to look for gamma-rays predicted from the IC/CMB model in order to test its viability. For twenty one out of the thirty one MSC jets analyzed for this thesis, the IC/CMB model was ruled out due to IC/CMB violating gamma-ray upper limits with the *Fermi*/LAT, where the predicted inverse-Compton gamma-ray flux is fixed by the requirement of fitting the observed X-ray flux density with the IC/CMB model. *Fermi* upper limits had previously ruled out the IC/CMB model in the sources 3C 273 and PKS 0637-752 (Meyer et al. 2017; Meyer et al. 2015; Meyer and Georganopoulos 2014). Therefore, the total number of MSC jets in which the IC/CMB model has been ruled out by *Fermi* observations now amounts to twenty three.

Additionally, based on the radio core dominance and crossing frequencies of the sample of MSC jets analyzed in this work, we have shown that these jets must be fairly misaligned, not extremely well-aligned blazars as is required under the IC/CMB model. In the case of PKS 1136-135 and PKS 2209+080 (among others not presented in this work), several knots show a steeply rising optical spectrum which would predict much higher X-ray flux densities than observed if fit with an IC/CMB model. Finally, we showed that the X-ray emission in the sample of MSC jets presented here did not show evidence for higher relativistic beaming (more emission close to than farther from the jet axis) relative to the synchrotron radio emission as is required in the IC/CMB model. However, these results are not the only lines of evidence against the IC/CMB model. In the following section, I will summarize the other independent lines of evidence against the IC/CMB model from the recent literature.

4.2.2 Other Lines of Evidence Against the IC/CMB Model

Offsets — In the IC/CMB model, the same electron population (usually assumed to be a power-law in energy) produces the radio through X-ray emission in MSC jets. The radio-to-optical spectrum is attributed to synchrotron radiation of electrons with Lorentz factors of a few thousand, while the X-ray spectrum is attributed to the inverse-Compton scattering of the CMB by electrons with Lorentz factors on the order of a hundred (Harris and Krawczynski 2006). Therefore, the emission regions should be co-spatial, and the peak brightness of knots should coincide for radio through X-ray wavelengths when observed with telescopes of similar angular resolution. However, offsets in peak brightness between radio and X-ray wavelengths are typical for X-ray jets, and there is no reasonable explanation for them in the IC/CMB model (e.g., Clautice et al. 2016; Hardcastle, Birkinshaw, and Worrall 2001; Hardcastle et al. 2002). Furthermore, the peak brightness of the X-ray emission is observed to be upstream (closer to the black hole) of the radio emission (e.g., Schwartz et al. 2000; Marshall et al. 2001; Jorstad and Marscher 2004; Siemiginowska et al. 2002). Since the X-ray emission in the IC/CMB model is suppose to originate from electrons of much lower energy than the electrons producing the observed GHz radio emission, we would expect the X-ray producing electrons to have much longer lifetimes (see section 1.5). Correspondingly, we would expect the X-ray emission to persist downstream of the radio emission, opposite to what is seen.

X-ray Variability — Another requirement of X-ray emission in the IC/CMB model is that it should be steady in time due to the low radiative efficiency of the $\gamma \sim 100$ electrons producing it. In the MSC jet associated with the quasar Pictor A, X-ray variability was observed with *Chandra* on the timescale of a few years at the 3.4σ level for a knot 48″ from the core (Marshall et al. 2010). This led the authors to conclude the X-ray emission was due to synchrotron radiation from a small unresolved volume of the jet with increased magnetic field strength compared to the rest of the jet. A similar result was seen in the jet associated with the Seyfert galaxy Cen A (Goodger et al. 2010).

X-ray Spectral Index — In the IC/CMB model, the X-ray spectral index should match the radio spectral index. Additionally, since the electrons producing the GHz radio emission are much more energetic than the ones producing IC/CMB X-rays, it is possible that radiative losses could soften (increase) the observed radio spectral index relative to the X-ray. However, in the MSC jet associated with the quasar 3C 273, the observed X-ray spectral index was found to be softer than the radio in several knots (Jester et al. 2006), opposite from the expectation.

Polarization — In the IC/CMB model, the radiation resulting from the inverse-Compton scattering of the CMB is expected to have very low polarization (McNamara, Kuncic, and Wu 2009;

Uchiyama 2008b). However, in the case of PKS 1136-135, a degree of polarization greater than 30% was observed in the UV portion of the high-energy spectral component for several knots (Cara et al. 2013). This result is incompatible with the IC/CMB model, but is consistent with synchrotron emission from a high-energy distribution of electrons.

Jet to Counter-Jet Flux Ratios — In the two MSC jets associated with the quasars 3C 353 and Pictor A, *Chandra* observations revealed a counter-jet in X-rays (Kataoka et al. 2008 and Hardcastle et al. 2016 respectively). In the IC/CMB model, the jet is oriented at very small angles to the line-of-sight and highly relativstic on kpc scales. Due to the extreme relativistic beaming of IC/CMB radiation (see section 1.5.3), the X-ray emission should be highly focused along the axis of the jet. Therefore, if these jets are oriented at low angles to the line-of-sight, the X-rays from the counter-jet should be beamed out of our line-of-sight, assuming the two jets are intrinsically identical. In both of these cases, the authors found a jet to counter-jet flux ratio orders of magnitude lower than required from the IC/CMB model, in which the strong relativistic beaming requires a very high ratio.

Redshift Evolution — Another prediction from the IC/CMB model is an increase in X-ray emissivity of the jet with an increase in redshift, since the CMB energy density has a $(1+z)^4$ dependence on redshift. Therefore, IC/CMB X-ray jets should be more luminous and prevalent at higher redshifts, possibly even outshining the quasar core, which is expected to decrease in flux as the square of the luminosity distance (Schwartz 2002). However, this prevalence of high-redshift IC/CMB X-ray jets which outshine their core has not yet been observed (e.g., Lopez et al. 2006; Bassett et al. 2004; Miller and Brandt 2009). In this work, we analyzed three X-ray jets at a redshift > 3.6: 4C+62.29, 1418-064, and QSO B1508+572. In the two sources 4C+62.29 and 1418-064, we found upper limits which conclusively rule out the IC/CMB model. This result provides strong evidence against the IC/CMB model.

Another expectation from the IC/CMB model is an increase of the X-ray luminosity relative to the radio with increasing redshift, since the radio emission is not expected to depend on redshift (following a $(1+z)^4$ trend). However, such a trend with redshift has not yet been observed (see Marshall et al. 2018; Kataoka and Stawarz 2005a).

When combining the above lines of evidence with the results from this thesis, it is clear that other physical models must be explored in order to explain the X-ray emission of MSC jets. In the following sections, I will discuss some of the implications resulting from finally abandoning the IC/CMB model.

4.2.3 Implications

Deceleration of Powerful Quasar Jets — VLBI observations of radio-loud AGN have shown highly relativistic (typical lower limits on Γ are around 10) motion of pc-scale features at the base of the radio jets (Lister et al. 2009). The IC/CMB model purported to explain the kpc-scale X-ray emission of MSC jets by suggesting they remain highly relativistic out to kpc scales. However, we have now shown the IC/CMB model is inadequate for many MSC jets, suggesting these jets are *not* highly relativistic on kpc scales. Additionally, we showed for nine of the MSC jets analyzed, that jets which start out highly relativistic on pc scales are slowed substantially once reaching kpc scales, with upper limits on Γ less than 5 in all cases. This result is in good agreement with previous studies which have shown FR II radio galaxies to be mildly relativistic on kpc scales (e.g., Arshakian and Longair 2004; Mullin and Hardcastle 2009). In the context of FR I radio galaxies, mass entrainment has been suggested as a mechanism for which a velocity shear develops between layers of the jet, and the jet subsequently decelerates (Laing, Canvin, and Bridle 2003). It is possible that the same reasoning may apply to FR II sources, contrary to the findings of previous authors (e.g., Bicknell 1995). Alternatively, another model of deceleration may be operating in FR II jets. Future VLBI and *Fermi* observations may be able to provide more evidence for highly relativistic FR II jets which are slowed substantially on the kpc to hundreds of kpc scale.

Alternative Models — Since these results lead us to reject the IC/CMB model as the X-ray emission mechanism for these MSC jets, we must consider alternative emission mechanisms. The main contenders for these emission mechanisms are a second population of electrons producing a second synchrotron component (see Atoyan and Dermer 2004; Harris, Mossman, and Walker 2004; Kataoka and Stawarz 2005b; Hardcastle 2006; Jester et al. 2006; Uchiyama et al. 2006) or hadronic emission models (see Aharonian 2002; Petropoulou, Vasilopoulos, and Giannios 2017; Kusunose and Takahara 2017). In the second synchrotron model, the electrons have Lorentz factors of $\sim 10^7$ (Worrall 2009) with a low energy cut-off such that they do not over-predict the optical emission. An obvious consequence of such high-energy electrons is that they will have very short cooling timescales (see section 1.5). Therefore, the existence of such high-energy electrons many kpc from the central engine implies highly efficient, in situ particle acceleration. In some cases, the X-ray emission extends along the length of the jet, and so *distributed* acceleration would be necessary. It has been suggested that if a velocity shear develops between a slow outer sheath and fast inner spine of the jet, this distributed particle acceleration could occur on the kpc scale, giving rise to such a high-energy electron population (Jester et al. 2006). In this scenario, the high-energy electron population is accelerated in the shear layer, while the lower-energy electron population is in the jet spine. Alternatively, Hardcastle et al. (2016) have suggested magnetic reconnection might be at work to accelerate the high-energy electrons. More work will be needed to determine what process is accelerating electrons to such high energies if this model turns out to be correct. Another consequence of such high-energy electrons is TeV gamma-rays produced when this electron population inverse-Compton scatters the CMB. Meyer et al. (2015) suggest the TeV emission from such MSC jets in a second synchrotron scenario might even provide a significant contribution to the TeV backgound and heating of the intergalactic medium (IGM) through the pair production with the extragalactic background light. They further suggest that this source of TeV photons might even dominate over TeV BL Lacs, possibly being the dominant source of blazar heating.

If the source of X-rays in MSC jets is due to hadronic processes, it means these jets can accelerate protons to very high energies. Hadronic models imply highly super-Eddington jets, which offers challenges to the current accretion paradigm in AGN (Zdziarski and Böttcher 2015). Tchekhovskoy, Narayan, and McKinney (2011) argue that highly super-Eddington jets might be accommodated if the jets extract a significant fraction of their energy from black hole spin, thereby having huge implications for how these jets are formed and how black holes can interact with their environment.

Additionally, hadronic jet models suggest AGN jets may provide a source of Ultra High Energy Cosmic Rays (UHECR), which are high-energy ($\gtrsim 5 \times 10^{19}$eV) protons and atomic nuclei observed to come from all directions of the sky (Resconi et al. 2017). The origin of these UHECR remains a mystery, although they are believed to be extragalactic and emanating from sources within $\sim$200 Mpc (Pierre Auger Collaboration et al. 2007). Recent observations of a high-energy (290 TeV) neutrino with the IceCube detector, coincident in direction and time with a gamma-ray flare from the blazar TXS 0506+056 at the 3σ level, strengthen the case for hadronic jets contributing to the observed UHECR flux (IceCube Collaboration et al. 2018; Ansoldi et al. 2018). In this scenario, UHECRs interact with ambient photons in the jet, which gives rise to both electromagnetic and neutrino radiation. This result suggests blazars are the first astrophysical source of high-energy neutrinos.

4.2.4 Future Directions

While the sample of MSC jets analyzed in this thesis is large, it is not complete. There are more *Fermi*-detected sources from the 3FGL catalog in which we can look for the IC/CMB gamma-rays from MSC jets, which we expect to publish in an upcoming paper (Breiding et al. 2019; *in prep*). For those sources presented in this work which were not detected by *Fermi* and in which we could not rule out the IC/CMB model, it is possible future *Fermi* observations may yield a detection of the IC/CMB gamma-rays, or provide deeper flux upper limits and, therefore, stronger constraints on B/δ. Alternatively, in these cases we may just detect the gamma-rays from the highly variable and luminous core.

For the *Fermi*-detected 3FGL catalog sources presented here (in addition to 3C 273 and PKS 0637-752 presented in Meyer and Georganopoulos (2014), Meyer et al. (2015), and Meyer et al. (2017)), it is possible future *Fermi* observations during times when the variable core is quiescent will be able to yield a detection of the IC/CMB gamma-ray emission component, as more *Fermi* time on source accumulates. Even if the IC/CMB model is ruled out as the X-ray emission mechanism, it must still be operating at *some* level. Therefore, these *Fermi*-detected sources should be reanalyzed as more time on source accumulates. If the IC/CMB gamma-ray component is not detected, longer time on source will translate to deeper flux upper limits and constraints on B/δ. A detection of these gamma-rays would be an important discovery in its own, and help to further constrain the jet parameters, including a *measurement* of B/δ.

One prediction from the IC/CMB model which has not yet been tested is the existence of the low-energy ($\gamma \sim 100$) electrons responsible for inverse-Compton scattering the CMB to X-ray energies. These electrons should produce synchrotron radiation at hundreds of MHz frequencies. Therefore, low-frequency, high resolution, radio observations of MSC jets would provide a direct test for the existence of these low-energy electrons. This may be accomplished with the upcoming Square Kilometer Array (SKA), being built in South Africa and Australia.

If the X-ray emission is due to synchrotron radiation from high-energy electrons, it is possible that the radiation could have a high degree of polarization (whereas IC/CMB radiation is expected to be unpolarized). A future high-resolution X-ray polarimetry mission could potentially rule out the IC/CMB model in favor of high-energy synchrotron emission in this case (hadronic models may also allow for polarization). Future TeV observations with the Cherenkov Telecope Array (CTA) at very high gammay-ray energies may provide another means of verifying these high-energy electrons, as they inverse-Compton scatter the CMB to TeV energies. A systematic comparison of the radio to X-ray spectral indices in these MSC jets for which we have ruled out the IC/CMB model may provide additional insight into the acceleration mechanism giving rise to such high-energy electrons many kpc from the core. For hadronic models, future observations of high-energy neutrinos with the IceCube detector may demonstrate that hadronic processes may be necessary to explain the large scale X-ray emission of MSC jets.

Appendix

A.1 Synchrotron fits

The empirical fits to the observed synchrotron SEDs are simple power laws with scaled exponential cutoffs, corresponding to a simple power-law electron energy distribution with maximum Lorentz factor. They have the following form:

$$\nu f_\nu = N \left(\frac{\nu}{10^{10} Hz}\right)^{\gamma} exp\left(-\left(\frac{\nu}{\nu_1}\right)^{\beta}\right) \tag{1}$$

In this equation ν is the observed frequency of the radiation, γ the power-law index, ν_1 the frequency at which the exponential turnover begins, β the steepness of the cutoff, and N is the normalization of the spectrum which has the units $erg\ cm^{-2}\ s^{-1}$.

A.2 Fermi Results

In Tables A.1-A.5, we report the results of the *Fermi* analyses. For all 5 *Fermi* bands, we give the minimum and maximum energy in columns 4 and 5, the logarithmic mean frequency of the band in column 6 corresponding to the frequency of the predicted IC/CMB flux densities (column 7) and the observed 95% upper limits (column 8). In columns 9 and 10 we report whether the IC/CMB model is ruled out by the 95% *Fermi* limits and give the corresponding limit on the Doppler factor (assuming an equipartition magnetic field) for the jet feature given in column 2.

TABLE A.1: Results of the Fermi Data Analysis

(1) Source Name	(2) Feature	(3) Band	(4) E_1 (GeV)	(5) E_2 (GeV)	(6) log freq (Hz)	(7) Predicted $\nu F_{\nu,IC/CMB}$ $(erg\,s^{-1}cm^{-2})$	(8) 95% νF_ν limit $(erg\,s^{-1}cm^{-2})$	(9) IC/CMB Ruled Out?	(11) δ limit
0838+133	A	1	0.1	0.3	22.6	1.7×10^{-12}	1.11×10^{-12}	Y	5.6
		2	0.3	1	23.1	2.8×10^{-12}	7.49×10^{-13}		
		3	1	3	23.6	4.3×10^{-12}	1.03×10^{-13}		
		4	3	10	24.1	6.1×10^{-12}	1.11×10^{-13}		
		5	10	100	24.7	8.0×10^{-12}	7.81×10^{-14}		
1317+520	C	1	0.1	0.3	22.6	1.4×10^{-14}	1.88×10^{-14}	Y	9.0
		2	0.3	1	23.1	7.1×10^{-15}	3.06×10^{-14}		
		3	1	3	23.6	1.8×10^{-15}	5.72×10^{-14}		
		4	3	10	24.1	1.4×10^{-16}	9.61×10^{-14}		
		5	10	100	24.7	2.1×10^{-19}	6.80×10^{-14}		
1418-064	Jet	1	0.1	0.3	22.6	1.3×10^{-13}	6.75×10^{-14}	Y	28
		2	0.3	1	23.1	1.5×10^{-13}	1.22×10^{-13}		
		3	1	3	23.6	1.6×10^{-13}	2.70×10^{-13}		
		4	3	10	24.1	1.3×10^{-13}	2.04×10^{-13}		
		5	10	100	24.7	5.0×10^{-14}	2.59×10^{-13}		
1508+572	Jet	1	0.1	0.3	22.6	8.6×10^{-15}	8.21×10^{-15}	N	26
		2	0.3	1	23.1	1.8×10^{-15}	1.71×10^{-14}		
		3	1	3	23.6	7.0×10^{-17}	5.78×10^{-14}		
		4	3	10	24.1	2.2×10^{-19}	1.79×10^{-13}		
		5	10	100	24.7	7.2×10^{-26}	9.56×10^{-14}		
2216-038	B	1	0.1	0.3	22.6	2.8×10^{-13}	4.21×10^{-13}	N	7.2
		2	0.3	1	23.1	2.0×10^{-13}	1.22×10^{-12}		
		3	1	3	23.6	6.4×10^{-14}	8.93×10^{-13}		
		4	3	10	24.1	6.3×10^{-15}	5.67×10^{-13}		
		5	10	100	24.7	9.4×10^{-18}	2.37×10^{-13}		
3C 120	k25	1	0.1	0.3	22.6	1.5×10^{-12}	6.76×10^{-14}	Y	7.0
		2	0.3	1	23.1	2.0×10^{-12}	8.42×10^{-13}		
		3	1	3	23.6	2.5×10^{-12}	1.07×10^{-12}		
		4	3	10	24.1	2.9×10^{-12}	3.45×10^{-13}		
		5	10	100	24.7	2.6×10^{-12}	1.23×10^{-13}		
3C 17	A	1	0.1	0.3	22.6	1.2×10^{-14}	1.01×10^{-13}	N	7.8
		2	0.3	1	23.1	1.3×10^{-14}	3.28×10^{-13}		
		3	1	3	23.6	1.3×10^{-14}	2.03×10^{-13}		
		4	3	10	24.1	1.1×10^{-14}	1.76×10^{-13}		
		5	10	100	24.7	6.3×10^{-15}	8.73×10^{-14}		

TABLE A.2: Results of the Fermi Data Analysis – Continued

(1) Source Name	(2) Feature	(3) Band	(4) E_1 (GeV)	(5) E_2 (GeV)	(6) log freq (Hz)	(7) Predicted $\nu F_{\nu,IC/CMB}$ ($erg\ s^{-1} cm^{-2}$)	(8) 95% νF_ν limit ($erg\ s^{-1} cm^{-2}$)	(9) IC/CMB Ruled Out?	(11) δ limit
3C 227	P4	1	0.1	0.3	22.6	2.1×10^{-14}	8.38×10^{-14}	N	16.5
		2	0.3	1	23.1	2.1×10^{-14}	1.81×10^{-13}		
		3	1	3	23.6	1.5×10^{-14}	2.28×10^{-13}		
		4	3	10	24.1	6.5×10^{-15}	6.80×10^{-14}		
		5	10	100	24.7	5.6×10^{-16}	1.06×10^{-13}		
3C 321	Jet	1	0.1	0.3	22.6	1.8×10^{-14}	5.06×10^{-14}	N	6.8
		2	0.3	1	23.1	1.4×10^{-14}	9.76×10^{-14}		
		3	1	3	23.6	7.5×10^{-15}	1.58×10^{-13}		
		4	3	10	24.1	2.0×10^{-15}	1.51×10^{-13}		
		5	10	100	24.7	1.5×10^{-14}	6.64×10^{-14}		
3C 353	J1	1	0.1	0.3	22.6	2.5×10^{-13}	8.75×10^{-14}	Y	3.2
		2	0.3	1	23.1	1.9×10^{-13}	4.79×10^{-14}		
		3	1	3	23.6	7.3×10^{-14}	1.08×10^{-13}		
		4	3	10	24.1	8.7×10^{-15}	2.76×10^{-13}		
		5	10	100	24.7	1.9×10^{-17}	5.76×10^{-13}		
3C 465	2	1	0.1	0.3	22.6	1.7×10^{-12}	3.34×10^{-14}	Y	7.9
		2	0.3	1	23.1	2.6×10^{-12}	3.91×10^{-14}		
		3	1	3	23.6	3.5×10^{-12}	2.53×10^{-13}		
		4	3	10	24.1	3.4×10^{-12}	1.12×10^{-13}		
		5	10	100	24.7	1.5×10^{-12}	3.05×10^{-13}		
4C 13.41	Jet	1	0.1	0.3	22.6	5.6×10^{-13}	9.55×10^{-14}	Y	10.8
		2	0.3	1	23.1	5.5×10^{-13}	1.08×10^{-13}		
		3	1	3	23.6	3.1×10^{-13}	2.60×10^{-13}		
		4	3	10	24.1	6.8×10^{-14}	2.05×10^{-13}		
		5	10	100	24.7	7.9×10^{-16}	1.91×10^{-13}		
4C 20.24	Jet	1	0.1	0.3	22.6	1.3×10^{-12}	4.97×10^{-14}	Y	1.2
		2	0.3	1	23.1	4.8×10^{-14}	1.2×10^{-12}		
		3	1	3	23.6	1.3×10^{-14}	5.6×10^{-13}		
		4	3	10	24.1	1.0×10^{-15}	1.1×10^{-13}		
		5	10	100	24.7	1.2×10^{-18}	7.70×10^{-16}		
4C 35.05	Jet	1	0.1	0.3	22.6	2.9×10^{-13}	3.53×10^{-14}	Y	6.6
		2	0.3	1	23.1	2.7×10^{-13}	3.30×10^{-14}		
		3	1	3	23.6	1.9×10^{-13}	9.79×10^{-14}		
		4	3	10	24.1	7.5×10^{-14}	1.74×10^{-13}		
		5	10	100	24.7	5.1×10^{-15}	8.14×10^{-14}		

TABLE A.3: Results of the Fermi Data Analysis – Continued

(1) Source Name	(2) Feature	(3) Band	(4) E_1 (GeV)	(5) E_2 (GeV)	(6) log freq (Hz)	(7) Predicted $\nu F_{\nu,IC/CMB}$ ($erg\ s^{-1} cm^{-2}$)	(8) 95% νF_ν limit ($erg\ s^{-1} cm^{-2}$)	(9) IC/CMB Ruled Out?	(11) δ limit
4C 62.29	Jet	1	0.1	0.3	22.6	3.7×10^{-14}	7.40×10^{-15}	Y	4.0
		2	0.3	1	23.1	2.9×10^{-14}	1.24×10^{-14}		
		3	1	3	23.6	1.7×10^{-14}	2.37×10^{-14}		
		4	3	10	24.1	6.7×10^{-15}	7.13×10^{-14}		
		5	10	100	24.7	5.3×10^{-16}	1.23×10^{-13}		
4C 65.15	Bend	1	0.1	0.3	22.6	2.6×10^{-16}	6.22×10^{-15}	N	14.9
		2	0.3	1	23.1	1.1×10^{-16}	1.11×10^{-14}		
		3	1	3	23.6	2.7×10^{-17}	2.52×10^{-14}		
		4	3	10	24.1	2.7×10^{-18}	1.55×10^{-13}		
		5	10	100	24.7	9.1×10^{-21}	6.16×10^{-14}		
4C 69.21	B	1	0.1	0.3	22.6	1.6×10^{-14}	5.67×10^{-15}	Y	5.1
		2	0.3	1	23.1	1.1×10^{-14}	1.08×10^{-14}		
		3	1	3	23.6	4.3×10^{-15}	1.09×10^{-13}		
		4	3	10	24.1	7.6×10^{-16}	3.76×10^{-13}		
		5	10	100	24.7	2.5×10^{-16}	4.53×10^{-13}		
4C 73.18	A	1	0.1	0.3	22.6	1.4×10^{-13}	1.15×10^{-14}	Y	4.7
		2	0.3	1	23.1	1.5×10^{-13}	1.72×10^{-14}		
		3	1	3	23.6	1.3×10^{-13}	7.30×10^{-14}		
		4	3	10	24.1	9.1×10^{-14}	1.76×10^{-13}		
		5	10	100	24.7	2.7×10^{-14}	1.06×10^{-13}		
B2 0738+313	A	1	0.1	0.3	22.6	1.4×10^{-13}	1.15×10^{-14}	Y	22
		2	0.3	1	23.1	1.5×10^{-13}	1.72×10^{-14}		
		3	1	3	23.6	1.3×10^{-13}	7.30×10^{-14}		
		4	3	10	24.1	9.1×10^{-14}	1.76×10^{-13}		
		5	10	100	24.7	2.7×10^{-14}	1.06×10^{-13}		
PKS 0413-21	Jet	1	0.1	0.3	22.6	1.1×10^{-13}	4.22×10^{-14}	Y	6.5
		2	0.3	1	23.1	6.3×10^{-14}	6.81×10^{-14}		
		3	1	3	23.6	1.6×10^{-14}	2.07×10^{-13}		
		4	3	10	24.1	1.2×10^{-15}	3.36×10^{-13}		
		5	10	100	24.7	1.2×10^{-18}	2.49×10^{-13}		
PKS 0920-397	B	1	0.1	0.3	22.6	2.4×10^{-13}	...	N	8.8
		2	0.3	1	23.1	2.8×10^{-13}	...		
		3	1	3	23.6	2.9×10^{-13}	7.42×10^{-13}		
		4	3	10	24.1	2.3×10^{-13}	5.68×10^{-13}		
		5	10	100	24.7	9.2×10^{-14}	1.54×10^{-13}		

TABLE A.4: Results of the Fermi Data Analysis – Continued

(1) Source Name	(2) Feature	(3) Band	(4) E_1 (GeV)	(5) E_2 (GeV)	(6) log freq (Hz)	(7) Predicted $\nu F_{\nu,IC/CMB}$ $(erg\ s^{-1} cm^{-2})$	(8) 95% νF_ν limit $(erg\ s^{-1} cm^{-2})$	(9) IC/CMB Ruled Out?	(11) δ limit
PKS 1030-357	D	1	0.1	0.3	22.6	1.5×10^{-13}	2.57×10^{-14}	Y	8.4
		2	0.3	1	23.1	1.6×10^{-13}	5.78×10^{-14}		
		3	1	3	23.6	1.4×10^{-13}	1.87×10^{-13}		
		4	3	10	24.1	8.5×10^{-14}	1.11×10^{-13}		
		5	10	100	24.7	1.7×10^{-14}	1.39×10^{-13}		
PKS 1045-188	C	1	0.1	0.3	22.6	3.3×10^{-15}	6.01×10^{-14}	N	5.6
		2	0.3	1	23.1	2.0×10^{-15}	1.85×10^{-13}		
		3	1	3	23.6	7.2×10^{-16}	3.34×10^{-13}		
		4	3	10	24.1	1.1×10^{-16}	2.37×10^{-13}		
		5	10	100	24.7	9.1×10^{-19}	2.67×10^{-13}		
PKS 1046-409	Jet	1	0.1	0.3	22.6	9.1×10^{-14}	1.85×10^{-14}	Y	5.4
		2	0.3	1	23.1	7.5×10^{-14}	3.48×10^{-14}		
		3	1	3	23.6	4.1×10^{-14}	1.02×10^{-13}		
		4	3	10	24.1	1.1×10^{-14}	4.97×10^{-13}		
		5	10	100	24.7	2.6×10^{-16}	1.72×10^{-13}		
PKS 1127-145	B	1	0.1	0.3	22.6	6.5×10^{-14}	2.03×10^{-12}	N	6.5
		2	0.3	1	23.1	5.5×10^{-14}	1.10×10^{-12}		
		3	1	3	23.6	2.7×10^{-14}	2.07×10^{-13}		
		4	3	10	24.1	5.7×10^{-15}	8.89×10^{-14}		
		5	10	100	24.7	6.4×10^{-17}	9.49×10^{-14}		
PKS 1136-135	B	1	0.1	0.3	22.6	5.7×10^{-13}	1.18×10^{-13}	Y	5.4
		2	0.3	1	23.1	7.7×10^{-13}	7.27×10^{-14}		
		3	1	3	23.6	9.9×10^{-13}	1.02×10^{-13}		
		4	3	10	24.1	1.2×10^{-12}	9.81×10^{-14}		
		5	10	100	24.7	1.3×10^{-12}	1.13×10^{-13}		
PKS 1150+497	B	1	0.1	0.3	22.6	4.1×10^{-13}	7.53×10^{-13}	Y	6.5
		2	0.3	1	23.1	5.4×10^{-13}	3.55×10^{-13}		
		3	1	3	23.6	7.1×10^{-13}	9.02×10^{-14}		
		4	3	10	24.1	9.0×10^{-13}	1.82×10^{-13}		
		5	10	100	24.7	1.1×10^{-12}	7.78×10^{-14}		
PKS 1229-021	BCD†	1	0.1	0.3	22.6	4.9×10^{-13}	1.32×10^{-13}	Y	8.0
		2	0.3	1	23.1	5.2×10^{-13}	2.44×10^{-13}		
		3	1	3	23.6	4.8×10^{-13}	1.43×10^{-13}		
		4	3	10	24.1	3.9×10^{-13}	3.07×10^{-13}		
		5	10	100	24.7	2.1×10^{-13}	3.10×10^{-13}		

† Knot BCD includes the combined data from knots B, C, and D.

TABLE A.5: Results of the Fermi Data Analysis – Continued

(1) Source Name	(2) Feature	(3) Band	(4) E_1 (GeV)	(5) E_2 (GeV)	(6) log freq (Hz)	(7) Predicted $\nu F_{\nu,IC/CMB}$ $(erg\ s^{-1} cm^{-2})$	(8) 95% νF_ν limit $(erg\ s^{-1} cm^{-2})$	(9) IC/CMB Ruled Out?	(11) δ limit
PKS 1354+195	Jet†	1	0.1	0.3	22.6	1.4×10^{-13}	4.53×10^{-14}	Y	6.0
		2	0.3	1	23.1	1.4×10^{-13}	7.05×10^{-14}		
		3	1	3	23.6	1.3×10^{-13}	1.14×10^{-13}		
		4	3	10	24.1	9.9×10^{-14}	6.83×10^{-14}		
		5	10	100	24.7	5.1×10^{-14}	9.36×10^{-14}		
PKS 2209+080	E	1	0.1	0.3	22.6	1.1×10^{-12}	1.45×10^{-13}	Y	8.6
		2	0.3	1	23.1	1.3×10^{-12}	7.19×10^{-14}		
		3	1	3	23.6	1.5×10^{-12}	1.54×10^{-13}		
		4	3	10	24.1	1.5×10^{-12}	3.42×10^{-13}		
		5	10	100	24.7	1.1×10^{-12}	3.15×10^{-13}		
QSO 0957+561		1	0.1	0.3	22.6	1.4×10^{-15}	8.63×10^{-15}	N	6.0
		2	0.3	1	23.1	3.7×10^{-16}	1.43×10^{-14}		
		3	1	3	23.6	2.8×10^{-17}	6.03×10^{-14}		
		4	3	10	24.1	2.8×10^{-19}	4.86×10^{-14}		
		5	10	100	24.7	1.8×10^{-24}	1.16×10^{-13}		

† Data was combined for the whole jet past knot A.

A.3 Radio SEDs

In Figures A.1-A.2, I give the radio SED fits for the remaining sources. Data was obtained through the NED database. Cyan squares represent extended lobe emission and the blue circles represent emission from the core. A power-law model was used to fit the lobe emission and a log parabola was used to fit the core emission, with dashed black lines showing each of the individual fits. The solid red line shows the total model fit adding both of these components for the radio spectrum. The solid black line connects the core and extended emission at 1.4 GHz, the ratio of which was used to determine the radio core dominance.

FIGURE A.1

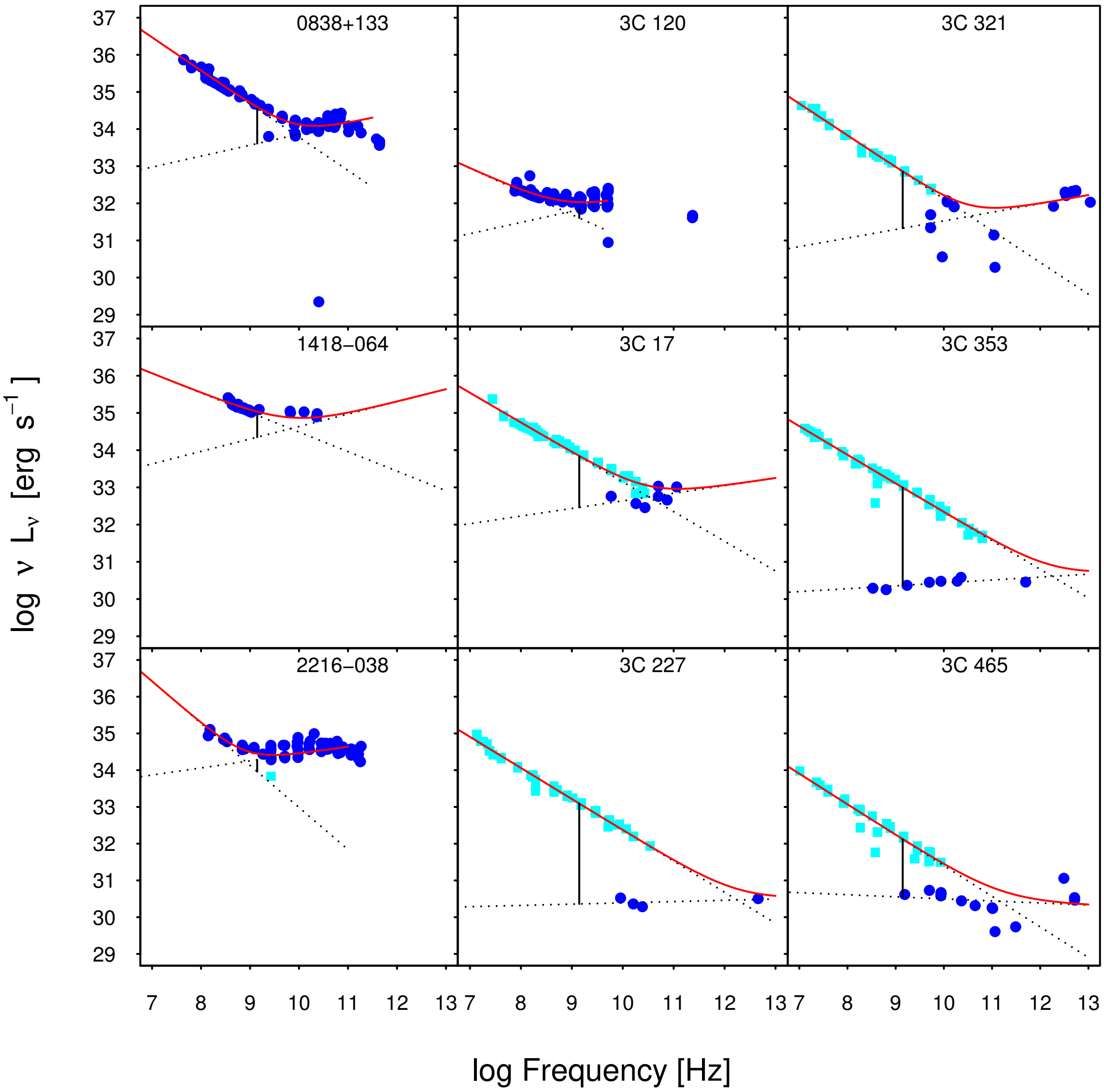
0838+133
3C 120
3C 321
1418–064
3C 17
3C 353
2216–038
3C 227
3C 465
log ν L$_\nu$ [erg s^{-1}]
log Frequency [Hz]
37
36
35
34
33
32
31
30
29
7
8
9
10
11
12
13

FIGURE A.2

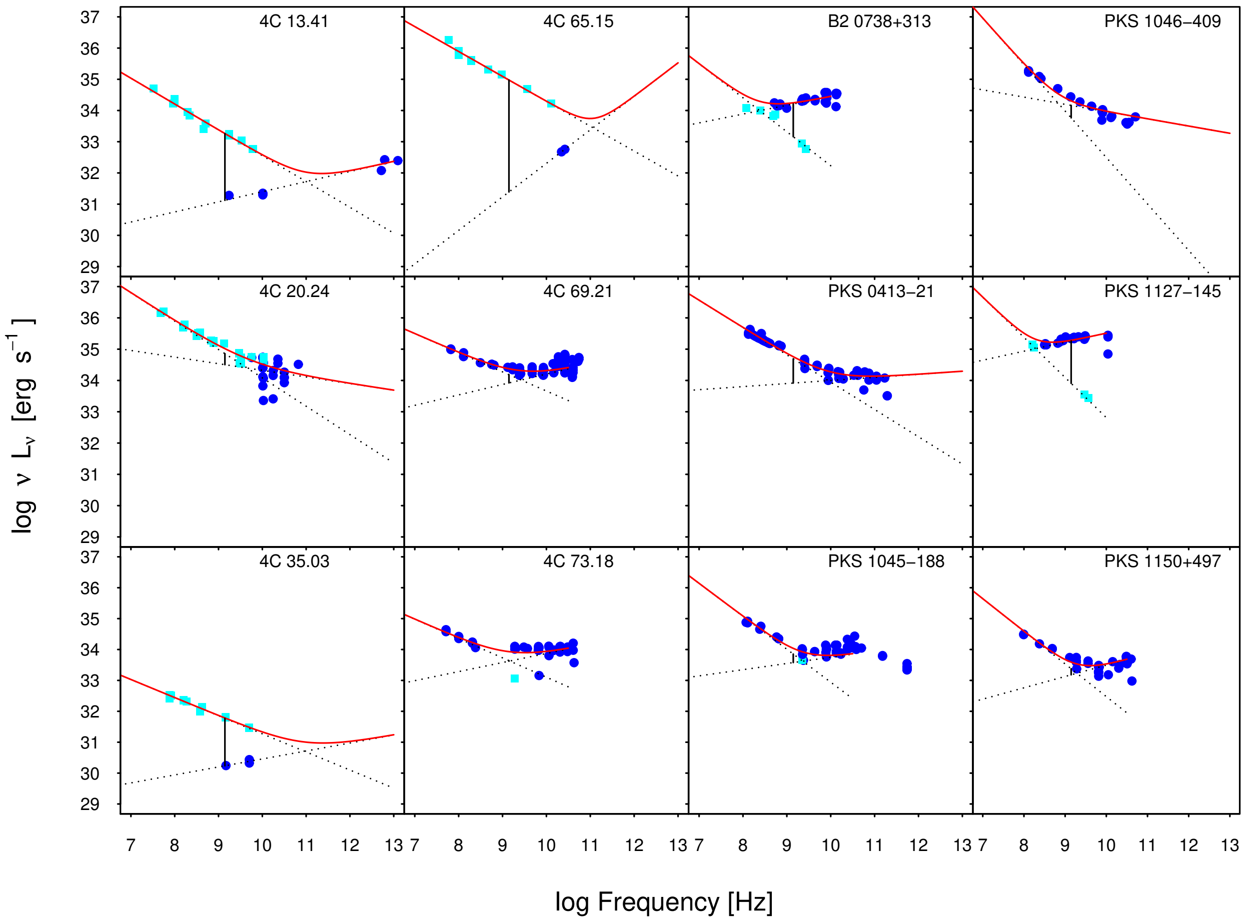

A.4 Total Source SEDs

In Figures A.3-A.4, I give the total SED fits for the remaining sources. The SED for each source was fit with the parametric model from Meyer et al. 2011 shown in red to estimate parameters for the synchrotron peak frequencies and luminosities. All data was obtained through NED, with the cyan squares representing the lobe spectrum with the line of best fit as the dotted black line. Blue circles represent the rest of data and gray open circles represent the data that was filtered out and not used in the fitting. The *Fermi*/LAT data points are shown in black, with values taken from the 3FGL catalog for the 3FGL catalog sources, and the rest being upper limits taken from this work.

FIGURE A.3

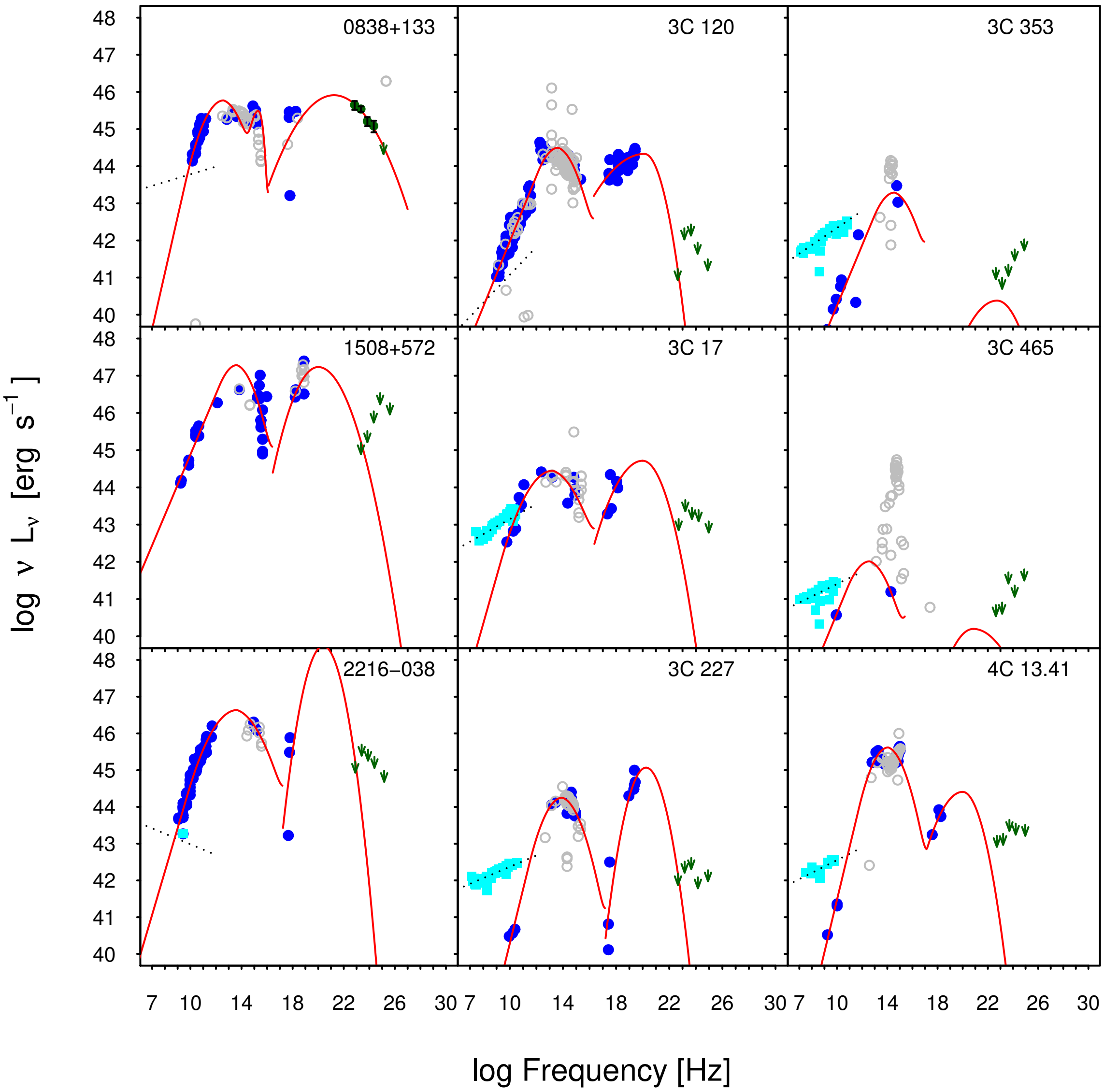
0838+133
3C 120
3C 353
1508+572
3C 17
3C 465
2216−038
3C 227
4C 13.41
log ν Lν [erg s−1]
log Frequency [Hz]
48
47
46
45
44
43
42
41
40
7
10
14
18
22
26
30

FIGURE A.4

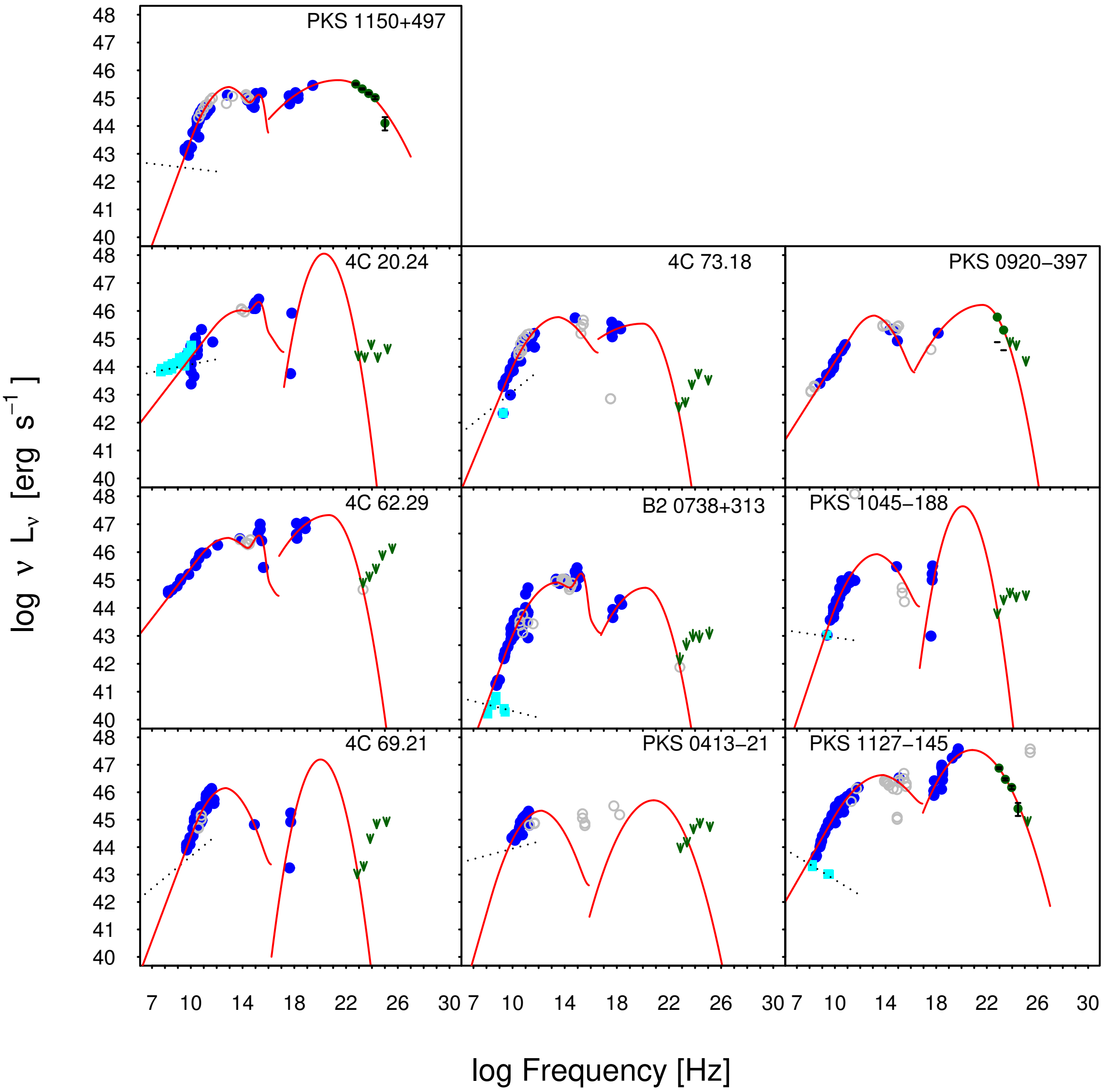

A.5 Jet SEDs and Images

Here I give the broadband SEDs for the jet feature in which we are testing the IC/CMB model with *Fermi*. In each SED, the red arrows represent the 95% *Fermi* upper limits, the thin black lines correspond to the synchrotron model fits, the thick black lines correspond to the IC/CMB model fits, and the flux densities for the jet feature analyzed are shown as blue or green points.

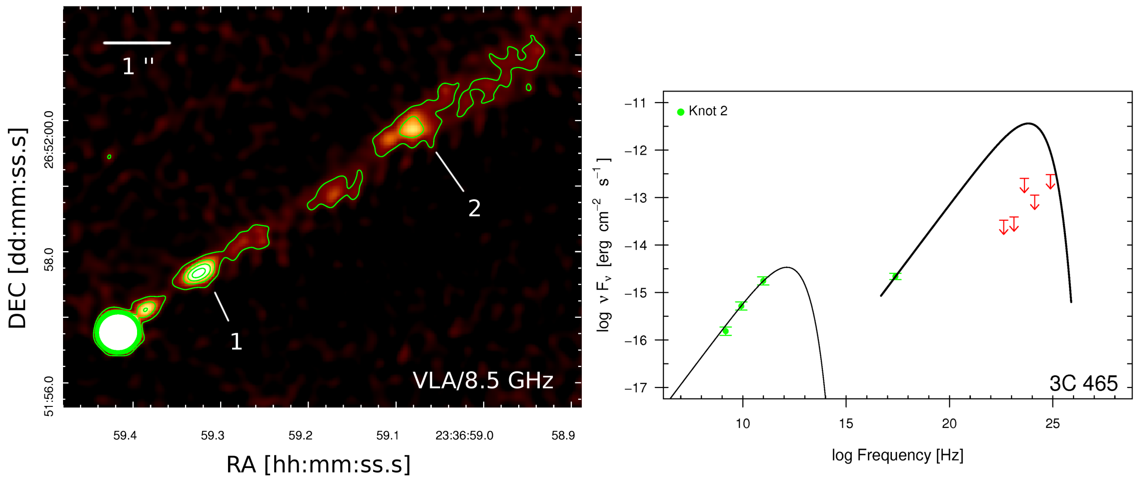

FIGURE A.5: Left: VLA 8.5 GHz image of 3C 465 with VLA 8.5 GHz contours. The contours are spaced from 0.2-2 mJy, with 10 levels. Right: SED for knot 2 of 3C 465, where the green data points are flux densities taken from Hardcastle, Sakelliou, and Worrall 2005 (except the ALMA Band 3 flux density at 97.5 GHz which came from this work). The IC/CMB model is clearly ruled out at a high level for this source.

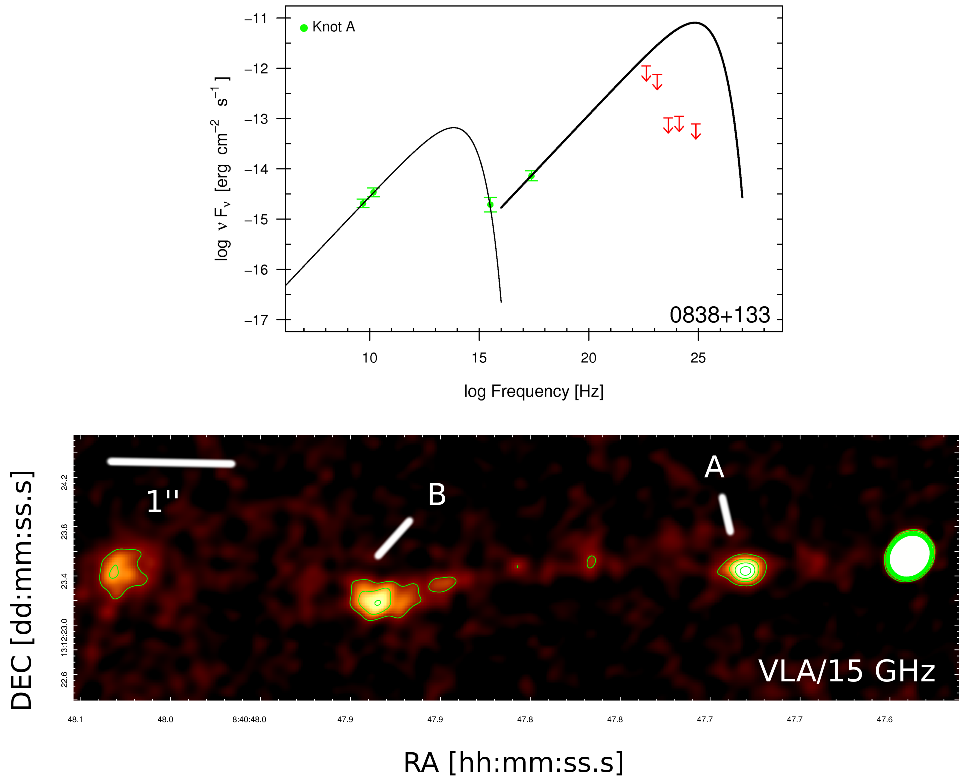

FIGURE A.6: Bottom: VLA 15 GHz image of 0838+133 with VLA 15 GHz contours. The contours are spaced from 2-20 mJy, with 10 levels. Top: SED for knot A of 0838+133, where the green data points are flux densities taken from Sambruna et al. 2004 (except the VLA Ku band flux density at 15 GHz which came from this work). The IC/CMB model is clearly ruled out at a high level for this source.

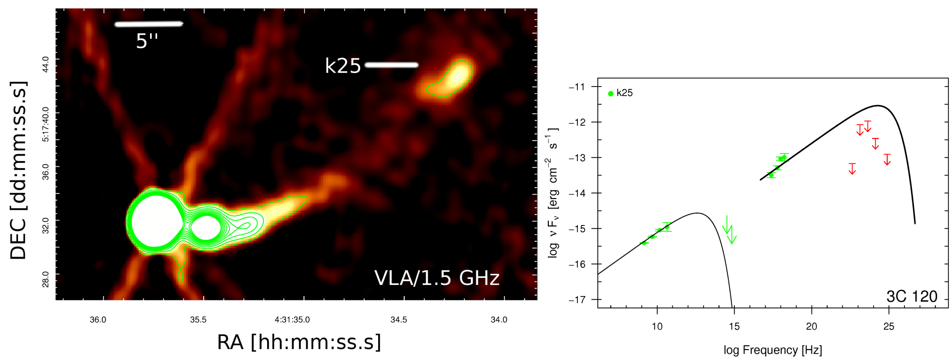

FIGURE A.7: Left: VLA 1.5 GHz image of 3C 120 with VLA 1.5 GHz contours. The contours are spaced from 5-50 mJy, with 10 levels. Right: SED for knot k25 of 3C 120, where the green data points are flux densities taken from Harris, Mossman, and Walker 2004 (and the green arrows are optical upper limits taken from the same work). The IC/CMB model is clearly ruled out at a high level for this source.

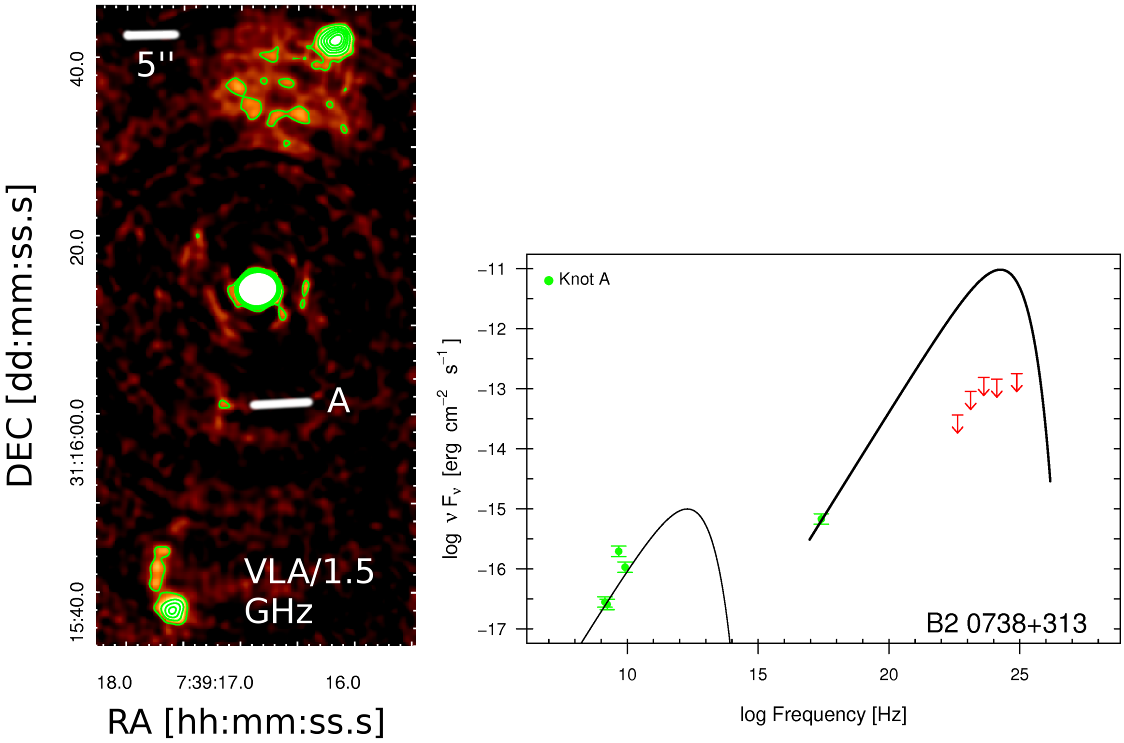

FIGURE A.8: Left: VLA 1.5 GHz image of B2 0738+313 with VLA 1.5 GHz contours. The contours are spaced from 0.6-6 mJy, with 10 levels. Right: SED for knot A of B2 0738+313, where the green data points are flux densities taken from Siemiginowska et al. 2003. The IC/CMB model is clearly ruled out at a high level for this source.

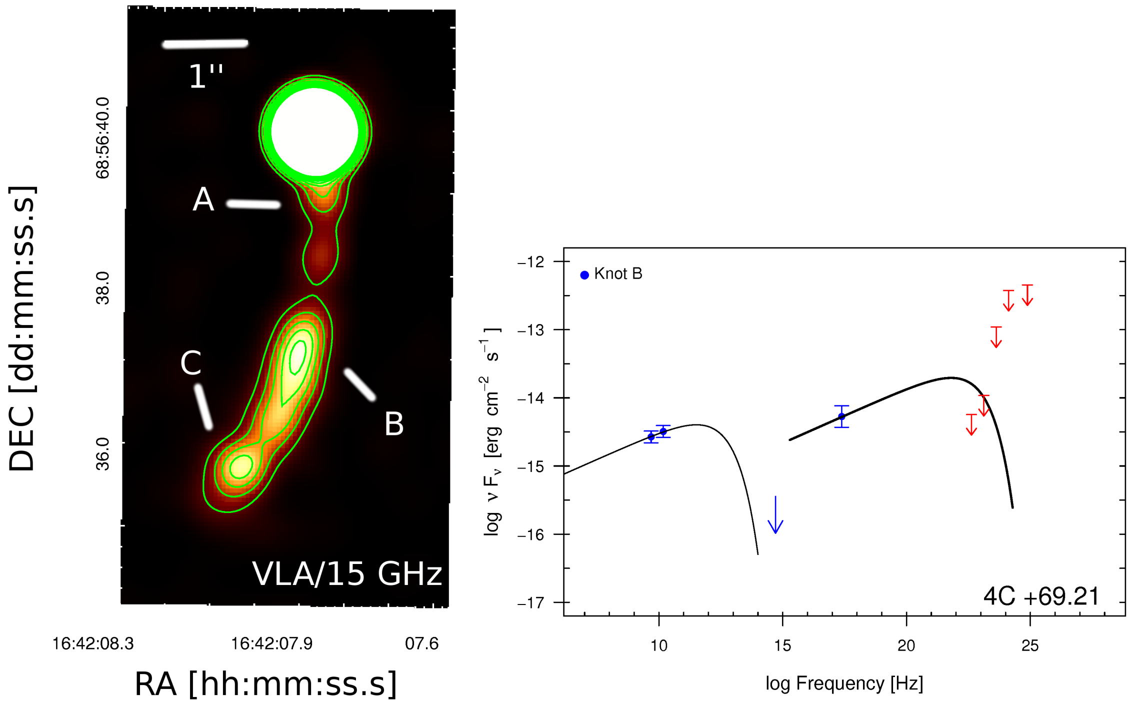

FIGURE A.9: Left: VLA 15 GHz image of 4C 69.21 with VLA 15 GHz contours. The contours are spaced from 3-30 mJy, with 10 levels. Right: SED for knot B of 4C 69.21, where the blue data points are flux densities taken from Sambruna et al. 2004, and the blue arrow is an optical upper limit taken from the same work (except the VLA Ku band flux density at 15 GHz which came from this work). The IC/CMB model is ruled out by the lowest energy *Fermi* limit.

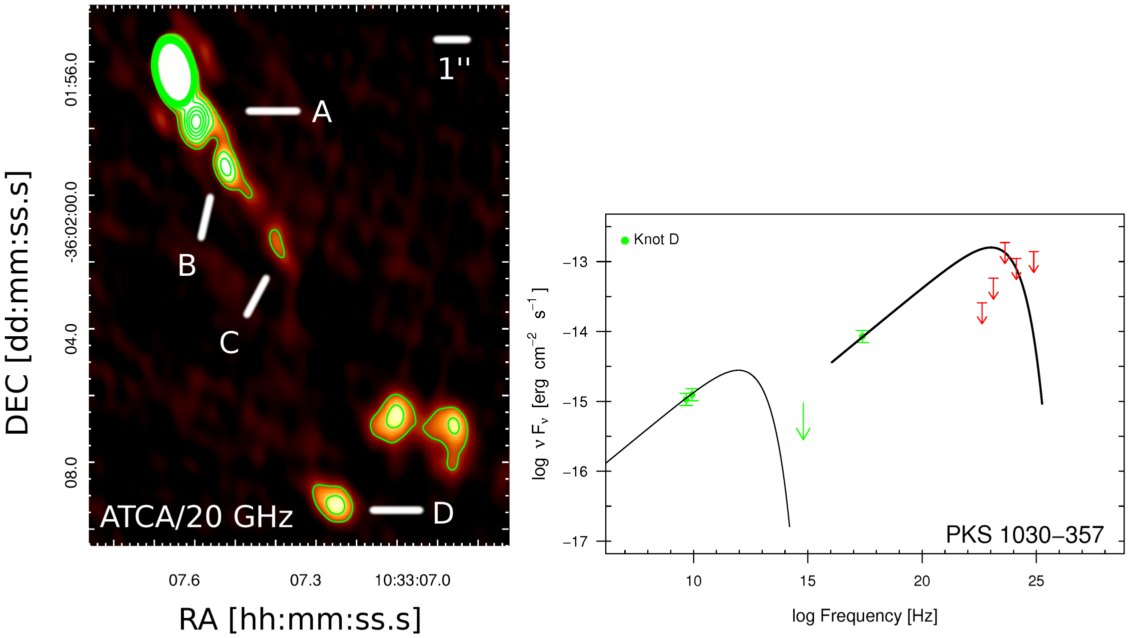

FIGURE A.10: Left: *ATCA* 20 GHz image of PKS 1030-357 with *ATCA* 20 GHz contours. The contours are spaced from 0.7-7 mJy, with 10 levels. Right: SED for knot D of PKS 1030-357, where the green data points are flux densities taken from Schwartz et al. 2006, and the green arrow is an optical upper limit taken from the same work. The IC/CMB model is ruled out by the two lowest energy *Fermi* limits.

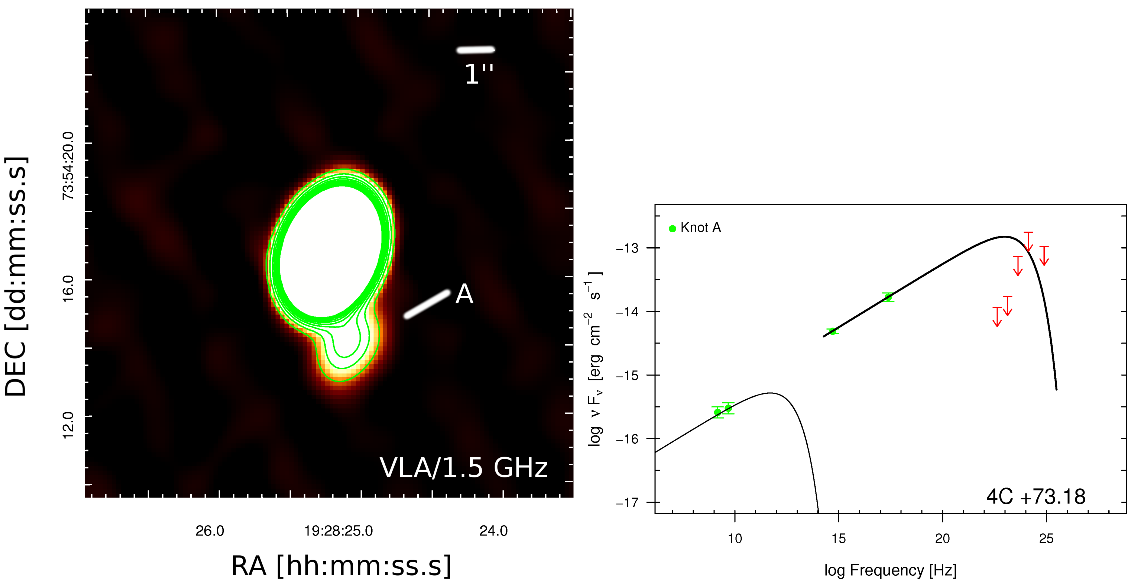

FIGURE A.11: Left: VLA 1.5 GHz image of 4C+73.18 with VLA 1.5 GHz contours. The contours are spaced from 5-50 mJy, with 10 levels. Right: SED for knot A of 4C+73.18, where the green data points are flux densities taken from Sambruna et al. 2004 (except the VLA L band flux density at 1.5 GHz which came from this work). The IC/CMB model is clearly ruled out for this source.

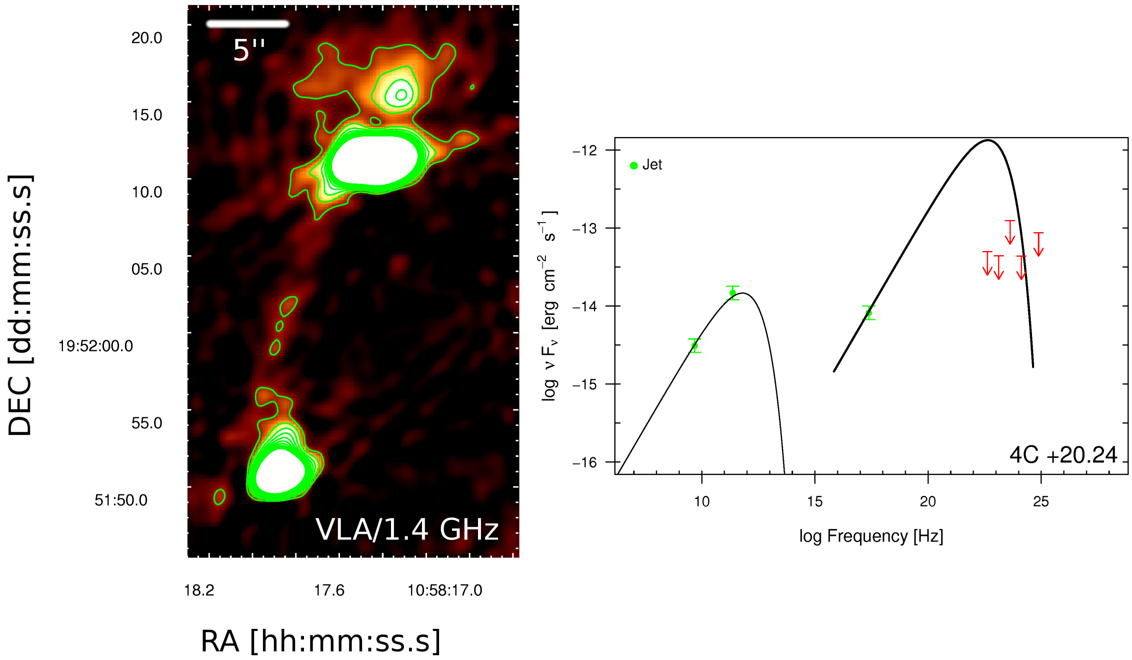

FIGURE A.12: Left: VLA 1.4 GHz image of 4C+20.24 with VLA 1.4 GHz contours. The contours are spaced from 6-60 mJy, with 10 levels. Right: SED for the whole jet of 4C+20.24, where the green data points are flux densities taken from Marshall et al. 2011 (except for the ALMA band 6 flux density at 233 GHz which came from this work). The IC/CMB model is ruled out by the lowest energy *Fermi* limits. Note that the ALMA flux density is key in fixing the peak of the synchrotron and IC/CMB spectrum in this case, therefore implying the IC/CMB model is ruled out at a high level by the *Fermi* limits.

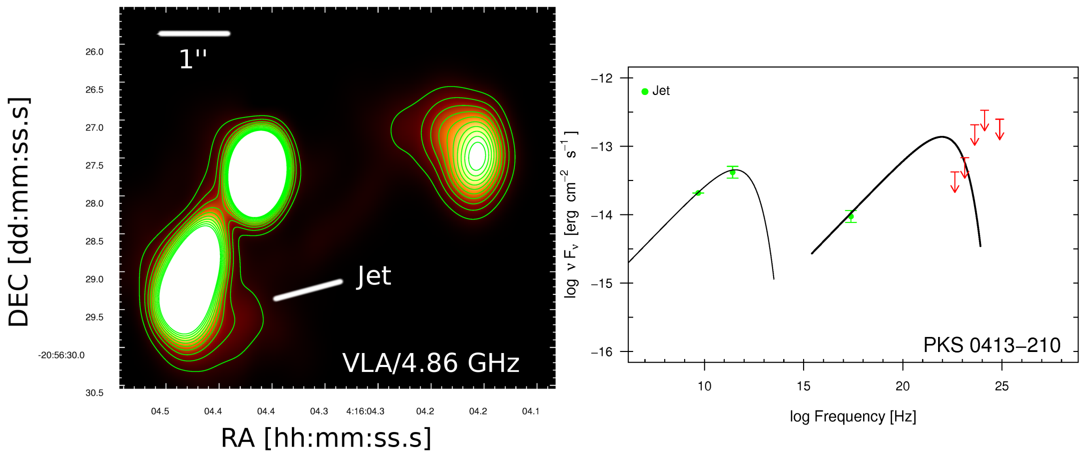

FIGURE A.13: Left: VLA 4.86 GHz image of PKS 0413-210 with VLA 4.86 GHz contours. The contours are spaced from 5-50 mJy, with 10 levels. Right: SED for the whole jet of PKS 0413-210, where the green data points are flux densities taken from Marshall et al. 2011 (except for the ALMA band 6 flux density at 263 GHz which came from this work). The IC/CMB model is ruled out by the lowest energy *Fermi* limit.

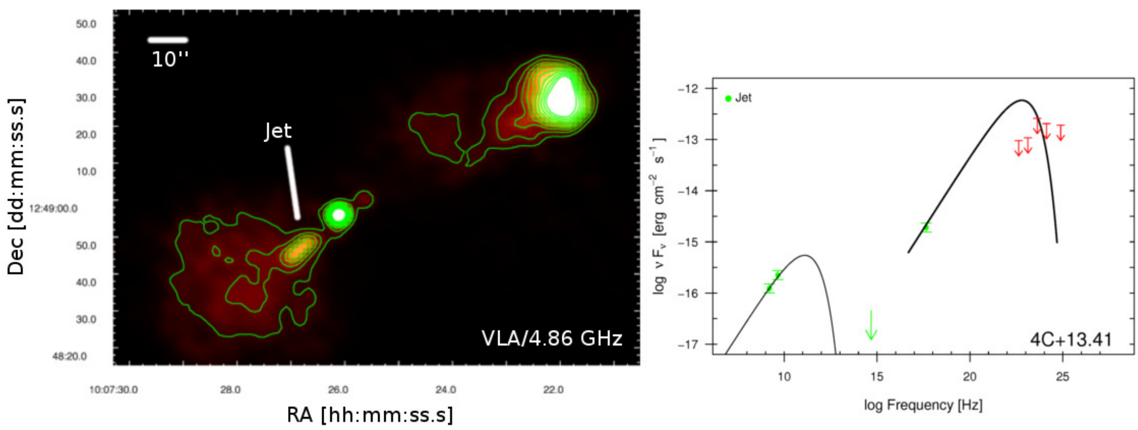

FIGURE A.14: Left: VLA 4.86 image of 4C +13.41 with VLA 4.86 GHz contours (image obtained from VLA archive survey images page website at https://archive.nrao.edu/nvas/). Contours are spaced from 1.5-15 mJy, with 10 levels. Right: SED for the whole jet of 4C+13.41, where the green data points are flux densities taken from Miller et al. 2006 (and the green arrow is an optical upper limit taken from the same work). The IC/CMB model is ruled out by the two lowest energy *Fermi* limits.

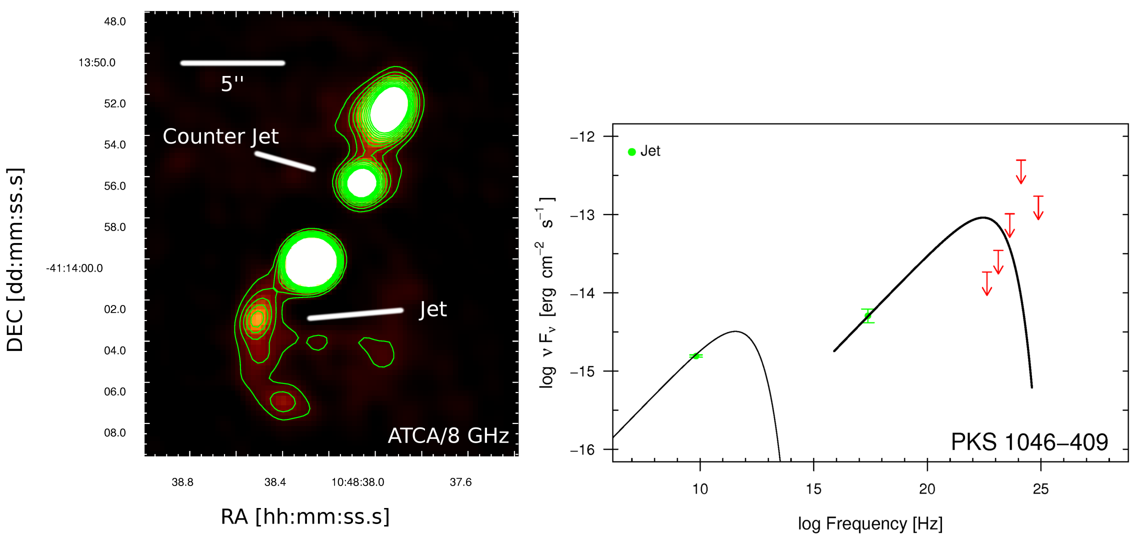

FIGURE A.15: Left: ATCA 8 GHz image of PKS 1046-409 with ATCA 8 GHz contours (image obtained from the *XJET* database at http://hea-www.harvard.edu/XJET/). The contours are spaced from 2-20 mJy, with 10 levels. Right: SED for the whole jet of PKS 1046-409, where the green data points are flux densities taken from Marshall et al. 2005. A radio spectral index of 0.7 was assumed as this value is typical for jets, and only one radio flux density was available. The IC/CMB model is ruled out by the two lowest energy *Fermi* limits.

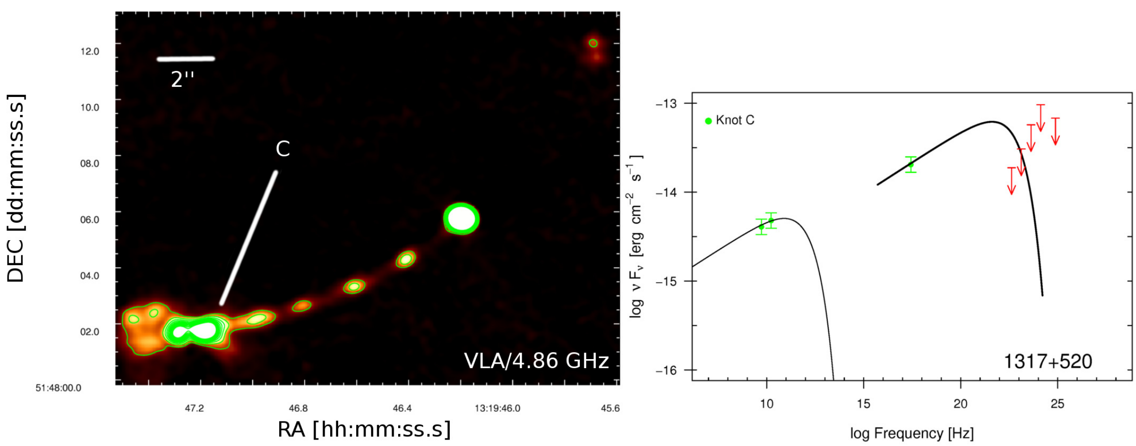

FIGURE A.16: Left: VLA image of 1317+520 with VLA 4.86 GHz contours. The contours are spaced from 1-10 mJy, with 10 levels. Right: SED for knot C of 1317+520, where the green data points are flux densities taken from Jorstad and Marscher 2006. The IC/CMB model is ruled out by the lowest energy *Fermi* limit.

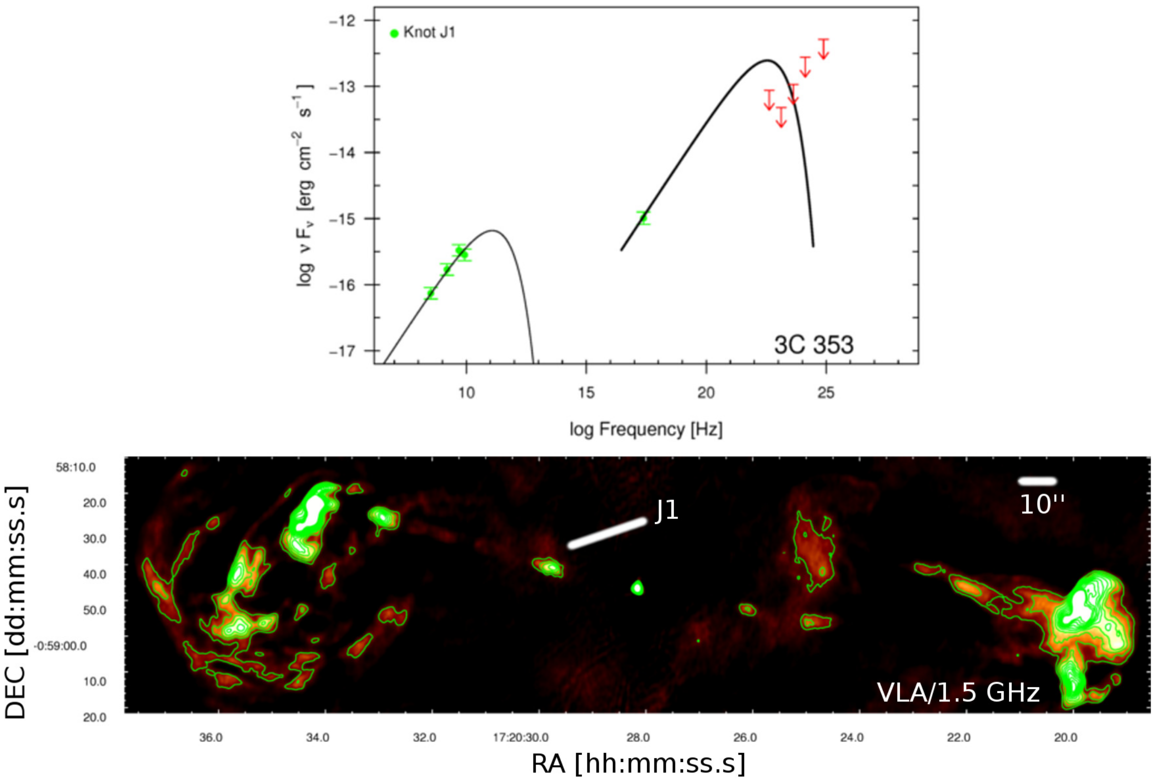

FIGURE A.17: Bottom: VLA 1.5 GHz image of 3C 353 with VLA 1.5 GHz contours (image obtained from VLA archive survey images page website at https://archive.nrao.edu/nvas/). The contours are spaced from 2-20 mJy, with 10 levels. Top: SED for knot J1 of 3C 353, where the green data points are flux densities taken from Kataoka et al. 2008. The IC/CMB model is ruled out by the two lowest energy *Fermi* limits.

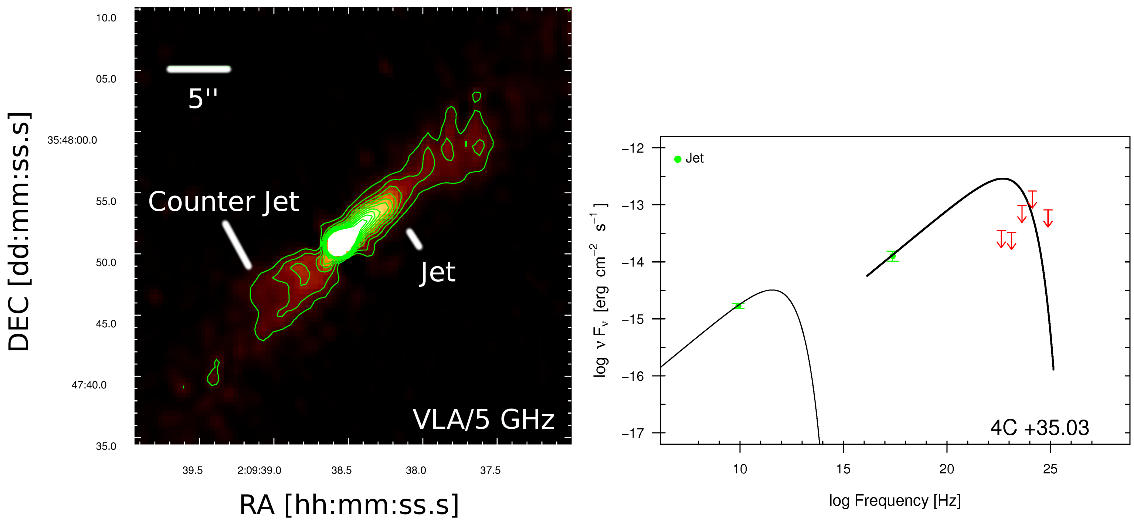

FIGURE A.18: Left: VLA 5 GHz image of 4C+35.03 with VLA 5 GHz contours (image obtained from *XJET* database at http://hea-www.harvard.edu/XJET/). The contours are spaced from 1-10 mJy, with 10 levels. Right: SED for the whole jet of 4C+35.03, where the green data points are flux densities taken from Worrall and Birkinshaw 2001. A radio spectral index of 0.7 was assumed as this value is typical for jets, and only one radio flux density was available. The IC/CMB model is ruled out by the three lowest energy *Fermi* limits.

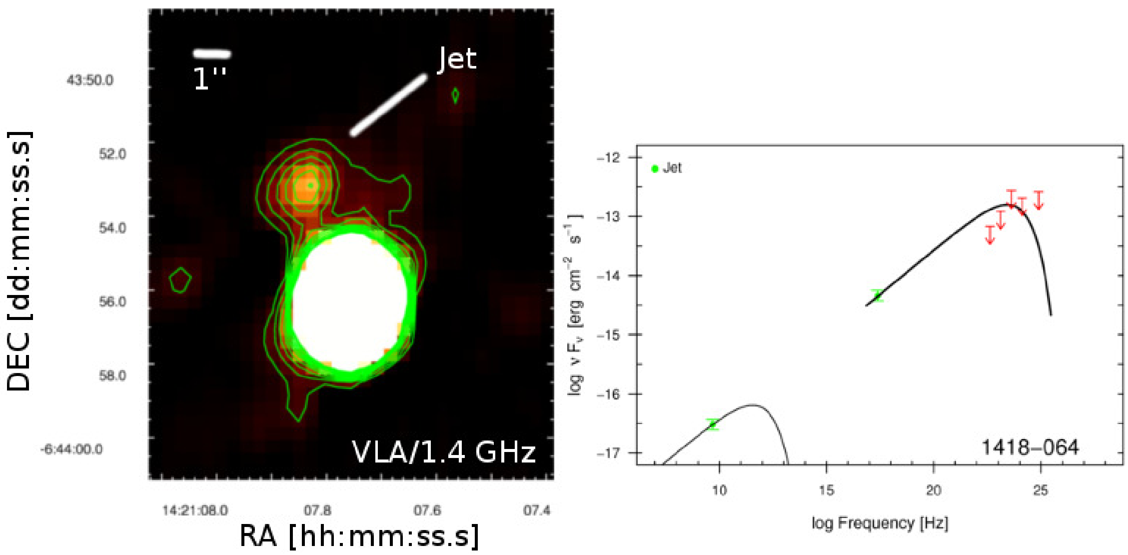

FIGURE A.19: Left: VLA 1.4 GHz image of 1418-064 with VLA 1.4 GHz contours (image obtained from VLA archive survey images page website at https://archive.nrao.edu/nvas/). The contours are spaced from 0.6-6 mJy, with 10 levels. Right: SED for the whole jet of 1418-064, where the green data points are flux densities taken from McKeough et al. 2016. The IC/CMB model is ruled out by the two lowest energy *Fermi* limits.

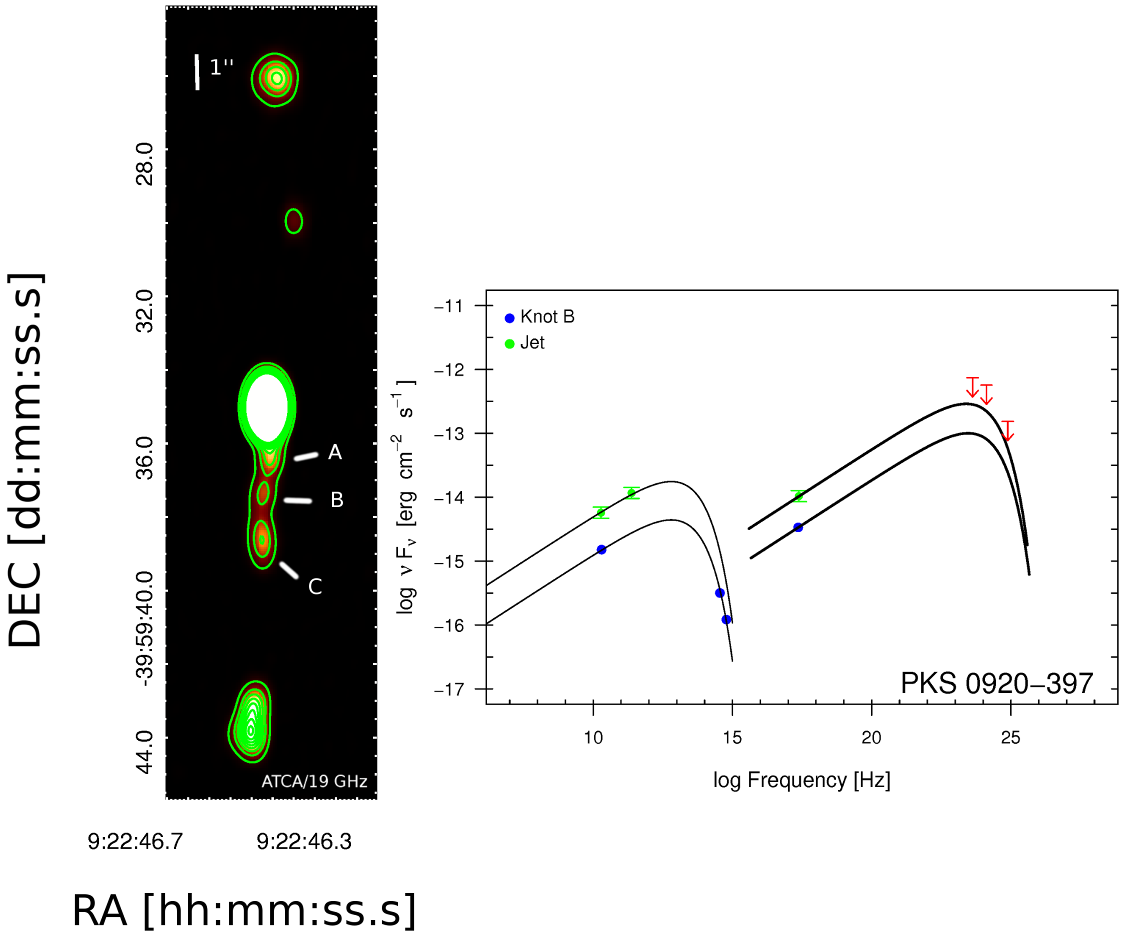

FIGURE A.20: Left: ATCA 19 GHz image of PKS 0920-397 with ATCA 19 GHz contours. The contours are spaced from 2-20 mJy, with 10 levels. Right: SED for the jet of PKS 0920-397. The green data are flux densities taken from Marshall et al. 2005 for the whole jet (except the ALMA Band 6 flux density at 238 GHz which came from this work). The blue data are flux densities taken from Schwartz et al. 2010 for knot B, where we assume the same spectral shape as the whole jet, as the radio-to-optical synchrotron spectrum was largely unconstrained. The IC/CMB model is not ruled out for this source.

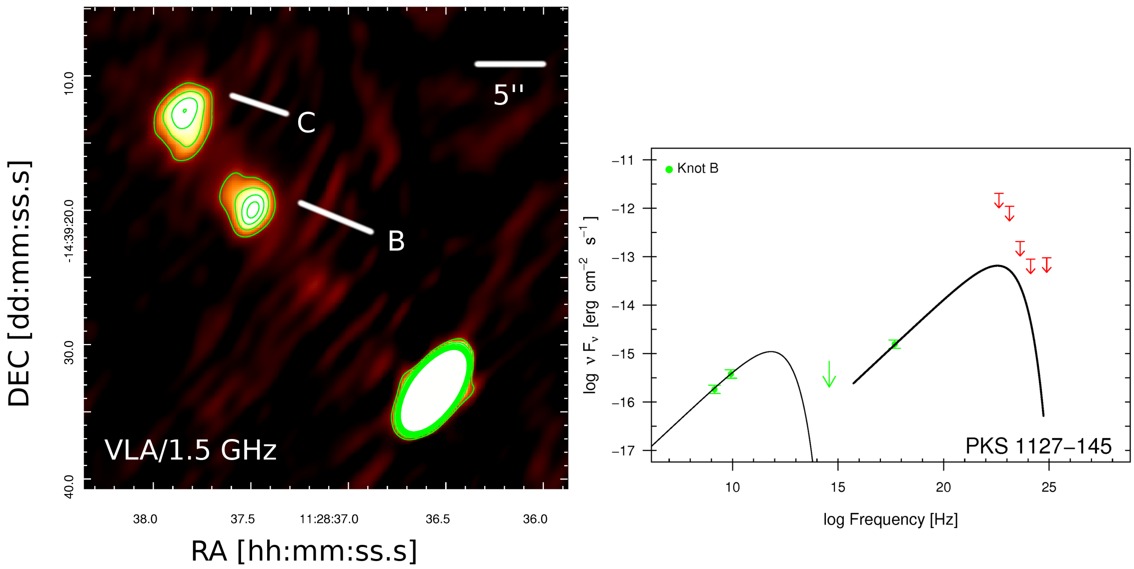

FIGURE A.21: Left: VLA 1.5 GHz image of PKS 1127-145 with VLA 1.5 GHz contours. The contours are spaced from 4-40 mJy, with 10 levels. Right: SED for the jet of PKS 1127-145. The green data are flux densities taken from Siemiginowska et al. 2002 for knot B (and the green arrow is an optical upper limit taken from the same work). The IC/CMB model is not ruled out for this source.

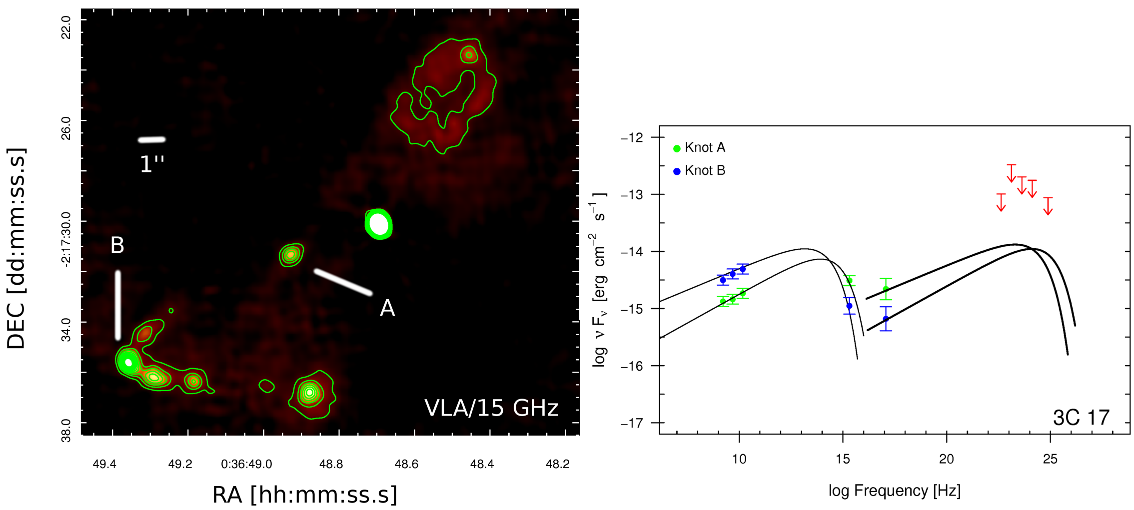

FIGURE A.22: Left: VLA 15 GHz image of 3C 17 with VLA 15 GHz contours. The contours are spaced from 4-40 mJy, with 10 levels. Right: SED for knots A (green) and B (blue) of 3C 17, where the data points are flux densities taken from Massaro et al. 2009. The IC/CMB model is not ruled out for this source.

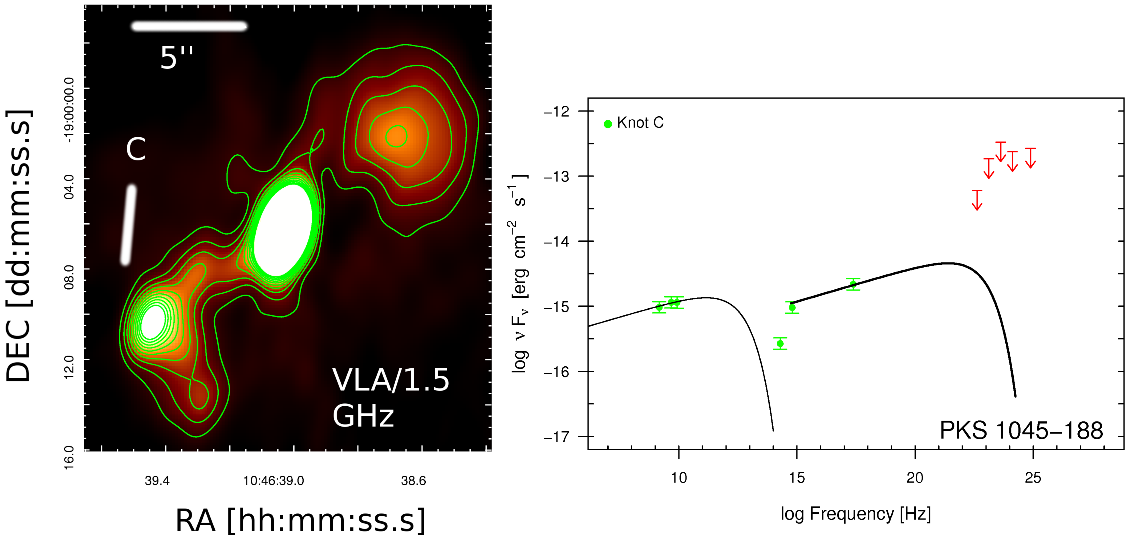

FIGURE A.23: Left: VLA 1.5 GHz image of PKS 1045-188 with VLA 1.5 GHz contours. The contours are spaced from 5-50 mJy, with 10 levels. Right: SED for knot C of PKS 1045-188, where the green data points are flux densities taken from Stanley et al. 2015. The IC/CMB model is not ruled out for this source.

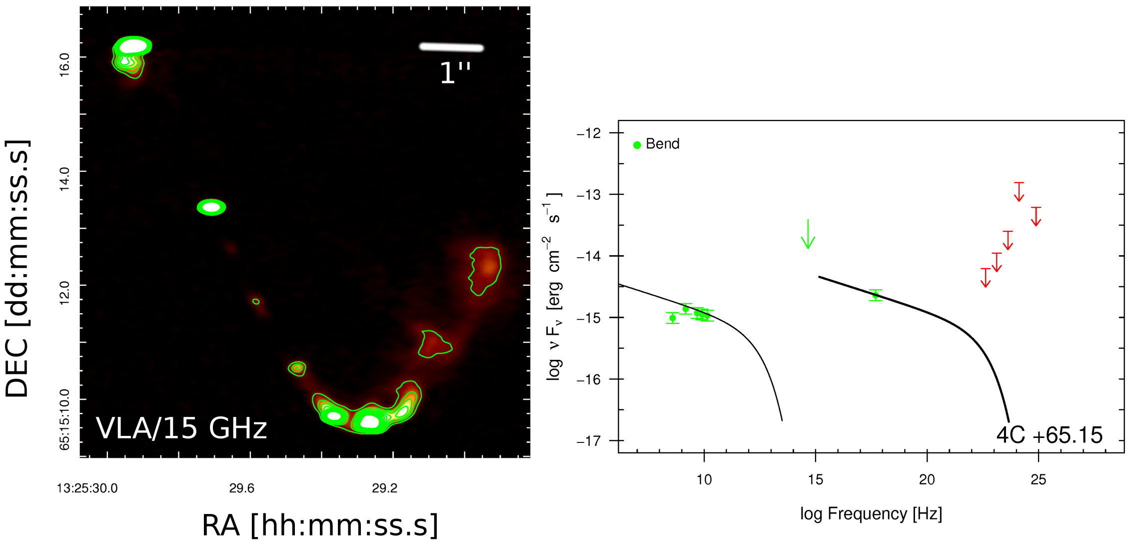

FIGURE A.24: Left: VLA 15 GHz image of 4C +65.15 with VLA 15 GHz contours. The contours are spaced from 0.1-1 mJy, with 10 levels. Right: SED for the jet bend, where the green data points are flux densities taken from Miller and Brandt 2009 (and the green arrow is an optical upper limit taken from the same work). The radio spectrum is fit with an index omitting the lowest frequency radio point, as done in Miller and Brandt 2009. The IC/CMB model is not ruled out for this source.

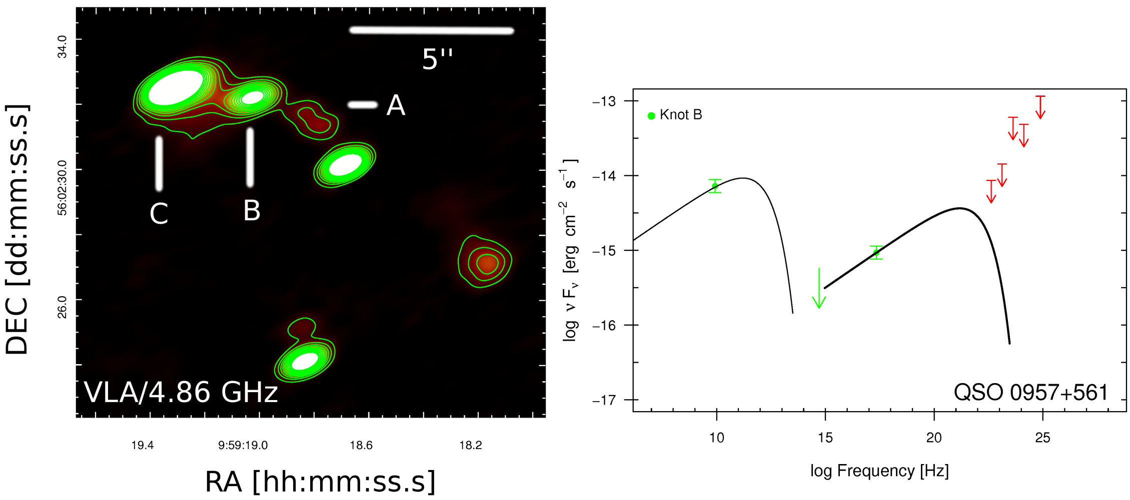

FIGURE A.25: Left: VLA 4.86 GHz image of QSO 0957+561 with VLA 4.86 GHz contours. The contours are spaced from 1-10 mJy, with 10 levels. Right: SED for knot B, where the green data points are flux densities taken from Chartas et al. 2002 (and the green arrow is an optical upper limit taken from the same work). The radio spectrum was fit with a spectral index of 0.7 as this value is typical for jets, and only one radio flux density was available. The IC/CMB model is not ruled out for this source.

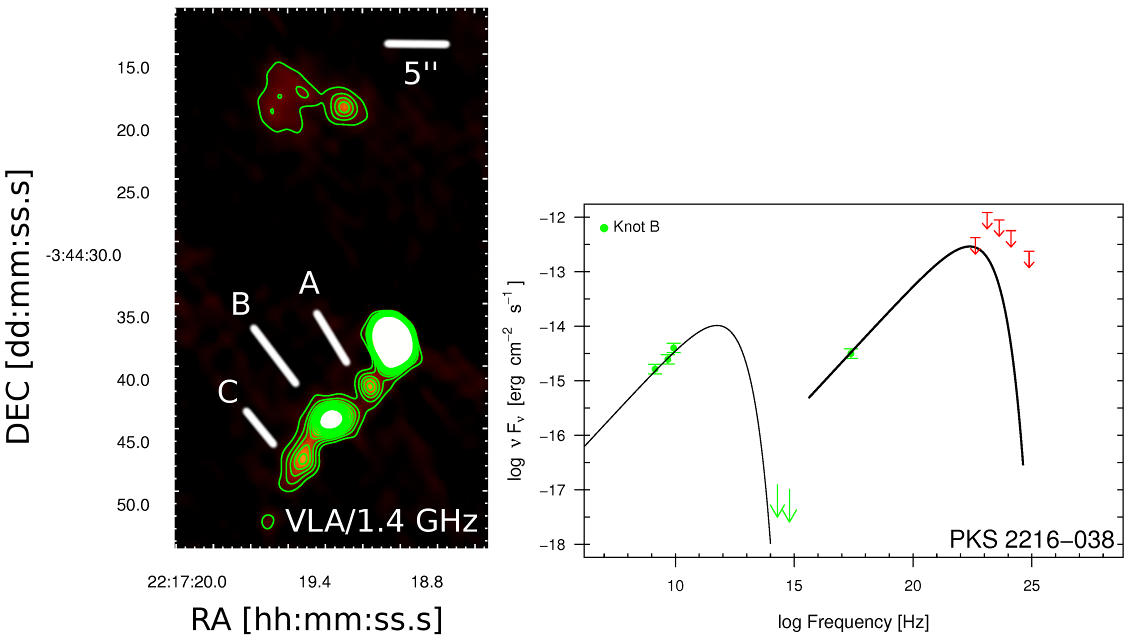

FIGURE A.26: Left: VLA 1.4 GHz image of PKS 2216-038 with VLA 1.4 GHz contours. The contours are spaced from 3-30 mJy, with 10 levels. Right: SED for knot B, where the green data points are flux densities taken from Stanley et al. 2015 (and the green arrows are optical upper limits taken from the same work). The IC/CMB model is not ruled out for this source.

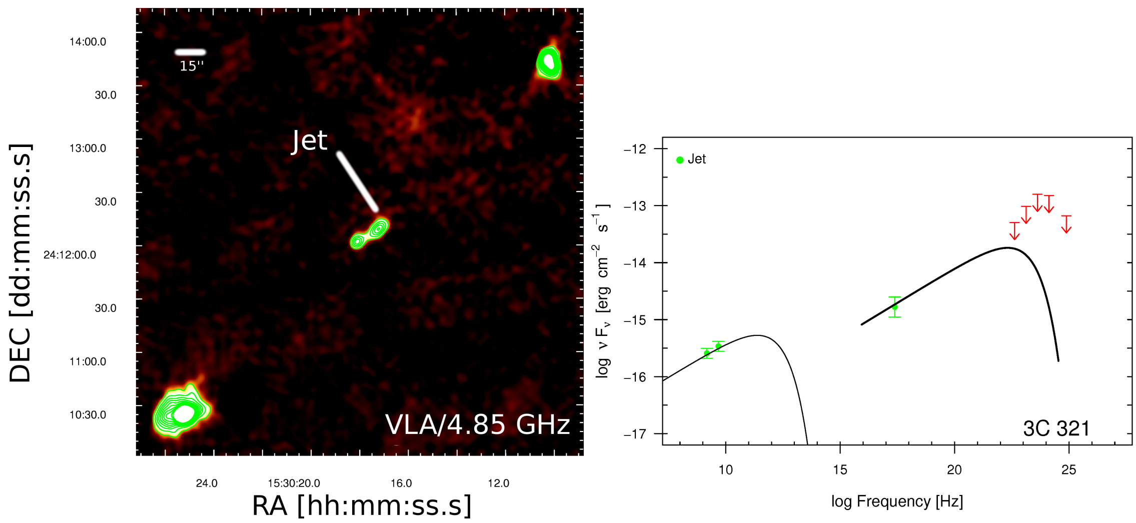

FIGURE A.27: Left: VLA 4.85 GHz image of 3C 321 with VLA 4.85 GHz contours. The contours are spaced from 6-60 mJy, with 10 levels. Right: SED for the whole jet, where the green data points are flux densities taken from Evans et al. 2008. The IC/CMB model is not ruled out for this source.

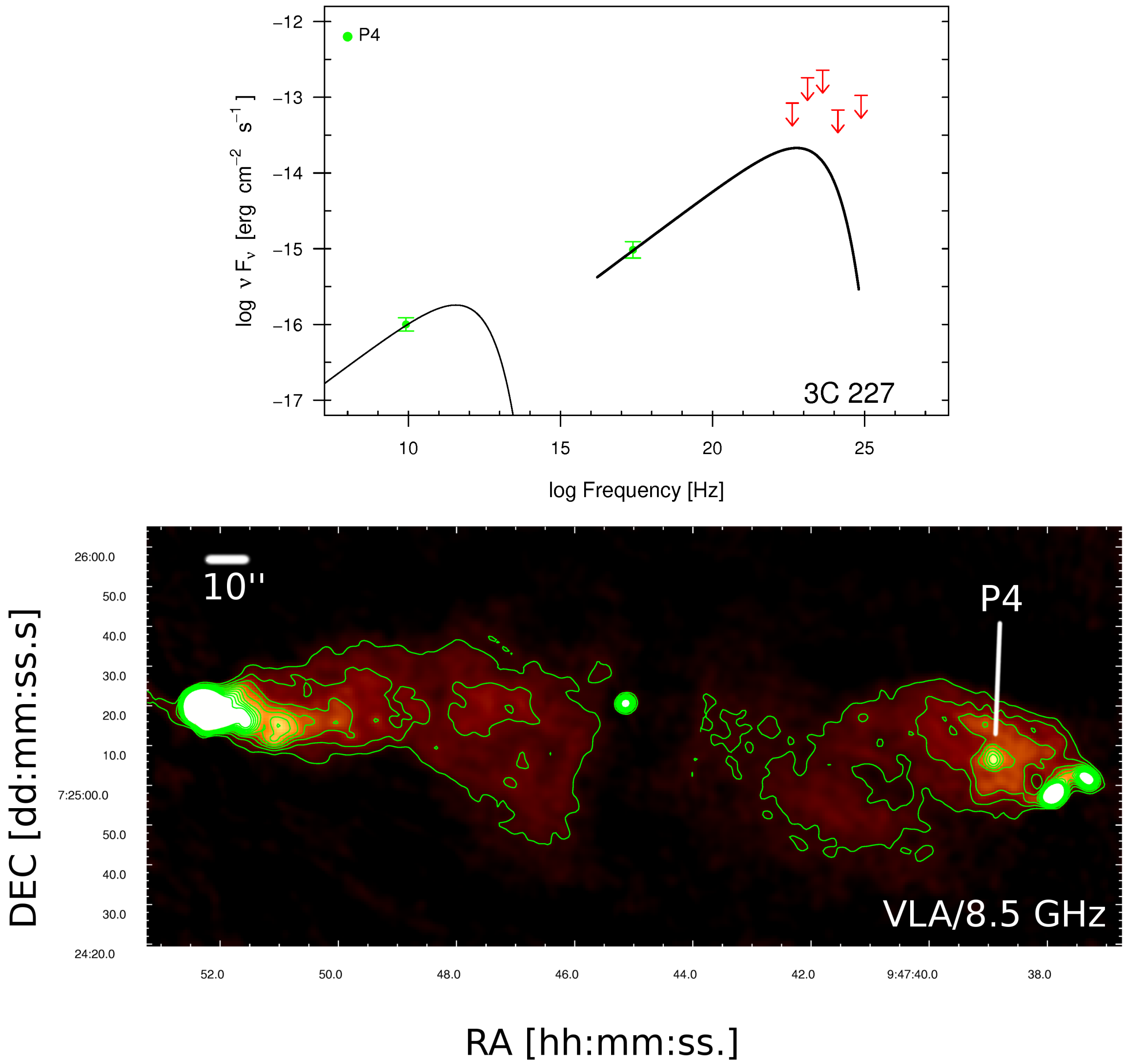

FIGURE A.28: Left: VLA 8.5 GHz image of 3C 227 with VLA 8.5 GHz contours (image obtained from *XJET* database at http://hea-www.harvard.edu/XJET/). The contours are spaced from 0.7-7 mJy, with 10 levels. Right: SED for knot P4, where the green data points are flux densities taken from Hardcastle, Croston, and Kraft 2007. A radio spectral index of 0.7 was assumed as this value is typical for jets, and only one radio flux density was available. The IC/CMB model is not ruled out for this source.

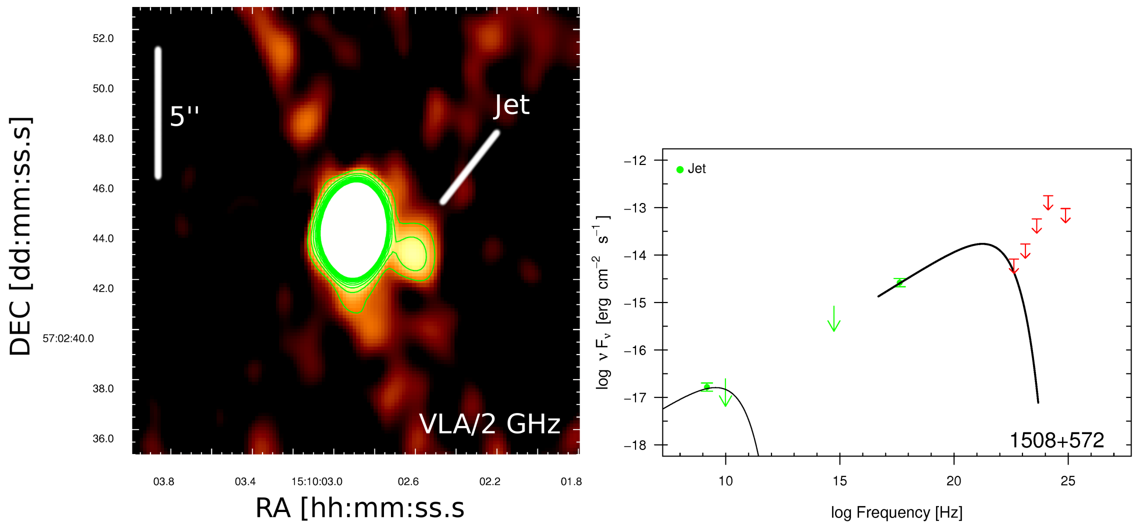

FIGURE A.29: Left: VLA 2 GHz image of 1508+572 with VLA 2 GHz contours (image obtained from the *XJET*database at http://hea-www.harvard.edu/XJET/). The contours are spaced from 0.3-3 mJy, with 10 levels. Right: SED for the whole jet, where the green data points are flux densities taken from Cheung 2004 (and the green arrow is an upper limit taken from the same work). A radio spectral index of 0.7 was assumed as this value is typical for jets, and only one radio flux density was available. The IC/CMB model is not ruled out for this source.

Bibliography

Abdo, A. A. et al. (2010). "Gamma-ray Light Curves and Variability of Bright Fermi-detected Blazars". In: *ApJ* 722, pp. 520–542. DOI: 10.1088/0004-637X/722/1/520. arXiv: 1004.0348 [astro-ph.HE].

Ackermann, M. et al. (2014). "Multifrequency Studies of the Peculiar Quasar 4C +21.35 during the 2010 Flaring Activity". In: *ApJ* 786, 157, p. 157. DOI: 10.1088/0004-637X/786/2/157. arXiv: 1403.7534 [astro-ph.HE].

Adams, T. F. (1977). "A Survey of the Seyfert Galaxies Based on Large-Scale Image-Tube Plates". In: *ApJS* 33, p. 19. DOI: 10.1086/190416.

Agudo, I. et al. (2011). "Location of γ-ray Flare Emission in the Jet of the BL Lacertae Object OJ287 More than 14 pc from the Central Engine". In: *ApJL* 726, L13, p. L13. DOI: 10.1088/2041-8205/726/1/L13. arXiv: 1011.6454.

Aharonian, F. et al. (2007). "An Exceptional Very High Energy Gamma-Ray Flare of PKS 2155-304". In: *ApJL* 664, pp. L71–L74. DOI: 10.1086/520635. arXiv: 0706.0797.

Aharonian, F. A. (2000). "TeV gamma rays from BL Lac objects due to synchrotron radiation of extremely high energy protons". In: *NA* 5, pp. 377–395. DOI: 10.1016/S1384-1076(00)00039-7. eprint: astro-ph/0003159.

— (2002). "Proton-synchrotron radiation of large-scale jets in active galactic nuclei". In: *MNRAS* 332, pp. 215–230. DOI: 10.1046/j.1365-8711.2002.05292.x. eprint: astro-ph/0106037.

Angel, J. R. P. and H. S. Stockman (1980). "Optical and infrared polarization of active extragalactic objects". In: *ARAA* 18, pp. 321–361. DOI: 10.1146/annurev.aa.18.090180.001541.

Ansoldi, S. et al. (2018). "The blazar TXS 0506+056 associated with a high-energy neutrino: insights into extragalactic jets and cosmic ray acceleration". In: *ArXiv e-prints*. arXiv: 1807.04300 [astro-ph.HE].

Antonucci, R. (1993). "Unified models for active galactic nuclei and quasars". In: *ARAA* 31, pp. 473–521. DOI: 10.1146/annurev.aa.31.090193.002353.

Antonucci, R. R. J. and J. S. Miller (1985). "Spectropolarimetry and the nature of NGC 1068". In: *ApJ* 297, pp. 621–632. DOI: 10.1086/163559.

Arshakian, T. G. and M. S. Longair (2004). "On the jet speeds of classical double radio sources". In: *MNRAS* 351, pp. 727–732. DOI: 10.1111/j.1365-2966.2004.07823.x. eprint: astro-ph/0310503.

Atoyan, A. and C. D. Dermer (2001). "High-Energy Neutrinos from Photomeson Processes in Blazars". In: *Physical Review Letters* 87.22, 221102, p. 221102. DOI: 10.1103/PhysRevLett.87.221102. eprint: astro-ph/0108053.

— (2004). "Synchrotron versus Compton Interpretations for Extended X-Ray Jets". In: *ApJ* 613, pp. 151–158. DOI: 10.1086/422499. eprint: astro-ph/0402647.

Atwood, W. B. et al. (2009). "The Large Area Telescope on the Fermi Gamma-Ray Space Telescope Mission". In: *ApJ* 697, pp. 1071–1102. DOI: 10.1088/0004-637X/697/2/1071. arXiv: 0902.1089 [astro-ph.IM].

Baade, W. and R. Minkowski (1954). "Identification of the Radio Sources in Cassiopeia, Cygnus A, and Puppis A." In: *ApJ* 119, p. 206. DOI: 10.1086/145812.

Bahcall, J. N. et al. (1995). "Hubble Space Telescope and MERLIN Observations of the Jet in 3C 273". In: *ApJL* 452, p. L91. DOI: 10.1086/309717. eprint: astro-ph/9509028.

Bassett, L. C. et al. (2004). "Chandra Observations of Radio-Loud Quasars at $zGT4$: X-Rays from the Radio Beacons of the Early Universe". In: *AJ* 128, pp. 523–533. DOI: 10.1086/422019. eprint: astro-ph/0404543.

Begelman, M. C., R. D. Blandford, and M. J. Rees (1984). "Theory of extragalactic radio sources". In: *Reviews of Modern Physics* 56, pp. 255–351. DOI: 10.1103/RevModPhys.56.255.

Bentz, M. C. et al. (2009). "The Lick AGN Monitoring Project: Broad-line Region Radii and Black Hole Masses from Reverberation Mapping of Hβ". In: *ApJ* 705, pp. 199–217. DOI: 10.1088/0004-637X/705/1/199. arXiv: 0908.0003.

Bhattacharyya, W. and N. Gupta (2016). "Proton Synchrotron Radiation from Extended Jets of PKS 0637-752 and 3C 273". In: *ApJ* 817, 121, p. 121. DOI: 10.3847/0004-637X/817/2/121. arXiv: 1511.00258 [astro-ph.HE].

Bicknell, G. V. (1995). "Relativistic Jets and the Fanaroff-Riley Classification of Radio Galaxies". In: *ApJS* 101, p. 29. DOI: 10.1086/192232. eprint: astro-ph/9406064.

Biretta, J. A., W. B. Sparks, and F. Macchetto (1999). "Hubble Space Telescope Observations of Superluminal Motion in the M87 Jet". In: *ApJ* 520, pp. 621–626. DOI: 10.1086/307499.

Blandford, R. D. and D. G. Payne (1982). "Hydromagnetic flows from accretion discs and the production of radio jets". In: *MNRAS* 199, pp. 883–903. DOI: 10.1093/mnras/199.4.883.

Blandford, R. D. and M. J. Rees (1978). "Some comments on radiation mechanisms in Lacertids". In: *BL Lac Objects*. Ed. by A. M. Wolfe, pp. 328–341.

Blandford, R. D. and R. L. Znajek (1977). "Electromagnetic extraction of energy from Kerr black holes". In: *MNRAS* 179, pp. 433–456. DOI: 10.1093/mnras/179.3.433.

Błażejowski, M. et al. (2000). "Comptonization of Infrared Radiation from Hot Dust by Relativistic Jets in Quasars". In: *ApJ* 545, pp. 107–116. DOI: 10.1086/317791. eprint: astro-ph/0008154.

Boettcher, M. (2010). "Models for the Spectral Energy Distributions and Variability of Blazars". In: *ArXiv e-prints*. arXiv: 1006.5048 [astro-ph.HE].

Bolton, J. G. and G. J. Stanley (1948). "Variable Source of Radio Frequency Radiation in the Constellation of Cygnus". In: *Nature* 161, pp. 312–313. DOI: 10.1038/161312b0.

Bolton, J. G., G. J. Stanley, and O. B. Slee (1949). "Positions of Three Discrete Sources of Galactic Radio-Frequency Radiation". In: *Nature* 164, pp. 101–102. DOI: 10.1038/164101b0.

Bonnoli, G. et al. (2011). "The γ-ray brightest days of the blazar 3C 454.3". In: *MNRAS* 410, pp. 368–380. DOI: 10.1111/j.1365-2966.2010.17450.x. arXiv: 1003.3476.

Böttcher, M. et al. (2013). "Leptonic and Hadronic Modeling of Fermi-detected Blazars". In: *ApJ* 768, 54, p. 54. DOI: 10.1088/0004-637X/768/1/54. arXiv: 1304.0605 [astro-ph.HE].

Breiding, P., M. Georganopoulos, and E. T. Meyer (2018). "Blazar Sheath Illumination of the Outer Molecular Torus: A Resolution of the Seed Photon Problem for the Far-GeV Blazar Flares". In: *ApJ* 853, 19, p. 19. DOI: 10.3847/1538-4357/aaa1ee. arXiv: 1712.07498.

Breiding, P. et al. (2017). "Fermi Non-detections of Four X-Ray Jet Sources and Implications for the IC/CMB Mechanism". In: *ApJ* 849, 95, p. 95. DOI: 10.3847/1538-4357/aa907a. arXiv: 1710.04250.

Bridle, A. H. et al. (1994). "Deep VLA imaging of twelve extended 3CR quasars". In: *AJ* 108, pp. 766–820. DOI: 10.1086/117112.

Burbidge, G. R. (1959). "Estimates of the Total Energy in Particles and Magnetic Field in the Non-Thermal Radio Sources." In: *ApJ* 129, pp. 849–852. DOI: 10.1086/146680.

Cara, M. et al. (2013). "Polarimetry and the High-energy Emission Mechanisms in Quasar Jets: The Case of PKS 1136-135". In: *ApJ* 773, 186, p. 186. DOI: 10.1088/0004-637X/773/2/186. arXiv: 1305.2535.

Cavagnolo, K. W. et al. (2010). "A Relationship Between AGN Jet Power and Radio Power". In: *ApJ* 720, pp. 1066–1072. DOI: 10.1088/0004-637X/720/2/1066. arXiv: 1006.5699.

Celotti, A., G. Ghisellini, and M. Chiaberge (2001). "Large-scale jets in active galactic nuclei: multi-wavelength mapping". In: *MNRAS* 321, pp. L1–L5. DOI: 10.1046/j.1365-8711.2001.04160.x. eprint: astro-ph/0008021.

Chang, J. S. and G. Cooper (1970). "A Practical Difference Scheme for Fokker-Planck Equations". In: *Journal of Computational Physics* 6, pp. 1–16. DOI: 10.1016/0021-9991(70)90001-X.

Chartas, G. et al. (2000). "The Chandra X-Ray Observatory Resolves the X-Ray Morphology and Spectra of a Jet in PKS 0637-752". In: *ApJ* 542, pp. 655–666. DOI: 10.1086/317049. eprint: astro-ph/0005227.

Chartas, G. et al. (2002). "Constraining H_0 from Chandra Observations of Q0957+561". In: *ApJ* 565, pp. 96–104. DOI: 10.1086/324485. eprint: astro-ph/0108277.

Chen, Y. Y. et al. (2015). "Core-dominance parameter, black hole mass and jet-disc connection for Fermi blazars". In: *MNRAS* 451, pp. 4193–4206. DOI: 10.1093/mnras/stv658. arXiv: 1503.08425 [astro-ph.HE].

Cheung, C. C. (2004). "Radio Identification of the X-Ray Jet in the z=4.3 Quasar GB 1508+5714". In: *ApJL* 600, pp. L23–L26. DOI: 10.1086/381366. eprint: astro-ph/0310733.

Cheung, C. C., Ł. Stawarz, and A. Siemiginowska (2006). "Confronting X-Ray Emission Models with the Highest Redshift Kiloparsec-Scale Jets: The z=3.89 Jet in Quasar 1745+624". In: *ApJ* 650, pp. 679–692. DOI: 10.1086/506908. eprint: astro-ph/0606255.

Cheung, C. C. et al. (2012). "Discovery of a Kiloparsec-scale X-Ray/Radio Jet in the z = 4.72 Quasar GB 1428+4217". In: *ApJL* 756, L20, p. L20. DOI: 10.1088/2041-8205/756/1/L20. arXiv: 1208.0584 [astro-ph.HE].

Chiaberge, M. and A. Marconi (2011). "On the origin of radio loudness in active galactic nuclei and its relationship with the properties of the central supermassive black hole". In: *MNRAS* 416, pp. 917–926. DOI: 10.1111/j.1365-2966.2011.19079.x. arXiv: 1105.4889.

Chiaberge, M. et al. (2015). "Radio Loud AGNs are Mergers". In: *ApJ* 806, 147, p. 147. DOI: 10.1088/0004-637X/806/2/147. arXiv: 1505.07419.

Clarke, D. A., M. L. Norman, and J. O. Burns (1986). "Numerical simulations of a magnetically confined jet". In: *ApJL* 311, pp. L63–L67. DOI: 10.1086/184799.

Clautice, D. et al. (2016). “The Spectacular Radio-near-IR-X-Ray Jet of 3C 111: The X-Ray Emission Mechanism and Jet Kinematics”. In: *ApJ* 826, 109, p. 109. DOI: 10.3847/0004-637X/826/2/109. arXiv: 1602.04794.

Cohen, M. H. et al. (1971). “The Small-Scale Structure of Radio Galaxies and Quasi-Stellar Sources at 3.8 Centimeters”. In: *ApJ* 170, p. 207. DOI: 10.1086/151204.

Costamante, L. et al. (2001). “Extreme synchrotron BL Lac objects. Stretching the blazar sequence”. In: *AAP* 371, pp. 512–526. DOI: 10.1051/0004-6361:20010412. eprint: astro-ph/0103343.

Curtis, H. D. (1918). “Descriptions of 762 Nebulae and Clusters Photographed with the Crossley Reflector”. In: *Publications of Lick Observatory* 13, pp. 9–42.

Dabhade, P. et al. (2017). “Discovery of giant radio galaxies from NVSS: radio and infrared properties”. In: *MNRAS* 469, pp. 2886–2906. DOI: 10.1093/mnras/stx860. arXiv: 1704.00516.

D’Arcangelo, F. D. et al. (2007). “Rapid Multiwaveband Polarization Variability in the Quasar PKS 0420-014: Optical Emission from the Compact Radio Jet”. In: *ApJL* 659, pp. L107–L110. DOI: 10.1086/517525. eprint: astro-ph/0703118.

Dermer, C. D. (1995). “On the Beaming Statistics of Gamma-Ray Sources”. In: *ApJL* 446, p. L63. DOI: 10.1086/187931.

Dermer, C. D. and A. Atoyan (2004). “Nonthermal Radiation Processes in X-Ray Jets”. In: *ApJL* 611, pp. L9–L12. DOI: 10.1086/423667. eprint: astro-ph/0404139.

Dermer, C. D. and R. Schlickeiser (1994). “On the location of the acceleration and emission sites in gamma-ray blazars”. In: *ApJS* 90, pp. 945–948. DOI: 10.1086/191929.

Dermer, C. D., R. Schlickeiser, and A. Mastichiadis (1992). “High-energy gamma radiation from extragalactic radio sources”. In: *AAP* 256, pp. L27–L30.

Edwards, P. G. et al. (2006). “The Parsec-Scale Jet of PKS 0637-752”. In: *PASJ* 58, pp. 233–241. DOI: 10.1093/pasj/58.2.233.

Elitzur, M. (2012). “On the Unification of Active Galactic Nuclei”. In: *ApJL* 747, L33, p. L33. DOI: 10.1088/2041-8205/747/2/L33. arXiv: 1202.1776.

Evans, D. A. et al. (2008). “A Radio through X-Ray Study of the Jet/Companion-Galaxy Interaction in 3C 321”. In: *ApJ* 675, pp. 1057–1066. DOI: 10.1086/527410. arXiv: 0712.2669.

Fanaroff, B. L. and J. M. Riley (1974). “The morphology of extragalactic radio sources of high and low luminosity”. In: *MNRAS* 167, 31P–36P. DOI: 10.1093/mnras/167.1.31P.

Fath, E. A. (1909). “The Spectra of Some Spiral Nebulae and Globular Star Clusters”. In: *Popular Astronomy* 17, pp. 504–508.

Feigelson, E. D. et al. (1981). "The X-ray structure of Centaurus A". In: *ApJ* 251, pp. 31–51. DOI: 10.1086/159439.

Fossati, G. et al. (1998). "A unifying view of the spectral energy distributions of blazars". In: *MNRAS* 299, pp. 433–448. DOI: 10.1046/j.1365-8711.1998.01828.x. eprint: astro-ph/9804103.

Frank, J., A. King, and D. J. Raine (2002). *Accretion Power in Astrophysics: Third Edition*, p. 398.

Friedman, H. and E. T. Byram (1967). "X-rays from Sources 3C 273 and M 87". In: *Science* 158, pp. 257–259. DOI: 10.1126/science.158.3798.257.

Fuller, L. et al. (2016). "Investigating the dusty torus of Seyfert galaxies using SOFIA/FORCAST photometry". In: *MNRAS* 462, pp. 2618–2630. DOI: 10.1093/mnras/stw1780. arXiv: 1607.07918.

Gallimore, J. F. et al. (2016). "High-velocity Bipolar Molecular Emission from an AGN Torus". In: *ApJL* 829, L7, p. L7. DOI: 10.3847/2041-8205/829/1/L7. arXiv: 1608.02210.

García-Burillo, S. et al. (2016). "ALMA Resolves the Torus of NGC 1068: Continuum and Molecular Line Emission". In: *ApJL* 823, L12, p. L12. DOI: 10.3847/2041-8205/823/1/L12. arXiv: 1604.00205.

García-González, J. et al. (2017). "A mid-infrared statistical investigation of clumpy torus model predictions". In: *MNRAS* 470, pp. 2578–2598. DOI: 10.1093/mnras/stx1361. arXiv: 1706.07425.

Garmire, G. P. et al. (2003). "Advanced CCD imaging spectrometer (ACIS) instrument on the Chandra X-ray Observatory". In: *X-Ray and Gamma-Ray Telescopes and Instruments for Astronomy.* Ed. by J. E. Truemper and H. D. Tananbaum. Vol. 4851. PROCSPIE, pp. 28–44. DOI: 10.1117/12.461599.

Gaskell, C. M. (2009). "What broad emission lines tell us about how active galactic nuclei work". In: *NAR* 53, pp. 140–148. DOI: 10.1016/j.newar.2009.09.006. arXiv: 0908.0386.

Genzel, R., F. Eisenhauer, and S. Gillessen (2010). "The Galactic Center massive black hole and nuclear star cluster". In: *Reviews of Modern Physics* 82, pp. 3121–3195. DOI: 10.1103/RevModPhys.82.3121. arXiv: 1006.0064.

Georganopoulos, M., J. G. Kirk, and A. Mastichiadis (2001). "The Beaming Pattern and Spectrum of Radiation from Inverse Compton Scattering in Blazars". In: *ApJ* 561, pp. 111–117. DOI: 10.1086/323225. eprint: astro-ph/0107152.

Georganopoulos, M. et al. (2006). "Quasar X-Ray Jets: Gamma-Ray Diagnostics of the Synchrotron and Inverse Compton Hypotheses: The Case of 3C 273". In: *ApJL* 653, pp. L5–L8. DOI: 10.1086/510452. eprint: astro-ph/0610847.

Ghisellini, G. (2000). "Special Relativity at Action in the Universe". In: *Recent Developments in General Relativity*. Ed. by B. Casciaro et al., p. 5. eprint: astro-ph/9905181.

Ghisellini, G. and P. Madau (1996). "On the origin of the gamma-ray emission in blazars". In: *MNRAS* 280, pp. 67–76. DOI: 10.1093/mnras/280.1.67.

Ghisellini, G., F. Tavecchio, and M. Chiaberge (2005). "Structured jets in TeV BL Lac objects and radiogalaxies. Implications for the observed properties". In: *AAP* 432, pp. 401–410. DOI: 10.1051/0004-6361:20041404. eprint: astro-ph/0406093.

Ghisellini, G. et al. (1998). "A theoretical unifying scheme for gamma-ray bright blazars". In: *MNRAS* 301, pp. 451–468. DOI: 10.1046/j.1365-8711.1998.02032.x. eprint: astro-ph/9807317.

Godfrey, L. E. H. et al. (2012). "Periodic Structure in the Megaparsec-scale Jet of PKS 0637-752". In: *ApJL* 758, L27, p. L27. DOI: 10.1088/2041-8205/758/2/L27. arXiv: 1209.4637.

Goodger, J. L. et al. (2010). "Long-Term Monitoring of the Dynamics and Particle Acceleration of Knots in the Jet of Centaurus A". In: *ApJ* 708, pp. 675–697. DOI: 10.1088/0004-637X/708/1/675. arXiv: 0911.2115.

Graff, P. B. et al. (2008). "A Multizone Model for Simulating the High-Energy Variability of TeV Blazars". In: *ApJ* 689, pp. 68–78. DOI: 10.1086/592427. arXiv: 0808.2135.

Greenstein, J. L. and M. Schmidt (1964a). "The Quasi-Stellar Radio Sources 3C 48 and 3C 273." In: *ApJ* 140, p. 1. DOI: 10.1086/147889.

— (1964b). "The Quasi-Stellar Radio Sources 3C 48 and 3C 273." In: *ApJ* 140, p. 1. DOI: 10.1086/147889.

Gursky, H. et al. (1971). "Detection of X-Rays from the Seyfert Galaxies NGC 1275 and NGC 4151 by the UHURU Satellite". In: *ApJL* 165, p. L43. DOI: 10.1086/180713.

Hada, K. et al. (2011). "An origin of the radio jet in M87 at the location of the central black hole". In: *Nature* 477, pp. 185–187. DOI: 10.1038/nature10387.

Hardcastle, M. J. (2006). "Testing the beamed inverse-Compton model for jet X-ray emission: velocity structure and deceleration". In: *MNRAS* 366, pp. 1465–1474. DOI: 10.1111/j.1365-2966.2005.09923.x. eprint: astro-ph/0511511.

Hardcastle, M. J., M. Birkinshaw, and D. M. Worrall (2001). "Chandra observations of the X-ray jet in 3C 66B". In: *MNRAS* 326, pp. 1499–1507. DOI: 10.1111/j.1365-2966.2001.04699.x. eprint: astro-ph/0106029.

Hardcastle, M. J., J. H. Croston, and R. P. Kraft (2007). "A Chandra Study of Particle Acceleration in the Multiple Hot Spots of Nearby Radio Galaxies". In: *ApJ* 669, pp. 893–904. DOI: 10.1086/521696. arXiv: 0707.2865.

Hardcastle, M. J., I. Sakelliou, and D. M. Worrall (2005). "A Chandra and XMM-Newton study of the wide-angle tail radio galaxy 3C465". In: *MNRAS* 359, pp. 1007–1021. DOI: 10.1111/j.1365-2966.2005.08966.x. eprint: astro-ph/0502575.

Hardcastle, M. J. et al. (2002). "A Chandra observation of the X-ray environment and jet of 3C 31". In: *MNRAS* 334, pp. 182–192. DOI: 10.1046/j.1365-8711.2002.05513.x. eprint: astro-ph/0203374.

Hardcastle, M. J. et al. (2016). "Deep Chandra observations of Pictor A". In: *MNRAS* 455, pp. 3526–3545. DOI: 10.1093/mnras/stv2553. arXiv: 1510.08392 [astro-ph.HE].

Harris, D. E. and H. Krawczynski (2006). "X-Ray Emission from Extragalactic Jets". In: *ARAA* 44, pp. 463–506. DOI: 10.1146/annurev.astro.44.051905.092446. eprint: astro-ph/0607228.

— (2007). "Constraints on the Nature of Jets from KPC Scale X-Ray Data". In: *Revista Mexicana de Astronomia y Astrofisica, vol. 27*. Vol. 27. Revista Mexicana de Astronomia y Astrofisica, vol. 27, p. 188. eprint: astro-ph/0604527.

Harris, D. E., A. E. Mossman, and R. C. Walker (2004). "The X-Ray Jet of 3C 120: Evidence for a Nonstandard Synchrotron Spectrum". In: *ApJ* 615, pp. 161–172. DOI: 10.1086/424442. eprint: astro-ph/0407354.

Harris, D. E. et al. (2017). "A Multi-band Study of the Remarkable Jet in Quasar 4C+19.44". In: *ApJ* 846, 119, p. 119. DOI: 10.3847/1538-4357/aa845c. arXiv: 1708.01500 [astro-ph.HE].

Hoenig, S. F. (2013). "On donuts and crumbs: A brief history of torus models". In: *ArXiv e-prints*. arXiv: 1301.1349 [astro-ph.CO].

Hönig, S. F. and M. Kishimoto (2017). "Dusty Winds in Active Galactic Nuclei: Reconciling Observations with Models". In: *ApJL* 838, L20, p. L20. DOI: 10.3847/2041-8213/aa6838. arXiv: 1703.07781.

Hönig, S. F. et al. (2012). "Parsec-scale Dust Emission from the Polar Region in the Type 2 Nucleus of NGC 424". In: *ApJ* 755, 149, p. 149. DOI: 10.1088/0004-637X/755/2/149. arXiv: 1206.4307.

Hubble, E. P. (1929). “A spiral nebula as a stellar system, Messier 31.” In: *ApJ* 69. DOI: 10.1086/143167.

IceCube Collaboration et al. (2018). “Neutrino emission from the direction of the blazar TXS 0506+056 prior to the IceCube-170922A alert”. In: *Science* 361, pp. 147–151. DOI: 10.1126/science.aat2890. arXiv: 1807.08794 [astro-ph.HE].

Isler, J. C. et al. (2013). “A Time-resolved Study of the Broad-line Region in Blazar 3C 454.3”. In: *ApJ* 779, 100, p. 100. DOI: 10.1088/0004-637X/779/2/100. arXiv: 1310.0817.

Jester, S. et al. (2006). “New Chandra Observations of the Jet in 3C 273. I. Softer X-Ray than Radio Spectra and the X-Ray Emission Mechanism”. In: *ApJ* 648, pp. 900–909. DOI: 10.1086/505962. eprint: astro-ph/0605529.

Jester, S. et al. (2007). “Hubble Space Telescope far-ultraviolet imaging of the jet in 3C273: a common emission component from optical to X-rays”. In: *MNRAS* 380, pp. 828–834. DOI: 10.1111/j.1365-2966.2007.12120.x. arXiv: 0706.2564.

Jorstad, S. G. and A. P. Marscher (2004). “The Highly Relativistic Kiloparsec-Scale Jet of the Gamma-Ray Quasar 0827+243”. In: *ApJ* 614, pp. 615–625. DOI: 10.1086/423800. eprint: astro-ph/0405424.

— (2006). “The X-ray and radio jets of quasars on kiloparsec scales”. In: *Astronomische Nachrichten* 327, pp. 227–230. DOI: 10.1002/asna.200510512.

Jorstad, S. G. et al. (2001). “Multiepoch Very Long Baseline Array Observations of EGRET-detected Quasars and BL Lacertae Objects: Superluminal Motion of Gamma-Ray Bright Blazars”. In: *ApJS* 134, pp. 181–240. DOI: 10.1086/320858. eprint: astro-ph/0101570.

Jorstad, S. G. et al. (2017). “Kinematics of Parsec-scale Jets of Gamma-Ray Blazars at 43 GHz within the VLBA-BU-BLAZAR Program”. In: *ApJ* 846, 98, p. 98. DOI: 10.3847/1538-4357/aa8407. arXiv: 1711.03983.

Kadler, M. et al. (2016). “Coincidence of a high-fluence blazar outburst with a PeV-energy neutrino event”. In: *Nature Physics* 12, pp. 807–814. DOI: 10.1038/nphys3715. arXiv: 1602.02012 [astro-ph.HE].

Kaspi, S. et al. (2000). “Reverberation Measurements for 17 Quasars and the Size-Mass-Luminosity Relations in Active Galactic Nuclei”. In: *ApJ* 533, pp. 631–649. DOI: 10.1086/308704. eprint: astro-ph/9911476.

Kataoka, J. and Ł. Stawarz (2005a). "X-Ray Emission Properties of Large-Scale Jets, Hot Spots, and Lobes in Active Galactic Nuclei". In: *ApJ* 622, pp. 797–810. DOI: 10.1086/428083. eprint: astro-ph/0411042.

— (2005b). "X-Ray Emission Properties of Large-Scale Jets, Hot Spots, and Lobes in Active Galactic Nuclei". In: *ApJ* 622, pp. 797–810. DOI: 10.1086/428083. eprint: astro-ph/0411042.

— (2005c). "X-Ray Emission Properties of Large-Scale Jets, Hot Spots, and Lobes in Active Galactic Nuclei". In: *ApJ* 622, pp. 797–810. DOI: 10.1086/428083. eprint: astro-ph/0411042.

Kataoka, J. et al. (2001). "Characteristic X-Ray Variability of TeV Blazars: Probing the Link between the Jet and the Central Engine". In: *ApJ* 560, pp. 659–674. DOI: 10.1086/322442. eprint: astro-ph/0105022.

Kataoka, J. et al. (2008). "Chandra Reveals Twin X-Ray Jets in the Powerful FR II Radio Galaxy 3C 353". In: *ApJ* 685, pp. 839–857. DOI: 10.1086/591024. arXiv: 0806.1260.

Kellermann, K. I. et al. (1989). "VLA observations of objects in the Palomar Bright Quasar Survey". In: *AJ* 98, pp. 1195–1207. DOI: 10.1086/115207.

Kellermann, K. I. et al. (2004). "Sub-Milliarcsecond Imaging of Quasars and Active Galactic Nuclei. III. Kinematics of Parsec-scale Radio Jets". In: *ApJ* 609, pp. 539–563. DOI: 10.1086/421289. eprint: astro-ph/0403320.

Khachikian, E. Y. and D. W. Weedman (1974). "An atlas of Seyfert galaxies". In: *ApJ* 192, pp. 581–589. DOI: 10.1086/153093.

Kharb, P. et al. (2012). "Chandra and HST Imaging of the Quasars PKS B0106+013 and 3C 345: Inverse Compton X-Rays and Magnetized Jets". In: *ApJ* 748, 81, p. 81. DOI: 10.1088/0004-637X/748/2/81. arXiv: 1201.4178.

Khim, H. and S. K. Yi (2017). "On the Structure of the AGN Torus through the Fraction of Optically Selected Type 1 AGNs". In: *ApJ* 846, 155, p. 155. DOI: 10.3847/1538-4357/aa8774. arXiv: 1708.09110.

Kim, D. et al. (2015). "The AKARI 2.5-5.0 μm Spectral Atlas of Type-1 Active Galactic Nuclei: Black Hole Mass Estimator, Line Ratio, and Hot Dust Temperature". In: *ApJS* 216, 17, p. 17. DOI: 10.1088/0067-0049/216/1/17. arXiv: 1503.04925.

Kishimoto, M. et al. (2011). "The innermost dusty structure in active galactic nuclei as probed by the Keck interferometer". In: *AAP* 527, A121, A121. DOI: 10.1051/0004-6361/201016054. arXiv: 1012.5359.

Kormendy, J. and L. C. Ho (2013). "Coevolution (Or Not) of Supermassive Black Holes and Host Galaxies". In: *ARAA* 51, pp. 511–653. DOI: 10.1146/annurev-astro-082708-101811. arXiv: 1304.7762.

Koshida, S. et al. (2014). "Reverberation Measurements of the Inner Radius of the Dust Torus in 17 Seyfert Galaxies". In: *ApJ* 788, 159, p. 159. DOI: 10.1088/0004-637X/788/2/159. arXiv: 1406.2078.

Kozłowski, S. (2017). "Virial Black Hole Mass Estimates for 280,000 AGNs from the SDSS Broad-band Photometry and Single-epoch Spectra". In: *ApJS* 228, 9, p. 9. DOI: 10.3847/1538-4365/228/1/9. arXiv: 1609.09489.

Krolik, J. H. and M. C. Begelman (1986). "An X-ray heated wind in NGC 1068". In: *ApJL* 308, pp. L55–L58. DOI: 10.1086/184743.

— (1988). "Molecular tori in Seyfert galaxies - Feeding the monster and hiding it". In: *ApJ* 329, pp. 702–711. DOI: 10.1086/166414.

Kusunose, M. and F. Takahara (2017). "A Photohadronic Model of the Large-scale Jet of PKS 0637-752". In: *ApJ* 835, 20, p. 20. DOI: 10.3847/1538-4357/835/1/20. arXiv: 1611.08046 [astro-ph.HE].

Laing, R. A., J. R. Canvin, and A. H. Bridle (2003). "The physics of jets in FR I radio galaxies". In: *NAR* 47, pp. 577–579. DOI: 10.1016/S1387-6473(03)00097-6. eprint: astro-ph/0212486.

LaMassa, S. M. et al. (2015). "" In: *ApJ* 800, 144, p. 144. DOI: 10.1088/0004-637X/800/2/144. arXiv: 1412.2136.

Laor, A. and H. Netzer (1989). "Massive thin accretion discs. I - Calculated spectra". In: *MNRAS* 238, pp. 897–916. DOI: 10.1093/mnras/238.3.897.

León-Tavares, J. et al. (2013). "Flare-like Variability of the Mg II λ2800 Emission Line in the Γ-Ray Blazar 3C 454.3". In: *ApJL* 763, L36, p. L36. DOI: 10.1088/2041-8205/763/2/L36. arXiv: 1301.3064 [astro-ph.HE].

Lind, K. R. and R. D. Blandford (1985). "Semidynamical models of radio jets - Relativistic beaming and source counts". In: *ApJ* 295, pp. 358–367. DOI: 10.1086/163380.

Lister, M. L. et al. (2009). "MOJAVE: Monitoring of Jets in Active Galactic Nuclei with VLBA Experiments. VI. Kinematics Analysis of a Complete Sample of Blazar Jets". In: *AJ* 138, 1874-1892, pp. 1874–1892. DOI: 10.1088/0004-6256/138/6/1874. arXiv: 0909.5100 [astro-ph.CO].

Lister, M. L. et al. (2013). "MOJAVE. X. Parsec-scale Jet Orientation Variations and Superluminal Motion in Active Galactic Nuclei". In: *AJ* 146, 120, p. 120. DOI: 10.1088/0004-6256/146/5/120. arXiv: 1308.2713 [astro-ph.CO].

— (2016). "MOJAVE: XIII. Parsec-scale AGN Jet Kinematics Analysis Based on 19 years of VLBA Observations at 15 GHz". In: *AJ* 152, 12, p. 12. DOI: 10.3847/0004-6256/152/1/12. arXiv: 1603.03882.

Liu, Y., D. R. Jiang, and M. F. Gu (2006). "The Jet Power, Radio Loudness, and Black Hole Mass in Radio-loud Active Galactic Nuclei". In: *ApJ* 637, pp. 669–681. DOI: 10.1086/498639. eprint: astro-ph/0510241.

Lobanov, A. P. (1998). "Ultracompact jets in active galactic nuclei". In: *AAP* 330, pp. 79–89. eprint: astro-ph/9712132.

Lopez, L. A. et al. (2006). "A Chandra Snapshot Survey of Representative High-Redshift Radio-Loud Quasars from the Parkes-MIT-NRAO Sample". In: *AJ* 131, pp. 1914–1922. DOI: 10.1086/500827. eprint: astro-ph/0601037.

López-Gonzaga, N. et al. (2016). "Mid-infrared interferometry of 23 AGN tori: On the significance of polar-elongated emission". In: *AAP* 591, A47, A47. DOI: 10.1051/0004-6361/201527590. arXiv: 1602.05592.

Lucchini, M., F. Tavecchio, and G. Ghisellini (2017). "Revisiting the EC/CMB model for extragalactic large scale jets". In: *MNRAS* 466, pp. 4299–4306. DOI: 10.1093/mnras/stw3316. arXiv: 1610.01580 [astro-ph.HE].

Lynden-Bell, D. (1969). "Galactic Nuclei as Collapsed Old Quasars". In: *Nature* 223, pp. 690–694. DOI: 10.1038/223690a0.

MacDonald, N. R. et al. (2015). "Through the Ring of Fire: Gamma-Ray Variability in Blazars by a Moving Plasmoid Passing a Local Source of Seed Photons". In: *ApJ* 804, 111, p. 111. DOI: 10.1088/0004-637X/804/2/111. arXiv: 1505.01239 [astro-ph.HE].

Mannheim, K. and P. L. Biermann (1989). "Photomeson production in active galactic nuclei". In: *AAP* 221, pp. 211–220.

— (1992). "Gamma-ray flaring of 3C 279 - A proton-initiated cascade in the jet?" In: *AAP* 253, pp. L21–L24.

Maoz, E. (1998). "Dynamical Constraints on Alternatives to Supermassive Black Holes in Galactic Nuclei". In: *ApJL* 494, pp. L181–L184. DOI: 10.1086/311194. eprint: astro-ph/9710309.

Maraschi, L., G. Ghisellini, and A. Celotti (1992). “A jet model for the gamma-ray emitting blazar 3C 279”. In: *ApJL* 397, pp. L5–L9. DOI: 10.1086/186531.

Marscher, A. P. et al. (2010). “Probing the Inner Jet of the Quasar PKS 1510-089 with Multi-Waveband Monitoring During Strong Gamma-Ray Activity”. In: *ApJL* 710, pp. L126–L131. DOI: 10.1088/2041-8205/710/2/L126. arXiv: 1001.2574 [astro-ph.CO].

Marscher, A. P. et al. (2012). “Relation between Events in the Millimeter-wave Core and Gamma-ray Outbursts in Blazar Jets”. In: *ArXiv e-prints*. arXiv: 1204.6707 [astro-ph.HE].

Marshall, H. L. et al. (2001). “Structure of the X-Ray Emission from the Jet of 3C 273”. In: *ApJL* 549, pp. L167–L171. DOI: 10.1086/319161. eprint: astro-ph/0012162.

Marshall, H. L. et al. (2002). “A High-Resolution X-Ray Image of the Jet in M87”. In: *ApJ* 564, pp. 683–687. DOI: 10.1086/324396. eprint: astro-ph/0109160.

Marshall, H. L. et al. (2005). “A Chandra Survey of Quasar Jets: First Results”. In: *ApJS* 156, pp. 13–33. DOI: 10.1086/425578. eprint: astro-ph/0409566.

Marshall, H. L. et al. (2010). “A Flare in the Jet of Pictor A”. In: *ApJL* 714, pp. L213–L216. DOI: 10.1088/2041-8205/714/2/L213. arXiv: 1004.0191 [astro-ph.HE].

Marshall, H. L. et al. (2011). “An X-ray Imaging Survey of Quasar Jets: Testing the Inverse Compton Model”. In: *ApJS* 193, 15, p. 15. DOI: 10.1088/0067-0049/193/1/15. arXiv: 1101.5822 [astro-ph.HE].

Marshall, H. L. et al. (2018). “An X-Ray Imaging Survey of Quasar Jets: The Complete Survey”. In: *ApJ* 856, 66, p. 66. DOI: 10.3847/1538-4357/aaaf66. arXiv: 1802.04714 [astro-ph.HE].

Martel, A. R. et al. (2003). “Coronagraphic Imaging of 3C 273 with the Advanced Camera for Surveys”. In: *AJ* 125, pp. 2964–2974. DOI: 10.1086/375205.

Martínez-Paredes, M. et al. (2017). “The dusty tori of nearby QSOs as constrained by high-resolution mid-IR observations”. In: *MNRAS* 468, pp. 2–46. DOI: 10.1093/mnras/stx307. arXiv: 1702.02960.

Massaro, F. et al. (2009). “The Jet of 3C 17 and the Use of Jet Curvature as a Diagnostic of the X-ray Emission Process”. In: *ApJ* 696, pp. 980–985. DOI: 10.1088/0004-637X/696/1/980. arXiv: 0901.4718 [astro-ph.HE].

Matthews, T. A., W. W. Morgan, and M. Schmidt (1964). “A Discussion of Galaxies Indentified with Radio Sources.” In: *ApJ* 140, p. 35. DOI: 10.1086/147890.

McHardy, I. M. (1989). "X ray variability of active galactic nuclei". In: *Two Topics in X-Ray Astronomy, Volume 1: X Ray Binaries. Volume 2: AGN and the X Ray Background*. Ed. by J. Hunt and B. Battrick. Vol. 296. ESA Special Publication.

McKeough, K. et al. (2016). "Detecting Relativistic X-Ray Jets in High-redshift Quasars". In: *ApJ* 833, 123, p. 123. DOI: 10.3847/1538-4357/833/1/123. arXiv: 1609.03425 [astro-ph.HE].

McLure, R. J. et al. (1999). "A comparative HST imaging study of the host galaxies of radio-quiet quasars, radio-loud quasars and radio galaxies - I". In: *MNRAS* 308, pp. 377–404. DOI: 10.1046/j.1365-8711.1999.02676.x. eprint: astro-ph/9809030.

McNamara, A. L., Z. Kuncic, and K. Wu (2009). "X-ray polarization in relativistic jets". In: *MNRAS* 395, pp. 1507–1514. DOI: 10.1111/j.1365-2966.2009.14608.x. arXiv: 0902.1562 [astro-ph.HE].

McNamara, B. R., M. Rohanizadegan, and P. E. J. Nulsen (2011). "Are Radio Active Galactic Nuclei Powered by Accretion or Black Hole Spin?" In: *ApJ* 727, 39, p. 39. DOI: 10.1088/0004-637X/727/1/39. arXiv: 1007.1227.

Mertens, F. and A. Lobanov (2015). "Wavelet-based decomposition and analysis of structural patterns in astronomical images". In: *AAP* 574, A67, A67. DOI: 10.1051/0004-6361/201424566. arXiv: 1410.3732 [astro-ph.IM].

Mertens, F. and A. P. Lobanov (2016). "Detection of multiple velocity components in partially overlapping emitting regions". In: *AAP* 587, A52, A52. DOI: 10.1051/0004-6361/201527791. arXiv: 1601.05926 [astro-ph.HE].

Meyer, E. T. and M. Georganopoulos (2014). "Fermi Rules Out the Inverse Compton/CMB Model for the Large-scale Jet X-Ray Emission of 3C 273". In: *ApJL* 780, L27, p. L27. DOI: 10.1088/2041-8205/780/2/L27. arXiv: 1307.8421 [astro-ph.HE].

Meyer, E. T. et al. (2011). "From the Blazar Sequence to the Blazar Envelope: Revisiting the Relativistic Jet Dichotomy in Radio-loud Active Galactic Nuclei". In: *ApJ* 740, 98, p. 98. DOI: 10.1088/0004-637X/740/2/98. arXiv: 1107.5105 [astro-ph.CO].

— (2012). "Collective Evidence for Inverse Compton Emission from External Photons in High-power Blazars". In: *ApJL* 752, L4, p. L4. DOI: 10.1088/2041-8205/752/1/L4. arXiv: 1203.4991 [astro-ph.HE].

Meyer, E. T. et al. (2015). "Ruling out IC/CMB X-rays in PKS 0637-752 and the Implications for TeV Emission from Large-scale Quasar Jets". In: *ApJ* 805, 154, p. 154. DOI: 10.1088/0004-637X/805/2/154. arXiv: 1504.00577 [astro-ph.HE].

Meyer, E. T. et al. (2016). “An HST Proper-motion Study of the Large-scale Jet of 3C273”. In: *ApJ* 818, 195, p. 195. DOI: 10.3847/0004-637X/818/2/195. arXiv: 1601.03687.

Meyer, E. T. et al. (2017). “” In: *ApJL* 835, L35, p. L35. DOI: 10.3847/2041-8213/835/2/L35. arXiv: 1702.00015 [astro-ph.HE].

Meyer, E. T. et al. (2018). “Detection of an Optical/UV Jet/Counterjet and Multiple Spectral Components in M84”. In: *ApJ* 860, 9, p. 9. DOI: 10.3847/1538-4357/aabf39. arXiv: 1804.05122 [astro-ph.HE].

Miller, B. P. and W. N. Brandt (2009). “Chandra Observations of the Hybrid Morphology Radio Sources 3C 433 and 4C 65.15: FR IIs with Asymmetric Environments”. In: *ApJ* 695, pp. 755–764. DOI: 10.1088/0004-637X/695/1/755. arXiv: 0901.0925 [astro-ph.GA].

Miller, B. P. et al. (2006). “X-Ray Absorption and an X-Ray Jet in the Radio-loud Broad Absorption-line Quasar PG 1004+130”. In: *ApJ* 652, pp. 163–176. DOI: 10.1086/507509. eprint: astro-ph/0607031.

Morris, D., H. P. Palmer, and A. R. Thompson (1957). “Five radio sources of small angular diameter”. In: *The Observatory* 77, pp. 103–106.

Mullin, L. M. and M. J. Hardcastle (2009). “Bayesian inference of jet bulk-flow speeds in Fanaroff-Riley type II radio sources”. In: *MNRAS* 398, pp. 1989–2004. DOI: 10.1111/j.1365-2966.2009.15232.x. arXiv: 0906.2088 [astro-ph.HE].

Nalewajko, K., M. C. Begelman, and M. Sikora (2014). “Constraining the Location of Gamma-Ray Flares in Luminous Blazars”. In: *ApJ* 789, 161, p. 161. DOI: 10.1088/0004-637X/789/2/161. arXiv: 1405.7694 [astro-ph.HE].

Nenkova, M. et al. (2008). “AGN Dusty Tori. II. Observational Implications of Clumpiness”. In: *ApJ* 685, pp. 160–180. DOI: 10.1086/590483. arXiv: 0806.0512.

Netzer, H. (2015). “Revisiting the Unified Model of Active Galactic Nuclei”. In: *ARAA* 53, pp. 365–408. DOI: 10.1146/annurev-astro-082214-122302. arXiv: 1505.00811.

Neugebauer, G. et al. (1979). “Absolute spectral energy distribution of quasi-stellar objects from 0.3 to 10 microns”. In: *ApJ* 230, pp. 79–94. DOI: 10.1086/157063.

Northover, K. J. E. (1973). “The radio galaxy 3C 66”. In: *MNRAS* 165, p. 369. DOI: 10.1093/mnras/165.4.369.

O’Dea, C. P. (1998). “The Compact Steep-Spectrum and Gigahertz Peaked-Spectrum Radio Sources”. In: *PASP* 110, pp. 493–532. DOI: 10.1086/316162.

Osterbrock, D. E. (1991). "Active galactic nuclei". In: *Reports on Progress in Physics* 54, pp. 579–633. DOI: 10.1088/0034-4885/54/4/002.

Osterbrock, D. E. and W. G. Mathews (1986). "Emission-line regions of active galaxies and QSOs". In: *ARAA* 24, pp. 171–203. DOI: 10.1146/annurev.aa.24.090186.001131.

Perlman, E. S. et al. (2011). "Deep Multiwaveband Observations of the Jets of 0208-512 and 1202-262". In: *ApJ* 739, 65, p. 65. DOI: 10.1088/0004-637X/739/2/65. arXiv: 1107.2058 [astro-ph.HE].

Peterson, B. M. (2001). "Variability of Active Galactic Nuclei". In: *Advanced Lectures on the Starburst-AGN*. Ed. by I. Aretxaga, D. Kunth, and R. Mújica, p. 3. DOI: 10.1142/9789812811318_0002. eprint: astro-ph/0109495.

Petropoulou, M. and A. Mastichiadis (2012). "Temporal signatures of leptohadronic feedback mechanisms in compact sources". In: *MNRAS* 421, pp. 2325–2341. DOI: 10.1111/j.1365-2966.2012.20460.x. arXiv: 1201.2091 [astro-ph.HE].

Petropoulou, M., G. Vasilopoulos, and D. Giannios (2017). "The TeV emission of Ap Librae: a hadronic interpretation and prospects for CTA". In: *MNRAS* 464, pp. 2213–2222. DOI: 10.1093/mnras/stw2453. arXiv: 1608.07300 [astro-ph.HE].

Pierre Auger Collaboration et al. (2007). "Correlation of the Highest-Energy Cosmic Rays with Nearby Extragalactic Objects". In: *Science* 318, p. 938. DOI: 10.1126/science.1151124. arXiv: 0711.2256.

Piner, B. G. et al. (2007). "Relativistic Jets in the Radio Reference Frame Image Database. I. Apparent Speeds from the First 5 Years of Data". In: *AJ* 133, pp. 2357–2388. DOI: 10.1086/514812. eprint: astro-ph/0702317.

Piner, B. G. et al. (2012). "Relativistic Jets in the Radio Reference Frame Image Database. II. Blazar Jet Accelerations from the First 10 Years of Data (1994-2003)". In: *ApJ* 758, 84, p. 84. DOI: 10.1088/0004-637X/758/2/84. arXiv: 1208.4399.

Potter, W. J. and G. Cotter (2013). "Synchrotron and inverse-Compton emission from blazar jets - IV. BL Lac type blazars and the physical basis for the blazar sequence". In: *MNRAS* 436, pp. 304–314. DOI: 10.1093/mnras/stt1569. arXiv: 1310.0462 [astro-ph.HE].

Raiteri, C. M. et al. (2012). "Variability of the blazar 4C 38.41 (B3 1633+382) from GHz frequencies to GeV energies". In: *AAP* 545, A48, A48. DOI: 10.1051/0004-6361/201219492. arXiv: 1207.3979 [astro-ph.HE].

Rawlings, S. and R. Saunders (1991). "Evidence for a common central-engine mechanism in all extragalactic radio sources". In: *Nature* 349, pp. 138–140. DOI: 10.1038/349138a0.

Resconi, E. et al. (2017). "Connecting blazars with ultrahigh-energy cosmic rays and astrophysical neutrinos". In: *MNRAS* 468, pp. 597–606. DOI: 10.1093/mnras/stx498. arXiv: 1611.06022 [astro-ph.HE].

Röser, H.-J. et al. (2000). "The jet of 3C 273 observed with ROSAT HRI". In: *AAP* 360, pp. 99–106. eprint: astro-ph/0005592.

Roth, N. et al. (2012). "Three-dimensional Radiative Transfer Calculations of Radiation Feedback from Massive Black Holes: Outflow of Mass from the Dusty "Torus"". In: *ApJ* 759, 36, p. 36. DOI: 10.1088/0004-637X/759/1/36. arXiv: 1204.0063.

Rybicki, G. B. and A. P. Lightman (1979). *Radiative processes in astrophysics*.

Sahu, S., A. F. O. Oliveros, and J. C. Sanabria (2013). "Hadronic-origin orphan TeV flare from 1ES 1959+650". In: *PRD* 87.10, 103015, p. 103015. DOI: 10.1103/PhysRevD.87.103015. arXiv: 1305.4985 [hep-ph].

Salpeter, E. E. (1964). "Accretion of Interstellar Matter by Massive Objects." In: *ApJ* 140, pp. 796–800. DOI: 10.1086/147973.

Sambruna, R. M. et al. (2002). "A Survey of Extended Radio Jets in Active Galactic Nuclei with Chandra and the Hubble Space Telescope: First Results". In: *ApJ* 571, pp. 206–217. DOI: 10.1086/339859. eprint: astro-ph/0201412.

Sambruna, R. M. et al. (2004). "A Survey of Extended Radio Jets with Chandra and the Hubble Space Telescope". In: *ApJ* 608, pp. 698–720. DOI: 10.1086/383124. eprint: astro-ph/0401475.

Sambruna, R. M. et al. (2006). "Deep Chandra and Multicolor HST Follow-up of the Jets in Two Powerful Radio Quasars". In: *ApJ* 641, pp. 717–731. DOI: 10.1086/500526. eprint: astro-ph/0511459.

Scarpa, R. and R. Falomo (1997). "Are high polarization quasars and BL Lacertae objects really different? A study of the optical spectral properties." In: *AAP* 325, pp. 109–123.

Schinzel, F. K. et al. (2012). "Relativistic outflow drives γ-ray emission in 3C 345". In: *AAP* 537, A70, A70. DOI: 10.1051/0004-6361/201117705. arXiv: 1111.2045.

Schlickeiser, R. (1996). "Models of high-energy emission from active galactic nuclei." In: *AAPS* 120, pp. 481–489.

Schmidt, M. (1963). "3C 273 : A Star-Like Object with Large Red-Shift". In: *Nature* 197, p. 1040. DOI: 10.1038/1971040a0.

— (1968). "Space Distribution and Luminosity Functions of Quasi-Stellar Radio Sources". In: *ApJ* 151, p. 393. DOI: 10.1086/149446.

Schmidt, M. and R. F. Green (1983). “Quasar evolution derived from the Palomar bright quasar survey and other complete quasar surveys”. In: *ApJ* 269, pp. 352–374. DOI: 10.1086/161048.

Schmidt, M., D. P. Schneider, and J. E. Gunn (1995). “Spectrscopic CCD Surveys for Quasars at Large Redshift.IV.Evolution of the Luminosity Function from Quasars Detected by Their Lyman-Alpha Emission”. In: *AJ* 110, p. 68. DOI: 10.1086/117497.

Schreier, E. J., P. Gorenstein, and E. D. Feigelson (1982). “High-resolution X-ray observations of M87 - Nucleus, jet and radio halo”. In: *ApJ* 261, pp. 42–50. DOI: 10.1086/160316.

Schwartz, D. (2010). “Chandra enables study of x-ray jets”. In: *Proceedings of the National Academy of Science* 107, pp. 7190–7195. DOI: 10.1073/pnas.0913890107.

Schwartz, D. A. (2002). “X-Ray Jets as Cosmic Beacons”. In: *ApJL* 569, pp. L23–L26. DOI: 10.1086/340482.

Schwartz, D. A. et al. (2000). “Chandra Discovery of a 100 kiloparsec X-Ray Jet in PKS 0637-752”. In: *ApJL* 540, pp. 69–72. DOI: 10.1086/312875. eprint: astro-ph/0005255.

Schwartz, D. A. et al. (2006). “Chandra Observations of Magnetic Fields and Relativistic Beaming in Four Quasar Jets”. In: *ApJ* 640, pp. 592–602. DOI: 10.1086/500102. eprint: astro-ph/0601632.

Schwartz, D. A. et al. (2010). “Modeling X-Ray Emission of a Straight Jet:. PKS 0920-397”. In: *International Journal of Modern Physics D* 19, pp. 879–885. DOI: 10.1142/S0218271810017147.

Seyfert, C. K. (1943). “Nuclear Emission in Spiral Nebulae.” In: *ApJ* 97, p. 28. DOI: 10.1086/144488.

Shields, G. A. (1999). “A Brief History of Active Galactic Nuclei”. In: *PASP* 111, pp. 661–678. DOI: 10.1086/316378. eprint: astro-ph/9903401.

Siemiginowska, A. et al. (2002). “Chandra Discovery of a 300 Kiloparsec X-Ray Jet in the Gigahertz-peaked Spectrum Quasar PKS 1127-145”. In: *ApJ* 570, pp. 543–556. DOI: 10.1086/339629. eprint: astro-ph/0201116.

Siemiginowska, A. et al. (2003). “Chandra Discovery of an X-Ray Jet and Extended X-Ray Structure in the z = 0.63 Quasar B2 0738+313”. In: *ApJ* 595, pp. 643–655. DOI: 10.1086/377369. eprint: astro-ph/0306129.

Sikora, M., M. C. Begelman, and M. J. Rees (1994). “Comptonization of diffuse ambient radiation by a relativistic jet: The source of gamma rays from blazars?” In: *ApJ* 421, pp. 153–162. DOI: 10.1086/173633.

Sikora, M. et al. (2005). “Are Quasar Jets Dominated by Poynting Flux?” In: *ApJ* 625, pp. 72–77. DOI: 10.1086/429314. eprint: astro-ph/0502115.

Sikora, M. et al. (2009). "Constraining Emission Models of Luminous Blazar Sources". In: *ApJ* 704, pp. 38–50. DOI: 10.1088/0004-637X/704/1/38. arXiv: 0904.1414 [astro-ph.CO].

Singh, K. P. (2013). "An X-ray view of quasars". In: *Bulletin of the Astronomical Society of India* 41, p. 137. arXiv: 1310.0270 [astro-ph.CO].

Sobolewska, M. A. et al. (2014). "Stochastic Modeling of the Fermi/LAT γ-Ray Blazar Variability". In: *ApJ* 786, 143, p. 143. DOI: 10.1088/0004-637X/786/2/143. arXiv: 1403.5276 [astro-ph.HE].

Stanley, E. C. et al. (2015). "A Multiwavelength Study of Three Hybrid Blazars". In: *ApJ* 807, 48, p. 48. DOI: 10.1088/0004-637X/807/1/48. arXiv: 1505.05851 [astro-ph.HE].

Stawarz, Ł. and M. Ostrowski (2002). "Radiation from the Relativistic Jet: A Role of the Shear Boundary Layer". In: *ApJ* 578, pp. 763–774. DOI: 10.1086/342649. eprint: astro-ph/0203040.

Stawarz, Ł. et al. (2004). "On Multiwavelength Emission of Large-Scale Quasar Jets". In: *ApJ* 608, pp. 95–107. DOI: 10.1086/392502. eprint: astro-ph/0401356.

Tavecchio, F., G. Ghisellini, and A. Celotti (2003). "Clumps in large scale relativistic jets". In: *AAP* 403, pp. 83–91. DOI: 10.1051/0004-6361:20030375. eprint: astro-ph/0303161.

Tavecchio, F. et al. (2000). "The X-Ray Jet of PKS 0637-752: Inverse Compton Radiation from the Cosmic Microwave Background?" In: *ApJL* 544, pp. L23–L26. DOI: 10.1086/317292. eprint: astro-ph/0007441.

Tavecchio, F. et al. (2007). "Chandra and Hubble Space Telescope Observations of Gamma-Ray Blazars: Comparing Jet Emission at Small and Large Scales". In: *ApJ* 662, pp. 900–908. DOI: 10.1086/518085. eprint: astro-ph/0703359.

Tchekhovskoy, A., R. Narayan, and J. C. McKinney (2011). "Efficient generation of jets from magnetically arrested accretion on a rapidly spinning black hole". In: *MNRAS* 418, pp. L79–L83. DOI: 10.1111/j.1745-3933.2011.01147.x. arXiv: 1108.0412 [astro-ph.HE].

Trakhtenbrot, B. et al. (2011). "Black Hole Mass and Growth Rate at z ˜= 4.8: A Short Episode of Fast Growth Followed by Short Duty Cycle Activity". In: *ApJ* 730, 7, p. 7. DOI: 10.1088/0004-637X/730/1/7. arXiv: 1012.1871.

Tristram, K. R. W. et al. (2014). "The dusty torus in the Circinus galaxy: a dense disk and the torus funnel". In: *AAP* 563, A82, A82. DOI: 10.1051/0004-6361/201322698. arXiv: 1312.4534 [astro-ph.GA].

Turland, B. D. (1975). "3C 219 - A double radio source with a jet". In: *MNRAS* 172, pp. 181–189. DOI: 10.1093/mnras/172.1.181.

Uchiyama, Y. (2008a). "Emission from Large-Scale Jets in Quasars". In: *International Journal of Modern Physics D* 17, pp. 1475–1481. DOI: 10.1142/S0218271808013054. arXiv: 0809.2620.

— (2008b). "Emission from Large-Scale Jets in Quasars". In: *International Journal of Modern Physics D* 17, pp. 1475–1481. DOI: 10.1142/S0218271808013054. arXiv: 0809.2620.

Uchiyama, Y. et al. (2006). "Shedding New Light on the 3C 273 Jet with the Spitzer Space Telescope". In: *ApJ* 648, pp. 910–921. DOI: 10.1086/505964. eprint: astro-ph/0605530.

Ulvestad, J. S., R. R. J. Antonucci, and R. Barvainis (2005). "VLBA Imaging of Central Engines in Radio-Quiet Quasars". In: *ApJ* 621, pp. 123–129. DOI: 10.1086/427426. eprint: astro-ph/0411678.

Urry, C. M. (1996). "An Overview of Blazar Variability". In: *Blazar Continuum Variability*. Ed. by H. R. Miller, J. R. Webb, and J. C. Noble. Vol. 110. Astronomical Society of the Pacific Conference Series, p. 391. eprint: astro-ph/9609023.

Urry, C. M. and P. Padovani (1995). "Unified Schemes for Radio-Loud Active Galactic Nuclei". In: *PASP* 107, p. 803. DOI: 10.1086/133630. eprint: astro-ph/9506063.

van Breugel, W. J. M. and G. K. Miley (1977). "Radio 'jets'". In: *Nature* 265, pp. 315–318. DOI: 10.1038/265315a0.

Warmels, R. et al. (2018). *ALMA Technical Handbook, ALMA Doc. 6.3, ver. 1.0*. ISBN 978-3-923524-66-2.

Whitney, A. R. et al. (1971). "Quasars Revisited: Rapid Time Variations Observed Via Very-Long-Baseline Interferometry". In: *Science* 173, pp. 225–230. DOI: 10.1126/science.173.3993.225.

Willingale, R. (1981). "Use of the maximum entropy method in X-ray astronomy". In: *MNRAS* 194, pp. 359–364. DOI: 10.1093/mnras/194.2.359.

Willott, C. J. et al. (1999). "The emission line-radio correlation for radio sources using the 7C Redshift Survey". In: *MNRAS* 309, pp. 1017–1033. DOI: 10.1046/j.1365-8711.1999.02907.x. eprint: astro-ph/9905388.

Wilson, A. S. and Y. Yang (2002). "Chandra X-Ray Imaging and Spectroscopy of the M87 Jet and Nucleus". In: *ApJ* 568, pp. 133–140. DOI: 10.1086/338887. eprint: astro-ph/0112097.

Woo, J.-H. and C. M. Urry (2002). "Active Galactic Nucleus Black Hole Masses and Bolometric Luminosities". In: *ApJ* 579, pp. 530–544. DOI: 10.1086/342878. eprint: astro-ph/0207249.

Worrall, D. M. (2009). "The X-ray jets of active galaxies". In: *AAPR* 17, pp. 1–46. DOI: 10.1007/s00159-008-0016-7. arXiv: 0812.3401.

Worrall, D. M. and M. Birkinshaw (2001). “The X-Ray Emission of 3C 346 and Its Environment”. In: *ApJ* 551, pp. 178–185. DOI: 10.1086/320068. eprint: astro-ph/0012350.

Zdziarski, A. A. and M. Böttcher (2015). “Hadronic models of blazars require a change of the accretion paradigm”. In: *MNRAS* 450, pp. L21–L25. DOI: 10.1093/mnrasl/slv039. arXiv: 1501.06124 [astro-ph.HE].

Zel’dovich, Y. B. (1964). “The Fate of a Star and the Evolution of Gravitational Energy Upon Accretion”. In: *Soviet Physics Doklady* 9, p. 195.

Zhang, J. et al. (2018). “Examining the High-energy Radiation Mechanisms of Knots and Hotspots in Active Galactic Nucleus Jets”. In: *ApJ* 858, 27, p. 27. DOI: 10.3847/1538-4357/aab9b2. arXiv: 1803.08639 [astro-ph.HE].